

University of Nottingham
UK | CHINA | MALAYSIA

Recreating 3D limbal architectures by Two-Photon Polymerization for cornea regeneration

Elisabetta Prina, MSc, BSc

Thesis Submitted
to the University of Nottingham
for the Degree of Doctor of Philosophy

September 2017

Abstract

Limbal Epithelial Crypts (LECs) are stem cell niches located in the limbus, the area between the cornea and the conjunctiva, and are responsible for cornea epithelium regeneration. Their anatomical structures were identified and described by Dua et al (2005). Stem cells migrate from this area toward the cornea where they differentiate into corneal epithelial cells. The lack of the LECs determines a pathology called Limbal Stem Cell Deficiency (LSCD) that can cause conjunctivalization, neovascularisation, corneal opacification, eventually resulting in vision loss. Currently, the main carriers to support limbal stem cell proliferation and differentiation used in clinics do not include enclosed structures able to act as cell reservoirs. In addition, the driving forces that determine the migration and the differentiation of limbal stem cells are not clarified yet. The hypotheses of this thesis were that the stiffness and the geometry of the scaffold influence the limbal stem cell differentiation process. Understanding these key factors could help to inform the design of scaffolds for future cornea regeneration strategies. The effect of the stiffness on cell differentiation is a well-known mechanism, but is less investigated in the limbus-corneal tissue. In this work, it was studied by producing macro-scaffolds (d=8 mm) obtained by UV-crosslinking. The stiffness was varied by increasing the concentration of Gelatin Methacrylate (GelMA), a biocompatible, photocrosslinkable material. Compression tests, rheology, AFM, and swelling analysis were performed on the developed hydrogels and compared to the *ex vivo* human cornea values. The gels with a concentration between 5% and 15% (w/v) exhibited mechanical properties in the same order of magnitude obtained

for the cornea. The results indicated that the increased stiffness did not have a significant impact either in the expression of cytokeratin (CK3/CK14, stem cell marker, and CK14, differentiation marker), or in the gene expression (KRT3 and KRT19). However, the secondary key factors explored, differentiation media and oxygen concentration, supported cell differentiation. Inkjet printing was investigated as an additive manufacturing technique to produce 3D architectures. Although with this technique it was possible to develop a 3D structure with a stiffness gradient, its resolution was not sufficiently high to obtain a structure with dimensions comparable to the *in vivo* limbal stem cell niche. The second hypothesis was verified by developing a biocompatible scaffold mimicking the structure of the limbal stem cell niche and by evaluating the impact of its architecture on stem cell differentiation. The crypt geometry was modelled as U-shaped scaffolds with a diameter narrowing from 200 µm to 20 µm and was micro-fabricated from GelMA/PEGDA-based hydrogels using a Two-Photon Polymerization system (2PP). However, it was proven that the use of riboflavin as photoinitiator was inefficient at 780 nm, the wavelength used in the 2PP system. For this reason, P2CK was used as photoinitator to obtain stable hydrogels. The 2PP system allowed the precise recreation of the exact dimensions of the native crypts. Swelling, susceptibility to enzymatic degradation and stiffness were all evaluated. The biocompatibility of the printed scaffolds was assessed using immortalized human corneal epithelial cell proliferation up to 14 days. The ability of limbal stem cells to repopulate the crypts was demonstrated via two strategies. In the first strategy, human limbal stem cells were seeded directly inside the niche whilst in the second strategy,

primary human limbal explants were placed adjacent to the printed structures and cells migrated towards the scaffold. Cell distribution and differentiation along the z-axis were evaluated using confocal microscopy. Cytokeratin 14 (CK14) with p63 and Cytokeratin CK3/12 (CK3/12) were used as limbal stem cell and differentiated corneal epithelial cell markers, respectively. Limbal epithelial stem cells were cultured in two conditions: xeno-free media, and with primary cells in serum containing media on a feeder layer. Both conditions showed the zonation of markers along the z-axis, which was not observed on flat scaffolds, demonstrating that the geometry alone influences cell phenotype. This suggests that the enclosed geometry results in the generation of a microenvironment inside the niche that influences cell phenotype. The presence of soluble factors, generated by cellular secretions, a specific oxygen concentration, and a more 'stressful' biomechanical milieu for the cells are some hypotheses that need further investigation and will be the basis of future work.

In conclusion, the hypotheses of this thesis were partially confirmed. The variation in gel stiffness did not allow for the control of the hLESC differentiation process. However, the results demonstrated the influence of the geometry on stem cell differentiation without the use of signaling molecules. Further studies are necessary to have a description of the detailed spatial variability of the scaffold's characteristics. Overall, the 2PP approach is flexible and could be applied to the generation of stem cell niches of other tissues, and could represent a significant advance in regenerative medicine.

Acknowledgments

First of all, I would like to thank my supervisors Dr Felicity Rose for her advice and guidance through this PhD, and Prof. Ricky Wildman and Dr Jing Yang for introducing me to the world of additive manufacturing. I would also like to thank Laura Sidney for her constant assistance, and Robert Markus for all the help with the confocal microscope. I would like to acknowledge Prof. Harminder Dua for his support and understanding of the clinical aspects of the project. I would like to thank Dr Stefano Ferrari for the opportunity he gave me to join the Veneto Eye Bank Foundation. Thanks to all the team in Mestre for the warm welcome and their enthusiasm during the placement. Special thanks to Marina Bertolin and Claudia Breda for their support in the lab. Thanks to Dr Andy Hopkinson for supporting my placement.

I would like to thank the Additive Manufacturing group, in particular Hagit Gilon for printing the 3D scaffold and for all the scientific discussions.

I would like to thank Maximilian Tromayer and Jonathan Moore for providing the photoinitiator, Chen Xinyong for his advice on the AFM, David Onion for his help with the flow cytometry, and Christine Grainger-Boultby for her help with SEM imaging.

I would like to thank the EPSRC CDT programme for funding my research and for the opportunity to work on this project (MRC-EPSRC EP/L015072/1 grant).

I would like to thank all the Regenerative Medicine and Cellular Therapies group in Nottingham for their support during these years. In particular, I would like to thank my 'fourth supervisor' Tesh for all the time spent in answering questions, in discussing and discussing and discussing again my project. Thanks for letting me breathe, laugh and sing along these four years. Special thanks to Lalitha, Meena, Annesi, Aiswarya, Afnan, Lara, Rehma, Mahi, Aruna, Francesco, Antonio, Marta, Hosam and Sandhya these years would not have been the same without you.

Thanks to Bryan and all the Nottingham Rockets volleyball team!

Thanks to Lorenzo for always having time for a coffee, for listening and of course for playing tennis, thanks to Sophie for all the ‘special’ dinners and for the time spent together.

Thanks to all the friends in Sheffield, Stefano, Valeria, Claudia, Enrico, Felicia, Giuliano, Federica, Blazey, Iwona, and little Leon to have made my days in the east midlands and Yorkshire lighter. Thanks to my ‘old’ friends, far but always so close, Laura, Chiara, Laura, Silvia, Anna, Bosco, Francesca…and of course thanks to the Peak district… to be always so peaceful.

Thanks to my mum and dad for always supporting me and always being there for me. Thanks to my sisters, Alessandra and Elena to be always ready to answer the phone, listen to me, help me, and calm me down! Thanks to Gabri, Franci, the little one, Sevan and Otavio for filling my days back at home, and thanks to Luciana and Peter for supporting our decisions.

And thanks to Fabio to be always at my side, to walk (and sometimes run) with me under the rain, and under the sun.

List of publications

- 3D Microfabricated Scaffolds and Microfluidic Devices for Ocular Surface Replacement: a Review. Prina E, Mistry P, Sidney LE, Yang J, Wildman RD, Bertolin M, Breda C, Ferrari B, Barbaro V, Hopkinson A, Dua HS, Ferrari S, Rose FRAJ. Stem Cell Rev. 2017; 13(3):430-441.

- Surface chemistry of Ti6Al4V components fabricated using selective laser melting for biomedical applications. Vaithilingam J, Prina E, Goodridge RD, Hague RJM, Edmondson S, Rose FRAJ, Christie SDR. Mater Sci Eng C Mater Biol Appl. 2016; 67:294-303.

Table of content

Abstract..... i

Acknowledgments..... iv

List of publications..... vi

Table of content..... vii

List of figures..... xi

List of tables..... xv

Table of abbreviations..... xvi

1. General introduction..... 1

1.1 An Introduction to the cornea..... 1

1.2 The Limbus..... 3

1.2.1 Cornea cells and limbal stem cells: marker characterization..... 5

1.2.2 Stem cell differentiation: important factors..... 7

1.2.3 Limbus geometry and dimensions..... 8

1.2.4 Limbus and cornea mechanical properties..... 11

1.2.3 Extracellular matrix composition..... 17

1.2.4 Hypoxic environment..... 18

1.2.4 Soluble factors and additional factors..... 21

1.3 Clinical context and current solutions..... 21

1.3.1 Limbal stem cells deficiency..... 22

1.3.2 Current treatments: donor graft tissues and amniotic membrane..... 23

1.3.3 Current strategies for limbus replacement in tissue engineering..... 26

1.4 Additive manufacturing..... 30

1.4.1 Two-Photon Polymerization (2PP) system..... 33

1.5 Aims and objectives..... 38

2. Materials and Methods..... 40

2.1 Material preparation..... 40

2.1.1 GelMA synthesis..... 40

2.1.2 GelMA preparation..... 42

2.2 Scaffold characterization..... 44

2.2.1 Rheology..... 44

2.2.2 Texture analysis..... 46

2.2.3 Atomic force microscopy (AFM)..... 46

2.2.4 Swelling analysis..... 48

2.2.5 Susceptibility to Enzymatic Degradation..... 49

2.3 Cell culture..... 50

2.3.1 General methods for cell cultivation 50
2.3.2 Frozen storage of cells 50
2.3.3 Cell revival from frozen storage 51
2.3.4 Cornea epithelial cells 51
2.3.5 Commercial human limbal stem cells 52
2.3.6 Primary cells extracted from human cornea biopsy 52
2.4 Cell characterisation 55
2.4.1 PrestoBlue® assay 55
2.4.2 Live/Dead™ Fluorescence assay 55
2.4.3 Cell fixation 56
2.4.4 Immunohistochemistry 56
2.4.5 qPCR 58
2.5 Microscopy and imaging 60
2.5.1 Confocal microscopy 60
2.5.2 Scanning electron microscopy (SEM) 60
2.5.3 CryoSEM 60
2.6 Additive manufacturing techniques 61
2.6.1 3D inkjet printer 61
2.6.2 Two photon polymerization 62
2.7 Statistical analysis 64
3. Cornea and stiffness: Gelatin methacrylate and 3D printed structures 66
3.1 Introduction 66
3.1.1 Chapter objectives 68
3.2 Experimental design 69
3.2.1 Evaluation of corneal mechanical properties and swelling value 69
3.2.2 Evaluation the degree of methacrylation of GelMA 70
3.2.3 Preparation of GelMA at different concentrations 70
3.2.4 Selection of GelMA concentrations according to stiffness values of the human cornea 71
3.2.5 Manufacturing of a 3D printed scaffold using a Pico-dot printer 74
3.2.6 Effect of GelMA stiffness and 3D architecture on cornea cell viability 76
3.3 Results 77
3.3.1 Determination of the mechanical properties of the human cornea 77
3.3.2 GelMA solution was successfully synthesised 77
3.3.3 GelMA hydrogels matches human cornea tissue mechanical properties 79
3.3.4 Viscosity of GelMA solutions that can be 3D printed 84
3.3.5 hCECs are able to grow on both cast and printed GelMA scaffolds 88

3.4 Discussion and conclusion 92
4. Investigation of Riboflavin as a photoinitiator for GelMA destined for corneal applications 100
4.1 Introduction 100
4.1.1 Chapter objectives 102
4.2 Experimental sections 102
4.2.1 GelMA hydrogel preparation by Riboflavin solution 103
4.2.2 Irgacure preparation 104
4.2.3 Gel characterization 104
4.2.4 Cell viability 105
4.2.5 R20 crosslinking by 2PP 107
4.3 Results 108
4.3.1 Riboflavin-GelMA can be crosslinked by UV light 108
4.3.2 Riboflavin solutions are compatible in the range 0.01-140 µM, triethanolamine below 35 mM. 113
4.3.3 2PP structures: riboflavin is not suitable for 2PP printing: comparison of UV and 2PP crosslinking 115
4.4 Discussion and conclusions 116
5. Development of a 3D scaffold that mimics the geometry of limbal epithelial crypts using a two photon polymerization system 122
5.1 Introduction 122
5.1.1 Chapter objectives 125
5.2 Experimental design 126
5.2.1 Optimization of 2PP structures and development of 3D niche structures 126
5.2.2 Investigation of a stiffness gradient of 2PP structures 129
5.3 Results 134
5.3.1 GelMA can be used to print LECs structure 134
5.3.2 GelMA and GelMA-PEGDA can be used to print LECs structures with a stiffness gradient 137
5.3.3 Analysis of water content and degradation rate of the printed scaffolds 140
5.3.4 Evaluation of PI cytotoxicity 143
5.3.5 Cells are able to grow on 2PP scaffolds 144
5.4 Discussion 147
6. Investigation of limbal stem cell differentiation in the 3D printed scaffold: assessing the influence of geometry and stiffness 155
6.1 Introduction 155
6.1.1 Chapter objectives 157
6.2 Experimental design 158

6.2.1 Evaluation of the stiffness effect on limbal stem cell differentiation in normoxic and hypoxic conditions 159
6.2.2 Evaluation of scaffold geometry on limbal stem cell distribution and differentiation 160
6.3 Results 164
6.3.1 Stiffness had an impact on stem cell differentiation depending on the media composition 164
6.3.2 Cells assembled as homogenous monolayers in xeno-free culture conditions and formed colonies in the serum-media and feeder layer culture conditions 170
6.3.3 Cells were distributed along the niche on the printed structures 171
6.3.4 Cells differentiated according to z-position 174
6.3.5 Cells did not differentiate on micro-scaffolds with increased stiffness 177
6.3.6 Effect of hypoxic environment on c_hLESC differentiation within the 2PP printed crypt shaped scaffolds 178
6.4 Discussion and conclusion 180
7. Summary, conclusion and future work 191
References 200
Appendix A 215
Appendix B 216
Appendix C 217
Appendix D 218

List of figures

Figure 1.1: Representation of the ocular structures (centre), and cross-section of the cornea showing six distinct layers (left). 1
Figure 1.2: Anterior surface of the human eye, and limbus location....4
Figure 1.3: The X, Y, Z hypothesis of Corneal Epithelial Maintenance. 5
Figure 1.4: Schematic representation of the extrinsic factors that may have a synergistic effect on limbal stem cell differentiation. 8
Figure 1.5: LECs as defined by Dua et al. (2005). 9
Figure 1.6: LCs and FSPs defined by Shortt et al. 2007. 10
Figure 1.7: Force-displacement curves for the cornea, sclera, and limbus. 11
Figure 1.8: Schematic representation of the cornea layers and elastic modulus. 12
Figure 1.9: schematic representation of durotaxis in relation to limbal stem cell maintenance and differentiation. 15
Figure 1.10: representation of the regional variation of tenascin C and desmoglein 3....18
Figure 1.11: Effect of a hypoxic environment on limbal epithelial cells investigated in four independent studies. 20
Figure 1.12: Effect of limbal stem cell deficiency due to a chemical burn injury. 22
Figure 1.13: Representation of *ex vivo* cultivated limbal epithelial protocol, includes two strategies: the limbal explant and suspension culture method. 24
Figure 1.14: Clinical photographs showing the SLET technique. 25
Figure 1.15: A tissue engineering strategy for limbal replacement. 29
Figure 1.16: Laser intensity distribution. 34
Figure 1.17: (a) Single photon absorption and two-photon absorption mechanisms. (b) Schematic representation of the confinement of the focal point defined by the NA and the threshold intensity. 35
Figure 1.18: Number of publication about 2PP between 1974 and 2016. 37
Figure 1.19: Overview of the thesis structure. 39
Figure 2.1: Chemical synthesis scheme of methacrylate substitution of the primary amines of gelatin. 40
Figure 2.2: Representation of the steps to prepare GelMA and mechanism involved in the polymerization process. 43
Figure 2.3: Schematic representation of rheological measurement....45
Figure 2.4: Force-curve graph with tip-surface interaction. 48
Figure 2.5: phase contrast images of human corneal epithelial cell line (hCECs). 51
Figure 2.6: Steps to extract limbal stem cells from a cornea-limbus-conjunctiva biopsy....53
Figure 2.7: Steps to culture tissue derived primary limbal stem cells (td_hLESCs) extracted from the biopsy. 54
Figure 2.8: 3D inkjet printing system for gelatine based inks....62

Figure 2.9: Set-up of the two photopolymerization system. 63
Figure 2.10: Configuration of gel set up and 2PP system. 64
Figure 3.1: Preparation of human cornea samples for mechanical testing. 70
Figure 3.2: Preparation of gel for compression and rheological test. 71
Figure 3.3: Flow chart for the selection of GelMA concentrations. 72
Figure 3.4: Schematic representation of the 3D bioprinted structures. 75
Figure 3.5: Frequency sweep test of *ex-vivo* human cornea. 77
Figure 3.6: Gelatin methacrylate characterization. 78
Figure 3.7: Elastic modulus of hydrogels varying GelMA percentage obtained from compression testing. 80
Figure 3.8: Elastic modulus of G5, G15, G25, and G40 in comparison to *ex-vivo* human cornea values obtained with the compression test. 80
Figure 3.9: Mass swelling ratio of hydrogels at various GelMA concentrations % (w/v) and *ex-vivo* human cornea. 81
Figure 3.10: Pore dimensions of hydrogels and Cryo SEM images. 82
Figure 3.11: Frequency sweep test of cross-linked GelMA and *ex-vivo* human cornea. 83
Figure 3.12: Surface elastic modulus of four concentrations of GelMA determined by AFM measurements. 84
Figure 3.13: Viscosity and gel point of GelMA solutions at different concentrations by varying the temperature and GelMA concentration. 85
Figure 3.14: Representative brightfield images of crosslinked pillars. 86
Figure 3.15: Frequency sweep test of printed GelMA (G25 and G40) compared to the cast samples. 87
Figure 3.16: Metabolic activity of hCECs seeded and cultured on gels at different GelMA concentrations. 89
Figure 3.17: Inverted microscope images of calcein AM-labelled hCECs seeded on pillars structure G15/G40 after seeding. 90
Figure 3.18: SEM images of hCECs seeded on 3D printed scaffolds. 91
Figure 4.1: Workflow describing the approach for R20 optimization. 103
Figure 4.2: Storage (closed symbols) and loss modulus (open symbols) as a function of temperature (25°C-45°C) of R20 gels. 110
Figure 4.3: Storage (closed symbol) and loss modulus (open symbol) of R-gel 200-200 as a function of temperature between 25°C and 100°C. 110
Figure 4.4: Storage (closed symbols) and loss modulus (open symbols) of R20-gel 200-200 (square symbol) and G20 crosslinked for 10 min (triangle symbol) as a function of frequency measured between 0.1 and 10 Hz. 111
Figure 4.5: Cryo SEM pictures and average pore dimensions of R-gels and IR-gels. 112
Figure 4.6: Mass swelling ratio of IR-gels and R20-gels. 113

Figure 4.7: 3T3 viability vs increasing concentration of (a) riboflavin, (b) triethanolamine and (c) a solution composed of both riboflavin and triethanolamine. 114
Figure 4.8 : Metabolic activity of hCECs seeded on IR-gels, R200-200 and the control (well plate). 115
Figure 4.9: CAD file and scaffolds produced by 2PP using riboflavin-triethanolamine as the photoinitiator. 116
Figure 4.10: Hypothesis of the mechanism involved in the preparation of hydrogels. 119
Figure 5.1: Limbal stem cell niche representation. 129
Figure 5.2: Set-up for printing a 3D structure with a stiffness gradient. 130
Figure 5.3: Printability of hydrogels of varying GelMA and P2CK concentrations. 135
Figure 5.4: Study how the printing parameters affect the scaffold stability. 136
Figure 5.5: 2PP printed GelMA scaffolds replicating the dimensions of the LEC stem cell niche. 137
Figure 5.6: Printed structure following the first strategy (increasing hatching distance from the bottom to the top). 139
Figure 5.7: Printed structure following the second strategy (two materials were printed on top of each other). 139
Figure 5.8: Elastic modulus of macro-scaffolds (G15, G15-5, and G15-20) determined by compression testing. Data presented as mean ± SD (n=2). 139
Figure 5.9: (a) Volumetric water content (%) of 2P15 and 2P15-5 after 24 h in PBS. 140
Figure 5.10: Volume remaining (%) after the addition of 1 mg/mL collagenase to micro- and macro-scaffolds. 142
Figure 5.11: Viability of hCEC in contact with P2CK and Irgacure. 144
Figure 5.12: hCECs proliferation on GelMA and PEGDA-based scaffold. 145
Figure 5.13: hCEC distribution along the printed niches. 146
Figure 5.14: Representative confocal images in z-stack of hCEC cells stained with Calcein AM live cell stain after 1 day (seeded at high concentration). 147
Figure 6.1: Representation of the two strategies adopted to study the cell distribution and differentiation along the z-axis of the 3D printed niches. 162
Figure 6.2: Representation of the areas on which the elastic modulus of the 2PP scaffold were mesaured by AFM. 163
Figure 6.3: Number of stem cells (c_hLESCs) and differentiated cells cultured on GelMA hydrogels (G5, G15, G25, and G40). 165
Figure 6.4: Confocal microscope images of limbal stem cells (c_hLESCs) grown on GelMA hydrogels (G5, G15, G25, and G40) and cultured in CnT-PR, the basal media. 166
Figure 6.5: Confocal microscope images of limbal stem cells (c_hLESCs) grown on GelMA hydrogels (G5, G15, G25, and G40) and cultured in CnT-PR-D, the differentiation media. 167

Figure 6.6: c_hLESCs gene expression in response to gel stiffness, media composition and oxygen concentration measured by qPCR. 169
Figure 6.7: Cultivation of limbal epithelial cells. 171
Figure 6.8: Proliferation of td_LESCs seeded on the 2PP scaffolds. 172
Figure 6.9: Z-stack confocal images of Hoechst-stained hLESCs. 172
Figure 6.10: Cell migration from a limbus biopsy towards the scaffold. 173
Figure 6.11: Z-stack confocal images of Hoechst-stained cells for the second strategy. 174
Figure 6.12: Series of confocal Z-stack images showing c_hLESCs seeded within the scaffolds, according to the first strategy (seeding cell suspension inside the niches). 175
Figure 6.13: Series of confocal Z-stack images showing td_hLESCs seeded within the scaffolds, according to the first strategy (seeding cell suspension inside the niches). 176
Figure 6.14: Surface elastic modulus of the scaffold according to the z-position. 177
Figure 6.15: Confocal images of c_hLESCs on flat surfaces stained with CK3/12 (green; differentiated cells), CK14 (red; stem cells) and HOECHST (blue; cell nuclei). 178
Figure 6.16: Series of confocal Z-stack images showing c_hLESCs seeded within the 2PP printed crypt shaped scaffolds, cultured in hypoxic condition and fixed after 10 days. 179
Figure 6.17: Representation of the results obtained by seeding LESCs inside the 2PP scaffold. Mechanisms involved in the limbal stem cell differentiation process. 190
Figure 6.18: Representation of the mechanisms that could have been involved in the limbal stem cell differentiation process. 190

List of tables

Table 1.1: common markers for basal limbal and corneal epithelial cells. 6
Table 1.2: Summary of the current techniques used to measure the cornea mechanical properties. 13
Table 2.1: Gel nomenclatures with corresponding photoinitiators, light source and mechanisms used to photocrosslink the hydrogels. 44
Table 2.2: Primary and secondary antibodies used in immunofluorescence. 57
Table 3.1: Gels nomenclature. 71
Table 3.2: Elastic moduli of three *ex-vivo* human cornea donor samples. 77
Table 3.3: DS of three different batches of GelMA measured by TNBS assay. 79
Table 3.4: Gel points of G5, G15, G25, and G40. 85
Table 3.5: Storage modulus at 1 Hz of cornea samples, cast G5, G15, G25, G40, and printed G25, G40. 87
Table 3.6: Summary of the mechanical characterization of the GelMA and human corneal tissue. 88
Table 4.1: Gels nomenclature. 104
Table 4.2: Riboflavin and triethanolamine solutions. 106
Table 4.3: Gels selected for further analysis. Riboflavin and triethanolamine were diluted in PBS and mixed with GelMA solution at 20% (w/v). 108
Table 5.1: Gels nomenclature. 131
Table 5.2: Molar, and weight concentration of P2CK and Irgacure. 132
Table 5.3: Summary of the tests and the method used to characterize the micro-scaffolds and macro-scaffolds. 134

Table of abbreviations

Abbreviation	Definition
2PP	Two-Photon-Polymerization system
AFM	Atomic Force Microscopy
AM	Amniotic Membrane
BSA	Bovine Serum Albumine
c_hLESCs	Commercial Human Limbal Epithelial Stem Cells
CAD	Computed Aided Design
CFE	Colony Forming Efficiency
CK	Cytokeratin
CnT-PR-D	Differentiation media
CnT-Prime	Basal medium
DMEM	Dulbecco's Modified Eagle Medium
DMSO	Dimethyl Sulfoxide
DS	Degree of substitution
E	Elastic (or Young's) modulus
ECM	Extracellular matrix
EGF	Epidermal Growth Factor
EthD-1	Ethidium homodimer-1
FBS	Foetal Bovine Serum
FSP	Focal Stromal Projection
G'	Storage modulus
G''	Loss modulus
GelMA	Gelatin Methacrylate
hCECs	Human Corneal Epithelial Cells
LC	Limbal Crypt
LEC	Limbal Epithelial Crypt
LESCs	Limbal Epithelial Stem Cells
LSCD	Limbal Stem Cell Deficiency
NA	Numerical Aperture
NMR	Nuclear Magnetic Resonance
P/S	Penicillin-Streptomycin
P2CK	Benzylidene ketone-based water-soluble photoinitiator
PBS	Phosphate-buffered saline
PEGDA	Poly(ethylene glycol) diacrylate
PFA	Paraformaldehyde
PI	Photoinitiator
RT	Room Temperature
SD	Standard Deviation

SEM	Scanning Electron Microscopy
TAC	Transient Amplifying cell
td_hLESCs	Tissue-derived human Limbal Epithelial Stem Cells
TEOHA	Triethanolamine
TNBS	2,4,6-Trinitrobenzene Sulfonic Acid
UV	Ultraviolet
VLR	Visco-Linear Region

1. General introduction

1.1 An Introduction to the cornea

The cornea is a transparent window at the front of the eye, and is primarily responsible for focusing light onto the retina. It accounts for two thirds of the focusing of light, the remainder being achieved by the crystalline lens. The cornea is composed of five major layers: the epithelium, Bowman's layer, stroma, Descemet's membrane and the endothelium (figure 1.1). In addition to this classical subdivision, Dua et al. (2013) recently discovered the presence of a new layer (Dua's Layer).

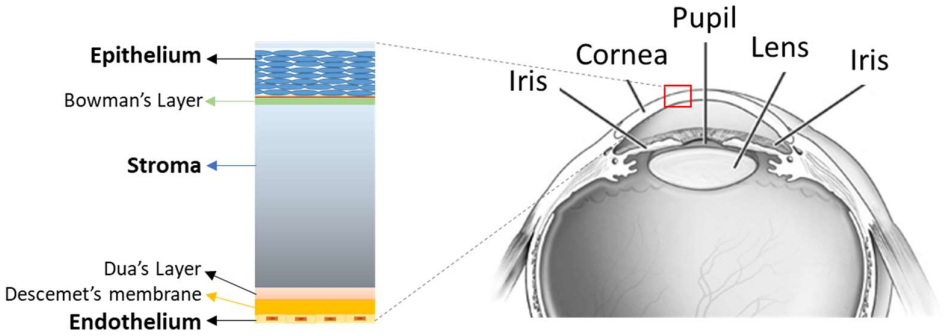


Figure 1.1: Representation of the ocular structures (centre), and cross-section of the cornea showing six distinct layers (left). Adapted from (Murphy, 2013).

At the anterior cornea, facing the outside environment is the epithelium, a stratified cellular layer composed of non-keratinized squamous epithelial cells bathed by the tear film, which gives it its final optical polish. The original source of these epithelial cells are the limbal epithelial crypts, stem cell niches found in the outer ring of the cornea (Dua and Azuara-Blanco, 2000; Dua *et al.*, 2005). These limbal stem cells allow the epithelium to self-renew and heal defects.

Separating the epithelium from the stroma below is the Bowman's layer, a tough acellular layer composed predominantly of collagen and laminin. The middle layer of the cornea, the stroma, makes up the bulk of the thickness of the cornea, and consists primarily of lamellar sheets of collagen-I fibrils arranged in a highly-ordered manner compatible with corneal transparency. The stroma is populated with cells of mesenchymal origin called keratocytes, responsible for maintaining the structured extracellular matrix (ECM) of collagen and proteoglycans (Marshall *et al.*, 1991; Meek and Boote, 2004). In a healthy cornea, keratocytes exhibit a dendritic morphology, with extensive cellular contacts (Poole *et al.*, 1993; West-Mays and Dwivedi, 2006). However, during trauma or disease, these cells can become activated and exhibit morphological characteristics of fibroblasts and commence tissue remodelling (Funderburgh *et al.*, 2003). In later stages of remodelling, a myofibroblast phenotype also appears, expressing α-smooth muscle actin (α-SMA). This can cause scar formation, contraction and loss of corneal transparency (Jester *et al.*, 1995; West-Mays and Dwivedi, 2006). Evidence has been presented demonstrating that the limbal region of the corneal stroma also contains a mesenchymal stem cell population that can be used to regenerate the cornea (Hashmani *et al.*, 2013; Sidney *et al.*, 2015).

The posterior two layers of the cornea are the Descemet's membrane, a thin acellular layer composed mainly of collagen-IV which acts as a modified basement membrane for the final layer, and the corneal endothelium. The corneal endothelium is composed of simple cuboidal cells that maintain fluid balance within the cornea. These cells are not related to vascular or lymphatic

endothelial cells. Corneal endothelial cells have very limited proliferative capacity *in vivo*, dividing rarely in the adult cornea (Waring *et al.*, 1982; Capella and Kaufman, 1969). As a result, wounding and trauma of the endothelium is difficult to reverse. A relatively increased concentration of elastin has been shown to run as an annulus along the limbus in the peripheral cornea and in the pre-Descemet's layer (recently named 'Dua's layer') (Lewis *et al.*, 2016).

1.2 The Limbus

The corneal epithelial cells lost during the healing process and during physiological turnover are replaced by new cells derived from Limbal Epithelial Stem Cells (LESCs) (Davanger and Evensen, 1971; Dua *et al.*, 1994). Generally, stem cells are located in unique microenvironments, called niches, where they can reside for an indefinite period of time and produce progeny cells whilst self-renewing (Ohlstein *et al.*, 2004). In the eye, niches populated by LESCs are located in the limbus, the 1 mm-wide ring region separating the sclera from the cornea (figure 1.2). The niches are located deep in the stroma that acts as protection from physical trauma and pathologies.

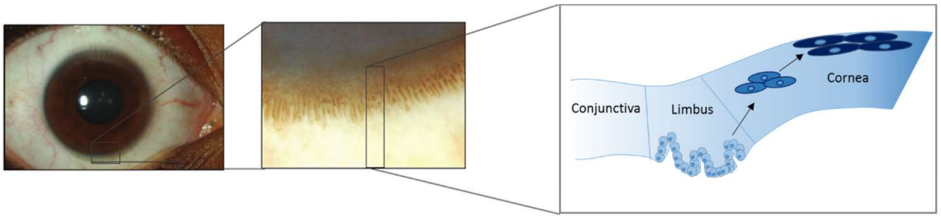


Figure 1.2: Anterior surface of the human eye, and limbus location. The limbus is clearly visible in some individuals, allowing the visualisation of the limbal palisades of Vogt due to their pigmentation. Representation of conjunctiva, limbus and cornea cross section. Limbal progenitor cells (light blue cells) differentiate into transient amplifying cells (blue cells) and then fully differentiated epithelial cells (dark blue cells). Adapted from (Haagdorens *et al.*, 2016).

The niche also regulates the LESC cell cycle to keep them in an undifferentiated resting state (Schofield, 1983). Limbal progenitor cells differentiate into Transient Amplifying Cells (TAC), then after a high but limited number of mitoses, they differentiate into post-mitotic cells and finally terminally differentiated cells (Tseng, 1989; Dua *et al.*, 2000). During this differentiation process, cells migrate centripetally from the niche to the corneal surface according to the XYZ hypothesis, first described by Thoft and Frien (1983). In this mechanism, X, Y and Z represent the proliferation of epithelial basal cells, the centripetal movement of peripheral cells, and the cell loss from the surface, respectively (figure 1.3).

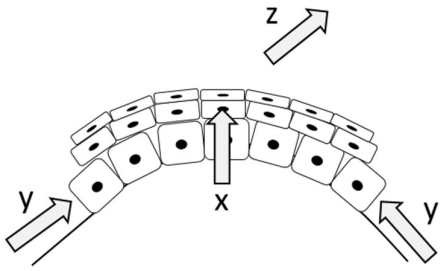


Figure 1.3: The X, Y, Z hypothesis of Corneal Epithelial Maintenance. X is the proliferation of basal cells, y the centripetal movement of cells and z the cell loss from the surface (Thoft and Friend, 1983).

1.2.1 Cornea cells and limbal stem cells: marker characterization

Even if the existence and proliferation of LESCs in the limbus is now accepted within the research and clinical communities, their precise distribution in this anatomically-segregated region is still being debated. This is also due to the lack of specific markers and the poor understanding of molecular characteristics of LESCs. This has an impact on the effectiveness of the grafts prepared for therapeutic intervention. It has been demonstrated that limbal stem cells are only less than 10% of the total limbal basal cell population (Cotsarelis *et al.*, 1989; Wolosin *et al.*, 2004). Generally, LESCs can be discriminated from differentiated corneal epithelial cells based on their basal location within the Palisades of Vogt, morphological criteria, and a panel of stem cell markers. Regarding cell size, differences have been detected moving from the epithelium towards the stroma (Romano *et al.*, 2003; Shortt *et al.*, 2007; Levis *et al.*, 2013). The cells located at the base of the limbal crypts presented a smaller size (diameter 10.1 ± 0.8 μm, area 47.88 ± 12.82 μm^2) and a high nucleus to

cytoplasm ratio, compared to the cells of the basal corneal epithelium (diameter 17.1 ± 0.8 µm, area 207.8 ± 37.25 μm^2).

Some of the more widely accepted biochemical markers include cytoskeletal intermediate filament proteins such as CK14 (Figueira *et al.*, 2007), CK15 (Yoshida *et al.*, 2006), CK19, membrane transport protein including ABCG2 (de Paiva *et al.*, 2005), ABCB5 (Ksander *et al.*, 2014), transcription factors such as p63 (Pellegrini *et al.*, 2001; Di Iorio *et al.*, 2005), and cell adhesion molecules and receptors such as integrin αvβ5 (Ordonez *et al.*, 2013). On the contrary, CK3/12 are related to the cornea epithelial differentiation (Pitz and Moll, 2002; Chen *et al.*, 2004), and not expressed by epithelial cells in the basal layer (Chen *et al.*, 2004). In table 1.1, the more common markers for basal limbal and corneal epithelial cells are reported.

Table 1.1: common markers for basal limbal and corneal epithelial cells. The negative sign (-) means negative expression, while the positive sign (+) means positive expression of the marker in the corresponding epithelium area (limbal or corneal). Taken from (Hamrah and Sahin, 2013).

Marker	Limbal epithelium (Basal)	Corneal Epithelium (Basal)
Cytokeratin		
CK3/CK12	-	+++
CK14	++	-
CK19	++	-
CK5	++	-
Transporters		
Na+/K+ ATPase	+++	++
ABCG2	+++	-
Transcription factors		
p63	+++	±

1.2.2 Stem cell differentiation: important factors

Generally, cell turnover can be described with respect to symmetric and asymmetric division that can be controlled through intrinsic and extrinsic mechanisms. Symmetric division refers to a mechanism in which cells divide to produce two identical stem cells or differentiated daughter cells. In asymmetric division, cells generate one stem cell and one differentiated daughter cell (Di Girolamo, 2015).

In the cornea, it is likely that asymmetric mitosis is reserved for LESCs within the limbus while symmetric division is the most predominant mechanism of the more differentiated basal cells of the central cornea, and it is mainly defined by extrinsic signals. This process occurs when cells leave the basal compartment at the limbus (Castro-Muñozledo and Gómez-Flores, 2011).

Intrinsic factors are related to inherited polarity responsible for setting up asymmetric cell divisions, nuclear factors controlling gene expression and chromosomal modifications, and clocks that could set the number of rounds of division within the transit amplifying population (Watt, 2000). Extrinsic factors include all the signals related to the stem cell microenvironment. These aspects include anatomical geometry, composition of the extracellular matrix, cell-to-cell interactions mediated by integral membrane proteins, soluble factors, the mechanotransduction dictated by stiffness, and oxygen concentration (figure 1.4). They are likely to synergistically act to regulate gene expression and to maintain “stemness”, even their role it is not yet been clarfied. The geometry,

stiffness, ECM composition, and O_2 gradient will be investigated deeper in the next sections.

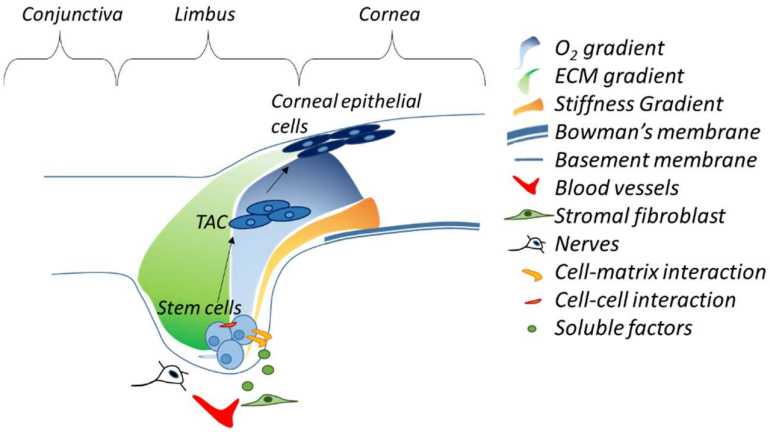
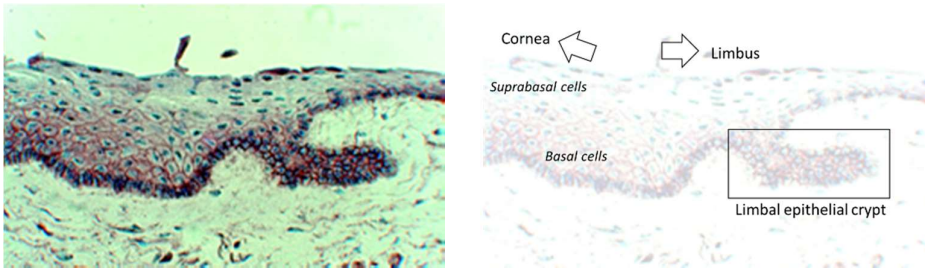


Figure 1.4: Schematic representation of the extrinsic factors that may have a synergistic effect on limbal stem cell differentiation.

1.2.3 Limbus geometry and dimensions

In 1971, a letter in Nature described a structure about 1 mm long and radially distributed in the limbus called the 'Palisades of Vogt' that was thought to be the location of corneal epithelial cell generation (Davanger and Evensen, 1971). In the last decade, several attempts were made to identify the precise location of the niches within the Palisades. In 2005, Dua et al., observed an anatomical and functional unit structure within the Palisades of Vogt which they called Limbal Epithelial Crypts (LECs, figure 1.5). LECs stretch perpendicular to the external limbal surface and then turn parallel to the surface or circumferentially along the limbus (Dua *et al.*, 2005). These cylindrical tubes gradually narrow from the rete ridge and terminate in the conjunctival stroma. Further characterization was then performed, based on LEC distribution, immunophenotype, and ultra-structure (Shanmuganathan *et al.*, 2007).



a b

Figure 1.5: LECs as defined by Dua et al. (2005). The niche goes from the under-surface of a Palisade of Vogt and gradually tapers towards its tail. a) The figure shows the immunohistology of a LEC with positive staining for ABCG2 (magnification ×400). Image taken from (Dua *et al.*, 2005). b) Replication of figure a) showing the main features of the area surrounding the crypt.

Subsequent research in 2007 combined *ex-vivo* and *in-vivo* investigations on the limbus (Shortt *et al.*, 2007). This study analysed 10 cadaveric corneas by confocal microscopy and examined 18 decellularised limbal rims by Scanning Electron Microscopy (SEM). The authors described two structures: Limbal Crypts (LCs) and Focal Stromal Projections (FSPs). The crypts were defined as "distinct invaginations of epithelial cells extended from the peripheral cornea into the corneal limbal stroma" (Shortt et al., 2007, p.1404) and originate from the under-surface of a palisade (figure 1.6). The focal stromal projections were described as finger-like structures, which surround a central blood vessel. More recently, Grieve et al. (2015) showed the presence of both structures: narrow, frequent radial structures as well as larger, wider crypts.

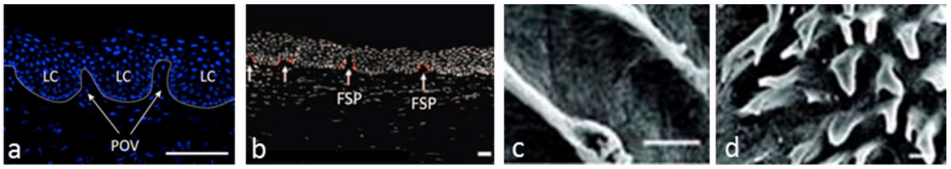


Figure 1.6: LCs and FSPs defined by Shortt et al. 2007. (a) Tangential histological sections of the limbal crypts, that correspond to the downward projections of the limbal epithelium into the limbal stroma between the palisades of Vogt; (b) tangential tissue section through FSPs, indicated by the arrows; (c) scanning electron microscopy of decellularized corneal limbus; (d) high-power SEM of FSPs. (a) Scale bars: 100 µm and (b-d) 50 µm. (a) Taken from Dziasko & Daniels (2016), (b-d) taken from Shortt et al. (2007).

Regarding the niche dimensions, while the Palisades of Vogt measure 1 mm in length(Shortt *et al.*, 2007), Dua et al. (2005) concluded that the average depth of the limbus reached up to 120 µm. The LECs dimensions have also been quantified using in vivo confocal microscopy (Miri *et al.*, 2012). This technique has the advantage of keeping the limbus in physiological conditions during testing; LECs depth in this study was found to be on average 124 µm (range: 111 µm - 142 µm). Levis et al. (2013) analysed cadaveric corneal donor rims using confocal Z-stack images. The results showed an average width of 107.9 ± 36.57 µm and an average depth of 68.9 ± 20.06 µm. Discrepancies between these results may be partly due to different structures used as landmarks in each study. Other possible confounding factors are inter-human variations, different and relatively small sample sizes, and methodologies used (Molvaer *et al.*, 2013). These results clearly suggest that niche dimensions are not well defined and are affected by a high degree of variability.

1.2.4 Limbus and cornea mechanical properties

Several studies were performed to analyse the mechanical properties of the cornea, mainly based on the bulk stiffness resulting in a wide stiffness range being reported (Zeng *et al.*, 2001; Jayasuriya *et al.*, 2003; Lombardo *et al.*, 2017). Fewer studies have been performed on the specific area of the corneosclera rim. Eberwein et al. (2014) measured, for the first time, the mechanical properties of cornea, limbus and sclera by using a novel nanoindentation device for soft tissues, with a large spherical indenter (500 µm). Similar force-displacement curves were obtained across the three regions: during initial loading, the response was typical of an elastic material; however, a creep response was recorded during the hold period. Upon unloading, the tissues had a very limited recovery, a typical behaviour of viscoelastic materials. The elastic moduli detected were 19.2 ± 3.1 kPa, 17 ± 4.5 kPa and 10.4 ± 4.4 kPa for the central cornea, sclera and limbal rim, respectively (figure 1.7). In addition, the limbal region was more compliant than the cornea.

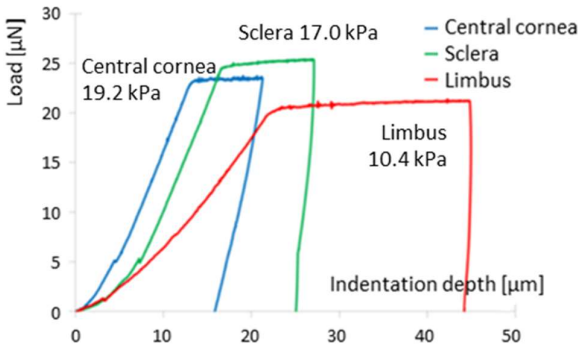


Figure 1.7: Force-displacement curves for the cornea, sclera, and limbus. The elastic modulus of the cornea, sclera, and limbus was 19.2 kPa, 17.0 kPa and 10.4 kPa, respectively. Taken from (Eberwein *et al.*, 2014).

The different characteristics of the three regions can be ascribed to different orientations of collagen fibres. Vertical and horizontal directions of the collagen fibres were detected in the cornea region and are maintained only until about 1 mm from the limbus, where the fibres assume a circumferential orientation (Abahussin *et al.*, 2009; Aghamohammadzadeh *et al.*, 2004). In addition, the limbal cells lay on the basement membrane, while in corneal areas both layers, the Bowman's and the basement membrane are present, showing different stiffness values. According to AFM results, the stiffness of the Bowman's membrane is 110 kPa, while the basement layer is 7.5 kPa (Last *et al.*, 2012). The elastic moduli investigated in this study are all shown in figure 1.8. Table 1.2 shows the existing techniques used to measure the cornea mechanical properties, with the values reported for the specific investigated areas.

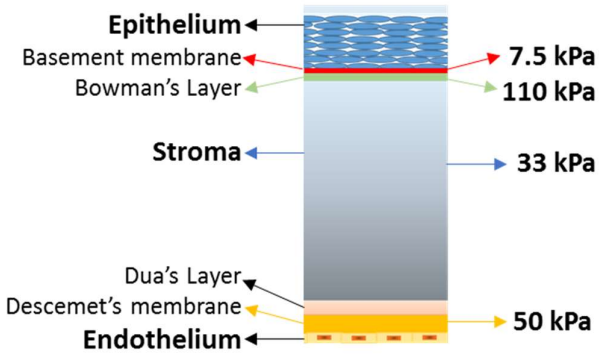


Figure 1.8: Schematic representation of the cornea layers and elastic modulus. The values were obtained by AFM (Last *et al.*, 2012).

Table 1.2: Summary of the current techniques used to measure the cornea mechanical properties. The measured values, the area investigated and the key points for each specific technique are also reported.

Technique	Values	Area investigated (species)	References	Key points
Rheometer	G'=1500 Pa G''=125 Pa	Full thickness cornea (human)	Grobe and Reichl (2011)	Pros: accurate description of the nonlinear viscoelastic properties. Cons: application of the shear stress on the entire samples, not giving detailed information of localised areas.
	G'=60 Pa G''=10 Pa	Full thickness cornea (porcine)	Ionescu et al. (2011)	
	Tensile G' = 18.9 MPa - 53.7 MPa	Full thickness cornea (bovine)	Hatami-Marbini (2014)	
	E=6.72 ± 4.62 kPa	Anterior cornea (human)	Petsche et al. (2012)	
	E=5.25 ± 2.07 kPa	Central cornea (human)		
	E=4.17 ± 4.58 kPa	Posterior cornea (human)		
	E=38.7 ± 8.6 kPa	Full thickness cornea (human)		
Nanoindenter	E=19.2 ± 3.1 kPa	Central cornea (human)	Eberwein et al. (2014)	Pros: measure of the surface mechanical properties, and localised mechanical strength. Cons: the limited z-excursion does not allow the measurement of irregular and deep samples
	E=17 ± 4.5 kPa	Sclera (human)		
	E=10.4 ± 4.4 kPa	Limbal rim (human)		
AFM	E=7.5 kPa	Basement membrane (human)	Last et al. (2012)	
	E=110 kPa	Bowman's Layer (human)		
	E=33 kPa	Stroma (human)		
	E=50 kPa	Descemet's membrane (human)		
	E=1.14-2.63 MPa	Full thickness cornea devoid of epithelium (human)	Lombardo et al. (2017)	
Texture Analyser	E=25 ± 0.91 kPa	Full thickness cornea (Porcine/mouse)	Worthington et al. (2014)	Pros: measure of the bulk mechanical properties. Cons: it is not applicable for determining the specific elastic modulus of each discrete corneal layer.
	E=7.71 ± 6.34 kPa	Anterior cornea (human)	Petsche et al. (2012)	
	E=1.99 ± 0.45 kPa	Central cornea (human)		
	E=1.31 ± 1.01 kPa	Posterior cornea (human)		
	9.48 ± 2.92 kPa	Full thickness cornea (human)		

1.3.2.1 The significance of substrate stiffness

Material stiffness has been reported as a crucial factor in influencing stem cell behaviour showing that mesenchymal stem cells committed to the neurogenic, myogenic or osteogenic lineage specified by matrix elasticity (Engler *et al.*, 2004; Discher *et al.*, 2005). There is some evidence that it plays a role also in the cornea regeneration process (Jones *et al.*, 2012; Moers *et al.*, 2013; Foster *et al.*, 2014). However, more investigations are necessary, since none of these works studied the mechanism using human primary limbal stem cells. Compressed and uncompressed collagen scaffolds with different mechanical properties were developed by Jones et al. (2012). The stiff gel (compressed) and the soft gel (uncompressed) presented a storage modulus of 2900 Pa and 3 Pa, respectively. Limbal stem cells expanded on these materials presented different marker expressions. An increase in the protein cytokeratin 3 (CK3), which is related to limbal epithelial cell differentiation, was detected on the stiffer collagen substrate. These results were confirmed by Chen et al. (2012) that compared the CK3 expression between a fully compressed collagen (2500 Pa) and a partially compressed collagen (170 Pa) matrix. Both studies were performed using bovine limbal epithelial cells.

Moers et al. (2013) found that the elastic modulus of PDMS and polyacrylamide surfaces has a significant impact on the differentiation of immortalised limbal stem cells, in physiological (40 and 80 kPa) and non-physiological ranges (1.5 MPa). Foster et al. (2014) studied the differentiation process on compressed and non-compressed collagen gels analysing the localization of the Yap-associated protein, a transcriptional co-activator previously shown to mediate cellular

response to mechanical stimuli. They hypothesised that the mechanism underpinning LESCs differentiation may be due to a mechanism called durotaxis. This mechanism, where cells migrate and differentiate from a compliant (limbus) towards a stiffer (cornea) substrate is partially driven by mechanotransduction (figure 1.9a). Nevertheless, this mechanism has not been demonstrated in the cornea environment yet. The explanation of the force-sensing mechanism, and the consequent transduction effect to regulate cell function is well described by Ross et al. (2013) and it is reported in figure 1.9b,c, related to YAP protein expression.

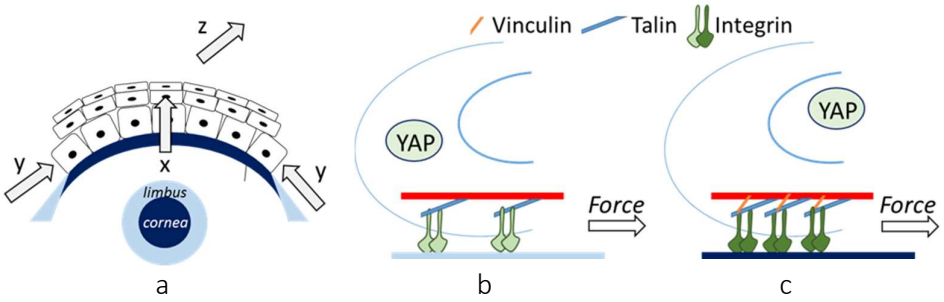


Figure 1.9: schematic representation of durotaxis in relation to limbal stem cell maintenance and differentiation. (a) Cells placed on the more compliant substrate remain undifferentiated (limbus, light blue area). The cells migrate towards the centre of the cornea (blue area) attracted by the stiffer substrate [y] via durotaxis. Via mechanostransduction, the cells differentiate [x]. Finally, cells leave the ocular surface and undergo apoptosis [z]. (b,c) Representation of YAP response to the interaction with soft and stiff substrates (b) under low force or (c) high force. Force stimulates the conversion of integrins from low affinity states (light green) to more stable, high affinity states (green); stretching of talin (blue) to recruit vinculin (orange); also, additional integrins are activated and recruited to the adhesions. YAP translocates to the nucleus to induce expression of cell cycle and differentiation genes. Adapted from (Ross *et al.*, 2013).

1.3.2.2 Stiffness of amniotic membrane

Studies of gel stiffness may increase the success rates of therapies that are currently in use for the treatment of limbal stem cell deficiency. It has been hypothesized that the high failure rates of amniotic membrane transplants may be due to the high variability of their mechanical properties (Chen *et al.*, 2012). Amniotic scaffolds are collected from anatomically distinct areas of the amniotic membrane. Areas of the membrane adjacent (<10 cm) or away from the placenta (>10 cm) show different thicknesses (115.6 ± 20.7 µm and 63.6 ± 13.0 µm, respectively) and elastic modulus values (storage modulus at 1 rad s^{-1} = 1135.27 ± 15.3 Pa and 61.68 ± 15 Pa, respectively). This induces a different expression of the cell marker CK3, increasing in the cells seeded on the distal amniotic membrane (Chen *et al.*, 2012). The mechanism underpinning cell differentiation has been clarified studying AM variation associated with the heterogeneity in the surface topography, which is responsible for controlling the differentiation process. It has been demonstrated that increasing the surface roughness increases the gene expression of stem markers p63 and ABCG2 and the protein expression of ABCG2 (Lai *et al.*, 2013). Furthermore, Ma and colleagues used carbodiimide-crosslinked denuded AM (CLDAM) to study the underlying mechanism of hLESCs homeostasis and found that cultures on CLDAM displayed greater expression of p63, ABCG2, integrin β1 and integrin-linked kinase (ILK), the latter of which was also found to be an important mediator in signal transduction. Their data suggests that signals are transduced from integrin β1 to the master gene in hLESCs regulation, deltaNp63α, via ILK

and the Wnt/β-catenin pathway, and that these signals are dictated by the roughness of the EBM substrate.

1.2.3 Extracellular matrix composition

The extracellular matrix of the limbal stroma presents some unique features with respect to the cornea. First of all, there is a difference in the composition between the basal membrane of cornea and limbus. The corneal basement membrane is composed of collagen type IV (α3, α4, and α5 chains), collagen type VII, laminin (Ln-α1, Ln-α3, Ln-β1, Ln-β3, Ln-γ1 and Lnγ2 chains), fibronectin, and heparan sulfate proteoglycans. The limbal basement membrane possesses additional laminin α2 and β2 chains together with α1 and α2 chains of collagen type IV but no collagen type XII or collagen type IV (α3, α4, and α5 chains) (Ljubimov *et al.*, 1995).

In addition, the distribution of collagens, glycoproteins, and proteoglycans was extensively characterized along the human ocular surface epithelia of the basement membrane. The results indicated that there is an increased immunoreactivity for agrin, BM40/SPARC, laminin (a1, a2, and b1) chains, collagen type IV (a1 and a2) chains, nidogen-2, collagen type XVI, versican, and tenascin-C in the limbal part compared to the corneal and conjunctival basement membrane (Schlötzer-Schrehardt *et al.*, 2007). In particular, desmoglein 3 and tenascin-C demonstrated regional variations depending on the proximity to the LEC. Desmoglein 3 is a cellular membrane protein whose function is to assist the formation of desmosomes, responsible for cell-cell adhesion. Tenascin-C is an ECM protein, located in the basement membrane and

considered to be responsible for maintaining the limbal stemness (Yeung, 2008). In figure 1.10, three areas were identified and the expression of tenascin-C and desmoglein 3 were reported as negative (-), moderately positive (+), and strongly positive (++). The areas correspond to the cornea, the limbus and the LEC. A reduced gradient of desmoglein 3 and an increased gradient of tenascin-C from the cornea to the limbus was identified (Yeung, 2008).

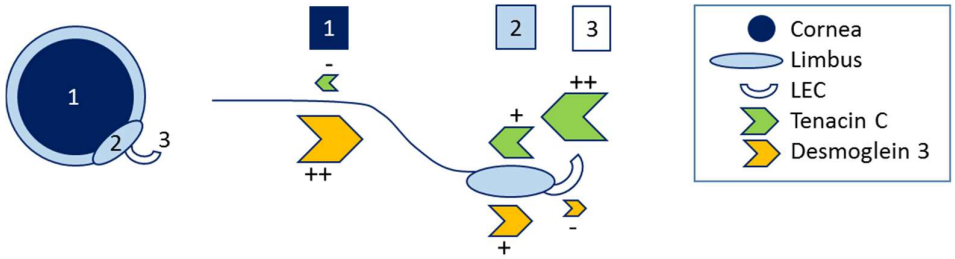


Figure 1.10: representation of the regional variation of tenascin C and desmoglein 3. Area 1 (blue circle) indicates the cornea, area 2 (light blue oval) indicates the limbus and area 3 (white semicircle) indicates the LEC. LEC has a higher number of desmoglein 3-negative, while limbus and cornea present moderately positive (+), and strongly positive (++) expression. On the contrary, tenascin-C is highly expressed in the LEC, but present a moderately positive (+) and negative expression (-) in the limbus and the cornea, respectively. Modified from (Yeung, 2008).

1.2.4 Hypoxic environment

The importance of oxygen in maintaining distinct phenotypes has been tested not only with regard to the corneal limbus but also for other niches (Mohyeldin *et al.*, 2010). There is a steep gradient of oxygen from the niche to the cornea as identified in the rabbit. The oxygen concentration decreases from 16-17% below the tear film to 8-9% at the stromal and endothelial area (Rwan *et al.*, 1972). In addition, the limbal niches are close to the limbal capillaries that may be responsible for the release of soluble factors. However, in terms of oxygen

concentration, the hypoxic nature of the niche should not be affected by the vasculature (Brahimi-Horn and Pouysségur, 2007). The impact of the oxygen on the proliferation and differentiation of limbal stem cells has been recently studied with controversial results. Bath at al. (2013) studied the impact of oxygen concentration (20%, 15%, 10%, 5%, and 2% O_2) by using two systems: 3T3 cells as feeder layer and serum-free media Epilife. The cell marker expression was tested by using ABCG2, and p63α as stem cell markers and cytokeratin CK3 as differentiation cell marker. Overall, they found that low oxygen levels favoured a stem cell phenotype (at 2% and 5% O_2), while an increased proportion cells expressed CK3 markers at higher oxygen concentration with both systems (Bath *et al.*, 2013). However, a clear trend was not observed, and the difference in the number of samples investigated make the results difficult to interpret from a statistical point of view. Miyashita et al. (2007) showed that cell proliferation was higher in hypoxic conditions (2% O_2) compared to a normoxic environment (20% O_2) due to the presence of rapidly cycling cells. No difference was detected in the stem cells markers (CK15 and p63), but higher CK3 expression was found at increased oxygen levels (20% O_2). They concluded that the hypoxic conditions facilitated the proliferation of transient amplifying cells, leaving the question about the impact of oxygen levels on the maintenance of the stem cells during cell culture still open (Miyashita *et al.*, 2007). Different results were found by O'Callaghan et al. (2010), which investigated rabbit limbal epithelial cell differentiation at 21%, 14%, 8%, and 2%. Oxygen concentration of 14% supported the highest colony-forming efficiency and 2% the lowest. Differentiation was enhanced at oxygen levels lower than

8%, a limited proliferative capacity was reached and differentiated cells were present at 2% oxygen. Limbal stem cell markers ABCG2 and p63α were expressed at 21%, 14%, and 8% oxygen, with a trend of lower expression in 8% oxygen. Wang et al. (2016) studied the regulation path induced by hypoxia in human limbal stem cells. Regarding cell differentiation, they reported that hypoxic environment induced cell differentiation, by decreasing p63 expression and increasing keratin 12 expression (Wang *et al.*, 2016). A summary of the results from these aforementioned articles is presented in figure 1.11. In addition, it was reported that it was possible to accelerate the fabrication of epithelial cell sheets without using any feeder cells by controlling the oxygen concentration. Rabbit limbal epithelial cell numbers were higher under hypoxia (2% O_2), but the stratification was enhanced by normoxia (20% O_2), after reaching confluence (Nakajima and Takeda, 2013).

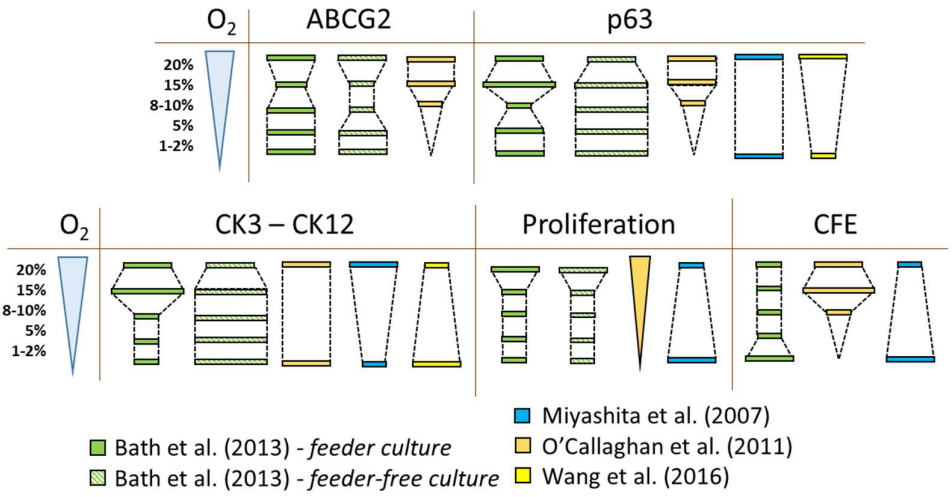


Figure 1.11: Effect of a hypoxic environment on limbal epithelial cells investigated in four independent studies. Bath et al. (2013, green for 3T3 system, and striped green for Epilife system), Miyashita et al. (2007, blue), and O'Callaghan et al. (2011, orange) and Wang et al. (2016, yellow) studied the effect of hypoxic conditions on stem cell markers (ABCG2, P63), differentiation marker (CK3 and CK12), cell growth and colony forming efficiency (CFE).

1.2.4 Soluble factors and additional factors

Another aspect that contributes to the maintenance of stemness is related to the soluble factors, modulated by the basement membrane beneath the LESC. For example, the presence of a blood supply at the limbus provides cytokines, growth factors and other nutrients (Huang *et al.*, 2015). Moreover, growth factors released by limbal fibroblasts in the underlying stroma determined the plasticity of limbal and corneal epithelial differentiation (Schlötzer-Schrehardt *et al.*, 2007; Espana *et al.*, 2003). In addition, chemotactic factors, for example, neurotrophic factor gradients are recognised as important signaling molecules (Touhami *et al.*, 2002).

1.3 Clinical context and current solutions

Worldwide, corneal disease is the second most prevalent cause of blindness after cataracts (Whitcher *et al.*, 2001). Corneal blindness is considered avoidable and treatable in many cases, as corneal transplantation surgery can be performed. However, there is a current global shortage of donor corneas and, in many developing countries, there is no dedicated and funded eye bank facility to procure corneas. Based on data from the World Health Organisation, it is estimated that at least 4 million people worldwide suffer from corneal blindness. However, only 100,000 corneal transplants are performed each year, primarily as a result of lack of access to suitable tissue. The majority (90%) of the global cases of ocular trauma and corneal ulceration leading to corneal blindness occur in developing countries (Whitcher *et al.*, 2001). For example, the incidence of corneal blindness in India is 25,000-30,000 every year with a prevalence of

approximately 6.8 million people who have visual acuity less than 6/60 in at least one eye due to corneal diseases (Dandona and Dandona, 2003).

1.3.1 Limbal stem cells deficiency

Severe ocular surface disease can result in Limbal Stem Cell Deficiency (LSCD, figure 1.12). This condition refers to the damage or the destruction of the limbus, causing conjunctivalization due to the migration of conjunctival cells, neovascularisation and corneal opacification, and resulting in vision loss (Dua *et al.*, 2010). LSCD can be acquired (e.g. via chronic inflammatory diseases, chemical and thermal burns) or hereditary.

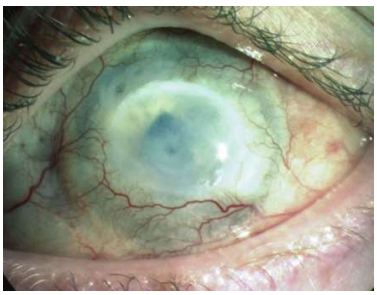


Figure 1.12: Effect of limbal stem cell deficiency due to a chemical burn injury. Taken from (Secker and Daniels, 2009).

Since the relatively recent discovery of the presence of stem cells in the limbus, stem cell autografting with the inclusion of the area of the Palisades of Vogt was first published in 1989 (Keivyon and Tseng, 1989). In 1994, the first allograft was performed by using a cadaveric limbal ring, divided into small pieces (Tsai and Tseng, 1994). The success in the use of stored corneoscleral rims encouraged the development of eye banks (Tsubota *et al.*, 1995). A successive step was the introduction of the *ex-vivo* expansion of the autologous or living related stem

cells. The expanded cells were delivered as epithelial sheets or attached to therapeutic bandage lenses (Pellegrini *et al.*, 1997). Successively, the amniotic membrane was used as a carrier for limbal stem cells. Nowadays, a numbers of carriers have been developed and there is no gold standard for the treatment of the LSCD.

1.3.2 Current treatments: donor graft tissues and amniotic membrane

The current treatment for total LSCD involves different approaches depending on the transplanted area (conjunctival, keratolimbal or mucosal), autologous or allogenic tissue (cadaveric or living-related) and the cell culture technique. This classification was recently proposed by the Cornea Society (Daya *et al.*, 2011). In the case of unilateral depletion, an amount of autologous conjunctival and limbal tissue (two grafts 5–7 mm in length) is obtained from the healthy eye and transplanted without immunosuppression therapy, following a procedure called conjunctival limbal autograft (CLAU) (Keivyon and Tseng, 1989). In the case where no autologous sources are available, a living-related conjunctival limbal allograft (LR-CLAL) or keratolimbal allograft (KLAL) procedure is performed. In the first treatment, the limbal and conjunctival tissues are harvested from a patient's living relative, while the second involves the collection of cadaveric corneoscleral rims, with the advantage of having a large cell supply. In both cases, the biopsy includes the limbus along with the conjunctiva. Another procedure has been developed, named *ex vivo* cultivated limbal epithelial transplantation (CLET), and includes two strategies: the limbal explant, and the suspension culture method (Pellegrini *et al.*, 2014) (figure 1.13).

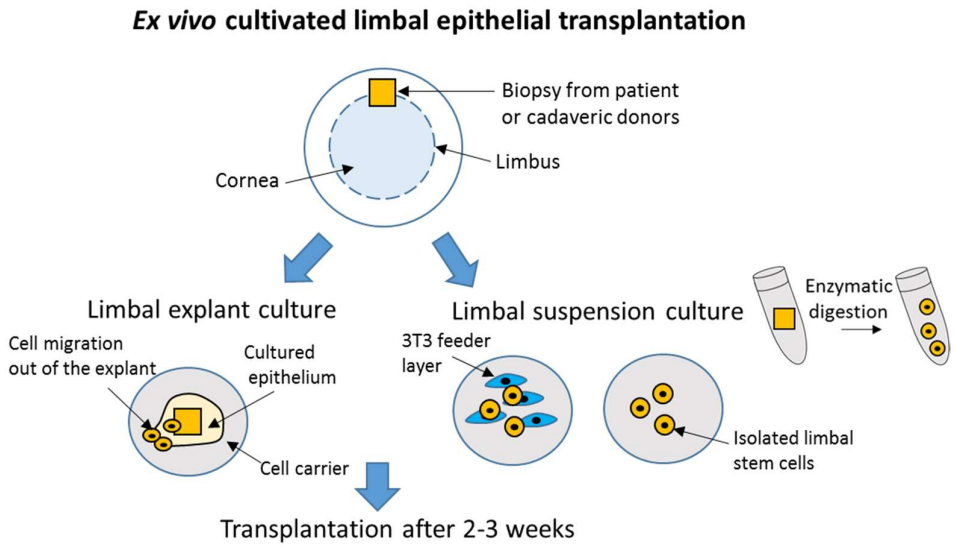


Figure 1.13: Representation of *ex vivo* cultivated limbal epithelial protocol, includes two strategies: strategies: the limbal explant and suspension culture method.

In the limbal explant strategy, the harvested limbal tissue is placed directly on a carrier, such as the amniotic membrane (Tsai *et al.*, 2000). In the suspension culture method, the biopsy is digested by enzymes and epithelial cells are seeded onto different scaffolds with or without mitotically inactivated 3T3 fibroblast feeder cells (Rama *et al.*, 2010). Fibrin substrate carrier or human AM (Dua *et al.*, 2004) are the most commonly used scaffolds. In both techniques, after approximately 2–3 weeks, when the cells cover the entire surface, the scaffold is used for transplantation. A variation of this technique was introduced in 2012 (Sangwan *et al.*, 2012) and is represented in figure 1.14. In this approach, a biopsy is divided into small pieces and placed on AM or fibrin and expanded *in vivo* (Simple Limbal Epithelial Transplantation, SLET).

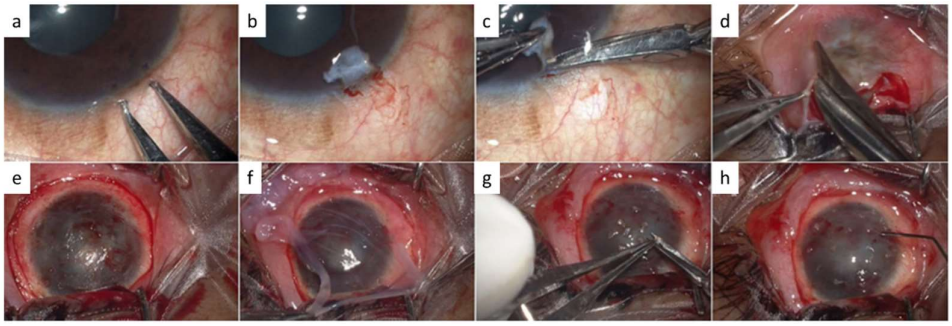


Figure 1.14: Clinical photographs showing the SLET technique. (a-c) The limbal biopsy tissue is excised in the superior part of the limbus of the donor's eye. (d, e) The fibrovascular pannus is removed from the ocular surface of the patient. (f) A human amniotic membrane graft is placed on the bare ocular surface and secured to it with fibrin glue. (g, h) The donor limbal tissue is cut into eight to ten small pieces and secured to the amniotic membrane overlying the cornea with fibrin glue. Taken from (Sangwan *et al.*, 2012).

The first stem cell-based product to receive a marketing authorization (even if conditional) by the European Medicines Agency was Holoclar (Chiesi Farmaceutici SpA), an *ex vivo* cultured autologous limbal stem cell graft. However, this treatment is only currently available in Europe, where it can be used to treat patients with severe corneal burns.

For most people, corneal transplantation appears to be very successful with an overall first year survival rate as high as 90%. However, the success rate diminishes to 74% at 5 years and 62% at 10 years. One in six full thickness transplants still experience some degree of rejection, predominantly due to the variable quality of the donor tissue's endothelial or epithelial health. In patients with alkali burns or recurrent graft failures, the chance of transplantation success is considerably lowered (Waldock, 2000). These issues with donor cornea shortage and rejection indicate that there is a need for new, innovative therapies to be developed that can be used to treat corneal blindness

worldwide. Moreover, the results obtained from randomized trials using amniotic membrane as a support are still controversial. The main drawbacks are high inter and intra variability and difficulty in the standardization of the membrane scaffolds, thus making clinical output difficult to interpret (Rahman *et al.*, 2009). Despite a high percentage of success recorded in the first year after treatment, after 3 years the success rate dropped to 45% (Basu *et al.*, 2011).

1.3.3 Current strategies for limbus replacement in tissue engineering

In the treatment of corneal pathologies, the preferred scaffold should provide a permanent source of epithelial progenitor cells to ensure the maintenance of corneal homeostasis. Such cells, if harvested from the human cornea, will ultimately change their phenotype and lose their stemness. Stemness may be maintained, in part, by matching the architecture of the scaffold to the source niche. For example, limbal epithelial cells outgrowing from an *ex vivo* explant on AM scaffolds progressively lose their stemness *in vitro*, as the distance from the explant increases (Kolli *et al.*, 2008). Recently, progress in the design of corneal scaffolds has been made by the inclusion of 3D structures. Ortega and colleagues used stereolithography to develop a poly(ethylene glycol) diacrylate (PEGDA) ring with micro-pockets (150-350 µm diameter and 80-100 µm depth) to mimic the limbal niche (Ílida Ortega *et al.*, 2013). The addition of fibronectin, in combination with the micro-pockets, enhanced cell attachment and outward migration of rabbit limbal fibroblasts. In addition, after 6 weeks of culture, a scaffold, seeded with rabbit limbal epithelial cells, was placed onto an *ex vivo* wounded cornea model. The outgrowth of cells and the formation of a multi-

layered epithelium was observed. However, only the expression of the differentiation marker cytokeratin 3 (CK3) was analysed on the PEGDA ring and was found to be expressed by the cells in the pockets.

In a further study, Ortega and colleagues combined stereolithography with electrospinning to reproduce the micro-pocket ring (Ilida Ortega *et al.*, 2013; Ortega *et al.*, 2014). Stereolithography was first used to fabricate a PEGDA template. Poly(lactic-co-glycolic acid) (PLGA) was then electrospun on top; the fibres adopted the shape of the microfabricated structure. This model included micro-pockets with diameters in the range of 300-500 μm (figure 1.13 a,b). Inside the pockets, 61% of the fibres showed high alignment, whilst outside, they were randomly orientated and presented a higher fibre density. This conferred differential mechanical properties between the inside and the outside of the artificial niches, and guided rabbit epithelial cells cultured inside the pockets to migrate outwards and towards the central region of the scaffold. This method facilitated the control of the directionality of cell migration, and the control of the morphology of rabbit cornea fibroblasts and epithelial cells, both of which were more elongated inside the pockets with respect to the outside, where they were shorter and polygonal. Rabbit limbal fibroblasts were seeded on the membrane and either a rabbit limbal epithelial cell suspension or a limbal explant was placed inside the niche (Ortega *et al.*, 2014). Regarding differentiation, expression of the putative stem cell marker p63 was detected in proximity to the explant, when placed inside the pockets. Yet, the p63 marker was not detected when a rabbit limbal epithelial cell suspension was seeded inside the pockets, and no differences in the expression of CK3 and p63 were

observed between cells inside and outside the pockets. It is unclear whether these niche structures alone are able to recreate the limbal stem cell niche *in vitro* and further investigations are required.

Another biomaterial that can be used to generate scaffolds with micro-patterns for use in tissue engineering applications is compressed collagen. Collagen is abundant in the cornea, and many groups have used this protein to fabricate scaffolds for cornea regeneration, especially for stroma applications (reviewed by (Zhao *et al.*, 2016)). A critical aspect, however, is its structural weakness. Compressed collagen, which displays improved mechanical strength with respect to its non-compressed counterpart, has been adopted for the expansion of limbal epithelial stem cells, and shows biocompatibility comparable to AM (Mi *et al.*, 2010; Xiao *et al.*, 2014). This technique has already been used to control the surface micro-topography of hydrogels (Alekseeva *et al.*, 2012). Using this technique, Levis et al. developed a Real Architecture for 3D Tissue (RAFT) system (figure 1.15 c,d), in which microscale grooves and ridges were reproduced to simulate the structure of limbal stem cell niches (Levis *et al.*, 2010; Levis *et al.*, 2013; Massie *et al.*, 2014). In their model, the ridges (in the range of 100-250 µm width and depth) were localised to the external part of the scaffold, keeping the central area flat. Human limbal stromal fibroblasts were embedded in the gel and human limbal epithelial cells were seeded on the surface. After 3 weeks of culture, the constructs formed numerous epithelial layers and maintained a mixed population of primitive and differentiated cells, with a high percentage of the cells lining the base of the crypts staining positive for the limbal stem cell marker p63α (Levis *et al.*, 2013). Their architecture represented the

interpalisadal grooves that stretch radially towards the cornea, termed limbal crypts (Shortt *et al.*, 2007), but was less representative of the enclosed structure that, from histological analysis, is widest at the origin and gradually narrows at its termination, extending beneath the sclera in radial, circumferential and oblique directions, described as epithelial limbal crypts (Dua *et al.*, 2005).

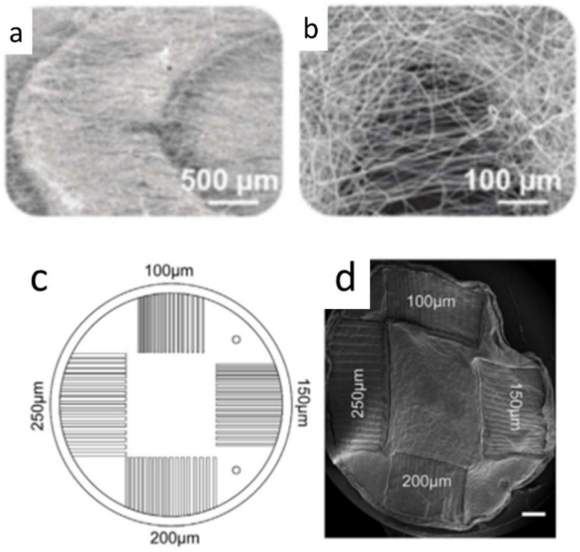


Figure 1.15: A tissue engineering strategy for limbal replacement. (a,b) Scaffold developed by Ortega et al (2014); (a) Lateral view of the ring scaffold containing a micropocket; (b) electropun mat (over the ring) showing a different fibre alignment inside and outside the pocket. (c,d) Scaffold developed by Levis et al (2010); (c) Schematic representation and SEM image of the topography of micro-ridges (100, 150, 200 and 250 µm); (d) compressed collagen showing the developed ridges.

1.4 Additive manufacturing

In the past few years, research groups have proposed innovative methods to exploit additive manufacturing techniques for studying cell-material interaction and to control the arrangement of cells and biomolecules in defined scaffold geometries.

Printing structures, with the specific size and shape of the target organ, which include cells from the patient or induced Pluripotent Stem Cells, could be used in replacement therapies to decrease the risk of rejection, which is an issue over the long term in current cell based therapies (Klebe *et al.*, 2009).

These attempts aimed to recreate controlled 3D architectures, better mimicking *in vivo* 3D microenvironments and dimensions, and facilitating the regenerative process. Additive manufacturing, also known as 3D printing, refers to a technique in which 3D digital models are created using Computer Aided Design (CAD) software, and then manufactured by the deposition of successive layers of materials to generate 3D objects (Gibson *et al.*, 2010). The additional complexity of 3D bioprinting in comparison to non-biological printing is given by the need to carefully select materials, cell lines, and growth factors. Although additive manufacturing comprises several techniques, the most common in the field of bioprinting are inkjet printing, extrusion-based bioprinting, laser-assisted printing, and stereolithography. Here we will discuss current techniques and how they may be applied towards cornea-related applications, for which studies using additive manufacturing are still scarce.

Extrusion-based bioprinting usually allows the deposition of materials layer-by-layer by means of a pneumatic or mechanical extrusion system. This technology permits the deposition of very high cell densities and the fabrication of larger structures at greater speed, at the expense of resolution (min 200 µm) and cell viability. In general, cell viability has been shown to be lower using extrusion methods than inkjet-based bioprinting, due to shear stresses induced by pressure at the nozzle gauge (Chang *et al.*, 2008), although it depends on multiple parameters, such as the material properties and the cell type. Examples of cell-laden tissue constructs developed using an extrusion-based bioprinter include stem cells encapsulated in decellularised extracellular matrix of adipose, cartilage and heart tissues (Pati *et al.*, 2014), human mesenchymal stem cells to engineer bone and cartilage architectures (Armstrong *et al.*, 2016) and embryonic stem cells (Ouyang *et al.*, 2015). Only one study reported in the literature has demonstrated the bioprinting of human cornea epithelial cells using an extrusion-based printer (Wu *et al.*, 2016). In this study, 94.6% of cells survived, following extrusion in a collagen/gelatine/alginate-based hydrogel. These cells went on to proliferate and express the cornea epithelial-specific marker cytokeratin 3. Nevertheless, a 3D shape unrepresentative of cornea was printed, suggesting that further studies are required.

During inkjet bioprinting, droplets of liquid, often picolitre in volume, are delivered to specific locations on a substrate by means of thermal or acoustic forces. In thermal inkjet systems, the droplet is forced out from the nozzle by air pressure pulses generated by electronically heated elements in the print-head.

In acoustic inkjet systems, the pulses are generated by ultrasound or piezoelectric actuators. Advantages of this technique are high fabrication speeds, high resolution (20–100 µm), low cost and wide availability, whilst drawbacks include both thermal and mechanical stresses, low accuracy of droplet localization, and low cell densities. The inkjet approach has been used to create stem cell patterning on polymer substrates (Kim *et al.*, 2010), to print a single cell type (Xu *et al.*, 2005) or a precise arrangement of multiple cell types (Xu *et al.*, 2013).

In laser-assisted bioprinting, a laser is focused on an absorbing substrate that overlays a layer of biological material. The laser indirectly induces a droplet of the biological material towards a collecting substrate. Laser-assisted bioprinting is advantageous as it avoids clogging and mechanical stresses, thus facilitating high cell viability post-printing. Furthermore, the spatial accuracy is below 5 µm (Barron *et al.*, 2004). Despite these advantages, this technique is time-consuming and more costly in comparison to the other strategies. Laser-assisted bioprinting has been used successfully to print layered patterns of human osteoprogenitor cells in 2D and 3D (Catros *et al.*, 2011), mesenchymal stem cells (Ali *et al.*, 2014), and multiple cell types simultaneously (Gruene *et al.*, 2011), but has yet to be used for cornea applications.

In stereolithography, a photo-sensitive material is solidified by means of light. Single or multi-photon methods allow 2D or 3D structures to be printed. A related technique called two-photon polymerization (2PP) is a promising

method for 3D nanofabrication, as it allows the generation of complex geometries while precisely controlling scaffold topography and, due to its nanoscale resolution, allows fabrication at a subcellular scale (1–10 μm). It will be described in detail in the next section.

1.4.1 Two-Photon Polymerization (2PP) system

Polymerization is defined as a process of reacting monomer molecules together in a chemical reaction to form three-dimensional networks or polymer chains (Young and Chung, 1982). In the case of photopolymerization, this process is initiated by light. While UV photocrosslinking is based on single photon absorption, two-photon polymerization is a 3D laser lithography technique, based on multiphoton absorption. This concept was first theorized by Maria Göppert-Meyer in 1929 but, due to the lack of a physical application, its demonstration was not possible until 1961. In the 1990s, following the commercialization of solid ultrashort pulse lasers (for example the Ti-Sapphire laser), this technique became widespread. One-photon absorption occurs when the photon matches the energy needed to raise an electron from the ground state to the excited singlet state. Differently, in the two-absorption phenomena, the transition from the ground to the excited state happens if two lower energy photons are absorbed by one molecule at the same time. This process requires a very high photon intensity that can be obtained by using pulsed lasers, the only light sources capable of delivering enough energy at very short pulses (10-18 s). The ultrashort pulsed laser beam, focused by a microscope objective, can generate laser intensities capable of exceeding the threshold to trigger a

nonlinear absorption process, which initiates cross-linking inside a pre-polymeric bath (figure 1.16). This technique can be used to generate microstructures with a resolution below the diffraction limit.

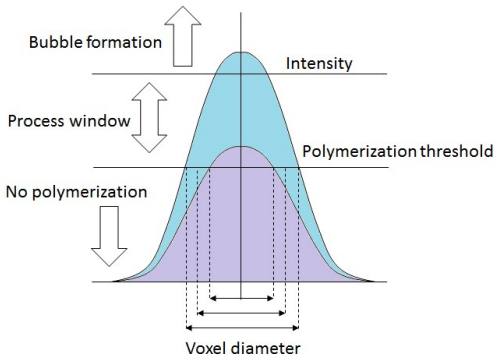


Figure 1.16: Laser intensity distribution. To achieve 2-photon polymerization the intensity must exceed the polymerization threshold.

In the 2PP system, the laser penetrates deeply into the material and directly induces polymerization from the inside without contamination of the area around the focal volume. The absorption is limited to the focal point since the probability of this simultaneous absorption decreases quadratically with the applied laser intensity. Therefore, the polymerization is not limited to the surface of the material, as it happens in UV photopolymerization (figure 1.17a). To achieve the intensity necessary to overcome the polymerization threshold, microscope objectives with high numerical apertures (NA) are used to increase the depth of field (figure 1.17b).

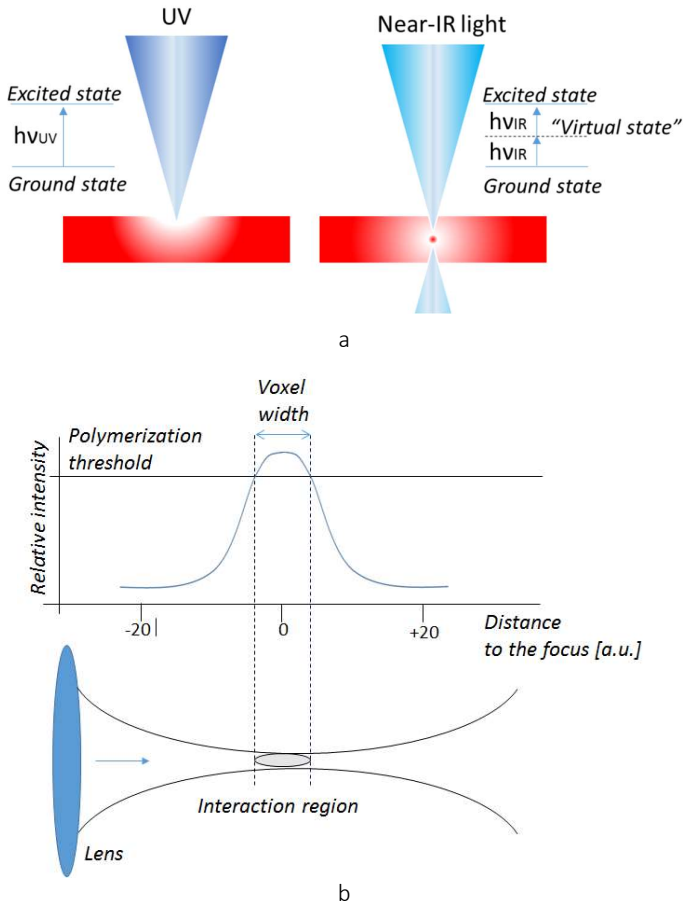
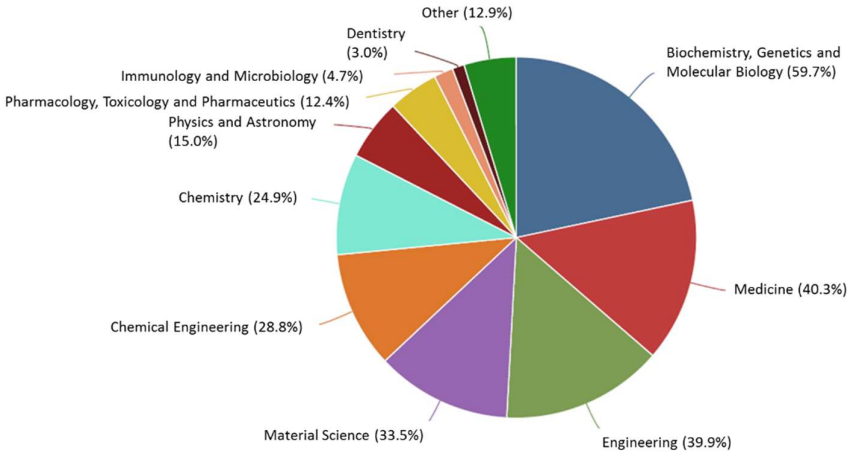


Figure 1.17: (a) Single photon absorption and two-photon absorption mechanisms. (b) Schematic Schematic representation of the confinement of the focal point defined by the NA and the threshold intensity. (a) UV light is absorbed at the surface while near IR light passes through the material without any interaction and the polymerization is confined in the focal point. (b) The volume of the focal point above the threshold defines the voxel dimension. Modified from (Ovsianikov, 2009).

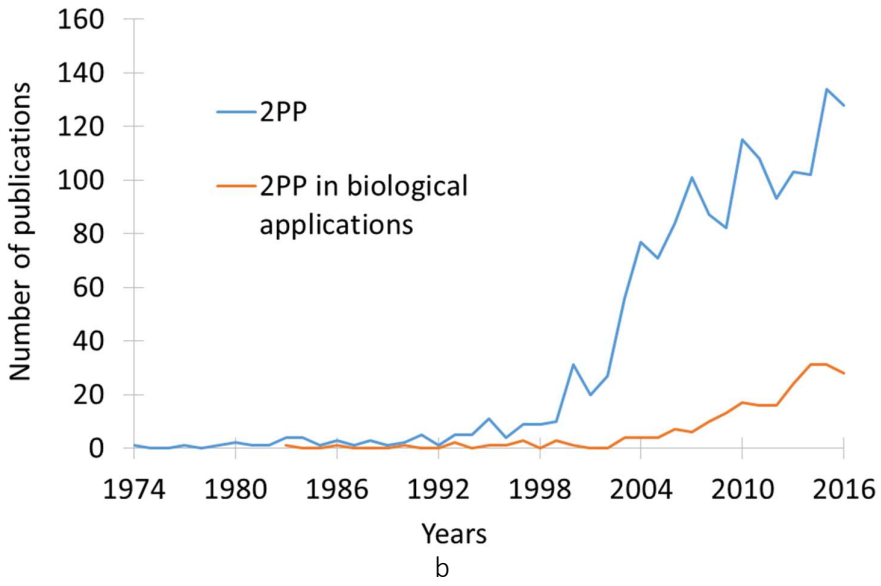
In addition to the intensity (I) and the objective's numerical aperture, the cross section (δ) and the radical quantum yield (Φ) play an important role in the polymerization process. The cross section is the ability of the initiator molecule to absorb photons via 2PA. The radical quantum yield is the fraction of photons that creates a radical. The radical formation rate (r_r) thus scales with the laser intensity squared, the 2PA cross section and the radical quantum yield ($r_r \sim \Phi\delta I^2$).

A photoinitiator with a high δ and ϕ is desired to achieve more efficient polymerization at lower power and faster processing speeds. In addition, the use of a long wavelength results in less absorption and less scattering, which allows a deeper penetration of light.

The 2PP methods have recently started to be applied in the biomedical sciences, thanks to the possibility to mimic native tissues in which resolution and scaffold dimensions play a determinant role. Figure 1.18 shows the trend indicating the increasing number of the publications regarding 2PP and specifically biological applications in the last 40 years. Among these studies, only a few of them focus on the development of stem cell niches and subsequently studied the cell differentiation process. In Raimondi et al. (2014), the crucial role played by the 3-D niche geometry on mesenchymal stem cell colonization and differentiation was highlighted by testing cell behaviour on scaffolds with different heights (20 µm to 100 µm) and different pore sizes. Koroleva et el. (2015) investigated the impact of geometry and stiffness on autologous bone tissue engineering application considering scaffolds with different pore sizes (150 µm, 200 µm, and 250 µm). Osvianikov et al. (2011) studied the proliferation of porcine mesenchymal stem cells and their differentiation after applying osteogenic stimulation.



a



b

Figure 1.18: Number of publication about 2PP between 1974 and 2016. (a) 2PP publications according to subject areas. (b) Number of publications on 2PP and 2PP for biological applications (Biochemistry, Genetics and Molecular Biology, Pharmacology, Toxicology and Pharmaceutics, Immunology and Microbiology, Dentistry, Medicine, and Neuroscience) according to a research conducted in Scopus (search term Two Photon Polymerization).

1.5 Aims and objectives

The overarching aim of this PhD was to recreate the key physical factors that can impact upon limbal cell differentiation to inform the design of scaffolds for future cornea regeneration strategies.

After corneal damage, limbal epithelial stem cells (LESCs) proliferate, and differentiate into cornea epithelial cells while migrating to the site of injury from the limbal epithelial crypts (LEC; situated in the limbus). The mechanisms that interplay between the cornea and the limbus during this process remain mostly unknown. The lack of LECs determines limbal stem cell deficiency causing conjuctivalization, neovascularisation and eventually loss of vision. This pathology can be treated by the transplantation of either cornea, or limbal tissue and LESC expansion on carriers. However, limitations of these methods are the lack of a controlled differentiation process, and the lack of a reservoir able to keep intact the stem cell resource. The long-term vision of this thesis was the development of novel scaffolds with the incorporation of a specific anatomic structure with defined mechanical parameters that provide a suitable microenvironment for limbal stem cells.

Therefore, the hypothesis of this PhD was that the geometry and the stiffness of the LEC are key physical factors that influence stem cell differentiation. The detailed objectives of this project were the following:

- to develop gelatin-based scaffolds (GelMA) with tunable **stiffness** and to compare them to the human cornea tissue.

- To investigate the use of riboflavin as a novel photoinitiator for GelMA crosslinking by UV and IR-photons.
- To develop 3D micro-scaffolds mimicking the **geometry** and the dimensions of native limbal stem cell niches by Two-photon polymerization (2PP).
- To study the impact of these key factors, geometry and stiffness, on limbal **stem cell differentiation**.

From the above objectives, the results were broken down into four distinct experimental sections, corresponding to Chapters 3 to 6. This thesis is presented in seven chapters, and an outline of each chapter is provided in figure 1.19.

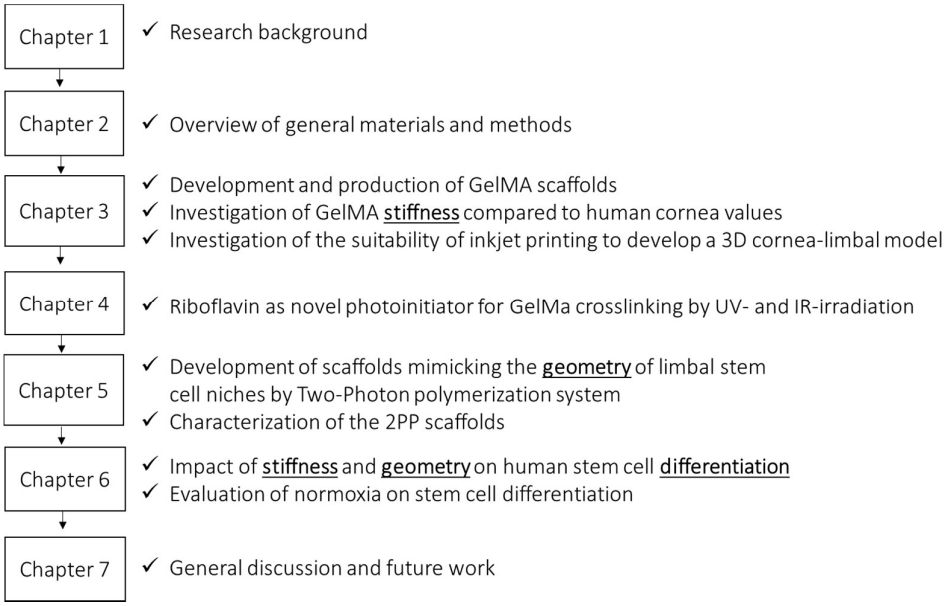


Figure 1.19: Overview of the thesis structure.

2. Materials and Methods

2.1 Material preparation

2.1.1 GelMA synthesis

Gelatin Methacrylate (GelMA) was synthesized as described by Nichol et al. 2010, and the chemical synthesis scheme shows in figure 2.1. Porcine skin gelatin (10% (w/v) Type A, 300 bloom, from Sigma-Aldrich, UK, G2500) was dissolved in Phosphate Buffered Saline (PBS, Gibco, Thermo Fischer Scientific, UK, BR014G) at 80°C and stirred until fully dissolved. Methacrylic anhydride (8% (v/v) Sigma-Aldrich, UK, 276685) was added at 0.5 mL/min and stirred at 60°C for 3 hours. To quench the reaction, the solution was diluted five times with PBS and stirred for a further 30 minutes. The solution was dialyzed against distilled water using 8 kDa cut-off dialysis tubing (BioDesignDialysis Tubing™ D118, USA) for 1 week at 50°C. The dialysis water was changed 3 times per day to eliminate the salt and the methacrylic acid. The solution was filtered through a 40 µm filter and lyophilized (Edwards Modulyo freeze dryer, IMA Edwards, UK) for 3 days. The freeze-dried GelMA was stored at -20°C until usage.

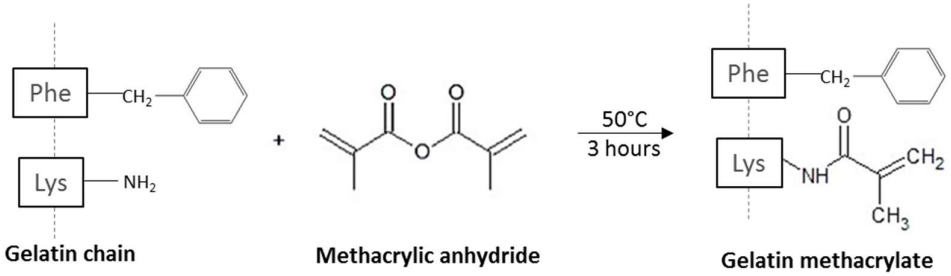


Figure 2.1: Chemical synthesis scheme of methacrylate substitution of the primary amines of gelatin.

2.1.1.1 Degree of crosslinking: NMR and TNBS assay

The percentage of methacrylation was quantified by using ^{1}H Nuclear Magnetic Resonance at 400 MHz (NMR, DPX UltraShield 400MHz, Bruker UK ltd, UK). The spectrum was collected at room temperature (RT). Phase and baseline corrections were applied before obtaining the integrals of the peaks of interest. MestReNova software (v6.0.2) was used to analyse the spectra (64 scans). Freeze dried GelMA and gelatin were dissolved in Deuterium Oxide (D_20, Sigma-Aldrich, UK, 151882) at a concentration of 10 mg/mL. The presence of the double bond signal (5.35-5.60 ppm) indicates the addition of the methacrylate vinyl group. The percentage of methacrylation was calculated using the method described by Hoch et al. (2012). Briefly, the integral of the methylene peak (d = 2.7 ppm to d = 2.9 ppm) was used for the quantification of the lysine signal. The degree of substitution was determined by comparing the lysine signals of the modified and unmodified gelatin according to the equation 2.1. The intensity of the aromatic region (7-7.5 ppm) was used as a reference.

Equation 2.1:

$$\text{Degree of methacrylation } (\%) = \left(1 - \frac{\text{lysine integration signal of GelMA}}{\text{lysine integration signal of gelatin}}\right) x\ 100$$

The degree of methacrylation was also confirmed by using the 2,4,6-Trinitrobenzene Sulfonic Acid (TNBS, Sigma-Aldrich, UK, P2297) assay. Gelatin and GelMA (4 mg), were dissolved in 0.25% v/v of TNBS (diluted in 0.01 M sodium hydrogen carbonate solution, Sigma-Aldrich, UK, 367176), and incubated at 40°C for 3 hours. Hydrochloric acid (3 mL, 6N, Alfa Aesar, UK, 44921) was added and the solution and incubated at 80°C for one hour to dissolve any insoluble matter. After cooling down to room temperature, 4 mL of

deionized water (dH_2O) was added and the absorbance was measured at 345 nm using a spectrofluorometer (Tecan Infinite® M200 microplate reader, UK). The absorbance value indicated the presence of free amino groups, and the degree of crosslinking was calculated according to the equation 2.2:

Equation 2.2:

$$\text{Degree of methacrylation } (\%) = (1 - \frac{\text{Absorbance GelMA}}{\text{Absorbance gelatin}})$$

2.1.2 GelMA preparation

Photopolymerization refers to the process of using light as an energy source to generate radicals to start the polymerization reaction and form crosslinks between molecules. In order to start the reaction, photoinitiators (PIs), which are molecules sensitive to light irradiation were added to the GelMA solution. In figure 2.2a, the steps to produce GelMA hydrogels were presented. GelMA was photocrosslinked by single (figure 2.2b) and two-photon absorption (figure 2.2c).

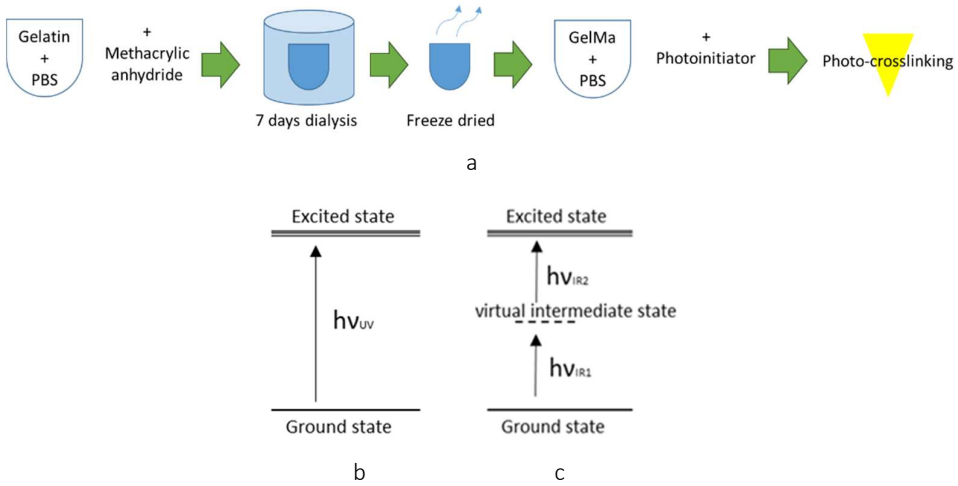


Figure 2.2: Representation of the steps to prepare GelMA and mechanism involved in the polymerization process. (a) GelMA is prepared by mixing gelatin and methacrylic anhydride then dialyzed and freeze dried. To obtain GelMA hydrogels, GelMA foam is mixed with PBS and PI and crosslinked with light sources. (b,c) Schematic representation of an atom excitation by (b) single-photon absorption, and (c) two-photon absorption. In the first approach, a single atom is excited by a single photon and the electron transition is linear to the UV light intensity. In the second mechanism, after the first photon is absorbed, the atom is in the virtual state, with a lifetime in order of a few femtoseconds. It can be excited to a higher state if the second photon reaches the atom within the lifetime of the energy level.

GelMA solution was mixed with different photoinitiators depending on the mechanism involved. For the first approach, GelMA was exposed to 365 nm long wave UV lamp at 15W (UVP, Black-Ray XX-15L UV bench Lamp, USA). For the second approach, femtosecond laser emitting at 780 nm was applied to the GelMA solution. This technique will be described in detail in section 2.6.2 (two photon polymerization system). Table 2.1 summarizes the photoinitiators, the lights sources, the photocrosslinking mechanisms and the nomenclatures that will be used in the present work.

Table 2.1: Gel nomenclatures with corresponding photoinitiators, light source and mechanisms used to photocrosslink the hydrogels.

Gel nomenclature	*Photoinitiator*	*Light source*	*Mechanism*
Macro-scaffold	Commercial photoinitiator Irgacure 2959 (2-Hydroxy-4′-(2-hydroxyethoxy)-2-methylpropiophenone (0.5% w/v Sigma-Aldrich, UK, 410896)	UV lamp	Single photon absorption
Micro-scaffold	P2CK, described in section 2.6.2 (Gel preparation)	IR laser	Two photon absorption

2.2 Scaffold characterization

2.2.1 Rheology

2.2.1.1 Measuring Viscosity

A crucial aspect in 3D bioprinting is related to ink viscosity. The viscosity (η) is the measure of resistance to flow, and is calculated as the ratio of shear stress (σ) to shear rate (γ). The shear stress, measured in Pascal (Pa) is defined as the ratio of force applied to a sample area. The shear rate is the rate of change of strain as a function of time. To test the viscosity of GelMA, rheology (Physica MCR 301, Anton Paar, UK) was performed. The polymeric solution was loaded in between a parallel and a cone plate (diameter = 25 mm, figure 2.3a) and the viscosity versus shear rate was measured.

2.2.1.2 Viscoelastic properties

The viscoelastic properties of the crosslinked gels were tested by dynamic shear oscillation measurements. Samples were cut with an 8 mm biopsy punch, and loaded in between the plates. While the bottom plate remains stationary, a motor rotates the top plate, imposing a time dependent strain on the sample. A

sinusoidal shear deformation is induced in the samples with a frequency of oscillation, ω, and the resultant stress response measured. The elastic and viscous behaviour has been described by elastic (real or storage) modulus G' and viscous (imaginary or loss) G'', respectively, according to the following equations:

Equations 2.3: $$\mathbf{G'} = \frac{\boldsymbol{\sigma}}{\boldsymbol{\varepsilon}} \mathbf{cos\,\delta} \qquad \mathbf{G''} = \frac{\boldsymbol{\sigma}}{\boldsymbol{\varepsilon}} \mathbf{sin\,\delta}$$

where δ is the loss angle, σ is the stress and ε is the strain. If the material is an ideal elastic solid, then the sample stress is proportional to the strain deformation. In contrast, if the material is a purely viscous fluid, the stress in the sample is proportional to the rate of strain deformation (figure 2.3b). G' and G'' have been measured as functions of temperature and frequency. Before applying the dynamic oscillation measurements, the Visco-Linear Region (VLR) was evaluated. The VLR is defined as the region in which the elastic modulus remains constant, in a range of increasing strain. To test the visco-elastic properties, parallel plates (diameter = 8 mm) were used (figure 2.3a).

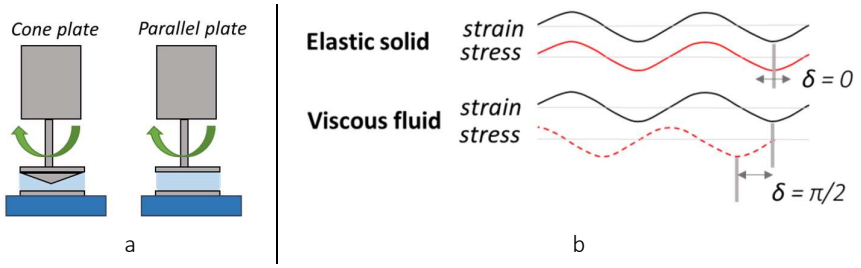


Figure 2.3: Schematic representation of rheological measurement. (a) Geometries used to test the viscosity of the hydrogel solution (cone-plate) and the viscoelastic properties of the crosslinked gels (parallel plate); (b) schematic stress response to oscillatory strain deformation for an ideal elastic solid, and a viscous fluid.

2.2.2 Texture analysis

To test the bulk mechanical properties of the samples, texture analysis (TA.HD plus Stable Micro System, USA) was performed. The system works by using a probe to compress the material at a constant rate, then the force applied to the material (stress) and the amount of material deformation (strain) is recorded on a graph. Young's modulus can be calculated from the gradient of the initial part of the stress-strain graph. Stress/strain curves were recorded by using a 10 mm Delrin® compression probe and analysed by the Exponent software.

2.2.3 Atomic force microscopy (AFM)

To measure the elastic modulus of the surface of the gel, AFM (MFP-1D, Asylum Research, USA) was performed. In figure 2.4, the principle of AFM is shown. A thin cantilever (nominal spring constant between 0.070 N/m and 0.025 N/m) with a silicon nitride tip (MSNL-10 type, probe A, from Bruker Nano, Coventry, UK) was used; it pointed perpendicular to the samples. The cantilever senses the intermolecular force between the sample surface and the probe. The z-deflection of the cantilever is transduced by a photodetector. When the tip is far from the surface, there is no interaction and consequently, there is no cantilever deflection. As the tip approaches the surface, the tip bends downwards due to attractive forces (jump to contact) and later due to hard-contact, the tip bends upwards. At a set maximum force value, the cantilever retracts to reach the initial rest position. The force graph was recorded. The elastic modulus (E) obtained from the retracting force curves based on the Hertz model (Roa *et al.*, 2011) was calculated according to the equation:

Equation 2.4: $$E = \frac{3}{4} \frac{1-\mu^2}{\sqrt{R\delta^3}} F$$

where F is the applied force, R is the radius of the probe, δ is the indentation of the samples, and μ is the Poisson's ratio. Before starting the test, sensitivity measure and the calculation of the spring constant were conducted. The first calibration was conducted to correlate the photodetector voltage with the tip deflection. A force-curve between a plain cantilever tip and a bare hard surface was obtained. In these experiments an undeformable glass surface with a higher stiffness than the cantilever was used. The sensitivity was calculated by the slope of the contact region of the force curve. The cantilever spring was determined by means of thermal noise method. The cantilever deflection spectrum that corresponds to the cantilever vibration due to thermal energy was recorded. The thermal noise spectrum is a plot of the cantilever fluctuations as a function of frequency, for which the greatest amplitude is at the cantilever resonance frequency. For an ideal spring, the calculation of the constant k is performed by the following equation:

Equation 2.5: $$k = \frac{k_b * T}{P}$$

where, P is the area of the power spectrum of the thermal fluctuation, k_b is Boltzmann's constant and T is the absolute temperature (Burnham et al., 2003).

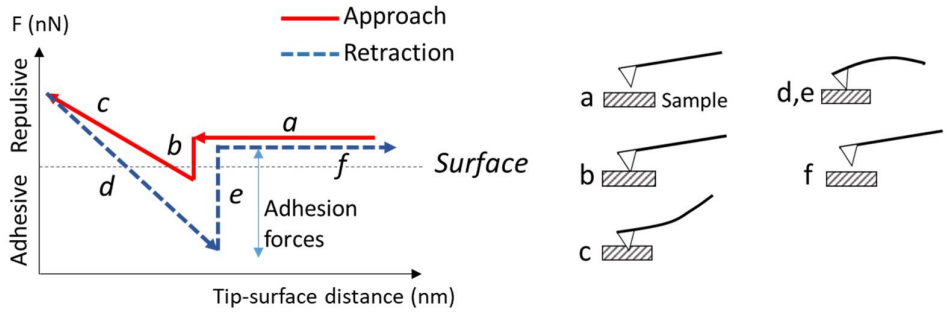


Figure 2.4: **Force-curve graph with tip-surface interaction.** a) There is no interaction between the probe and the sample as the tip is far from the surface; b,c) when the tip approaches the surface and it is close enough the tip bends downwards due to attractive forces. d,e,f) In the retracting cycle due to the contact between the sample and the surface the tip bends to upwards, and because of the adhesion established the tip does not detach from the surface until the force used to pull it exceeds the adhesion force between them.

2.2.4 Swelling analysis

Swelling analysis was performed on the samples to test their ability to uptake water since it can affect their physical and mechanical properties. The degree of swelling depends on the pore size of the polymer network and the interaction between the polymer and the solvent. The gel reaches equilibrium when two opposing forces, the thermodynamic mixing force and the elastic retractive force of the polymer chains, are equal (Peppas *et al.*, 2006). Mass and volume swelling ratios were studied on macro- (d = 8 mm and h = 1 mm) and micro-scaffolds (d = 300 µm and h = 200 µm), respectively.

For the mass swelling, immediately after sample preparation, each gel was weighed (t = 0), and placed in PBS at 37°C at pre-determined time points. The gels were removed from PBS and blotted with filter paper to remove the residual liquid, and the swollen weight (w_w) was recorded. Then, the gels were freeze-

dried and weighed (w_d). The mass swelling ratio was calculated from equation 2.6.

Equation 2.6: $$\textbf{Mass swelling ratio } (\%) = \frac{w_w - w_d}{w_w} \ (\boldsymbol{x\ 100})$$

The same procedure has been adopted to measure the volumetric swelling on the micro-scaffolds, but the swollen volume (V_s) was recorded by confocal (Zeiss PS1 780 high resolution confocal microscope, objective 10x immersed in water) using z-stacked images and analysed by ZEN software (Carl Zeiss). The volume was calculated from the top and the side views and the volumetric swelling ratio was calculated according to equation 2.7.

Equation 2.7: $$\textbf{Volumetric swelling ratio } (\%) = \frac{Vw - Vd}{Vw}\ \boldsymbol{x\ 100}$$

where V_d and V_w was the dry and the wet volume, respectively.

2.2.5 Susceptibility to Enzymatic Degradation

To study the susceptibility of the samples to the enzymatic degradation, 1 mg/mL of collagenase *Clostridium histolyticum* type I (0.25-1.0 FALGPA units/mg solid, ≥125 CDU/mg solid, Sigma-Aldrich, UK, C5138) was added to the gels. The collagenase solution was replaced every 24 h. For the macro-scaffolds, the degradation was calculated using:

Equation 2.8: $$\textbf{Weight remaining } (\%) = \frac{w_{d2}}{w_d}\ \boldsymbol{x\ 100}$$

Where w_d and w_{d2} are the mass of the dry scaffold before and after the immersion in the collagenase solution, respectively. For the micro-scaffolds, the degradation time was monitored by time-lapse microscopy (Leica DMRBE Microscope) at 37°C and images were acquired every 30 seconds. To measure the dry volumes before (V_d) and after (V_{d2}) the addition of collagenase, the

confocal microscope in z-stack mode was used. The degradation rate was calculated according to:

Equation 2.9: $$\textbf{Volume remaining}\ (\%) = \frac{V_{d2}}{V_d}\ \boldsymbol{x}\ \mathbf{100}$$

2.3 Cell culture

2.3.1 General methods for cell cultivation

All cells were cultured in T75 (75cm^3) culture flasks, using standard procedures and incubated at 37°C, with 5% CO_2, unless specified otherwise. Cell culture media was replaced every 2-3 days with pre-warmed fresh culture media. Cell morphology was observed daily with an optical microscope (Olympus CKX31, UK). Once the cells were 80–90% confluent, they were passaged. Cell media was removed from the flask, and cells were washed with PBS. Trypsin/EDTA (Sigma-Aldrich, UK, T4549, 1x), or Accutase® solution (Sigma-Aldrich, UK, A6964, 1x) was added and the flask was kept in the incubator (37°C) for 3-8 min. After monitoring cell detachment, the enzymatic action was neutralised by the addition of media containing 10% (v/v) of Foetal Bovine Serum (FBS, Sigma-Aldrich, UK F9665). The cell suspension was collected and centrifuged for 5 min at 200 g (Sigma 2-16K Scientific Lab Supplies). The supernatant was removed and the cell pellet was resuspended in fresh media and transferred to a T75 flask.

2.3.2 Frozen storage of cells

Cells were passaged as described previously, and the pellet was resuspended in FBS containing 10% (v/v) of dimethyl sulfoxide (DMSO, Sigma-Aldrich, UK, D2650), at a cell density between 0.3x10^6 to 1x10^6 cells/mL. The cell suspension

(1 mL) was dispensed into cryo-vials, and kept at -80°C in a CoolCell® (BioCision, USA) for 24 h. Then it was stored in the vapour phase of liquid nitrogen.

2.3.3 Cell revival from frozen storage

Cryo-vials were removed from the liquid nitrogen and quickly thawed in a water bath at 37°C. The cell suspension was gently transferred to a flask containing pre-warmed cell culture media. After 24 h, media was replaced with fresh media to remove residual DMSO.

2.3.4 Cornea epithelial cells

Adenovirus SV40-immortalised human corneal epithelial cells (cell line hCECs, passage 19-30, figure 2.5) were obtained as a kind gift from Professor Shigeru Kinoshita, Kyoto Prefectural University of Medicine, Kyoto, Japan) were used in this work. They were grown in supplemental basal Epithelial cell medium (EpiLife Medium with 60 mM Calcium, ThermoFisher, UK, MEPI500CA) containing 5 mL of Human Keratinocyte Growth Supplement (1X, ThermoFisher, UK, S0015), 100 units/mL of penicillin, 0.1 mg/mL of streptomycin and 0.25 µg/mL of amphotericin B (Sigma-Aldrich, UK, A5955).

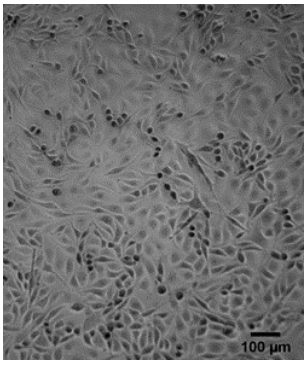


Figure 2.5: phase contrast images of human corneal epithelial cell line (hCECs).

2.3.5 Commercial human limbal stem cells

Commercial human Limbal Epithelial Stem Cells (c_hLESCs) were obtained from CELLnTEC Advanced Cell Systems (P.2, single-donor, Switzerland) and grown in serum free media (CnT-Prime, Epithelial Culture Medium, CnT-PR, CELLnTEC Advanced Cell Systems, Switzerland) with the addition of 100 units/mL of penicillin, 0.1 mg/mL of streptomycin and 0.25 µg/mL of amphotericin B and kept at 37°C, 5% CO_2. Cells were cultured in 75cm^2 culture flasks, at a cell density of 4,000 cells/cm^2.

2.3.6 Primary cells extracted from human cornea biopsy

Tissue-derived human Limbal Epithelial Cells (td_hLESCs) were collected from scleral-corneal tissue (obtained with written consent from the next of kin to be used for research) and preserved in media before processing. The biopsy was composed of cornea, limbus and conjunctiva. The biopsy was dissected into quarters (figure 2.6a-e), then the cornea and the conjunctiva were removed (figure 2.6f,g). The limbus was fragmented and soaked in PBS. Trypsin/EDTA was added (figure 2.6h) to digest the tissue for 30 min at 37°C.

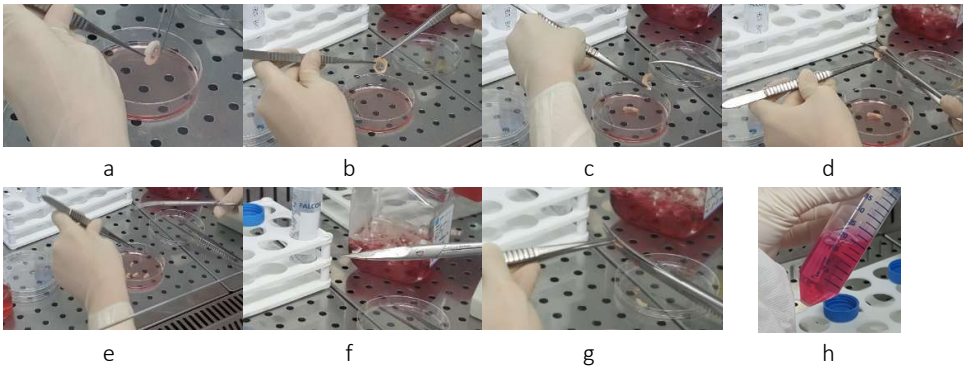


Figure 2.6: Steps to extract limbal stem cells from a cornea-limbus-conjunctiva biopsy. (a,b) entire biopsy; (c-e) the biopsy is cut in small parts; (f,g) cornea and conjunctiva are removed; (h) the fragments are soaked in Trypsin/EDTA.

After 30 min, media containing FBS was added to inhibit the trypsin action. The solution was centrifuged for 5 min at 1000 rpm (Thermo Scientific- Megafuge 1.0). After removing the supernatant, the pellet was re-suspended in fresh media and the cells were counted. This cycle was repeated three times to extract the majority of the cells. Cells were plated onto a 24 well plate (30,000 cells/well), pretreated with irradiated 3T3-J2 cells (figure 2.7). The standard control medium consisted of Dulbecco's Modified Eagle Medium (DMEM, ThermoFisher, Italy, VX42430025) and Ham's F12 (F12) (DMEM/F12 2:1, HAMS-F12, ThermoFisher, Italy, N6658) supplemented with 10% (v/v) FBS (10101-145, ThermoFisher, Italy), 50 µg/mL penicillin-streptomycin (P/S, Euroclone, Italy, ECB3001D), 4 mM glutamine (Euroclone, Italy, ECB3000D), 5 µg/mL insulin (Humulin R, Lilly, Canada, HI0210), 0.4 µg/mL hydrocortisone (Flebocortid Richter, Sanofi, Italy, AIC 013986029), 0.18 mM adenine (Adenine grade I, Pharma Waldhof GMBH, Germany, 4010212), 8.1 µg/mL cholera toxin (Cholera Toxin QD, List Biological Laboratories, USA, C8052-1MG), 2 nM triiodothyronine

(Liotir, IBSA, Italy, AIC 036906016) and 10 ng/mL epidermal growth factor (EGF, GMP Cellgro, Cell Genix GmbH, Germany, 1016-050).

2.3.6.1 Feeder layer preparation

Tissue derived human limbal stem cells were cultured on irradiated 3T3-J2 cells, used as a feeder layer. 3T3-J2 cells were kindly donated by Howard Green Harvard Medical School, Boston, US. 3T3-J2 cell media consisted of DMEM supplemented with 10% (v/v) Calf serum (10101-145, ThermoFisher, Italy), 50 µg/mL penicillin-streptomycin (P/S, Euroclone, Italy, ECB3001D), and 4 mM glutamine (Euroclone, Italy, ECB3000D). Once confluent, the cells were trypsinized and centrifuged. After removing the supernatant, the cells were counted and placed in a 50 mL tube with a maximum of 20 mL cell culture media and 500,000 cells/mL to be irradiated (X-Ray Irradiator, Faxitron-Cell Rad, 2328A50142). To prepare the feeder layer for the extracted limbal stem cells, 80,000 cells/well were plated in a 24 well plate.

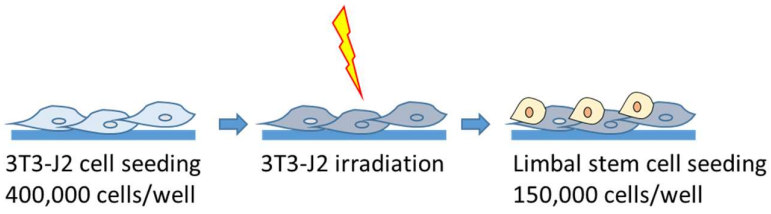


Figure 2.7: Steps to culture tissue derived primary limbal stem cells (td_hLESCs) extracted from the biopsy.

2.4 Cell characterisation

2.4.1 PrestoBlue® assay

PrestoBlue® assay (Invitrogen, UK, A-13262) was used to monitor the metabolic activity of the cells, and indirectly to quantify cell viability. After adding PrestoBlue® reagent (resazurin-based solution) to the cells, it becomes highly fluorescent if the cells are viable, due to the reduced microenvironment that convert the molecule to fluorescent resorufin. PrestoBlue® solution was prepared by diluting PrestoBlue® in cell culture media (1:10). After the required time, 100 µL of the assay solution was transferred to a 96 well plate and the fluorescence reading was taken using the spectrofluorometer at 560/590 nm excitation/emission wavelengths, respectively. The intensity of the blank sample (scaffold without cells) was subtracted from the reading determined for each well.

2.4.2 Live/Dead™ Fluorescence assay

Live/Dead™ Viability/Cytotoxicity Kit for mammalian cells (Invitrogen, L3224) was used to obtain a visual representation of cell viability. Cells were incubated with Live/Dead™ solution containing 2 µM calcein AM and 4 µM Ethidium homodimer-1 (EthD-1) in cell culture media, for 30 minutes. Calcein AM is converted by esterase activity to green-fluorescent signal, indicating the viability of cells. EthD-1 enters into non-viable cells with a damaged membrane. Cells were imaged using an inverted fluorescence microscope (Lumen Dynamics Leica DMIRB, USA equipped with X-Cite® Series 120 Fluorescence Illuminator,

Excelitas Technologies), with excitation/emission wavelengths of 495/515 nm for calcein AM and 495/635 nm for EthD-1.

2.4.3 Cell fixation

Cells seeded on the gels were fixed with paraformaldehyde (PFA, Sigma-Aldrich, UK, 158127) at 4% (w/v, in PBS 1x) to ensure the preservation of cell morphology and ECM architecture. For confocal imaging and scanning electron microscopy procedures, cells were fixed with PFA for 10 min at RT and at 4°C overnight, respectively. Then, the samples were washed three times with PBS and stored at 4°C. For qPCR cells were detached from the scaffold, washed by centrifuge and fixed with PFA for 10 min at RT.

2.4.4 Immunohistochemistry

To study limbal cell marker expression, cells were stained with C14 and P63 (limbal progenitor markers) and CK3/12 (corneal marker). After the fixation, to permeabilize the cell membrane, 0.1% v/v triton X-100 (Sigma-Aldrich, UK, T8787) in PBS was added for 10 min at RT. Then, the sample was washed with PBS three times for 5 min. To prevent non-specific binding of the antibodies, blocking solution was added for one hour at RT. Blocking solution was composed of PBS containing 1% (w/v) of Bovine Serum Albumin (BSA, BDH Prolabo®, VWR, USA, 421501J), 0.3 M of Glycine (Sigma-Aldrich, UK, G7126), and 3% (v/v) of serum from the animal in which the secondary antibody was raised (goat serum, Sigma-Aldrich, G9023). Primary antibody was diluted in wash buffer prepared with 1% (w/v) BSA, 0.3 M of glycine in PBS, according to the concentrations

reported in table 2.2. The first antibody was added to the samples at 4°C overnight. Then, samples were washed three times with wash buffer and the second antibodies were added and incubated for one hour at RT, according to the concentration described in table 2.2. Then, the samples were washed three times for 5 min each. To stain the nucleus, Hoechst (B2883, Sigma-Aldrich, UK) was added for 10 min at RT. The sample was then washed with PBS for three times, and mounting media solution (Fluorescent mounting medium Dako, VWR, UK, S3023) added to preserve the fluorescence staining. After immunostaining, cells were analysed by confocal microscopy (section 2.5.1, confocal microscopy).

Table 2.2: Primary and secondary antibodies used in immunofluorescence. In both cases, they were diluted in the washing solution.

Primary antibodies:

Markers for	Antigen	Manufacturer	Cat	Host	Concentration
Cornea cells	Anti-Cytokeratin 3/12 antibody	Abcam, US	2Q1040	mouse	1:200
Limbal stem cells	Anti-p63 antibody	Invitrogen	EPR5701	rabbit	1:200
	Anti-Cytokeratin 14 antibody	Invitrogen	MA5-16370	rabbit	1:100

Secondary antibodies:

Markers for:	Target	Manufacturer	Cat	Dye	Concentration
Cornea cells	Goat anti-Mouse IgG (H+L) Superclonal™ Secondary Antibody	Invitrogen	A11001	Alexa Fluor® 488 conjugate	5 µg/mL
Limbal stem cells	Goat anti-Rabbit IgG (H+L) Secondary Antibody	Invitrogen	A21070	Alexa Fluor® 633 conjugate	5 µg/mL

2.4.5 qPCR

RT-qPCR analysis was carried out by Dr. Laura Sidney, at the School of Medicine department, at the University of Nottingham. It was performed to obtain quantitative analysis of gene expression. It is based on the principle of the polymerase chain reaction (PCR) and allows a target DNA molecule to be amplified and quantified. The ribonucleic acid (RNA) samples were isolated from cells, then used to obtain DNA via reverse transcription, creating complementary DNA (cDNA). DNA polymerase, with specific probes were used to perform PCR and amplify the target DNA. During qPCR, primers bind to the single stranded cDNA template and double stranded DNA (dsDNA) is synthesised. To quantify the expression of gene, a DNA binding fluorescent dye is used. A fluorescent probe binds to the newly synthesised DNA. The amount of fluorescence generated is recorded and it is proportional to the amount of DNA. Relative quantification is employed, using reference genes to determine fold-differences in expression of the target gene.

The first step to calculate the levels of a target gene was to extract ribonucleic acid (RNA) samples. RNeasy kit (Qiagen, Manchester, UK) was used to isolate the total RNA, according to the manufacturer's instructions. Briefly, samples were lysed in RLT buffer, homogenised using QIAshredder columns (Qiagen) and then RNeasy mini spin columns were used to extract the RNA using a variety of buffers and centrifugation steps. The calculation of the RNA concentration was performed by using an LVIS plate on a Clariostar plate reader (BMG LabTech, Buckinghamshire, UK). The second step was to transcript, performed to form single stranded complementary DNA (cDNA) from the extracted RNA. Reverse

transcription of 100 ng RNA was obtained using the Superscript III System (Life Technologies) and random hexamer primers, according to the manufacturer's instructions. The random hexamer primers anneal randomly to the RNA and the reverse transcriptase enzyme then synthesises cDNA from the primer sites using deoxynucleotide triphosphates (dNTPs). PCR thermal cycler was used to denature the RNA at 85°C, and to allow primer adhesion. Then, the reverse transcriptase to form the cDNA was performed at 55°C. Resulting cDNA transcripts were stored in RNase/DNase free water at -20°C.

In the third step the PCR was performed by using the DNA polymerase, with specific probes, to amplify the target DNA. For PCR, 1 µL cDNA was used with inventoried Taqman assays and TaqMan® Gene Expression MasterMix. Each reaction contained 1 µL cDNA sample, 10 µL of each of mastermix, 1 µL relevant probe and 8 µL RNase-free water. Amplification was performed on an Mx3005P PCr system (Stratagene, Stockport, UK) with 1 cycle of 50°C for 2 min, 1 cycle of 95°C for 10 min and 50 cycles of 95°C for 15 s followed by 60°C for 1 min.

Online software based on a four parameter simple exponent model (Zhao and Fernald, 2005) was used to analyse data, and to calculate efficiency (E) and threshold cycle (C_T). All values were normalised to the endogenous reference gene GAPDH, and then expressed as a comparative fold change to a control. The genes investigated and their correspondent protein were KRT3 (Cytokeratin 3) and KRT19 (Cytokeratin 19)

2.5 Microscopy and imaging

2.5.1 Confocal microscopy

Confocal microscopy (Zeiss Elyra PS.1 microscope, Carl Zeiss, Germany) was used after immunostaining to image cell markers and to measure micro-scaffold volume for swelling studies, by using a 10x water immersion objective. Multi-channel imaging was performed by sequential scan mode (Z-stack mode). Negative control consisted of cell-free scaffolds. The images were analysed with ImageJ and Zen software.

2.5.2 Scanning electron microscopy (SEM)

Scanning electron microscopy (SEM) is a technique for high magnification imaging. A focused beam of electrons is scanned across a surface, where they interact with atoms in the sample. Secondary electrons are transmitted from the surface of the sample, providing information about the surface topography. SEM (Hitachi SEM TM3030, USA) was used to image cell morphology and cell material interaction. After fixing and washing the biological samples, they were dehydrated through a series of ethanol concentrations: 25% (v/v), 50% (v/v), 70% (v/v), 90% (v/v), 95% (v/v), for 10 min each and 100% (v/v) three times for 5 minutes. Finally, they were sputter-coated with gold under an argon atmosphere (EM SCD005, Leica Microsystem, UK).

2.5.3 CryoSEM

To study the pore structure and dimensions of the hydrogels, SEM (JEOL JSM-6060LV, USA) with a cryo-preparation chamber, sputter coating head and Dewar

cooling apparatus (Oxford CT 1500) were used. Samples were immersed into sub-cooled nitrogen (nitrogen slush) at -210°C, transferred *in vacuo* and fractured with a scalpel to observe the internal structure. After sublimation at -90°C, they were coated with gold and transferred to the SEM chamber for image acquisition. ImageJ software was used to measure the pore dimensions.

2.6 Additive manufacturing techniques

A 3D scaffold geometry was obtained by using two additive manufacturing techniques: 3D inkjet printer and two-photon polymerization system (2PP).

2.6.1 3D inkjet printer

The inkjet printed scaffolds were fabricated with the collaboration of Hagit Gilon at the Additive Manufacturing group, at the University of Nottingham. The architectures were developed using an integrated print head in a three-axis motion system. The setup is shown in figure 2.8. The print head is a jetting valve - Pico Dot LV (Nordson EFD) driven by a driver and controller (DCON, Nordson EFD). The jetting process of the print head is synchronized with a three-axis custom made high performance linear stage connected to a computer with an overall accuracy of 0.5 µm. LabVIEW (National Instruments, USA) software code was written to synchronize the three-axis motion and print head jetting. The ink was jetted through a 50 µm nozzle by an applied air pressure of 1 Bar and a rod movement driven by two piezoelectric actuators. The printing was performed on a substrate cooled by a custom-made Peltier cold stage, to accelerate the gelation process and to reduce the drop size. GelMA solution was used as an ink

and polymerized immediately after printing with UV lamp at 15W (UVP, Upland CA, USA, Cambridge, Black-Ray XX-15L UV bench Lamp).

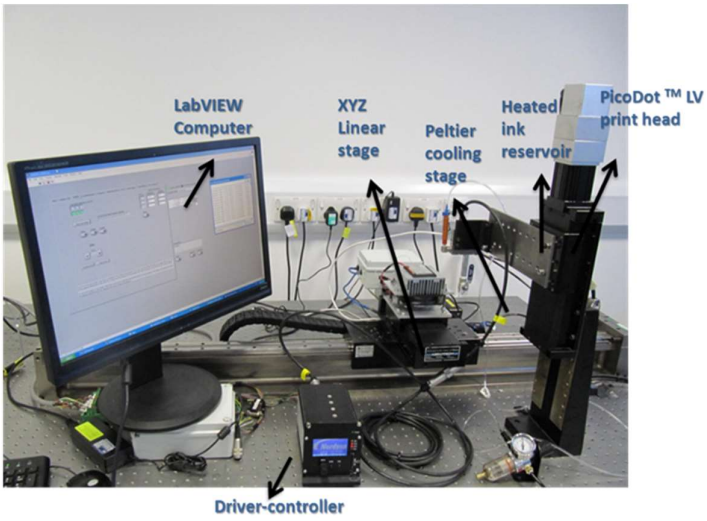
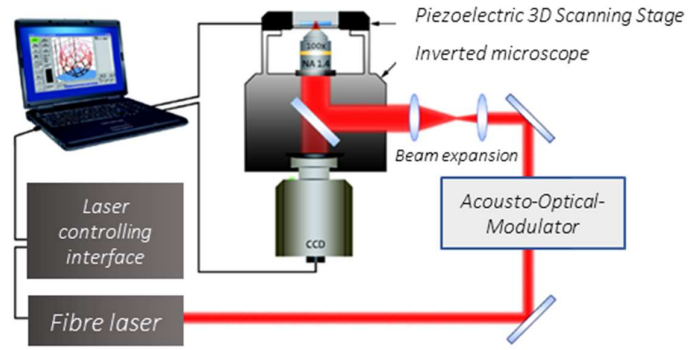


Figure 2.8: 3D inkjet printing system for gelatine based inks

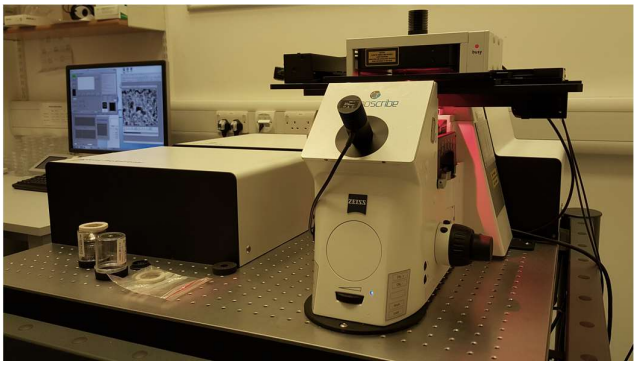
2.6.2 Two photon polymerization

2.6.2.1 CAD design and printing parameters

To fabricate micro-structures replicating the dimensions of the limbal stem cell niche, a two photon polymerization (2PP) system (NanoScribe Photonic Professional, GmbH, Germany) with a femtosecond laser emitting at 780 nm in galvo scan mode was used. The structure was developed using CAD 3D Autodesk Inventor software and the printing parameters were set by Describe software. In figure 2.9, the system setup is shown. The laser beam was focused using a conventional 25x or 63x microscope objective (Zeiss, NA 1.4, with oil immersion media), which was mounted on a linear stage for vertical positioning. The laser writing system was controlled by Nanowrite software.



a



b

Figure 2.9: Set-up of the two photopolymerization system. (a) Representation of the system, taken from (Nanoscribe, 2014); (b) Two photon polymerization system, NanoScribe Photonic Professional, GmbH, Germany.

A drop of each individual gel was cast between a 22x22 mm cover glass (thickness n. 1.5), and a 18x18 mm cover glass (thickness n. 1.5), separated by a 300 µm spacer (figure 2.10). The printing process was obtained by tuning laser power, scan speed and the hatching distance (distance between each layer). After printing, the structure was 'developed' by immersing the sample in PBS at 40°C for 1 hour to remove the non-polymerized hydrogel; the sample was then left at 4°C overnight. Irgacure 2959 solution (0.1% w/v) was added and the scaffold UV cured (365 nm long wave UV lamp at 15W) for 10 minutes to increase the stability of the structures.

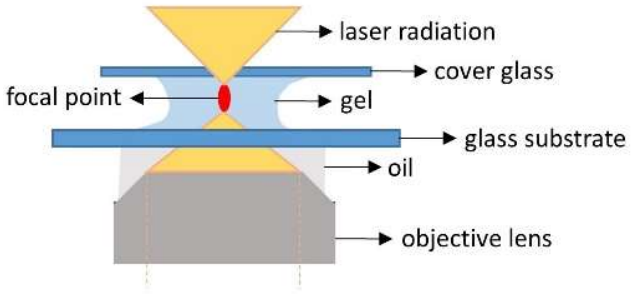


Figure 2.10: Configuration of gel set up and 2PP system. The gel is sandwiched between two cover glass and the laser is focused with 25x or 63x objectives.

2.6.2.2 Gel preparation

Benzylidene ketone-based water-soluble photoinitiator (P2CK) was kindly prepared by Dr. Jonathan Moore from the Chemistry Department, University of Nottingham and Mr. Maximilian Tromayer from the Institute of Applied Synthetic Chemistry, Vienna University of Technology following the procedure explained in Li et al. (2013). Briefly, the compound was obtained via a classical aldol condensation reaction between 4-aminobenzaldehydes with carboxylic acid salts at terminal amino groups and corresponding ketones.

P2CK stock solution was prepared by dissolving the powder in PBS to obtain a 5% (w/v) concentration. GelMA solution was prepared to dissolve dried GelMA in PBS to reach the desired concentration, and P2CK stock solution was added to obtain different PI concentrations that were tested with the system.

2.7 Statistical analysis

Results were expressed as mean ± standard deviation (SD). Statistical analysis was performed in Prism 6 (GraphPad Software, v6.01). Differences were considered statistically significant when p-value was lower than 0.05 ($p \leq 0.05$).

Further details about the statistical test performed will be presented in the respective chapters. Generally, the experiments were performed in three technical replicates, and repeated in three independent experiments (n=3). Any deviation from this is reported in the specific figure caption.

3. Cornea and stiffness: Gelatin methacrylate and 3D printed structures

3.1 Introduction

Hydrogels are an interesting class of biomaterials in relation to their structure and biochemical properties, which are similar to those of the extracellular matrix (Cushing and Anseth, 2007). GelMA is a photopolymerizable hydrogel based on gelatin, which is obtained from denatured collagen, the most abundant structural protein in many tissues, including the cornea. The poor mechanical properties of gelatin can be increased by the addition of methacrylamide groups, which allow for UV crosslinking (Van Den Bulcke *et al.*, 2000). In addition, the use of GelMA offers a hydrogel-based system in which the mechanical properties can be tuned by changing the gel concentrations (Nichol *et al.*, 2010). GelMA is a well-known material used in a variety of applications, such as vascular, cartilage, bone, and skin tissue engineering (reviewed in Yue *et al*., 2015), but has only recently been investigated as a limbal stem cell carrier (Rizwan *et al.*, 2017). However, it has great potentiality in ophthalmology applications as reported in Rose et al., (2014). Furthermore, it preserves the biomimetic properties of gelatin allowing cell adhesion and proliferation without

any additional modification due to the presence of RGD (Arg-Gly-Asp) motifs (Yue *et al.*, 2015).

The importance of substrate stiffness in the cell differentiation process is well known (Engler *et al.*, 2006, Discher *et al.*, 2005). Even in the eye, there is evidence of the presence of a centripetal stiffness gradient between the limbus and the cornea, which can drive the differentiation process (Foster *et al.*, 2014). Further research is required to have a clearer understanding of the mechanisms involved. An example of the importance of the mechanical properties has been demonstrated by research conducted with the amniotic membrane. The amniotic membrane has been used as a substrate for limbal epithelial stem cell expansion for many years due to its ability to preserve limbal stemness *in vitro* (Meller *et al.*, 2002; Dua *et al.*, 2004) and the presence of a number of biological factors and proteins which are involved in ocular surface homeostasis and wound healing (Hopkinson *et al.*, 2006). However, the clinical success rate varies greatly, ranging from 46% to 100%. It has been hypothesised that this may be caused by the inter- and intra-sample variation including the high variability of their mechanical properties (Chen *et al.*, 2012).

The study of the stiffness relates to durotaxis, defined as the directed cell migration towards regions of increased stiffness. Despite the fact that directed migration of cells in response to chemical gradients has been the focus of extensive research, durotaxis has only been investigated with 3T3 cells (Lo *et al.*, 2000), and this mechanism is not fully understood in ocular surface homeostasis. The development of 3D models based on centripetal stiffness gradients may help to understand the process underpinning stem cell differentiation. The use

of additive manufacturing techniques, allowing precise control of scaffold geometry and cell arrangement, has become more popular in recent years. In regenerative medicine, such structures can be fabricated to more closely mimic *in vivo* 3D microenvironments, facilitating regenerative processes. Nevertheless, reports of additive manufacturing for eye-related applications are still scarce and mostly unexplored. Among other additive manufacturing techniques, inkjet printing offers several advantages due to its simplicity, speed, versatility and its great control over the deposition pattern (Gudapati *et al.*, 2016). In inkjet bioprinting, droplets of liquid, often picolitre in volume are delivered to specific locations on a substrate by means of thermal or acoustic forces. This technique has been used in combination with GelMA for some applications such as fibrocartilage tissue models (Gurkan *et al.*, 2014). Nevertheless, the inkjet printer has yet to be applied to ocular applications.

3.1.1 Chapter objectives

The ultimate aim of this project was to study the mechanisms that are involved in the maintenance of the 'stemness' in order to design a scaffold that can improve the output for the treatment of LSCD. This chapter focuses on stiffness; the first part describes the preparation and characterization of GelMA hydrogels in terms of mechanical properties in comparison to the *ex-vivo* human cornea. In the second part of the chapter, the use of an inkjet printer was investigated in order to reproduce a centripetal 3D stiffness gradient model. Finally, the ability of corneal epithelial cells to adhere and proliferate on GelMA hydrogels presenting different stiffness values, and on 3D architecture was analysed.

In detail, the objectives of this chapter were:

- to investigate the mechanical properties of *ex vivo* human cornea;
- to study GelMA hydrogel mechanical and physical properties in comparison to human cornea tissue;
- to investigate the viscosity of GelMA solutions suitable for 3D printing;
- to print scaffolds with 3D architecture and a centripetal stiffness gradient;
- to investigate the ability of cornea cells to proliferate on a wide range of GelMA concentrations and on 3D printed scaffolds.

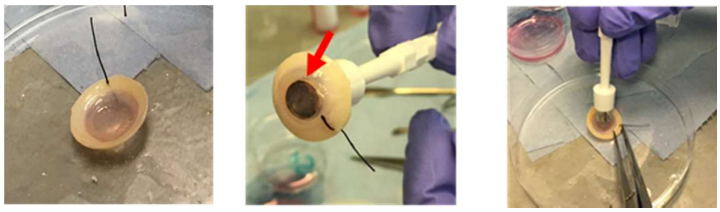
3.2 Experimental design

For detailed information regarding the equipment and the protocols used in the following chapter see Chapter 2: Materials and Methods. The specific sections will be indicated in each paragraphs. A table summarizing gel formulations and naming conventions can be found in appendix A.

3.2.1 Evaluation of corneal mechanical properties and swelling value

Human cornea biopsies were consented for research from Manchester Eye Bank (UK) and covered by local research ethics. They were stored at RT for a maximum of 5 months and preserved in an organ culture media consisting of Eagle's Minimum Essential Medium (EMEM) with 1% antibiotic/antimycotic (100 units/mL penicillin, 0.1 mg/mL streptomycin, 0.25 ug/mL amphotericin B) and 2% (v/v) FBS.

The corneal buttons were collected with an 8 mm puncher (figure 3.1). The bulk mechanical properties of the cornea button were performed using a texture analyzer and rheometer, following the same protocol of the GelMA hydrogels (section 3.2.4, selection of GelMA concentrations according to stiffness values of the human cornea). Each test was performed on three individual cornea donors (n=3). To measure the water content, swelling values were assessed immediately after removing the tissue from the medium. This test was performed on six corneas (n = 6, six donors).



a b

Figure 3.1: Preparation of human cornea samples for mechanical testing. (a) Human cornea removed from the media within 5 months after death; (b) corneal button (red arrow) was cut with 8 mm puncher.

3.2.2 Evaluation the degree of methacrylation of GelMA

To obtain a photopolymerizable material, gelatin was chemically modified by the addition of methacrylate groups. To evaluate the percentage of methacrylation, NMR (n = 5) and TNBS assays (n=3) were performed (see section 2.1.1, GelMA synthesis).

3.2.3 Preparation of GelMA at different concentrations

GelMA was synthesized as described in section 2.1.1 and 2.1.2 (GelMA synthesis and GelMA preparation). Hydrogels with a wide range of stiffnesses were

prepared by increasing the percentage (w/v) of GelMA from 5% to 40% (5%, 8%, 10%, 15%, 20%, 25%, 30% and 40% (w/v)). These hydrogels will be referred to as G5, G8, G10, G15, G20, G25, G30 and G40, respectively. They were dissolved in PBS, mixed with 0.5% (w/v) Irgacure 2959, at 80°C. GelMA solutions were pipetted between two glass coverslips separated by a 1 mm spacer and exposed to a 365 nm long wave UV lamp. After crosslinking (3 min), 8 mm discs were punched from each hydrogel using a biopsy tool, and placed in PBS to equilibrate at 37°C for 24 h before performing mechanical testing (figure 3.2).

Table 3.1: Gels nomenclature. GelMA hydrogels were prepared by dissolving GelMA at different concentrations in PBS with 0.5% (w/v) of Irgacure and crosslinked using a UV lamp at 365 nm for 3 min.

Nomenclature	G5	G8	G10	G15	G20	G25	G30	G40
GelMA concentration (% w/v)	5	8	10	15	20	25	30	40

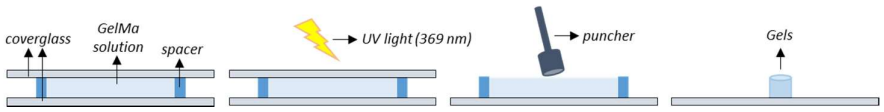


Figure 3.2: Preparation of gel for compression and rheological test. The GelMA solution is placed between two coverglasses separated by a spacer. After applying the UV light for 3 min (365 nm), the second coverglass is removed and the gels are tested with the texture analyser and rheometer.

3.2.4 Selection of GelMA concentrations according to stiffness values of the human cornea

To select the concentrations of GelMA suitable to study the effect of stiffness on corneal epithelial cells, macro- and micro- characterizations were performed and compared to values measured using human cornea. Figure 3.3 shows the

flow chart for the selection of suitable hydrogels. GelMA hydrogels were prepared considering a wide range of concentrations. Bulk stiffness was evaluated by compression testing using a texture analyzer, the viscoelastic properties were evaluated by rheology, and the surface stiffness assessment was conducted using AFM. The results were compared to *ex-vivo* tissue, and the concentrations with values closest to the human cornea were selected. The micro-characterization, obtained by measuring the surface stiffness, was compared to the cornea values reported in the literature. The selected concentrations were used for further tests, which will be the focus of Chapter 6.

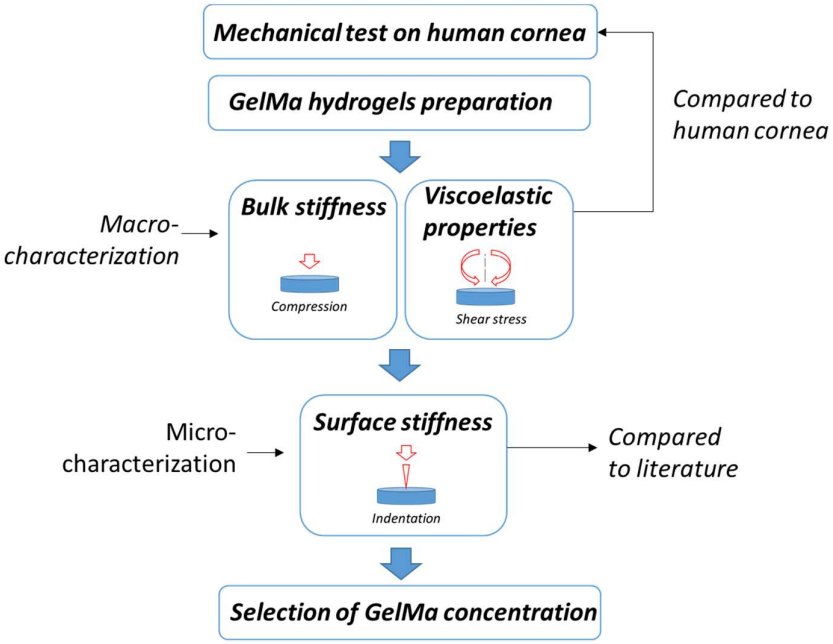


Figure 3.3: Flow chart for the selection of GelMA concentrations. First, the human cornea was characterized. Then, GelMA hydrogels with a concentration between 5% (w/v) and 40% (w/v) were prepared and tested by compression testing and rheology. Finally, the gels were tested by AFM, and compared to the range of stiffnesses of the human cornea reported in literature.

3.2.4.1 Measuring the bulk stiffness of the gels by the texture analyser

To calculate the elastic modulus, stress against strain was plotted and Young's modulus was taken as the slope of the initial linear region corresponding to 0-10% strain and purely elastic deformation. The compression was performed at 10% strain/s. Three samples for each gel were considered and the test was repeated on three different GelMA batches (n=3). For detailed information see section 2.2.2 (Texture analysis).

3.2.4.2 Measuring the viscoelastic properties of the gels by rheology

The gap between the plates was between 800 µm and 1000 µm. To evaluate the Viscoelastic Linear Region (VLR), a strain of increasing amplitude (0.1–10%) at a constant frequency of 1 Hz at 37°C was applied to the samples. The oscillatory frequency test was performed at 37°C and with a strain amplitude of 1% (within the VLR) and a frequency between 0.01 Hz and 10 Hz. Storage and loss moduli (G' and G'') were quantified. The tests were performed on three samples and repeated for three different GelMA batches (n=3). For detailed information see section 2.2.1 (Rheology).

3.2.4.3 Measuring the surface stiffness of the gels using AFM

The measure of surface stiffness was conducted with a cantilever with a spring constant in the range 68.59-84.50 pN/nm and a sensitivity of 74.41-79.48 nm/V. Force measurements were conducted on three discrete areas taking 20 measurements in each area. The Young's modulus, E, was calculated by averaging all force curves. For detailed information see section 2.2.1 (AFM).

3.2.4.4 Analysing the swelling ratio of the gels

The mass swelling ratio was calculated after 1 h, 6 h, 24 h, 72 h and 120 h. The test was performed on three samples, and the experiment was repeated by using three GelMA batches (n=3). For detailed information see section 2.2.4 (Swelling analysis).

3.2.4.5 Determining the gel pore size by cryoSEM

For detailed information see section 2.5.3 (cryoSEM). Ten pore sizes was average for each condition.

3.2.5 Manufacturing of a 3D printed scaffold using a Pico-dot printer

3.2.5.1 Design of a scaffold with a stiffness gradient and 3D architecture

As a simple model to recreate a 3D architecture that could mimic a steep surface with a centripetal stiffness gradient, an array of 10 by 10 pillars was printed on a pre-cast GelMA substrate (prepared as explained in section 3.2.3, Preparation of GelMA at different concentrations). The GelMA concentrations for the base and the pillars were chosen according to the tested mechanical properties of the *ex vivo* corneas. Pillars were printed with a drop spacing of 400 µm, following 3 minutes UV exposure to induce cross-linking. The distance between the GelMA substrate and the nozzle was set to 3 mm. The model is schematically represented in figure 3.4. The experiment was performed in collaboration with the Additive Manufacturing group, at the University of Nottingham, and Hagit Gilon produced the printed scaffolds. For more information see section 2.6.1 (3D inject printer).

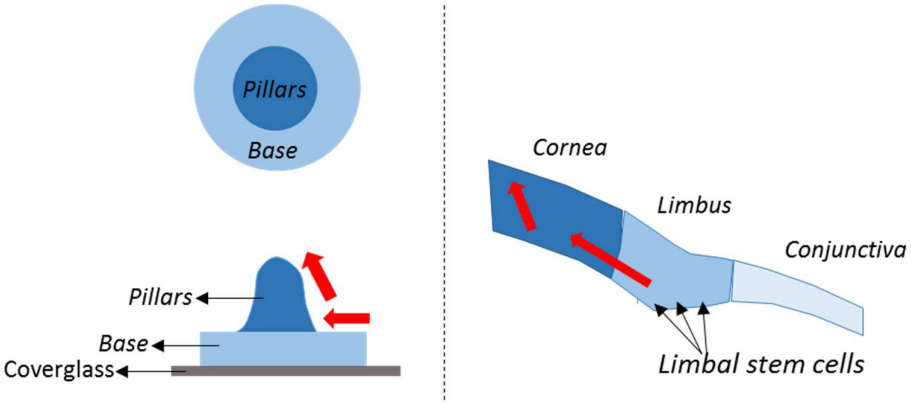


Figure 3.4: Schematic representation of the 3D bioprinted structures. The model (left) simulates the centripetal stiffness difference between limbus and cornea (right), where the pillars represent the cornea and the base simulates the limbus.

3.2.5.2 Investigation of GelMA viscosity and gel point

To select the GelMA concentration suitable for 3D printing, the viscosity of the polymeric solutions was analysed by rheology in the range 15-40°C with a shear rate of 1/100s. To select the concentration for the base of the scaffold, the gel point was evaluated. This represents the temperature at which the storage modulus becomes larger than the loss modulus, as an indication of the transition from a liquid-like behaviour to a gel-like behaviour. The oscillatory test was performed at 1 Hz whilst decreasing the temperature from 40°C to 10°C. The tests were performed on three samples, and on three batches (n=3). For more information see section 2.2.1 (Rheology).

3.2.5.3 Evaluation of the stiffness of the printed scaffold

To measure the stiffness and the viscoelastic properties of the printed gel, a disk (diameter = 8 mm) of GelMA was printed. The compression and rheological tests

were performed as described in section 3.2.3 (Preparation of GelMA at different concentrations). Three replicates for each material were tested.

3.2.6 Effect of GelMA stiffness and 3D architecture on cornea cell viability

The effect of GelMA stiffness on the metabolic activity of hCECs was tested using PrestoBlue®. Gels were soaked in 1 ml PBS and adding 100 units/mL of penicillin, 0.1 mg/mL of streptomycin and 0.25 µg/mL of amphotericin B at 37°C for 24 h. After removing PBS, 30 µl of hCEC suspension (3,000,000 cells/ml; 90,000 cells/scaffold) were seeded on top of flat and 3D printed gels. After 1 h, 300 µl of cell media were added to each well. The metabolic activities were tested with PrestoBlue® after 1, 3, 7 and 10 days for the flat scaffold. In each plate, the media was aspirated and 300 µl of PrestoBlue® were added to the seeded scaffolds. After 90 min, the absorbance was evaluated at 560/590 nm excitation/emission wavelengths. The test was performed on five samples. Cell morphology on the 3D printed scaffolds was assessed using SEM and to evaluate cell proliferation on steep materials, after 7 days from cell seeding. A preliminary test was conducted on G40 pillars printed on G15 base; hCECs were calcein AM labelled and imaged after seeding with fluorescence microscopy. For more information about the cell culture protocols and PrestoBlue® assay see section 2.3.1 (General method for cell cultivation), 2.3.2 (Cornea epithelial cells), 2.4.1 (PrestoBlue® assay), and 2.4.2 (Live/Dead™ Fluorescence assay).

3.3 Results

3.3.1 Determination of the mechanical properties of the human cornea

The bulk mechanical properties of the human cornea were investigated using rheology and compression testing. The rheology results (figure 3.5) indicated that the cornea storage modulus was constant at different frequencies and that the storage modulus is always higher that the loss modulus. The compression test (table 3.2) indicates that the Young's modulus of the cornea was 39.1 kPa ± 4.7. The three cornea samples presented similar behaviour.

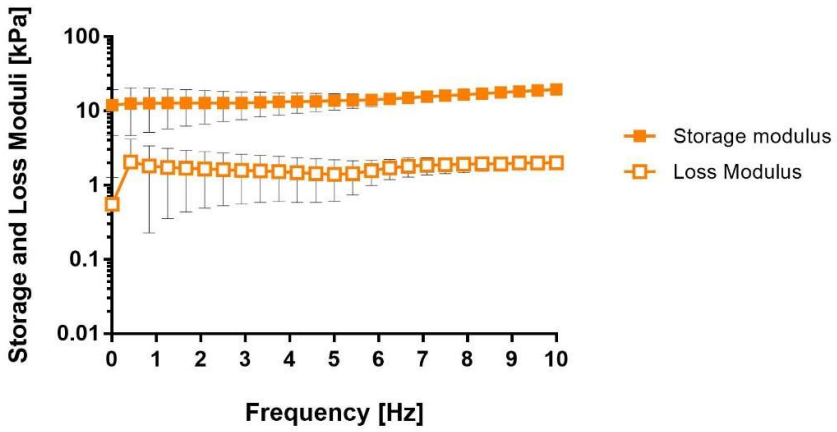


Figure 3.5: Frequency sweep test of *ex-vivo* human cornea. Storage and loss moduli of three donor samples were recorded varying the frequency from 0.1 to 10 Hz. Data are presented as average ± SD (n=3).

Table 3.2: Elastic moduli of three *ex-vivo* human cornea donor samples.

	A	B	C	Average ± SD
Elastic modulus [kPa]	34.5	43.8	39.0	39.0 ± 4.7

3.3.2 GelMA solution was successfully synthesised

According to the pioneering work of Van den Bulcke (2000), the methacrylation reaction occurs at the free amino groups given by the lysine and hydroxylysine.

The gelatin contains 0.35 mmol free amino groups per gram of gelatin (bovine skin, type B), however the concentration is variable, and depends on the raw material and process used to obtain the gelatin. The degree of methacrylation was confirmed by NMR, comparing the lysine/hydroxylysine signal in gelatin and in GelMA (Figure 3.6a).In figure 3.6b,c the NMR spectrum of gelatin and the resultant GelMA are shown. The presence of the peaks at 5.3 and 5.6 ppm relative to the acrylic protons of methacrylic groups are visible in the GelMA spectra but not in the gelatin, confirming the success of the methacrylation process.

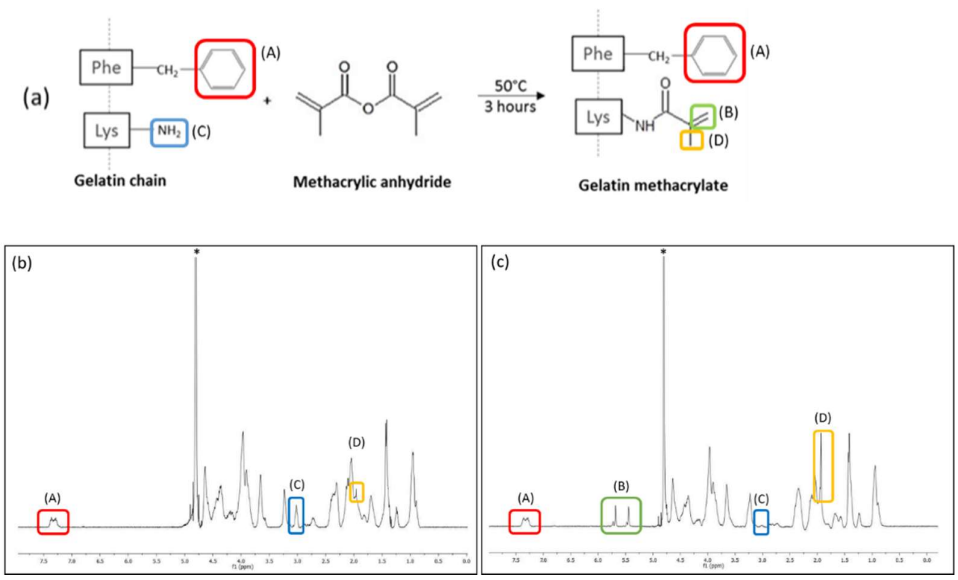


Figure 3.6: Gelatin methacrylate characterization. (a) Schematic representation of methacrylate substitution of the primary amines of gelatin. NMR spectra of 10 mg/mL of (b) gelatin and (c) GelMA recorded in D_20 (*) at RT. Both graphs present the peak at 7.2 ppm associated with the aromatic groups (peak A, red). In the GelMA spectrum, the lysine signal (peak C, blue) at 2.9 ppm decreases while the methacrylate vinyl group signal at d = 5.4 ppm and d = 5.7 ppm (peak B, green) and the methyl group signal at 1.8 ppm increase (peak D, yellow), indicating that the reaction occurred.

The degree of substitution (DS) calculated with NMR was 80.2% ± 6.1. These results were confirmed using the TNBS assay, where the average of three batches was 83.5% ± 4.9. In table 3.3, the results of each batch are reported.

Table 3.3: DS of three different batches of GelMA measured by TNBS assay. Average ± SD (n=3).

	Batch 1	*Batch 2*	*Batch 3*	*Average ± SD*
Degree of substitution	84.2	78.3	88.0	83.5 ± 4.9

3.3.3 GelMA hydrogels matches human cornea tissue mechanical properties

A preliminary study in altering gel stiffness by varying the GelMA concentration was conducted. Stiffness measurements were performed with increasing concentrations of GelMA. The results showed that the stiffness increased with increasing GelMA concentration and Young's moduli of the hydrogels ranged from 16.3 kPa to 1099.7 kPa. The gels G5, G15, G25, and G40 were selected for further tests since they showed an elastic modulus with statistically significant difference to each other ($p \leq 0.05$, figure 3.7), and covered a wide range of stiffness values.

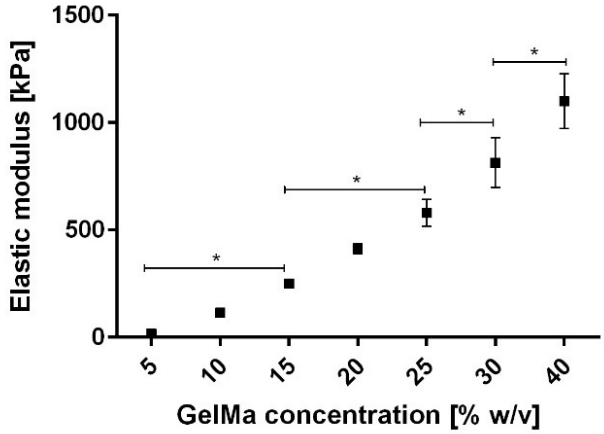


Figure 3.7: Elastic modulus of hydrogels varying GelMA percentage obtained from compression testing. The modulus was obtained as the gradient of the stress vs strain slope corresponding with 0-10 % strain. Data presented as mean of three samples ± SD. One-way ANOVA with post-hoc Tukey's test (*p≤0.05).

A well defined stiffness value was identified for each selected gel; the average (± SD) stiffness for G5, G15, G25 and G40 was 13.0 ± 2.9, 173.5 ± 78.2, 509.7 ± 60.4, and 1014.4 kPa ± 75.5, respectively (figure 3.8). The results showed that the stiffness of the human cornea fell between G5 and G15 values.

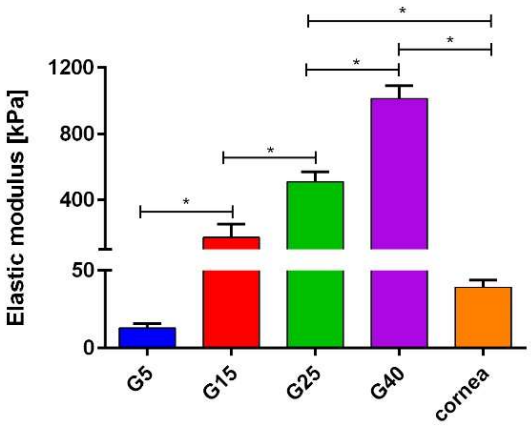


Figure 3.8: Elastic modulus of G5, G15, G25, and G40 in comparison to *ex-vivo* human cornea values obtained with the compression test. Data presented as mean ± SD (n=3). One-way ANOVA with post-hoc Tukey's test (*p≤0.05).

The swelling results after 24 h highlighted that equilibrium was reached within 6 h (figure 3.9). Increasing the percentage of GelMA, the swelling ratio decreased significantly ($p \leq 0.05$). Values of G5 and G15 fell within the range of human cornea water content values. A preliminary test considering the impact of GelMA concentration on gel porosity was performed by cryo-SEM. Figure 3.10 shows images of the swollen hydrogels. Average pore size was quantified for each gel. The images showed that the pore size of G10 was greater than G15 and G20. There was no difference between G15 and G20. It is likely that further increasing the GelMA percentage may give rise to a further decrease in pore size.

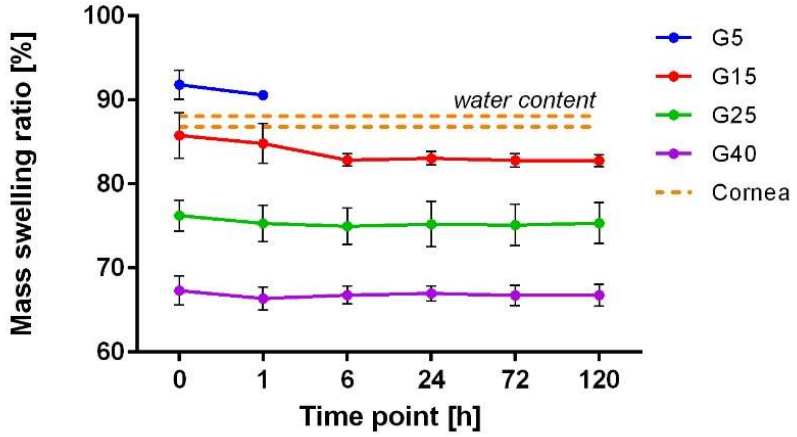


Figure 3.9: Mass swelling ratio of hydrogels at various GelMA concentrations % (w/v) and *ex-vivo* human cornea. GelMA at 5% (w/v) concentration was too weak to be handled and was not studied after 1 h. Swelling ratio calculated as defined in Equation 2.6. Data presented as mean ± SD (n=3).

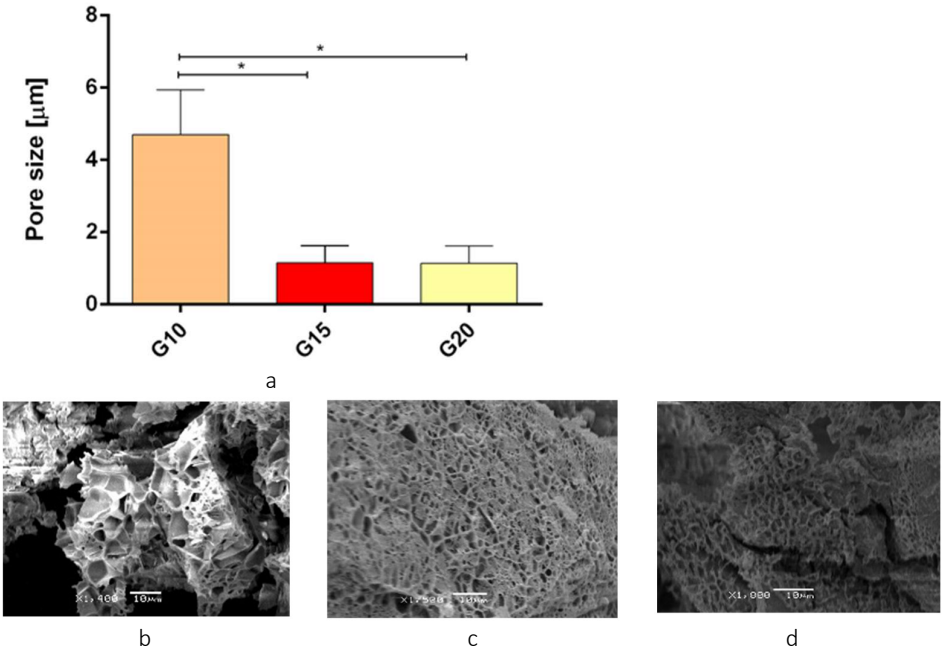
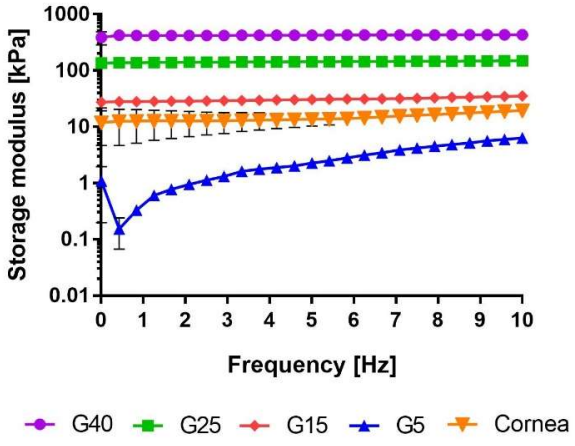
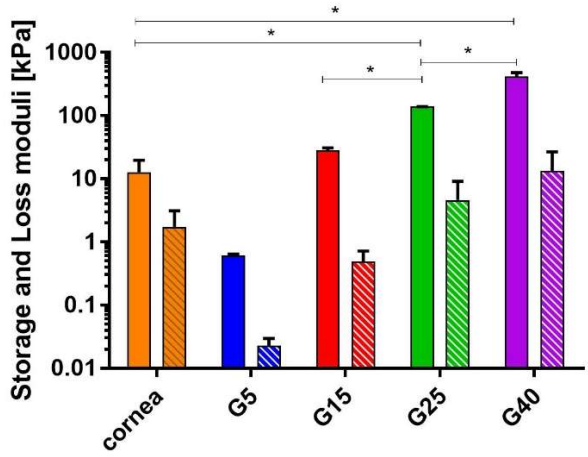


Figure 3.10: Pore dimensions of hydrogels and Cryo SEM images. a) Pore dimensions evaluated on SEM images for b) G10, c) G15, d) G20. Data presented as mean of 10 areas ± SD, one-way ANOVA with post-hoc Tukey's test (*p ≤0.05).

The rheological properties of the gels are reported in figure 3.11. The storage moduli were frequency-independent, except for G5, and were always higher than the loss modulus, indicating the viscoelasticity of the material. Increasing the concentration of GelMA, the storage modulus increased. Storage and loss moduli analysed at 1 Hz (with a shear strain within the VLR) are shown in figure 3.11b. The storage modulus of cornea generated a value between G5 and G15, and the variation of the loss modulus was not statistically significant.



a



b

Figure 3.11: Frequency sweep test of cross-linked GelMA and *ex-vivo* human cornea. (a) Storage as a function of frequency measured between 0.1 and 10 Hz; (b) storage (solid fill bars) and loss moduli (striped bars) at 1 Hz. Data presented as mean ± SD (n=3). Two-way ANOVA with post-hoc Tukey's test (*p≤0.05).

The calculation of surface stiffness was performed by AFM. The results given by the macro-characterization indicated that the gels between G5 and G15 were the closest to the *ex-vivo* cornea values. For this reason, more concentrations were tested in that range using AFM. G8 and G10 refer to 8% and 10% of GelMA, respectively. The results are shown in figure 3.12. Increasing the concentration of GelMA, the elastic modulus increased. G8 presented a value comparable to

G5, possibly because polymer chain entanglements are not yet having a major influence. The results have been compared to the values of human cornea reported in the literature (McKee *et al.*, 2011) and are indicated in figure 3.12 with a red rectangle.

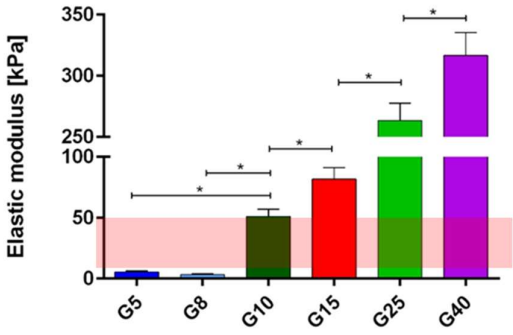


Figure 3.12: Surface elastic modulus of four concentrations of GelMA determined by AFM measurements. A total of 20 AFM measurements were taken per each of the three areas investigated. The surface stiffness of cornea is between 7.5 kPa and 50 kPa (McKee *et al.*, 2011), indicated in the figure by a red rectangle. Data presented as mean ± SD (n=3); One-way ANOVA with post-hoc Tukey's test, *$p \leq 0.05$.

3.3.4 Viscosity of GelMA solutions that can be 3D printed

An important factor influencing the 3D printing process is the viscosity of the ink. The results regarding GelMA viscosity are shown in figure 3.13. The solutions showed shear thinning behaviour, and as expected, the viscosity decreased by increasing the temperature and reducing GelMA concentration. G25 and G40 at 30°C values were 9.8 cP and 108.0 cP respectively and resulted in good candidates for jetting (PicoDot LV printer) for creating pillar-like structures (printing range is reported as a red rectangle in figure 3.13).

The gel point indicated the material's ability to present a solid-like behaviour, even before the crosslinking process. This property is important to allow the ink

drops to deposit on the surface, without sinking into the base. For all the solutions, the gel points were below 37°C, as expected; decreasing the GelMA concentrations, the gel point decreased due to the physical cross-links between the gelatin polymer chains. According to this results (table 3.4), G15 was the most suitable gel to print the base of the pillars.

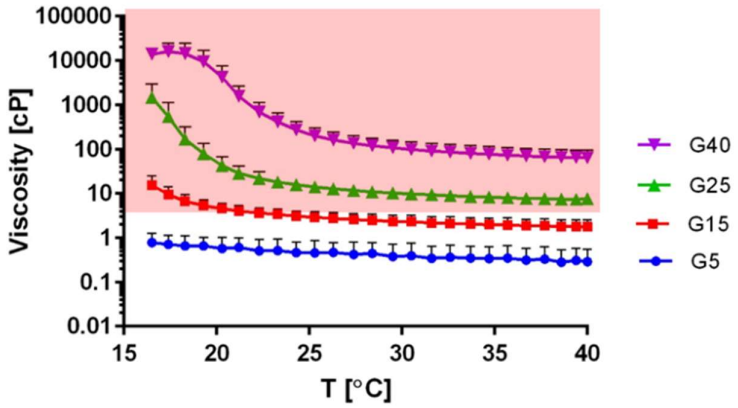


Figure 3.13: Viscosity and gel point of GelMA solutions at different concentrations by varying the temperature and GelMA concentration. Viscosity vs temperature. The red rectangle represents the range (from 8 to 200,000 cP) in which the manufacturer recommend to print. Data presented as mean ± SD (n=3).

Table 3.4: Gel points of G5, G15, G25, and G40. The gel point indicates at which temperature the gels show a transition from liquid-like to solid-like behaviour.

Gels	G5	G15	G25	G40
Gel point	<10°C	16.6°C ± 0.1	17.8°C ± 0.6	19.8°C ± 0.7

The selected GelMA concentrations, G25 and G40, were used to print the pillars, on a G15 base. A side view of the printed scaffolds (figure 3.14a,b) shows that the pillars were approximately 1 mm high, with around 500 µm spacing. The height could be reduced by decreasing the number of printed drops (data not shown). In figure 3.14c it appears that the pillars are uniformly spaced. G25,

unlike G40, is wider at the bottom and becomes narrower at the top. The difference in the shape is due to the higher viscosity of G40, which solidifies quicker allowing the gel to create steeper pillars.

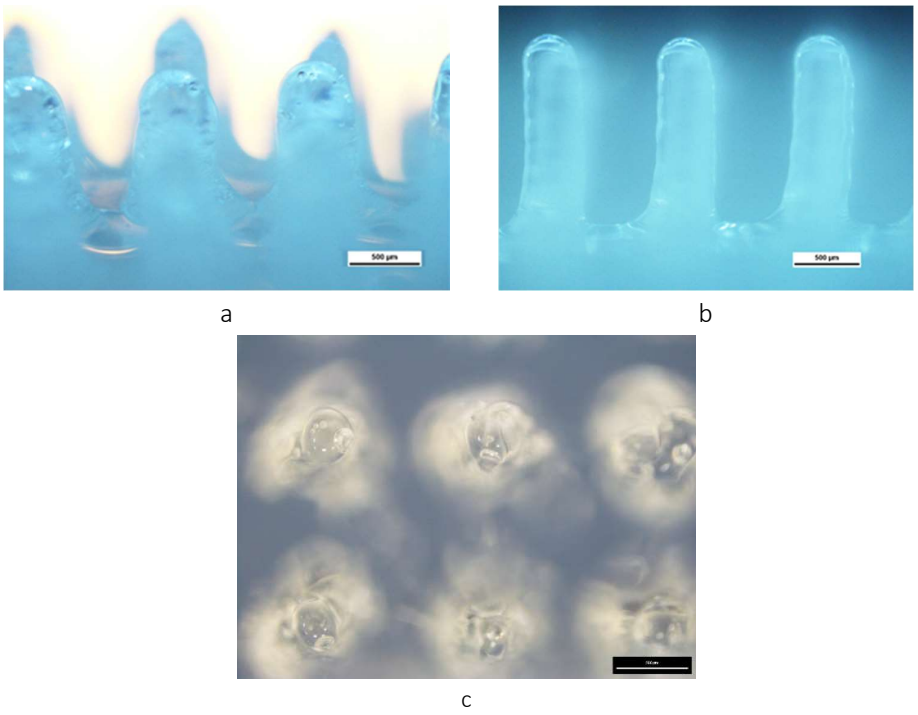


Figure 3.14: Representative brightfield images of crosslinked pillars. Side view of a) G25 and b) G40, and c) top view of G25.

The storage and the elastic modulus of flat printed scaffolds were measured to evaluate if the printing process introduces modifications affecting the scaffold mechanical properties (figure 3.15, table 3.5). The curve of the storage modulus of the printed scaffolds follows the same trend as the cast scaffolds. Nevertheless, the comparison of the values demonstrates that there was a significant difference in the storage modulus between the scaffolds prepared with and without the printing technique. This can be due to the introduction of air bubbles during pressurisation of the nozzle. According to these results, the

suitable material to obtain a layered gradient model is G40, since it showed an elastic modulus higher than G15.

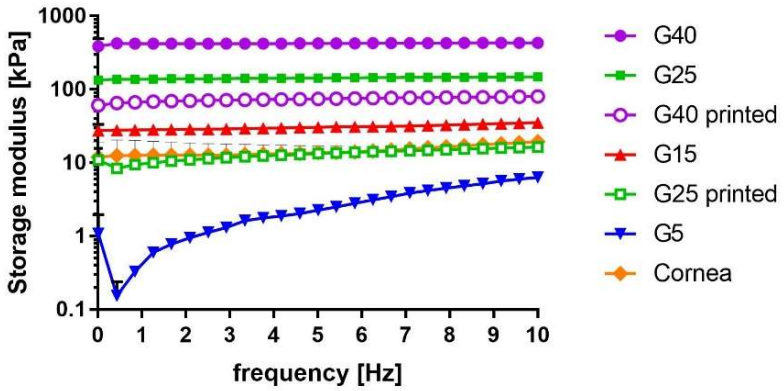


Figure 3.15: Frequency sweep test of printed GelMA (G25 and G40) compared to the cast samples. Storage as a function of frequency measured between 0.1 and 10 Hz (n=3).

Table 3.5: Storage modulus at 1 Hz of cornea samples, cast G5, G15, G25, G40, and printed G25, G40. Data presented as mean ± SD (n=3).

	Cornea	*G5*	*G15*	*G25*	*G25 printed*	*G40*	*G40 printed*
Storage Modulus [kPa] ± SD	12.8 ± 7.0	0.6 ± 0.1	28.4 ± 2.4	138.7 ± 0.6	10.1 ± 1.2	421.0 ± 60.2	68.3 ± 13.0

The table 3.6 summarizes the results of the GelMA samples and the cornea tissue as presented in this chapter.

Table 3.6: Summary of the mechanical characterization of the GelMA and human corneal tissue.

	GelMA (5% - 40%, included printed samples)	Human cornea
Degree of methacrylation (NMR and TNBS)	74.1 - 88.4 %	/
Viscosity pre-polymerization (15 - 40°C)	0.2 – 15914.4 cP	/
Bulk stiffness (Compression test)	11.1-1097 kPa	34.5-43.8 kPa
Surface stiffness (AFM)	4.5-335.6 kPa	/
Swelling ratio	65.6-92.9 % G5 difficult to handle	86.8-88 %
Pore size G10-G20 (Cryo-SEM)	0.6-6.5 µm	/
Storage and loss moduli (Rheometer)	0.5-463.3 kPa 0.02-28.6 kPa	8.0-20.1 kPa 0.8-3.3 kPa

3.3.5 hCECs are able to grow on both cast and printed GelMA scaffolds

The results from the hCEC proliferation tests are shown in figure 3.16. The results demonstrated that GelMA scaffolds have the capability to support the attachment of corneal epithelial cells. Across all gel samples/scaffolds the cell viability was comparable after 1 day, 3 days, 7 days and 10 days of culture. There was a significant increase in cell number over time ($p \leq 0.05$), indicating that cells proliferated on all selected concentrations. Due to the difficulty in handling G5, it was not possible to calculate the metabolic activity of cells cultured on all the batches analysed. No significant differences in cellular metabolic activity was found for cells cultured on the tested concentrations.

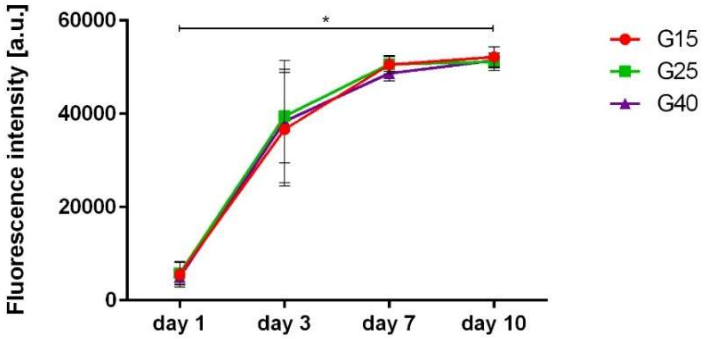
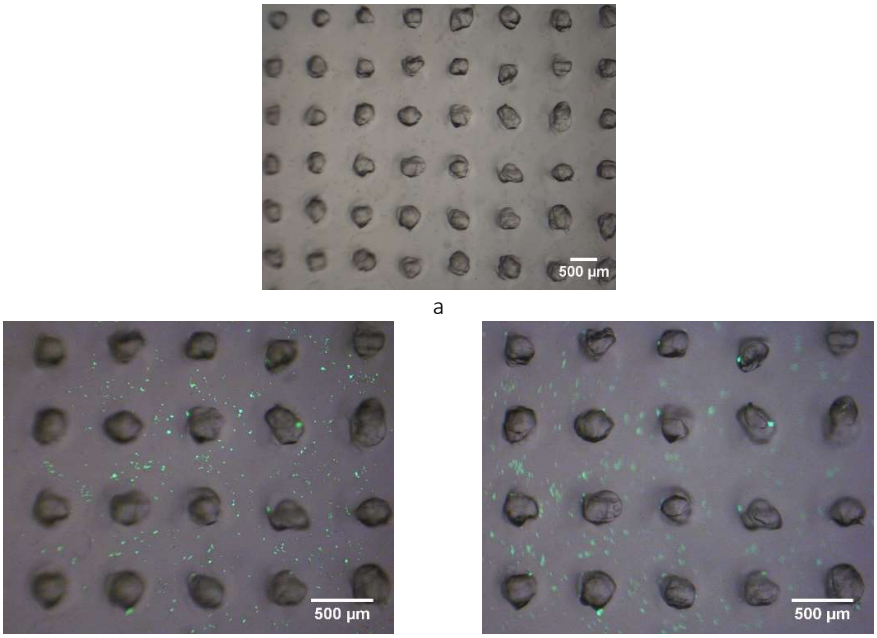


Figure 3.16: Metabolic activity of hCECs seeded and cultured on gels at different GelMA concentrations. G5 was too soft to be handled for testing. Data presented as mean of five samples ± SD, two-way ANOVA with post-hoc Tukey's test (*p ≤0.05).

Cells were seeded on the printed structures to evaluate if the 3D architecture or the stiffness gradient could affect cell viability. A preliminary test was conducted on a printed scaffold G15/G40, and cells labeled with 2 µM calcein AM after seeding. The results indicated that, after seeding, cells adhered first on the base of the scaffold (figure 3.17). The test has been replicated on a 3D model G15/G25 and G15/G40 as base/pillars, respectively. The cell distribution has been evaluated by SEM images. Figure 3.18 shows that cells covered the base and the top of the gel, indirectly indicating their proliferation for both models.



a

b c

Figure 3.17: Inverted microscope images of calcein AM-labelled hCECs seeded on pillars structure G15/G40 after seeding. (a) Pillar array, (b) focus of the base and (c) focus on the top of the pillars.

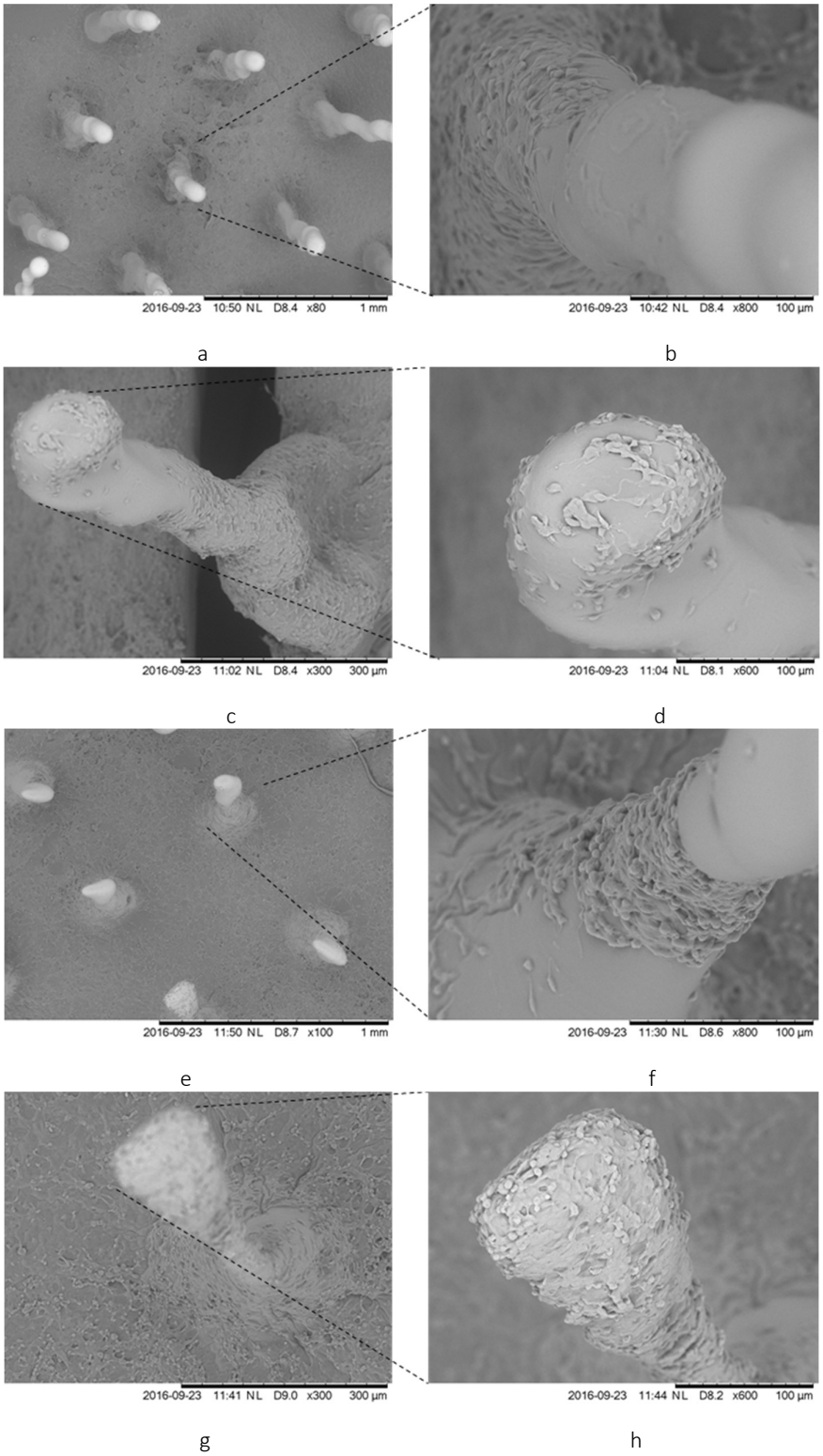


Figure 3.18: SEM images of hCECs seeded on 3D printed scaffolds. hCEC seeded on (a-d) G25 and (e-h) G40; (a,e) pillar arrays, (c,g) single pillar and (b,d,f,h) single pillar at higher magnification.

3.4 Discussion and conclusion

The experimental work described in this chapter presents an evaluation of GelMA hydrogel as a potential limbal stem cell carrier. The work primarily focused on the investigation of *ex-vivo* human cornea mechanical properties. Then, different concentrations of GelMA resulting in hydrogels of differing stiffnesses were investigated and compared to the human cornea in order to obtain a match between the implant and the native tissue. The selected gels were taken forward to test the influence of stiffness on limbal stem cell differentiation (chapter 6). A 3D printing technique was also assessed to recreate a stiffness gradient.

The mechanical properties of *ex-vivo* cornea were investigated by rheology, texture analysis, and by evaluating the tissue water content. The oscillatory experiments performed by rheology are an effective method to investigate the behaviour of viscoelastic materials (Barnes *et al.*, 1989). In addition, due to the viscoelastic behaviour of the cornea, its mechanical properties cannot be fully described by a single elastic parameter such as the Young's modulus (Ionescu *et al.*, 2011). Few studies have analysed the mechanical behaviour of the human cornea under shear stress, with inconsistent results mainly due to different testing conditions. The storage and loss moduli were plotted at 1 Hz, within the order of the natural oscillations of the human cornea (Ionescu *et al.*, 2011). For human cornea, the storage and loss moduli have been calculated as 1500 Pa and 125 Pa (Grobe and Reichl, 2011) and for porcine cornea 60 Pa and 10 Pa, respectively (Ionescu *et al.*, 2011). The results presented in this chapter (G' =

8.0-20.7 kPa and G'' = 0.8-3.3 kPa) are within the range identified by Petsche et al. (2012), where a storage modulus of 9.48 ± 2.92 kPa was determined. The higher values of G' and G'' found in this work could be due to the post-mortem extraction time and the sample preparation method. The increased post-mortem extraction time has been shown to cause an increase in cornea stiffness (Petsche *et al.*, 2012). In this work, the test was conducted on the full-thickness cornea, without selecting any specific tissue layer. The measurement of the elastic modulus was conducted by compression testing. The results obtained (39.1 kPa) are in the same order of magnitude of those reported in the literature for murine and porcine samples (25.0 kPa), but were slightly higher (Worthington *et al.*, 2014). The use of a different species, and different compressive parameters, may have influenced the results.

Gelatin was synthesised and NMR analysis was performed to verify the addition of methacrylate groups to the amine-containing side groups of the gelatin molecule, in combination with the TNBS assay to quantify the degree of methacrylation. The degree of methacrylation affects the resulting mechanical properties of the hydrogels (Nichol *et al.*, 2010), and can be controlled during the methacrylation process by several parameters, such as gelatin concentration, reaction temperature, and molar ratio (Shirahama *et al.*, 2016). The results showed that the methacrylation process occurred, and that the percentage of methacrylation calculated by NMR (80.3%, adding 8% (w/v) of methacrylic anhydride) was confirmed by the TNBS assay (83.5% ± 4.9). Indeed,

the value obtained were in between the results reported by Shin et al. (75%) and Coimbra et al. (90%) (Shin *et al.*, 2012; Coimbra *et al.*, 2014).

The preliminary tests on GelMA hydrogels were conducted with a texture analyser, providing a bulk elastic modulus values ranging from 11.13 kPa (G5) to 1099.67 kPa (G40). Increasing the percentage of GelMA, the Young's modulus increased and was in the same order of magnitude of values reported in literature (Nichol *et al.*, 2010). Small variations can be attributed to the parameters adopted to produce the gel and to perform the test. The type of gelatin, degree of methacrylation, percentage of GelMA, UV exposure time, and crosslinking temperature are all factors that contribute to the determination of the compression modulus (Nichol *et al.*, 2010; Schuurman *et al.*, 2013; Bertassoni, Cardoso, *et al.*, 2014). In addition, the results showed that increasing the concentration of GelMA, the swelling ratio decreased. This behaviour is influenced by the pore size and the interaction between the polymer and the solvent, and can be explained by describing the gel architecture. Higher concentrations of GelMA presented a tight pore size due to the increased crosslinking between gelatin fibrils. Analysis of the gels' morphology by SEM confirmed that the pore size decreased by increasing the percentage of GelMA in agreement to what has been reported (Rizwan *et al.*, 2017). In addition, the swelling ratios between G5 and G15 were comparable to the ratio obtained for the human cornea sample tested here.

The oscillatory frequency test allows the identification of the structuring mechanisms of the gels. All the materials presented higher storage modulus

than loss modulus. The G′ value exhibited a pronounced plateau in the investigated frequency range, indicating that the samples have a predominantly elastic rather than viscous character, as previously reported (Van Den Bulcke *et al.*, 2000). The behaviour of G5 confirms the weakness of the gels; increasing the frequency, the storage modulus increased mainly due to the increase in the interaction of polymer chain entanglements.

The curve of the storage modulus was reported because it has been investigated that even if the viscoelastic matrix has a fundamental role in the remodelling of the substrate, the cells initially exert strain on the matrix, determined by the elastic modulus of the matrix (Chaudhuri *et al.*, 2015).

Overall, the viscoelastic properties, bulk stiffness, and swelling results indicated that the hydrogels prepared with GelMA concentrations between 5% (w/v) and 15% (w/v) identified a range of mechanical properties in which *ex-vivo* human cornea values were included.

The atomic force microscope (AFM) has been used extensively since it emerged as a powerful tool to study the mechanics of cellular microenvironments (Buxboim *et al.*, 2010). The results obtained confirm that increasing the percentage of GelMA, the stiffness increases. Nevertheless, no differences were observed between G5 and G8. This may be due to the fact that polymer chain entanglements start playing a significant role in gel formation only above concentrations of 10% (w/v). Below this value, the chain entanglements may not be involved in the formation of the gels. As a result, the elastic modulus of G5 and G8 are comparable.

There is no published research investigating the surface stiffness of GelMA by AFM within the 5% - 40% (w/v) concentrations. The magnitude and range of Young's moduli appeared to change significantly when comparing these results to the values obtained with the compression test. This behaviour has been observed by Mckee et al. (2011), which compared the elastic modulus of soft tissues obtained by AFM and the texture analyser in tensile mode. Although both tests can provide valuable information, AFM was considered more relevant to the present work, due to the fact that cells were seeded on the surface of the substrate and hence was considered more reliable to describe the microenvironment experienced by the cells (Buxboim *et al.*, 2010). The results obtained from the AFM test were compared to the ones reported in the literature for the cornea, even if several factors can affect these values. Some of them are inherent to the system (indenter geometry, indentation depth), others related to the samples itself (state of the tissue hydration condition, the species). The range indicated by McKee et al. (2011), reviewing the results from several studies, were between 7.5 kPa and 50 kPa. In addition Last at al. (2012) were able to calculate the stiffness of the cornea layer by layer, indicating that 7.5 kPa was the elastic modulus of the epithelium and the anterior basement membrane, 110 kPa that of the Bowman's layer, 33 kPa the value for the stroma, and 50 kPa the modulus for the Descemet's membrane and the endothelium (Last *et al.*, 2012). These values reported in the literature suggest that the range can be identified between 7.5 kPa and 110 kPa. Overall, this range well fits in the results of the present work obtained for G5 and G15 (4.5 kPa – 91.0 kPa).

As it represents an essential parameter for 3D printing, the viscosity of the GelMA solution was evaluated by rheometer. All solutions presented distinctly different viscosities ranged between 1 to 100,000 cP at a shear rate of 100 s^{-1}. PicoDot LV is a jetting valve used for high viscosities fluids, and the manufacturer recommendation is to use an ink at a viscosity range of 8 - 200,000 cP. G25 and G40 fit in this range and were the candidates selected for 3D printing.

The pillar model was chosen to replicate the centripetal differences in stiffness from limbus to central cornea previously reported (Hjortdal *et al.*, 1996; Foster *et al.*, 2014) and to reproduce a mechanism of cell migration guided by durotaxis. According to the rheology results, G15 was chosen as base and G25 and G40 for the pillars. However, according to the mechanical properties of the printed flat scaffolds, only printed-G40 presented a storage modulus higher than G15. For this reason G15/G40 could be chosen for further analysis. This 3D scaffold well represents the concentrical stiffness gradient between the limbus and the cornea, and the centripetal movement that cells performed during migration under both wounded and normal conditions (Nagasaki and Zhao, 2003). Furthermore, the PicoDot printer was chosen because it is a one-step high speed technique, and allows printing of GelMA without any further modifications to the ink. The pillars that were obtained have a shape that depends on the viscosity of the ink and the rapidity to solidify after printing. One limitation is that the model doesn't replicate the limbus-cornea size and geometry.

Irgarcure 2959 was selected as the radical initiator for GelMA polymerization. As an alternative, the use of riboflavin as a novel photoinitiator (PI) in combination to GelMA was investigated, and the results are reported in Chapter 4. The addition of the photoinitiator Irgacure is a well know strategy to generate a photopolymerizable hydrogel. It is a commonly used PI for cell encapsulation since it has been shown to exhibit low cytotoxicity compared to other photoinitiators (Williams *et al.*, 2005). In addition, in this work, cells were seeded on top of the scaffolds, so the risk of cytotoxicity was reduced, as the samples were washed after crosslinking which meant that the cells were not exposed to high PI concentrations nor to prolonged exposure to UV light. The metabolic activity and, indirectly the cell viability, have been tested by seeding hCECs on the gels. HCECs were chosen as a model for the application in cornea regeneration. The data presented here showed that hCECs were able to proliferate on the flat GelMA and on the 3D architecture. One of the advantages of using naturally derived hydrogels is the presence of biologically active sequences that bind key integrins, enabling cells to adhere and migrate onto the 3D structure (Gauvin *et al.*, 2012).

In conclusion, the work in this chapter demonstrated that GelMA can be tuned to match the mechanical properties of the *ex-vivo* cornea. Additionally, GelMA solutions can be used to rapidly print biomimetic 3D architectures using a drop-on-demand jetting method. Furthermore, the hydrogels were able to support hCECs proliferation, and the addition of the printed topography did not have any negative effects on cell growth and behaviour. The 3D printed scaffolds were a

suitable model to investigate the effect of the centripetal stiffness gradient. Nevertheless, it did not reproduce accurately the geometry of the limbal niches. For this reason, in the next chapters, the use of a two photon polymerization system to print the native niche-mimicking scaffolds will be investigated.

4. Investigation of Riboflavin as a photoinitiator for GelMA destined for corneal applications

4.1 Introduction

One of the most common photoinitiators used in tissue engineering is Irgacure 2959, since it exhibits a good toxicological profile and presents moderate water solubility (Bryant *et al.*, 2000). It has caused minimal toxicity over a broad range of mammalian cell types tested, although different cell types exhibited a variable response. In accordance with previous research, and as shown in chapter 3, gel properties can be tuned by varying the percentage of GelMA and the UV curing time (Nichol *et al.*, 2010; Bertassoni, Cardoso, *et al.*, 2014). Irgacure has been used extensively with GelMA and can be used in combination with 3D printing techniques (Schuurman *et al.*, 2013) and with 2PP techniques equipped with a 500 nm laser (Ovsianikov *et al.*, 2011). However, Irgacure cannot be used at 780 nm, the laser wavelength used by the 2PP systems adopted in this work.

The main drawback of using lithography in combination with hydrogels is the necessity to develop biocompatible and water soluble photoinitiators. Other important aspects to be considered in the selection of the photoinitiators are the absorption spectrum, the cross section, and the high initiating efficiency to form radicals. These aspects are all related to the probability to obtain a two-

photon absorption event. However, the majority of the commercial photoinitiators present low cross section and are not water soluble (Schafer et al., 2004). For these reasons, in the last few years, the interest in the development of new photoinitiators that can be used in regenerative medicine in combination with the 2PP system has increased. One of the possible alternatives to Irgacure is represented by dye-amine combinations. They absorb above 400 nm and can be polymerized by 2PP. However, since they have a low cross section, high laser intensities (≈100 mW) and long exposure times (300 – 400 μs) are required (Torgersen *et al.*, 2013). Riboflavin (vitamin B2) is generated by plants and many organisms and is used as a pigment in many food products. The structure of riboflavin and its absorbance spectrum are suitable for the 780 nm laser (Kim and Chu, 2009). As shown for the first time in 2013, riboflavin is a promising photoinitiator for 2PP systems when used in combination with triethanolamine and 50% Polyethylene (glycol) Diacrylate. Although the riboflavin–amine mixture exhibited low photosensitivity and low efficiency in comparison with commercially available photoinitiators, it was successfully used for scaffold polymerization, presenting a low genotoxicity and a high viability (Nguyen *et al.*, 2013).

In addition, riboflavin has already been used clinically in the treatment of eye-related pathologies such as keratoconus, a pathology associated with the weakening of the cornea (Wollensak *et al.*, 2003). Riboflavin can increase the strength of the cornea and the thickness of the collagen fibres (Hatami-Marbini and Rahimi, 2015; Labate *et al.*, 2015). Even if its mechanism is still not fully

understood and more studies are necessary, it can be considered a promising photoinitiator for the treatment of diseases characterized by thinning of the cornea (Raiskup and Spoerl, 2013).

4.1.1 Chapter objectives

The hypothesis of this chapter was that riboflavin can be used in combination with GelMA, crosslinked by UV and 2PP to produce a material with excellent biocompatibility properties. In this chapter, a suitable formulation of a riboflavin-based gel was investigated first by UV irradiation, and later by using IR light. In detail, the research presented in this chapter aimed to:

- UV crosslink different concentrations of riboflavin and triethanolamine solutions and determine the stability of the products by the tube inversion test and rheology;
- evaluate gel porosity and swelling ratio of the riboflavin-gel compared to Irgacure;
- evaluate the ability of hCEC to adhere on the selected riboflavin cross-linked gel;
- study the possibility of crosslinking GelMA and riboflavin by IR-laser.

4.2 Experimental sections

For more detailed information regarding GelMA synthesis, hydrogel preparations, mechanical tests, cell culture protocols, PrestoBlue® assay, and 2PP set-up, see Chapter 2: Materials and Methods. A table summarizing gel formulations and naming conventions can be found in appendix A.

4.2.1 GelMA hydrogel preparation by Riboflavin solution

In the present chapter two photoinitiators were used: 2-Hydroxy-4′-(2-hydroxyethoxy)-2-methylpropiophenone (Irgacure 2959), and a solution composed of riboflavin 5′-phosphate sodium salt hydrate (Riboflavin, R7774 Sigma-Aldrich, UK) (photoinitiator) and triethanolamine (TEOHA, 90279 Sigma-Aldrich, UK), (co-initiator). The riboflavin was tested in the range 10-400 µM and triethanolamine in the range 10-200 mM. In all concentrations, the percentage of GelMA was kept constant (20% (w/v)). The riboflavin-gel, named R-gel, and this formulation will be referred to as R20-gel; table 4.1 summarizes gel formulations and naming conventions. The workflow used for R20 optimization is shown in figure 4.1. At first, the study of the use of GelMA in combination of riboflavin crosslinked by UV light was performed and later by IR-light.

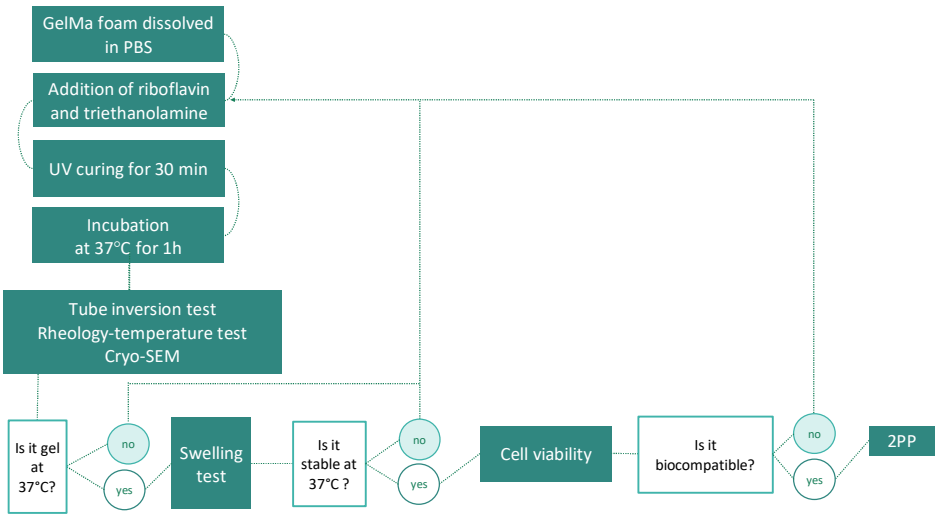


Figure 4.1: Workflow describing the approach for R20 optimization. The gels were prepared adding riboflavin and triethanolamine at different concentrations in a GelMA solution and they were UV cross-linked for 30 min. After that, the inversion test tube, the rheological temperature test and cryo-SEM were performed. If a stable gel at 37°C was obtained, the swelling ratio and cell viability tests were performed. Then, the selected gel was crosslinked by 2PP.

4.2.2 Irgacure preparation

The R20 gels were compared to Irgacure gels, named IR-gels (G10, G15, and G20, table 4.1). For more detailed information, see section 2.1.1 (GelMa synthesis) and 2.1.2 (GelMA preparation).

Table 4.1: Gels nomenclature. Gels prepared with Irgacure or riboflavin as a photoinitiator were named IR-gels and R-gels, respectively. For each set of gels, the GelMA concentration is reported.

Photoinitiator	Irgacure			Riboflavin
Nomenclature	IR-gel			R-gel
	G10	G15	G20	R20
GelMA concentration (% w/v)	10	15	20	20

4.2.3 Gel characterization

4.2.3.1 Tube inversion test

The ability of riboflavin and triethanolamine to create chemically cross-linked gels was initially verified by the tube inversion test. The gels were prepared at RT, cross-linked with a UV lamp (365 nm long wave, 15W) for 30 min, and the test-tube was turned upside-down. If the gel maintained its position in the tube, it was taken forward for rheology testing, otherwise, it was discarded.

4.2.3.2 Rheology

For more detailed information regarding rheological characterisation of the gels see Chapter 2: Materials and Methods, section 2.2.1 (Rheology). Briefly a parallel plate rheometer with a plate diameter of 8 mm was used. The gap between the plates was between 500 µm and 800 µm. The Viscoelastic Linear Region (VLR) was quantified before the frequency and temperature test. A stress of increasing

amplitude (0.1 - 10%) and constant frequency of 1 Hz (T=25°C) was applied to the samples. The oscillatory frequency test was performed at 25°C and with a stress amplitude of 5% (within the VLR) and a frequency between 0.1 Hz and 10 Hz. The temperature test was performed in the temperature ranges between 25°C to 45°C and 25°C to 100°C (1 Hz). Storage and loss moduli (G' and G'') were quantified in both tests. The test was performed on three samples.

4.2.3.3 SEM

Cryo-SEM was used to calculate the porous structure of the gel and the pore dimensions. Ten pore sizes was average for each condition. For more detailed information see Chapter 2: Materials and Methods, section 2.5.3 (CryoSEM).

4.2.3.4 Swelling ratio

The swelling ratio was calculated according to equation 2.6 and following the protocol presented in the section 2.2.4 (Swelling analysis). The swelling ratio (after 24 h) was performed on IR-gels prepared at 10%, 15% and 20% of GelMA (named G10, G15 and G20) crosslinked for 3 min and 10 min, and on Riboflavin gels (R-gels) prepared at 25% w/v, 30% w/v, 40% w/v, and 50% w/v (named R25, R30, R40 and R50). The test was performed on three replicates.

4.2.4 Cell viability

4.2.4.1 Cells cultured in riboflavin and triethanolamine solutions

The cytotoxicity of the riboflavin-triethanolamine solution was tested by using immortalized NIH 3T3 mouse embryonic fibroblast cells (3T3 cells, passage 30-

42). They were grown in Dulbecco's Modified Eagle Medium (Sigma-Aldrich, UK, 42430-025) supplemented with 10% (v/v) of Foetal Bovine Serum (Sigma-Aldrich, UK, F9665), 2 mM L-glutamine (Sigma-Aldrich, UK, G7513) and 100 units/mL of penicillin, 0.1 mg/mL of streptomycin and 0.25 µg/mL of amphotericin B (Sigma-Aldrich, UK, A5955) at 37°C, 5% CO_2 in air.

The cells were seeded onto a 96 well plate at concentrations of 8,000 cells/mL (0.1 mL). After 24 h, the cell culture media was removed and replaced by different solutions of riboflavin, triethanolamine and their combinations at different concentrations, as reported in table 4.2. After 24 h, the solutions were removed and the PrestoBlue® assay was performed (section 2.4.1, PrestoBlue® assay). The test was performed on three replicates.

Table 4.2: Riboflavin and triethanolamine solutions. Riboflavin, TEOHA, and riboflavin/TEOHA at different concentrations were diluted in cell culture media (solutions 1-7).

	Solution 1	Solution 2	Solution 3	Solution 4	Solution 5	Solution 6	Solution 7
Riboflavin	0.01 µM	0.1 µM	1 µM	10 µM	35 µM	70 µM	140 µM

	Solution 1	Solution 2	Solution 3	Solution 4	Solution 5	Solution 6	Solution 7
TEOHA	0.01 mM	0.1 mM	1 mM	10 mM	35 mM	70 mM	140 mM

	Solution 1	Solution 2	Solution 3	Solution 4	Solution 5	Solution 6	Solution 7
Riboflavin/ TEOHA	0.01 µM / 0.01 mM	0.1 µM / 0.1 mM	1 µM / 1 mM	10 µM / 10 mM	35 µM / 35 mM	70 µM / 70 mM	140 µM / 140 mM

4.2.4.2 Cell seeding on the gels

The biocompatibility of the gels was tested by seeding hCECs on the scaffolds. Each sample was prepared as reported in 4.2.2 (Irgacure preparation) and 200 µl of gel was cast in the 48 well plate. The gels were soaked in 1 ml PBS at 37°C

for 24 h, and then in 300 µl of cell culture media before cell seeding. After 2 h, the media was removed and 200 µl of fresh media was added. Cell suspension (100 µL; 600,000 cells/mL for hCEC) was seeded on top of each gel for 24 h and cells allowed to adhere for 2 h at 37°C, 5% CO_2 in air, followed by the addition of 300 µl of cell media to each well. The PrestoBlue assay was used to monitor the metabolic activity of the cells after 24 h of culture. The test was performed on three replicates.

4.2.5 R20 crosslinking by 2PP

For more detailed information about the 2PP set-up see Chapter 2: Materials and Methods, section 2.6.2 (CAD design and printing parameters). A reference structure was produced using the photopolymer IP-L 708, which is a commercially available gel from Nanoscribe GmbH. The structures were developed by immersing the sample in Propylene glycol monomethyl ether acetate for 30 min to remove the non-polymerized resin. The geometry of the samples was analysed by SEM (section 2.5.2, SEM). The optimized formulation of R20-gels was tested by the 2PP system, and developed by adding PBS at 37°C for 1 h.

4.3 Results

4.3.1 Riboflavin-GelMA can be crosslinked by UV light

4.3.1.1 Tube inversion test to determine gelation

Among the gels prepared with riboflavin and triethanolamine, those showing a solid-like behaviour were analysed by temperature oscillation rheology. The gels containing riboflavin at concentrations of 200 µM and 400 µM and triethanolamine concentrations at 10 mM and 200 mM, respectively presented a gel-like behaviour after crosslinking and were selected for further studies (table 4.3).

Table 4.3: Gels selected for further analysis. Riboflavin and triethanolamine were diluted in PBS and mixed with GelMA solution at 20% (w/v).

Nomenclature	R20 200-10	R20 400-10	R20 200-200
GelMA concentration (% w/v)	20	20	20
Riboflavin concentration (µM)	200	400	200
Triethanolamine concentration (mM)	10	10	200

4.3.1.2 Rheological characterization

The rheological properties of the R-gels (R20 200-10, R20 400-10, and R20 200-200) are shown in figure 4.2. They presented a solid-like behaviour as the storage modulus was always higher than the loss modulus. However when the temperature rose above the gelatin melting point (25-30°C), the moduli decreased for R20 200-10. Furthermore, low moduli values at temperatures above 30°C, for R20 200-10 and R20 400-10, indicated that few chemical cross-links were formed. At constant triethanolamine concentrations (10 mM), the

increase in the riboflavin concentration influenced only marginally the gel's behaviour. In contrast, a significant increase in the rheological properties was obtained by increasing the triethanolamine concentration (R20 200-200). Increasing the temperature, the storage and loss moduli of this gel were stable at 37°C. There was a slight decrease of G' while heating the gels, which corresponded to the melting of the physical cross-links between the gelatin chains. This effect was less evident than in R20 200-10. The values of the storage and loss moduli of R20 200-200 at 1 Hz were 4380 Pa and 205 Pa, respectively. The cross-over point was detected at 71°C for R20 200-200 (figure 4.3). Increasing the frequency up to 10 Hz the storage modulus was constant, however the loss modulus increased at higher frequencies indicating that the system becomes more liquid-like due to the melting of the physical network. On the contrary, for the IR-gel, the G' and G'' values exhibited a pronounced plateau in the frequency range investigated, indicating that the network is well-developed (figure 4.4).

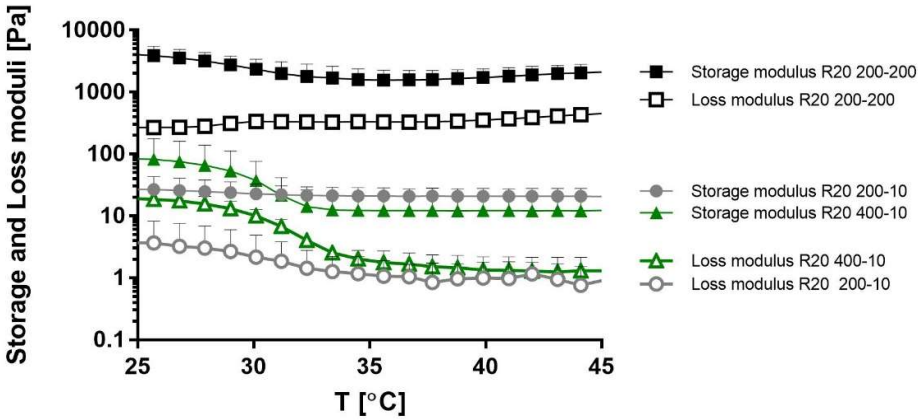


Figure 4.2: Storage (closed symbols) and loss modulus (open symbols) as a function of temperature (25°C-45°C) of R20 gels. R20 200-10 (grey line) and R20 400-10 (green line) were not stable at 37°C, however R20 200-200 (black line) showed a gel-like behaviour between the temperature range investigated. Data presented as mean of three samples ± SD.

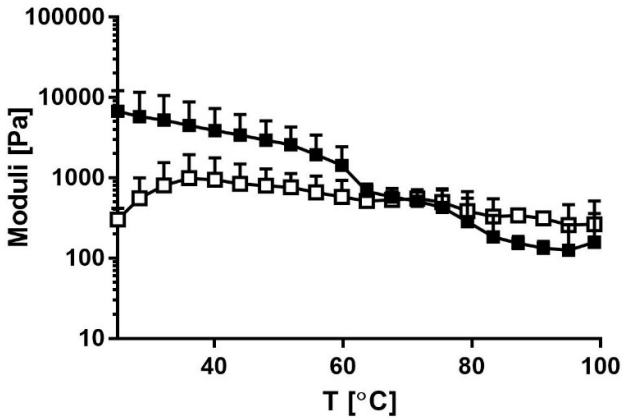


Figure 4.3: Storage (closed symbol) and loss modulus (open symbol) of R-gel 200-200 as a function of temperature between 25°C and 100°C. The crossover point was at 71°C. Data presented as mean of three samples ± SD.

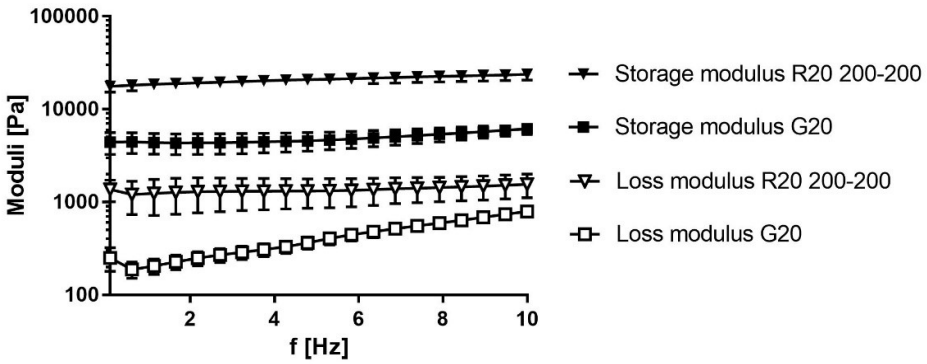


Figure 4.4: Storage (closed symbols) and loss modulus (open symbols) of R20-gel 200-200 (square symbol) and G20 crosslinked for 10 min (triangle symbol) as a function of frequency measured between 0.1 and 10 Hz. Data presented as mean of three samples ± SD.

4.3.1.3 Pore dimensions

Cryo-SEM images of the swollen hydrogels are shown in figure 4.5a-d. Average pore size was quantified for each gel and the results are summarized in figure 4.5e. Keeping constant the percentage of GelMA (at 20% w/v), the pore dimension increased by using riboflavin-triethanolamine as a photoinitiator, compared to Irgacure. Pore dimensions were not uniform across the section of the R20 200-200. Near the surface, the average pore size was 4.40 ± 1.33 µm, whilst inside the hydrogel the average pore size was 15.69 ± 6.6 µm. The increase in UV exposure time reduced the pore size but the effect was not statistically significant.

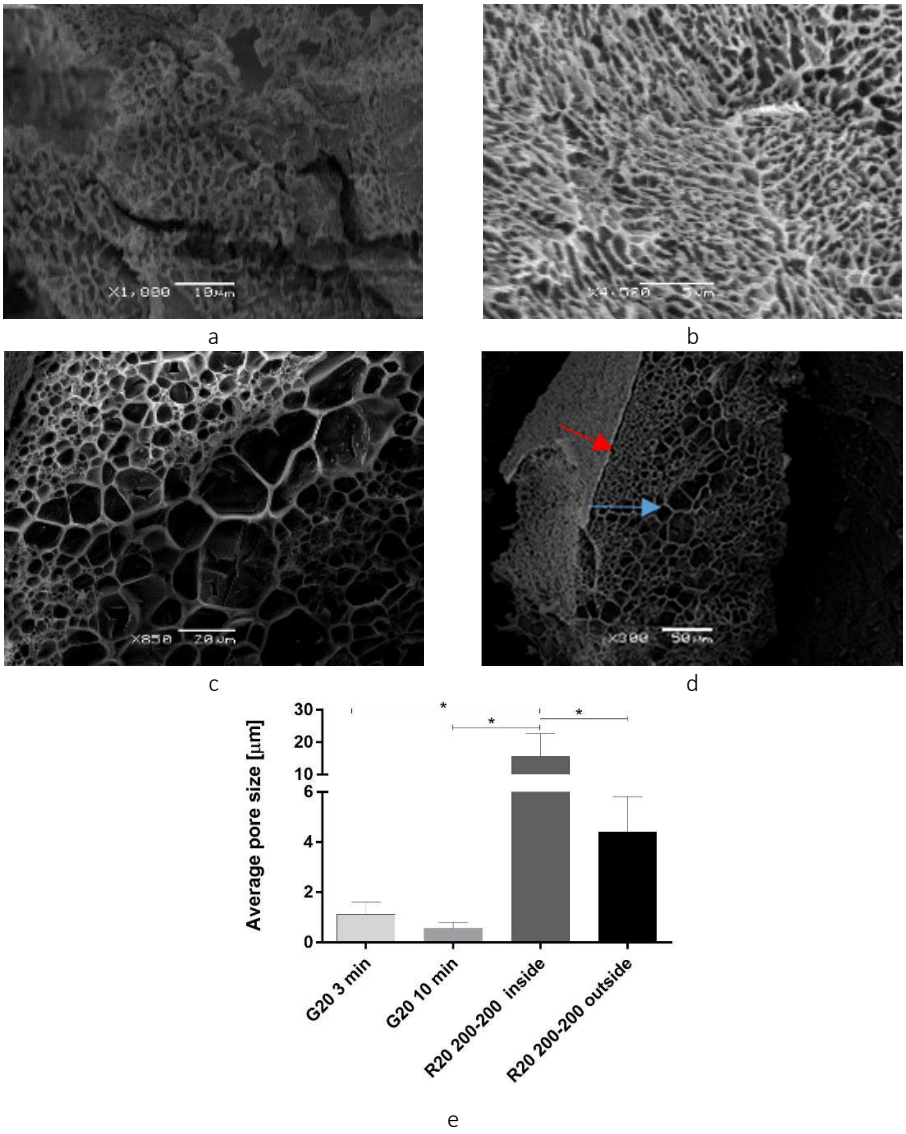


Figure 4.5: Cryo SEM pictures and average pore dimensions of R-gels and IR-gels. (a) G20 crosslinked for 3 min; (b) G20 crosslinked for 10 min; (c,d) R20 200-200. (d) The pore under the surface (red arrow) and inside of the gel (blue arrow) are pointed out. (e) Data presented as mean ± SD. A total number of 10 pore measurements were taken from each gel. One-way Anova with post-hoc Tukey's test (*p ≤0.05). Gels prepared with Riboflavin showed an average pore size dimension statistically significantly higher with respect to G20-gels.

4.3.1.4 Swelling analysis

The swelling analysis was performed by increasing the GelMA concentration for IR-gels and R-gels and the UV curing time for IR-gels (figure 4.6). Increasing the percentage of GelMA, the swelling ratio decreased significantly, while the UV

curing time did not affect the swelling ratio. For riboflavin gels, prepared with 200 µM of riboflavin and 200 mM of triethanolamine, increasing the percentage of GelMA (25% w/v 30% w/v 40% w/v 50% w/v, named R25, R30, R40 and R50) caused a significant decrease in the swelling ratio (p* ≤0.05 for each Riboflavin-gel except for 30% to 40% steps). Keeping the concentration of GelMA constant (20% (w/v)), the samples prepared with riboflavin presented a higher mass swelling ratio than the gels prepared with Irgacure. The R20-gel 200-10 and R20-gel 400-10 were too weak to be handled and were not studied. They were discarded for cell characterization and the R20 200-200 was selected for further studies.

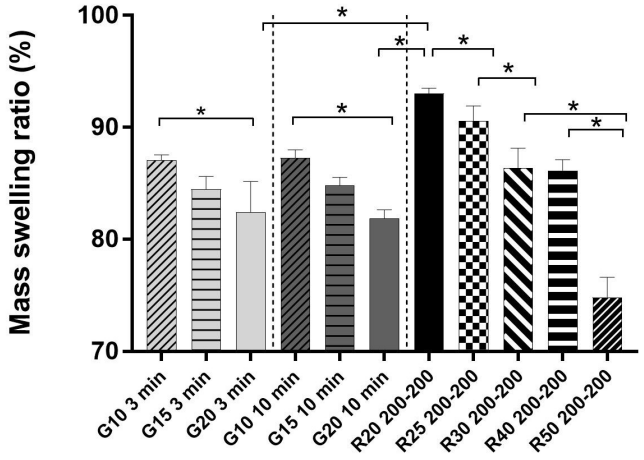


Figure 4.6: Mass swelling ratio of IR-gels and R20-gels. Swelling ratio of gels prepared with different concentrations of GelMA, different UV curing time, and different PIs were tested. Data presented as mean of three samples ± SD. One-way ANOVA with post-hoc Tukey's test, *p ≤0.05.

4.3.2 Riboflavin solutions are compatible in the range 0.01-140 µM, triethanolamine below 35 mM.

The addition of riboflavin to cell culture media did not have a significant impact on the 3T3s viability at any of the concentrations tested with cell viability

measured at higher than 70% (figure 4.7a). However, for the triethanolamine solution, cell viability showed a dose-dependent response (figure 4.7b). Increasing the concentrations of triethanolamine above 10 mM resulted in a significant reduction in cell viability, with values lower than 25% compared to the control. The combined effect of triethanolamine and riboflavin showed the same trend as the triethanolamine response (figure 4.7c).

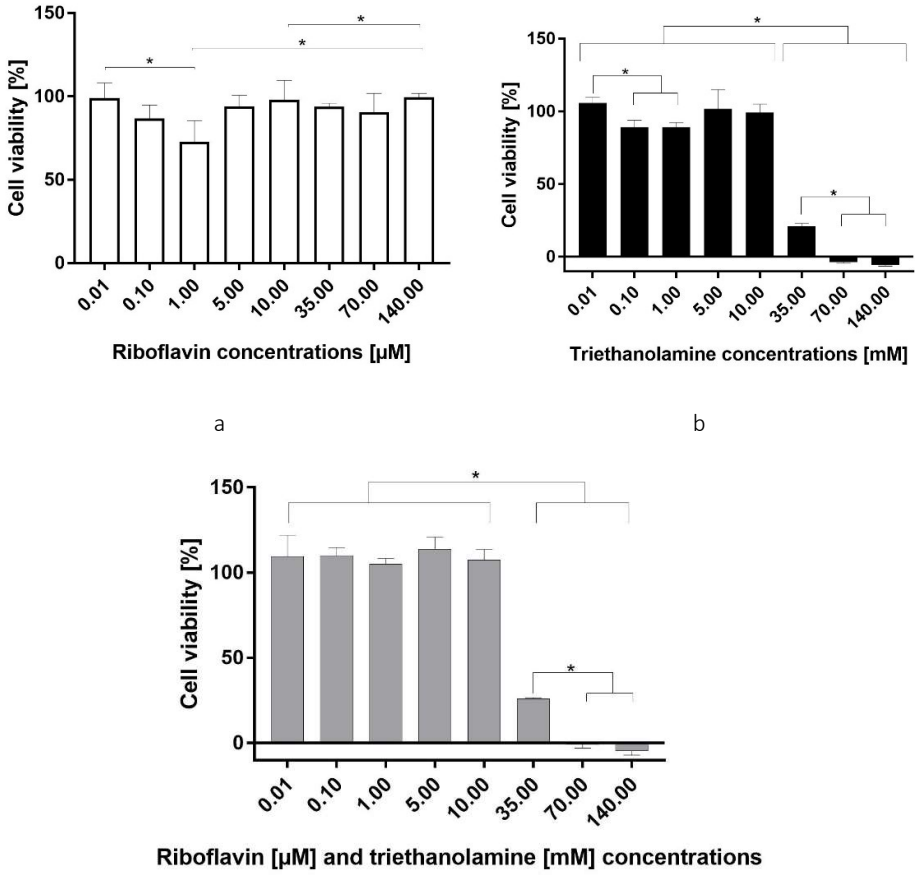


Figure 4.7: 3T3 viability vs increasing concentration of (a) riboflavin, (b) triethanolamine and (c) a solution composed of both riboflavin and triethanolamine. Data presented as mean of three samples ± SD. One-way Anova with post-hoc Tukey's test (*p ≤0.05).

The biocompatibility and the ability of the cells to adhere to gels containing selected PI concentrations were tested by seeding the cells directly on the gels. The results of the viability assay, after seeding hCEC on the top of the IR-gels and R20 200-200 for 24 h, are shown in figure 4.8. The fluorescence intensity was comparable among all the gels investigated and the control with no statistical significant difference observed between samples.

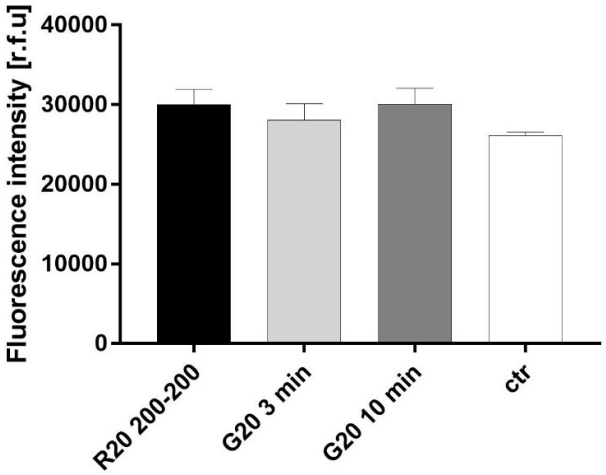


Figure 4.8 : Metabolic activity of hCECs seeded on IR-gels, R200-200 and the control (well plate). GelMA concentration was kept at 20% w/v, changing the UV curing times (3 min and 10 min), and PI (Riboflavin and Irgacure). Data presented as mean of three samples ± SD. One-way Anova with post-hoc Tukey's test (*p ≤0.05)

4.3.3 2PP structures: riboflavin is not suitable for 2PP printing: comparison of UV and 2PP crosslinking

As a proof of concept, an IPL-70 scaffold was developed (figure 4.9a-c) by 2PP according to the CAD structures presented in figure 4.9d,e. However, after multiple trials, it was not possible to obtain any GelMA scaffolds prepared with riboflavin-triethanolamine as photoinitiator. The picture 4.9f, captured during

the writing process, is showing evidence of weak polymerization that has been obtained with R20 200-200.

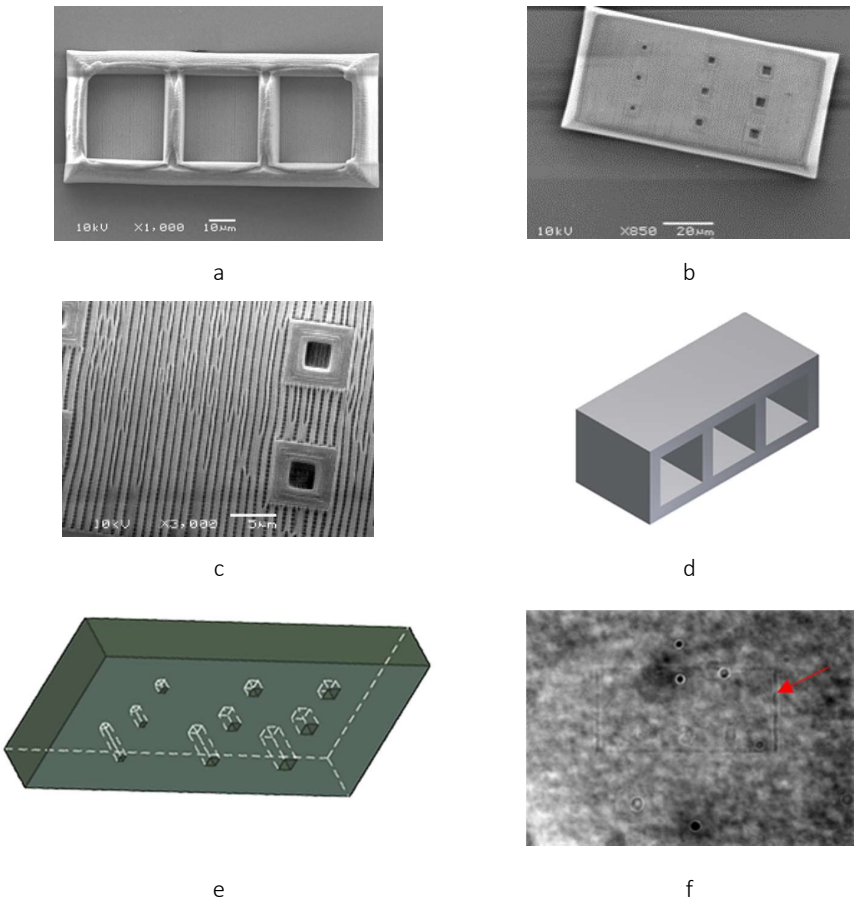


Figure 4.9: CAD file and scaffolds produced by 2PP using riboflavin-triethanolamine as the photoinitiator. (a-c) SEM pictures of IPL-70 scaffolds; (d,e) CAD structures; (f) pictures obtained during the writing process of R20 200-200 (the structure is pointed out with a red arrow).

4.4 Discussion and conclusions

In this chapter, the main hypothesis was that the riboflavin-TEOHA solution could represent a novel PI used to obtain stable GelMA hydrogels, crosslinked by both UV and IR laser to produce a material with excellent biocompatibility properties.

The use of riboflavin to crosslink methacrylate bonds in GelMA hydrogels requires an electron donor since its lifetime is too short to start a polymerization reaction (Orellana *et al.*, 1999; Bertolotti *et al.*, 1999; Sengupta *et al.*, 2015; Kim and Chu, 2009). There are a number of molecules that can be used as coinitiators, the most common being amines. Among them, it has been demonstrated that triethanolamine represents the most efficient in combination with riboflavin (Encinas *et al.*, 2001). In addition, it has been shown that riboflavin and triethanolamine behave as an efficient photoinitiator system to polymerize 2-hydroxyethyl methacrylate (HEMA) in aqueous medium (Orellana *et al.*, 1999).

In this chapter, gels prepared with different riboflavin (10-400 µM) and triethanolamine (10-200 mM) concentrations were investigated to obtain a suitable concentration to use in combination with GelMA and for effective cross-linking with 2PP.

To establish which formulations could reach a solid-like gel, they were exposed at 30 minutes of UV light. This value was chosen based on an investigation of UV curing time from 5 to 60 minutes which showed that an optimal exposure time to increase the modulus of the hydrogels was between 30 and 45 min at 3 mW/cm^2 (Ahearne *et al.*, 2006). In ophthalmic clinical applications, a 30 min irradiation period is considered as a standard time for the application of riboflavin on the cornea. It is used to stabilise the progression of keratoconus, a degenerative, non-inflammatory disorder, characterised by stromal thinning

(O'Brart *et al.*, 2011). As a first step, the time was kept constant, with the possibility to change it in the future to obtain a material with tunable properties.

The inverted tube test was used to exclude the formulations that did not form gels. The suitable ones were subjected to rheology to explore their viscoelastic behaviour as a function of temperature. The gels prepared with a concentration of 10 mM of triethanolamine formed gels at 37°C. Nevertheless, the swelling test proved that they were too weak to be handled after immersion in PBS. The reasons may be due to the low number of chemical cross-links, high temperature and addition of water leading to a disruption of the structure. The degree of gel swelling depends on the pore size and the interaction between the polymer and the solvent. A possible explanation of the mechanism that occurred during gel formation in the different formulations is presented in figure 4.10. When gelatin or non-UV cured GelMA undergo a coil-helix transition upon cooling, a strong physical network is formed. However, it is a reversible process. After UV irradiation, chemical bonds are formed. The competition between chemical and physical cross-links and the number of cross-links depends on variables such the percentage of GelMA and the UV curing time (Van Den Bulcke et al. 2000).

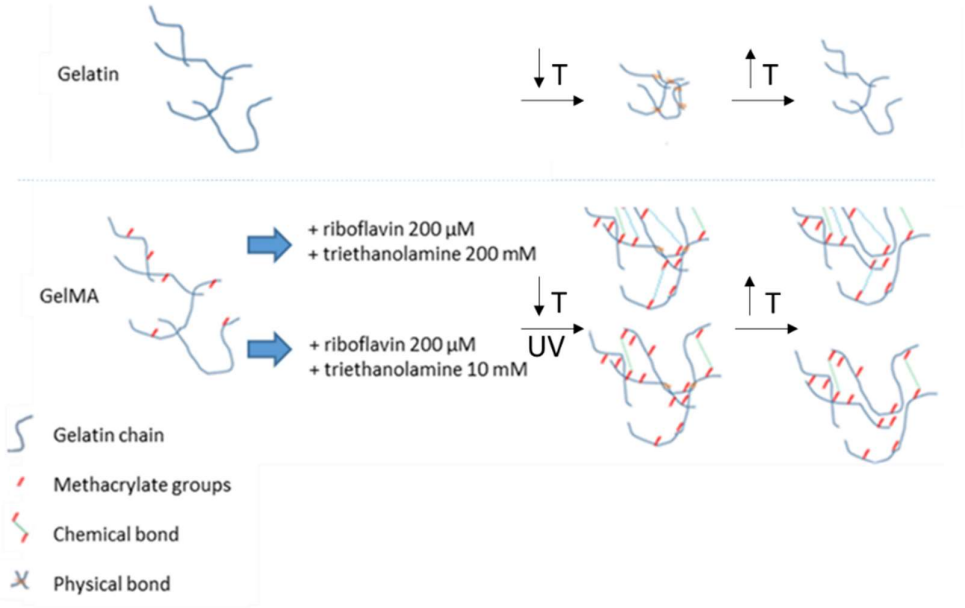


Figure 4.10: Hypothesis of the mechanism involved in the preparation of hydrogels. Physical and chemical gelation of gelatin and GelMA with a low and high concentration of riboflavin and triethanolamine.

After studying different concentrations of riboflavin and triethanolamine, the gel prepared with 200 µM and 200 mM, respectively, was selected for further analysis due to its stable structure at 37°C. The temperature test indicated that the storage modulus was always higher than the loss modulus, without the presence of any crossover point (which would indicate the transition from a solid-like to a liquid-like gel), and it was constant in the temperature range 25°C - 45°C. This suggests that a high number of chemical-cross-links were formed. However, the average G' was 4380 Pa, indicating the formation of a soft gel with low mechanical properties, similarly to the G5 gel presented in Chapter 3.

To test the biocompatibility of the riboflavin solution, 3T3 cells were cultured for 24 h in cell culture media mixed with different concentrations of riboflavin and

triethanolamine. The results indicated that the riboflavin is biocompatible, however triethanolamine was toxic for the cells above a concentration of 35 mM, which was the concentration used in this study. However, in the present work, cells were not embedded in the gel which provided the possibility to pre-wash the samples before cell seeding, and therefore removing toxic compound. This explained why cells cultured on top of the scaffolds presented a metabolic activity comparable to the control and the IR-gels. hCECs were chosen for this second test as it is a more appropriate exemplar cell type to mimic the behaviour of cells used in corneal applications. In Nguyen et al. (2014), gels prepared with PEGDA and the same concentration of riboflavin and triethanolamine proved a lower genotoxicity and cytotoxicity compared to the commercial Irgacure (Nguyen *et al.*, 2014).

Riboflavin has been tested successfully in combination with Polyethylene (glycol) Diacrylate and polymerization achieved with a 2PP system (Nguyen *et al.*, 2013). However, the results obtained in this chapter with GelMA presented limited success in producing the scaffold by UV due to the weakness of the gel and by 2PP not obtaining the desired scaffold shape. The difficulties associated with successful polymerization might be due to the fact that the riboflavin–TEOHA photoinitiator is inefficient at 780 nm, and requires a higher laser power.

Overall the gel R20 200-200 presented good results in terms of stability at 37°C, and biocompatibility, however the high time required to crosslink the

formulation and the weakness of the resultant gels compared to IR-gels makes this formulation not favourable to use with UV light.

The great advantage of using the riboflavin was its potential use as a photoinitiator with the IR lasers at 780 nm. It would represent a novel formulation, not yet explored with the 2PP system. However, due to the limitations encountered, other water-soluble photoinitiators with a large cross section in the near-IR wavelength spectra will be tested with GelMA and the results will be presented in the next chapters for the development of a scaffold with defined geometry.

5. Development of a 3D scaffold that mimics the geometry of limbal epithelial crypts using a two photon polymerization system

5.1 Introduction

During healing processes and physiological turnover, the corneal epithelial cells of the epithelium (the outer surface layer) are constantly replaced by Limbal Epithelial Stem Cells (LESCs) (Dua *et al.*, 2000). LESCs are located in physically protective niches within the limbus and differentiate whilst migrating towards the centre of the cornea (Pellegrini *et al.*, 1999; Schermer *et al.*, 1986). The mechanisms underpinning stem cell phenotype maintenance, cell migration and LESC differentiation are not yet clear. Among the intrinsic and extrinsic factors that no doubt drive this process, the physical properties and the ECM architecture play an important role. Through the modification of the local environment, which consequently manipulates cell–matrix interactions and cell–cell contacts, it is possible to control several functions, including proliferation and differentiation (Nelson *et al.*, 2005).

In 1971, a structure about 1 mm long and radially distributed in the limbus called the 'Palisades of Vogt' was identified as the site of corneal epithelial cell generation (Davanger and Evensen, 1971). Recently, a more detailed shape of the limbal epithelial stem cell niche, named Limbal Epithelial Crypts (LECs) has been recognised and characterized (Dua *et al.*, 2005; Shanmuganathan *et al.*, 2007). LECs stretch perpendicular to the external limbal surface and then turn parallel to the surface or circumferentially along the limbus. These cylindrical tubes gradually narrow from the rete ridge and terminate in the conjunctival stroma with an average limbus depth reaching up to 120 µm (Dua *et al.*, 2005). The limbal crypts correspond to downward projections of the limbal epithelium into the underlying limbal stroma, and can be referred to as rete pegs or rete ridge. This terminology has been used for the first time to describe the interface at the dermal-epidermal junction, defined as irregular ridges and cones ("rete pegs") of epidermis projecting toward the dermis (Odland, 1950).

Recently, a high number of studies aimed to develop alternative cell carriers for cornea replacement by using different tissue engineering strategies have been reported (reviewed in Haagdorens et al. 2016). However, only a few of them have focused on the limbal niche and its geometry. A combination of microlithography and electrospinning (Ilida Ortega *et al.*, 2013) and 3D plastic compressed collagen (Levis *et al.*, 2013) are methods that have been utilised/developed. Both groups highlighted the importance of the creation of niche-like structures to enhance stem-cell maintenance and differentiation. However, none of them developed a scaffold designed specifically for LEC

replacement that models the spatial morphology of the niche as described by Dua et al. (2005).

A promising additive manufacturing technique that could be used to produce stem cell niche-like structures is two-photon polymerization, as it is flexible and allows the generation of complex geometries at a subcellular scale (1–10 µm) while precisely controlling scaffold topography. The potential of 2PP techniques has been recently investigated in biomedical research, and has been used in combination with preosteoblast cells (Markovic *et al.*, 2015), adipose stem cells (Silva *et al.*, 2016), human adipose-derived stem cells, and human bone marrow stem cells (Koroleva *et al.*, 2015), but as yet not for applications in the eye.

The use of advanced microfabrication techniques for biomedical applications has shown great potential in combination with hydrogels (Zorlutuna *et al.*, 2012). However, there are some challenges related to the 2PP system, primarily associated with the selection of the required photoinitiators, as discussed in Chapter 4. High initiation efficiency, water solubility, biocompatibility, and the absorption spectrum that matches the half-wavelength of the applied laser radiation (780 nm) are some of the features that have to be taken into consideration (Li *et al.*, 2013). Recently, Li et al. (2013) studied novel water-soluble two-photon photoinitiators for direct 3D microfabrication of hydrogels (Li *et al.*, 2013), such as P2CK, and Ovsianikov et al. (2011) were the first that used this photoinitiator in combination with GelMA and 2PP for bone tissue engineering applications (Ovsianikov *et al.*, 2011).

Some limitations of using naturally derived materials are their susceptibility to enzymatic degradation, batch-to-batch variation, and relatively poor mechanical properties. The synthetic hydrogels are therefore attractive alternatives, although they can exhibit low bioactivity. Polyethylene Glycol Diacrylate (PEGDA) is one of the most widely used synthetic hydrogels and has been approved by the FDA for several medical applications due to its low toxicity and high biocompatibility (Zhu, 2010). PEGDA has been investigated for use with 2PP, due to its photocrosslinkable properties (Käpylä *et al.*, 2014), but as yet, there are no reports of it being used in combination with GelMA.

5.1.1 Chapter objectives

The design of a suitable scaffold for eye regeneration assumes a great importance in clinical application since the efficacy of current treatments with amniotic membranes is still controversial and not completely clarified. In Chapter 3, GelMA hydrogels presenting different stiffnesses were investigated for their ability to support cornea epithelial proliferation. In addition, the stiffness was compared to human cornea values. The aim of the present chapter was the development of a 3D scaffold mimicking the geometry of the native LECS as described by Dua et al. (2005) by the use of two-photon polymerization. These novel scaffolds could be transplanted “plugs” around the limbal area, technique that has not been explored yet.

The hypothesis beyond this chapter was that the geometry is able to support the maintenance of a stem cell population at the base of the crypt, and influence

epithelial cell proliferation and differentiation. This last aspect was investigated in Chapter 6. In addition, in the present chapter, a photocrosslinkable composite hydrogel made by the combination of poly(ethylene glycol) dimethacrylate (PEGDA MW 575 Da) and GelMA was investigated, due to the fast enzymatic degradation rate of GelMA.

In detail, the objectives of this chapter were:

- to evaluate the printability of GelMA;
- to optimize the printing parameter to obtain a stable hydrogel that can mimic the *in vivo* stem cell niche;
- to explore the use of GelMA and GelMA-PEGDA hydrogels and to evaluate their swelling abilities, and their susceptibility to the enzymatic degradation;
- to evaluate the ability of printed scaffolds to support epithelial cell proliferation.

5.2 Experimental design

For more detailed information regarding GelMA synthesis, mechanical tests, cell culture, PrestoBlue® assay, and 3D printing set-up, see Chapter 2: Materials and Methods. A table summarizing gel formulations and naming conventions can be found in appendix A.

5.2.1 Optimization of 2PP structures and development of 3D niche structures

A Two-Photon Polymerization system (2PP) with a femtosecond laser emitting at 780 nm in galvo scan mode was used to print the structures. A detailed

description of the system can be found in section 2.6.2 (Two photon polymerization system).

5.2.1.1 Material preparation

Firstly, the suitable parameters to obtain a stable scaffold with the quickest production time were investigated. Before printing, the polymeric solution was prepared by mixing GelMA to the photoinitiator P2CK. Different concentrations of GelMA and the photoinitiator P2CK were investigated in order to obtain a suitable formulation for the current application. GelMA 10%, 15% and 20% (w/v), named 2P10, 2P15 and 2P20 were dissolved in PBS to reach the desired concentration. P2CK stock solution (5% w/v) was added to obtain 0.01, 0.05, 0.3 and 0.5 (w/v) final concentration of PI.

5.2.1.2 Printability

The printability was determined qualitatively after the writing process, by monitoring the structure of the scaffolds. If a scaffold or maintained structure was obtained, it was considered 'printable', otherwise the formulation was classified as 'not printable' and was discarded.

5.2.1.3 Deformation

The optimization of printing parameters was performed on GelMA hydrogels varying the hatching distance (distance between printed layers) between 0.4 µm to 1.6 µm. The effect of the geometry was evaluated printing a square cup (height 40 µm) and changing the wall and base thickness (10 µm and 20 µm).

The effect of the speed was investigated in the range 25000-45000 µm/s. The deformation was calculated as the distance (in µm) between the wall edge as defined by the CAD figure and the wall edge as printed by 2PP. The measurement was calculated in ImageJ. This preliminary optimization was done using a 63x objective. Then, the scaffold was printed using a 25x objective, giving the possibility to increase the printable dimensions. The CAD structure that models the *in vivo* native shapes is shown in Figure 5.1a,b with measurements taken from histological sections of the corneal limbus reported in Dua et al. (2005). An important feature is that the scaffold presents a structure that narrows at the end. In order to design a model that could closely mimic the native structure, the CAD design was performed recreating a crypt-like invagination narrowing at the end. The printed dimensions (height=200µm, width and length=300 µm) were limited by the 2PP technique, but were still within the range described by Dua et al. (2005) for the *in vivo* niches. The geometry of the printed scaffold was investigated by inverted and confocal microscope (see section 2.5.1 Confocal microscopy and 2.5.2 Scanning electron microscopy).

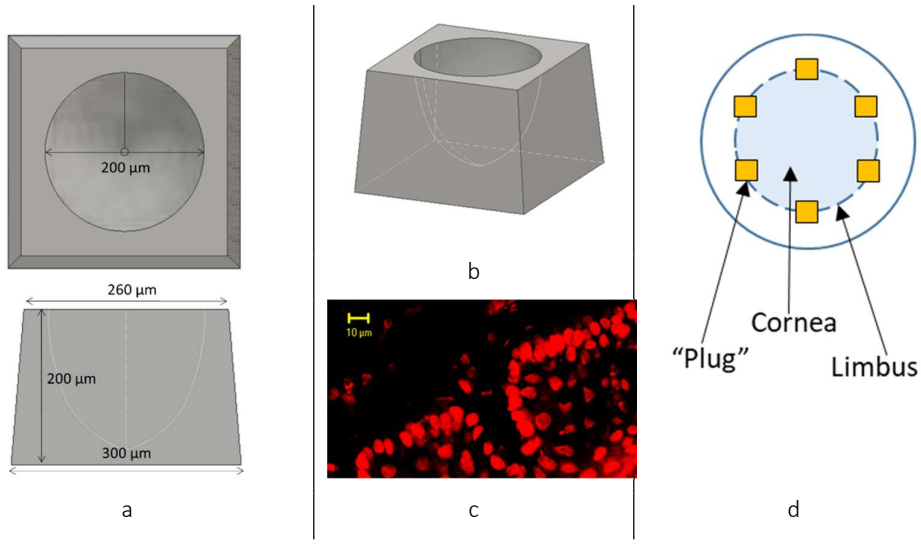


Figure 5.1: Limbal stem cell niche representation. (a,b) CAD structure developed to model the *in-vivo* structure; (a) top and side view and (b) 3D reconstruction. (c) Nuclei staining of cross section through normal limbal region, kindly donated by the Veneto Eye Bank Foundation, Venice, Italy (red indicates DRAQ5™, a red fluorescent staining specific for nuclei). (d) Representation of the concept of this novel scaffold, in which the developed crypts are considered as "plugs" to be transplanted around the limbal region to repopulate the area of stem cell niche.

5.2.2 Investigation of a stiffness gradient of 2PP structures

In addition to GelMA, after the optimization steps were complete, PEGDA 575 (Sigma, UK, 5% (v/v)) was added to the selected gel (15% w/v) to prepare GelMA-PEGDA scaffolds (named 2P15-5) with the aim of reducing the susceptibility to enzymatic (collagenase) degradation, and to modify the mechanical properties while preserving the same structure.

To create a structure with a stiffness gradient, two strategies were investigated. In the first one, the scaffold was printed whilst increasing the hatching distance. In detail, the CAD structure was divided into two parts. The base of the scaffold was printed with a 0.4, 0.8 or 1.6 µm hatching distance, while the top was

printed with a hatching distance of 0.4 µm (figure 5.2a). In the second strategy, two materials were printed on top of each other. The first gel was placed on the coverglass, and the base of the scaffold was printed. Then, the unpolymerized gel was washed with PBS at 40°C, keeping the coverglass in the same position to maintain the same coordinates during the printing process. The second gel was then cast on the first one, and the top of the scaffold printed (figure 5.2 b-e).

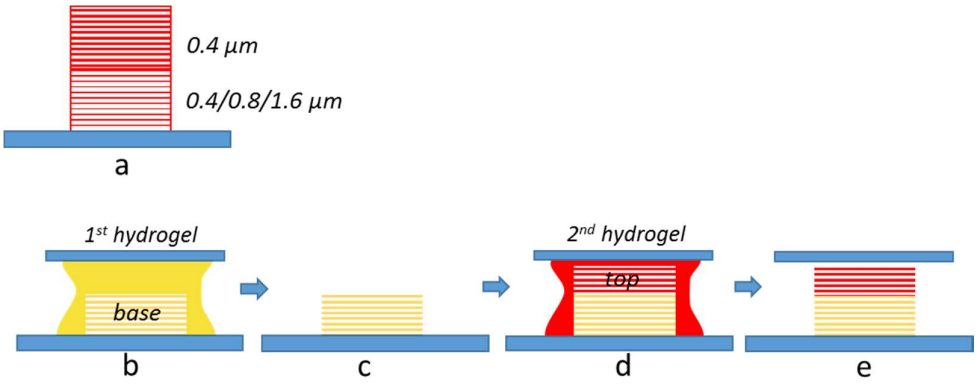


Figure 5.2: Set-up for printing a 3D structure with a stiffness gradient. (a) In the first strategy, the same material was printed but the hatching distance (red striped) was increased from the bottom to the top; (b-e) in the second strategy, two materials were printed on top of each other. (b) The first hydrogel (yellow) was placed between two coverglasses and the laser printed the base of the scaffold. (c) After washing away the unpolymerized gel, (d) the second hydrogel (red) was cast between two coverglasses and the top of the scaffold printed on the previously printed base. (e) The second solution was washed away to obtain the 3D structures.

To test if the materials presented different stiffnesses, a compression test was performed on macro-scaffolds (8 mm diameter, flat scaffold crosslinked by UV, see section 2.1.2, GelMA preparation) that were produced with GelMA, PEGDA, and Irgacure crosslinked with UV. In detail, G15, G15-5, and G15-20 that correspond to 15% (w/v) of GelMA mixed with 0% 5% and 20% (v/v) of PEGDA,

respectively and 0.1% (w/v) of Irgacure, were crosslinked for 10 min. In table 5.1 the nomenclature of the gels are reported.

Table 5.1: Gels nomenclature. Micro-scaffolds and macro-scaffolds refer to the light source involved for the polymerization: IR laser and UV light, respectively. For each set of gels, the GelMA and PEGDA concentrations are reported.

	Micro-scaffold				Macro-scaffold		
Nomenclature	**2P10**	**2P15**	**2P20**	**2P15-5**	**G15**	**G15-5**	**G15-20**
GelMA concentration (% w/v)	10	15	20	15	15	15	15
PEGDA concentration (% v/v)	0	0	0	5	0	5	20
Photoinitiator (name, concentration % w/v)	P2CK, 0.3%				Irgacure, 0.1%		
Light source	IR				UV		

5.2.2.1 Evaluation of photoinitiator cytotoxicity on hCECs

Cytotoxicity assessment of P2CK was performed by preparing solutions with increasing concentrations of PI diluted in cell culture media. The P2CK solutions at molar concentrations of 0.1, 0.2, 0.59, 0.99, 1.97, 5.92, and 9.87 mM were investigated. The same molar concentrations were used to dissolve Irgacure 2959, considered as a control. In table 5.2 the molar concentrations and the corresponding weight-to-volume percentage of both materials are reported. hCECs were seeded into each well of a 96 well plate at a concentration of 50,000 cells/mL suspension (100 µL). After 24 h, the media was removed and the solutions of P2CK or Irgacure were added and left for 0.5 h and 24 h in contact with the cells at 37°C, 5% CO_2 in air. PrestoBlue® (100 µL each well) was used to determine the metabolic activity of the cells as an indirect quantification of cell viability. After 30 min of incubation, the fluorescence intensity was read. Three samples per condition were tested.

Table 5.2: Molar, and weight concentration of P2CK and Irgacure. The investigated P2CK concentrations in the printing optimization process are highlighted in yellow.

Molar concentration (mM)	0.1	0.2	0.59	0.99	1.97	5.92	9.87
P2CK (% w/v)	$0.5x10^2$	$1x10^2$	$3x10^2$	$5x10^2$	0.1	0.3	0.5
Irgacure (% w/v)	$0.22 x10^2$	$0.44 x10^2$	$1x10^2$	$2 x10^2$	0.04	0.13	0.22

5.2.2.2 Swelling and enzymatic susceptibility of printed scaffolds

Gels 2P15 and 2P15-5 were analysed to study the impact of the addition of PEGDA on the swelling ratio and on the susceptibility to enzymatic degradation. 2PP scaffolds of 100x100x50 µm were printed according to the CAD file specifications. Then, each gel was placed in PBS at 37°C for 24 h. The swollen volume was calculated as reported in Equation 2.7.

For the 2PP scaffold, the degradation time was monitored by time-lapse microscopy over 5 days at 37°C and images were acquired every 30 seconds. (see section 2.2.5 degradation). As a comparison, macro-scaffolds were produced, as reported in section 5.2.2. The degradation rate was calculated according to equation 2.8 and 2.9, for the micro- and macro- scaffolds, respectively (section 2.2.5). The sample size was five gels per group.

5.2.2.3 Cell proliferation on printed flat hydrogels

The capacity of hCEC to adhere to the surface of selected materials (2P15 and 2P15-5) was tested by preparing scaffolds with the dimensions of 100x100x50 µm with a flat surface. After 2PP printing, the scaffolds were soaked in 1 mL PBS with 1,000 units/mL of penicillin, 1 mg/mL of streptomycin and 2.5 µg/mL of

amphotericin B at 37°C for 24 h, and then 2 mL of cell culture media was added before cell seeding. After 1 h, the media was removed and a cell suspension ($3x10^6$ cells/mL for hCEC; 100 µL) was seeded in each well for 24 h at 37°C, 5% CO_2 in air. The number of cells on top of each scaffold was recorded after 1, 3 and 7 days by taking images from the whole scaffold with optical microscopy. The test was performed on three samples. After 7 days, the samples 2P15 and 2P15-5 were prepared for SEM to monitor cell morphology, following the procedure explained in chapter 2, section 2.5.2 (SEM).

As a comparison, macro-scaffolds G15, G15-5, and G15-20, prepared with 0.1 (w/v) of Irgacure were produced and the metabolic activities tested with PrestoBlue® assay.

5.2.2.4 Cell proliferation on 3D printed niches

To test if the 3D geometry could affect cell adhesion and proliferation on the selected materials, 3D scaffolds mimicking the native niches were printed. hCECs were seeded at a low concentration of 300,000 cells/well and high concentration of 3,000,000 cells/well. After 1, 7 and 14 days culture at 37°C, 5% CO_2 in air, cells were stained with Calcein AM and incubated at 37°C, 5% CO_2. Fluorescence images were taken by confocal laser scanning microscopy (488 nm). For the high cell concentration, cell viability was monitored after 1 day, and images were taken by confocal microscopy (Z-scan mode).

The table 4.3 summarizes the tests and the methods used to characterize the micro-and macro-scaffolds. The characterization of the macro-scaffolds was performed to support the results obtain with the micro-scaffolds.

Table 5.3: Summary of the tests and the method used to characterize the micro-scaffolds and macro-scaffolds.

	Name	Micro-scaffold	Macro-scaffold
	Photoinitiator	P2CK	Irgacure
	Technique	2PP	UV
Test		**Method**	
Printability Definition of the printing parameters		Inverted and confocal microscopy	/
Evaluation of photoinitiators cytotoxicity		PrestoBlue®	PrestoBlue®
Study of the swelling and degradation ability of GelMA/PEGDA scaffold		Volume measure by time lapse and confocal microscopy	Gravimetric analysis
Study of the hCECs proliferation on flat GelMA/PEGDA scaffold		Cell counting and Live/Dead staining SEM	PrestoBlue® Inverted microscopy

5.3 Results

5.3.1 GelMA can be used to print LECs structure

The capacity of GelMA to form a structure during photopolymerization is summarized in figure 5.3. The increase of GelMA and PI concentration corresponds to an increase in the printability. It was not possible to polymerize hydrogels with 10% (w/v) of GelMA. It was possible however to polymerize 2P15 and 2P20 with a PI concentration of 0.3% (w/v) or higher.

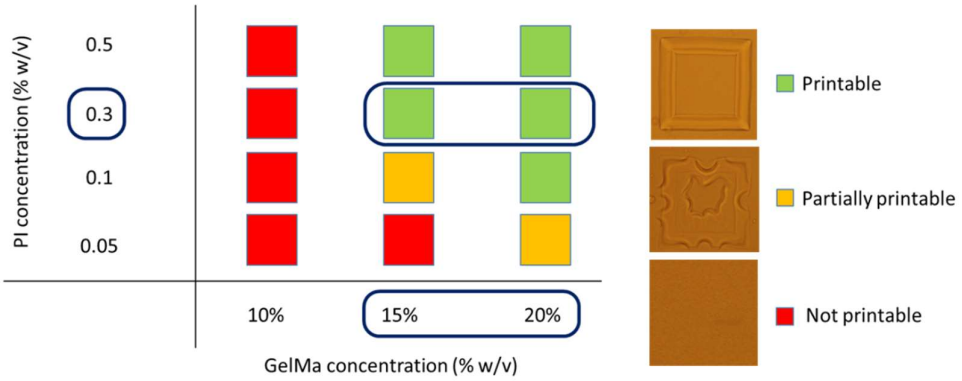
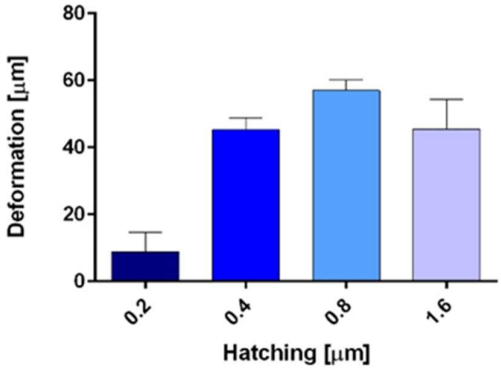
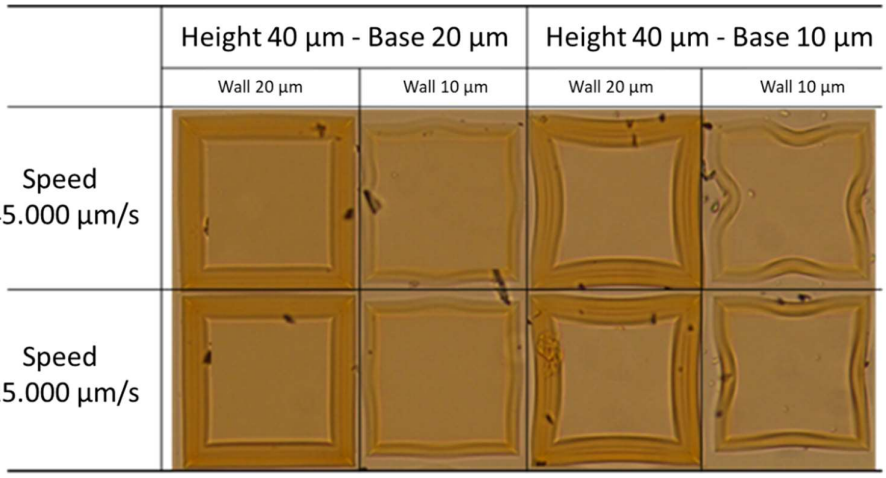


Figure 5.3: Printability of hydrogels of varying GelMA and P2CK concentrations. Green squares represent successful hydrogel formation with clear structure, amber squares represent a partial polymerization and red squares represent a failed scaffold formation (no discernible structure visible). Concentrations of 10% 15% 20% w/v of GelMA and 0.05% 0.1%, 0.3% and 0.5% w/v of PI were investigated.

To investigate the parameters necessary to obtain a stable structure, 2P15 and 2P20 were developed under different conditions. Figure 5.4 shows that the hatching distance and the dimensions of the scaffolds have an impact on the stability of the scaffold. The deformation decreases by increasing the hatching distance and reducing the wall thickness. The limitation is that the printing speed decreases.



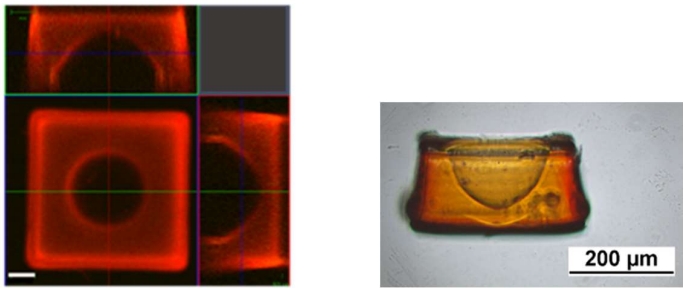
a



b

Figure 5.4: Study how the printing parameters affect the scaffold stability. (a) Deformation of the printed scaffolds as a function of the hatching distance.; (b) printed scaffolds as a function of geometry.

After the investigation of the printing parameters, the scaffolds mimicking the structure of the native LEC niches were printed. In figure 5.5 the printed structure is shown. The scaffold was stable and well represented the CAD model, with a shape that narrowed at the end. Further optimization was explored with a 63x objective. This objective, however, produces an elongated voxel that results in loss of z-resolution entailing a working distance lower than 200 µm, not acceptable for this application. Therefore the niche was printed by using a 25x objective.



a b

Figure 5.5: 2PP printed GelMA scaffolds replicating the dimensions of the LEC stem cell niche. (a) Confocal images of top and side view of 3D structure (scale bar 50 µm). (b) Brightfield image of the side view of the printed niche.

5.3.2 GelMA and GelMA-PEGDA can be used to print LECs structures with a stiffness gradient

To investigate if it was possible to print GelMA and PEGDA scaffolds with different mechanical properties along the z-axis, two strategies were investigated. Figure 5.6 shows that both materials can be printed separately. Increasing the hatching distance, the colour intensity, which is indirectly related to the stiffness, increased. With increased hatching distance, the 2P15-5 gels presented a more unstable niche structure in comparison to 2P15. The confocal images (figure 5.6f,g) showed the separation between the two areas. The results following the second strategy are presented in figure 5.7. A structure composed of two materials was achieved. The two structures were printed on top of each other at the same hatching distance (0.4 µm). Also in this approach, the 2P15-5 presented a less reproducible and precise structure compared to that achieved with 2P15. To give an indication of the relative difference in material properties between the two printed parts, the elastic modulus of the two materials was calculated on the macro-scaffolds by compression testing. By increasing the percentage of PEGDA, the stiffness increased; this was an indirect indication that

the 2PP printed scaffold showed an increased stiffness from the bottom to the top.

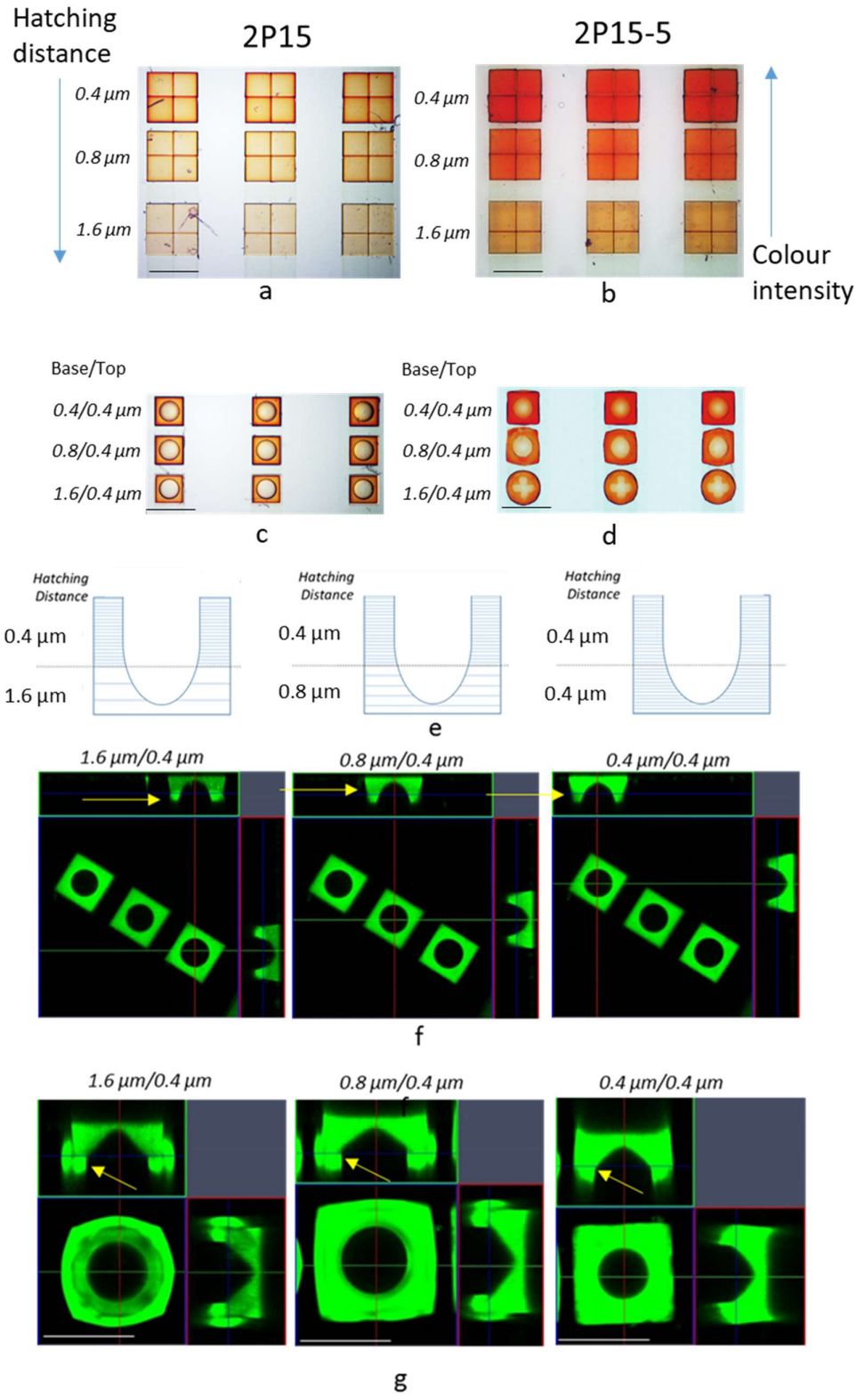


Figure 5.6: Printed structure following the first strategy (increasing hatching distance from the bottom to the top). (a,b) Flat scaffolds and (c,d) niche-like scaffolds with increased hatching distance of (a,c,f) 2P15 and (b,d,g) 2P15-5 gel. (e) Representation of the hatching distance investigated. (a-d) Scale bar 500 µm, (f,g) scale bar 300 µm. (a,b) By increasing the hatching distance, the colour intensity decreased for both materials. (d,g) 2P15-5 structures presented a higher deformation compared to (c,f) 2P15 for all the conditions investigated (base/top hatching distance of 0.4/0.4 µm, 0.8/0.4 µm, and 1.6/0.4 µm. (f,g) The orthogonal views showed the separation between the two parts printed with a different hatching distance. The yellow arrows indicate the separation point.

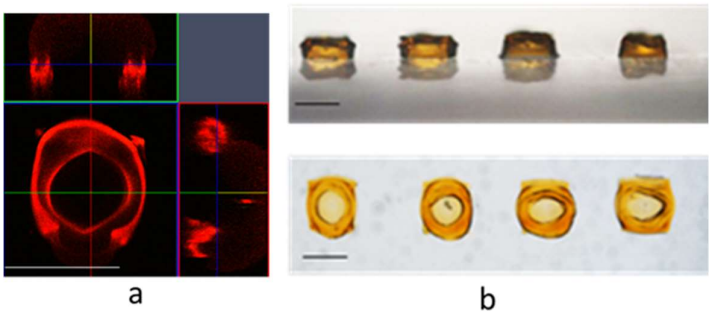


Figure 5.7: Printed structure following the second strategy (two materials were printed on top of each other). (a) Confocal images of the top and orthogonal view of 2P15/2P15-5. The hatching distance of the base and the top of the scaffold was 0.4 µm. (b) Side and top view obtained by inverted microscope. Scale bar 300 µm.

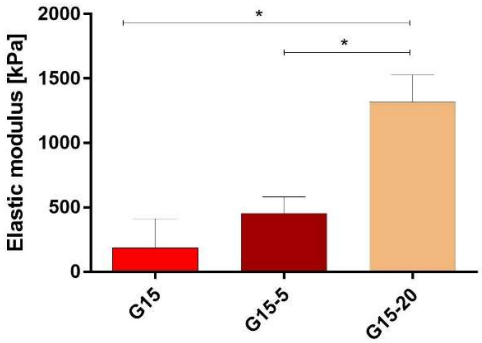


Figure 5.8: Elastic modulus of macro-scaffolds (G15, G15-5, and G15-20) determined by compression testing. Data presented as mean ± SD (n=2). One-way ANOVA with post-hoc Tukey's test ($p^* \leq 0.05$).

5.3.3 Analysis of water content and degradation rate of the printed scaffolds

The water content of 2P15 and 2P15-5 scaffolds after 24 h in PBS was 86.29% ± 3.17% and 72.46% ± 3.13% for 2P15 and 2P15-5, respectively (figure 5.9).

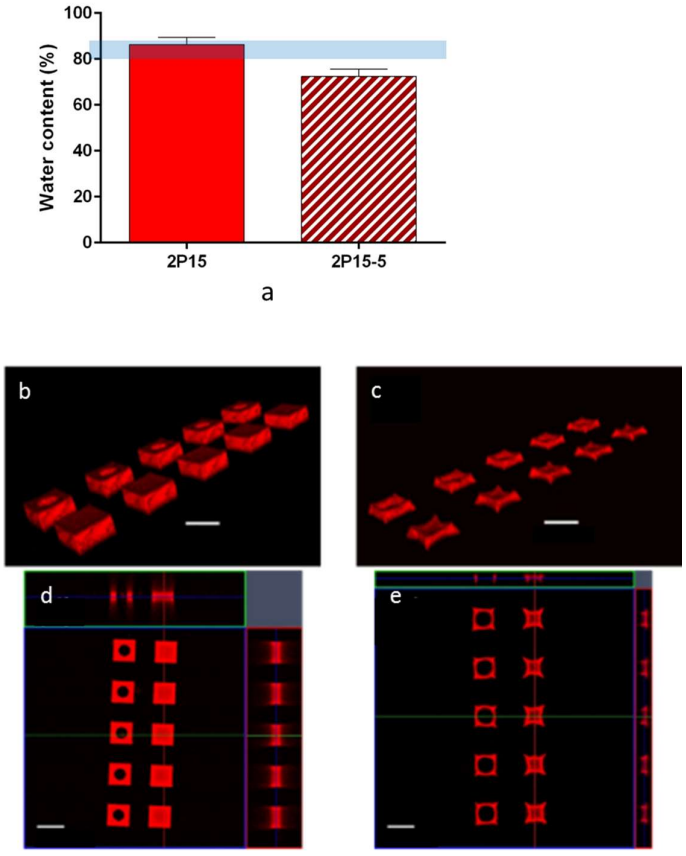
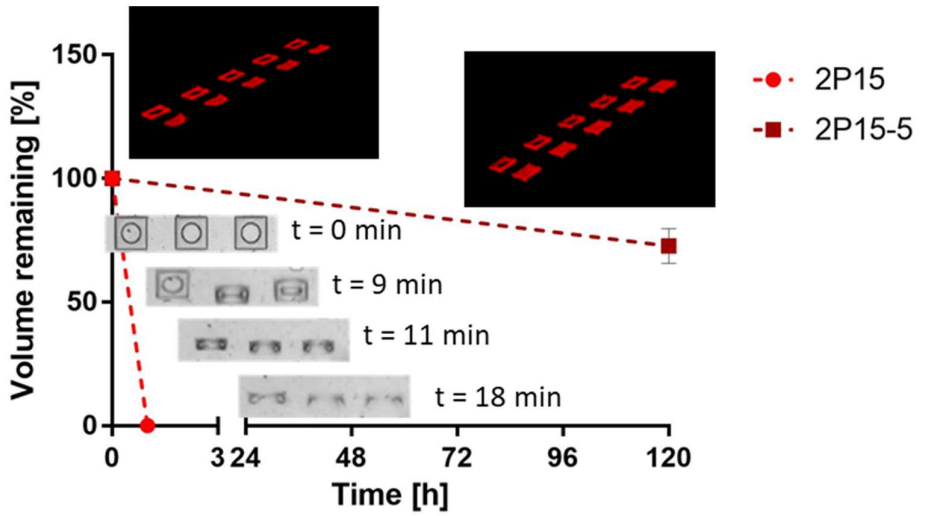


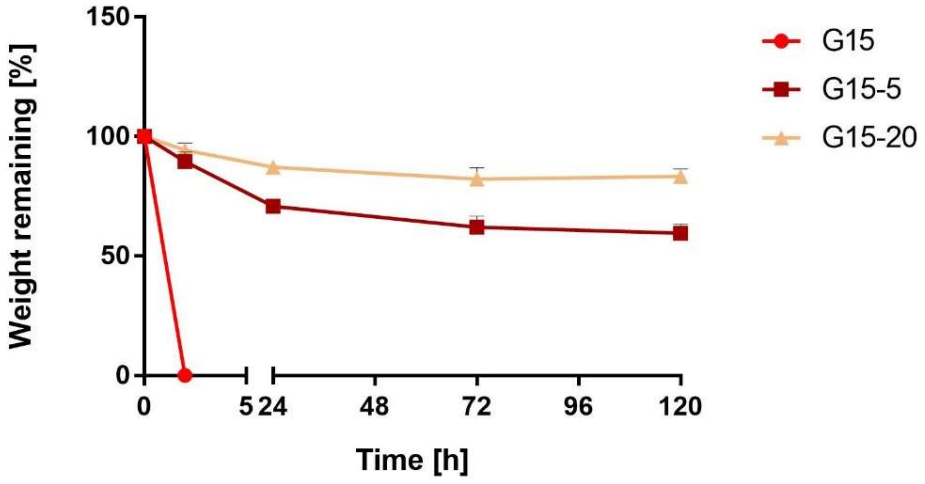
Figure 5.9: (a) Volumetric water content (%) of 2P15 and 2P15-5 after 24 h in PBS. Error bars represent the SD of measurements performed on five samples. The physiological water content range of the human cornea is shown in blue (Mikhailova *et al.*, 2016; Pircher *et al.*, 2003); (b,d) 2P15 hydrated scaffolds and (c,e) dry scaffolds as (b,c) 3D reconstruction and (d,e) orthogonal view. Scale bar 50 µm.

To study the degradation rate, GelMA was combined with PEGDA and printed according to the CAD file. The results obtained for the 2P15 and the 2P15-5 hydrogels are reported in figure 5.10. The behaviour of the gels in contact with collagenase was monitored via time-lapse microscopy in real time. The complete

degradation of 2P15 occurred within 30 minutes. In figure 5.10a the frames of the video at different time points (0, 9, 11, 18 minutes) are shown. On the contrary, the 2P15-5 gel did not degrade completely within 5 days. The comparison of the volume at day 1 and day 5, before and after the addition of the collagenase, is presented in figure 5.10a. The percentage of remaining volume after 5 days was 72.7% ± 6.95%. To confirm the results, macro-scaffolds were developed and the mass degradation was monitored (figure 5.10b). By increasing the percentage of PEGDA, the degradation rate decreased drastically.



a

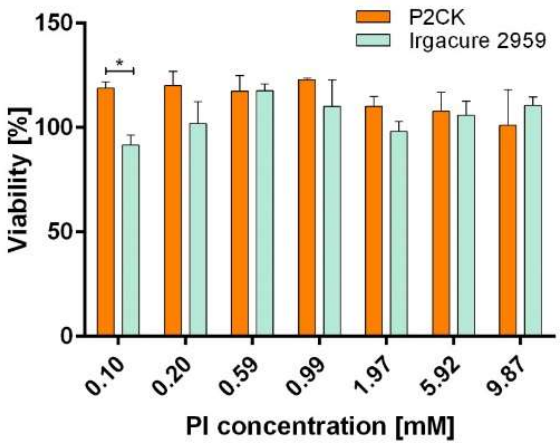


b

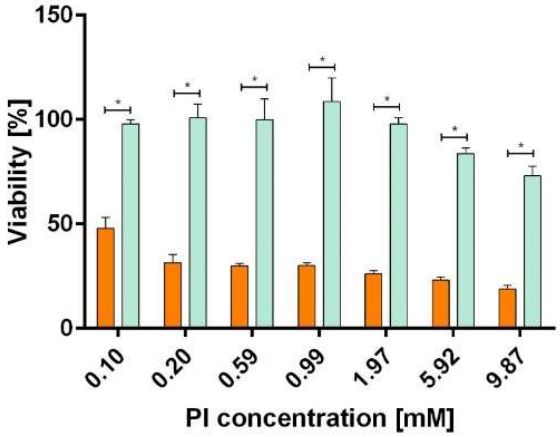
Figure 5.10: Volume remaining (%) after the addition of 1 mg/mL collagenase to micro- and macro-scaffolds. The addition of PEGDA to GelMA displays modifiable enzymatic degradation rate. (a) Degradation rate of micro-scaffolds (2P15 and 2P15-5) was recorded by combining time-lapse and confocal microscopy. 2P15, after 30 minutes was degraded and the frames of the video during the degradation process are shown at different times (t = 0, 9, 11, 18 minutes). 2P15-5 showed 72.7% ± 6.95% of volume remaining after 120 h. 3D reconstruction of 2P15-5 at day 1 and 5. (b) Degradation rate of macro-scaffolds (G15 and G15-5) was recorded by gravimetric test. G15 degrades within 2 h. G15-5 and G15-20 showed 59.5% ± 3.1 and 83.2% ± 3.7, of the initial weight remaining after 120 h respectively.

5.3.4 Evaluation of PI cytotoxicity

Cells were cultured in media prepared with increasing concentrations of P2CK and Irgacure and viability was investigated and compared after 0.5 and 24 h (figure 5.11). For both photoinitiators, and for all the concentrations, the viability was higher than 90% after 0.5 hours. By increasing the incubation time, a decrease in viability for the P2CK was observed, with values lower than 50% for all the investigated concentrations at 24 h. On the contrary, the cells cultured in the Irgacure solution presented a viability lower than 85% only for the highest concentrations (5.97 and 9.87 mM). In table 5.2, the molar concentrations and weight concentrations of Irgacure and P2CK are reported.



a



b

Figure 5.11: Viability of hCEC in contact with P2CK and Irgacure. Cell viability was calculated after (a) 0.5 h and (b) 24 h incubation at different molar concentrations. Error bars represent the SD of measurements performed on three samples. One-way ANOVA post-hoc Tukey's test was performed (*p ≤0.05).

5.3.5 Cells are able to grow on 2PP scaffolds

On flat scaffold

The capacity of hCECs to adhere and proliferate on flat 2P15 and 2P15-5 hydrogels was investigated after 1, 3 and 7 days. The number of cells increased over the experiment period indicating that the addition of PEGDA did not affect cell adhesion and proliferation (figure 5.12a). After 7 days, the cells were

analysed by SEM (figure 5.12b,c). On both gels, hCECs were confluent and the morphologies comparable. The cell viability on the macro-scaffolds confirmed that cells adhered on the gels containing 5% (v/v) of PEGDA. However increasing the concentration to 20% (v/v), the cell viability decreased drastically (figure 5.12 d-g).

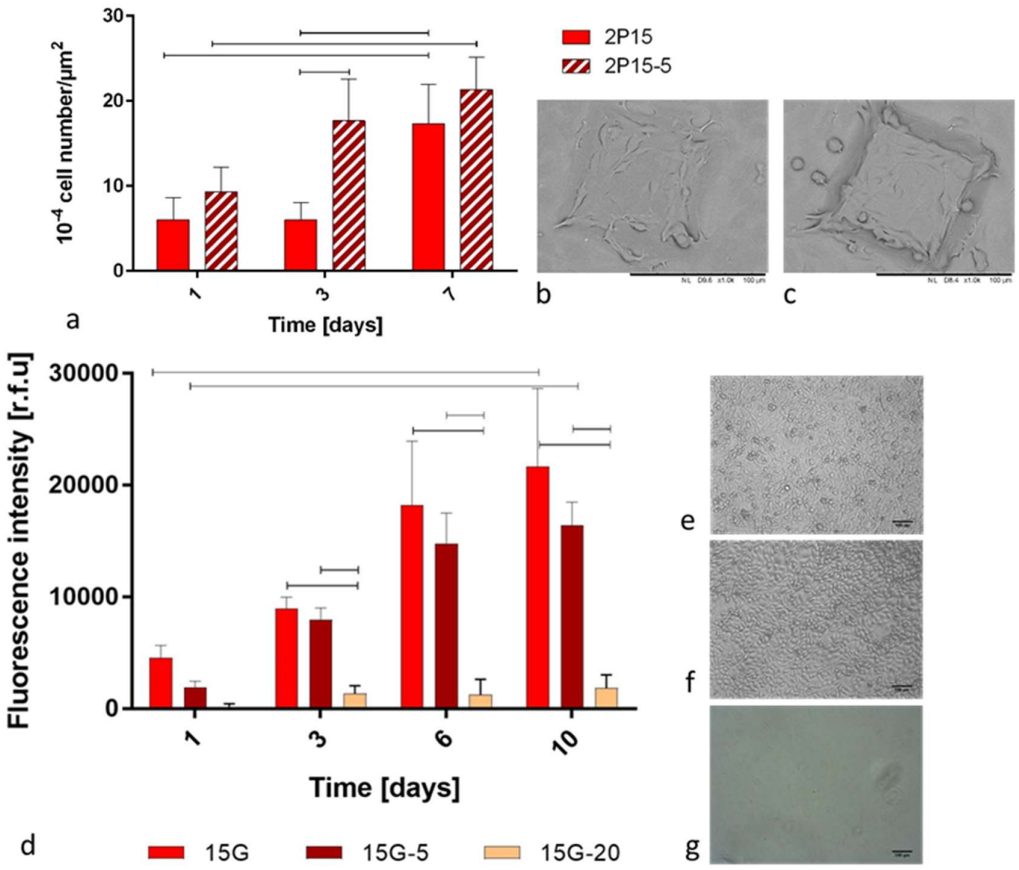


Figure 5.12: hCECs proliferation on GelMA and PEGDA-based scaffold. (a) hCECs proliferation on 2P15 and 2P15-5 after 1, 3 and 7 days. SEM images of (b) 2P15 and (c) 2P15-5 after 7 days of culture. (d) hCECs proliferation on 15G, 15G-5, but not on 15G-20 scaffolds. Brightfield pictures of (e) 15G, (f) 15G-5, and (g) 15G-20 after 10 days of culture. Error bars represent the SD performed on three samples, Two-way ANOVA, post-hoc Tukey's test was performed (*p≤0.05).

Inside the 2PP niches

To investigate the viability of hCEC cells seeded inside the niche-shape architecture, a 2PP scaffold was printed according to a designed CAD image (figure 5.1 a,b) and seeded with cells. After 1 day, cells were viable and positioned along the bottom of the scaffold (figure 5.13 a,d). Some cells were observed outside of the scaffolds and were adherent on the coverglass, due to the seeding method. After 7 and 14 days, the cells proliferated and covered the majority of the surface (figure 5.13 b,c,e,f).

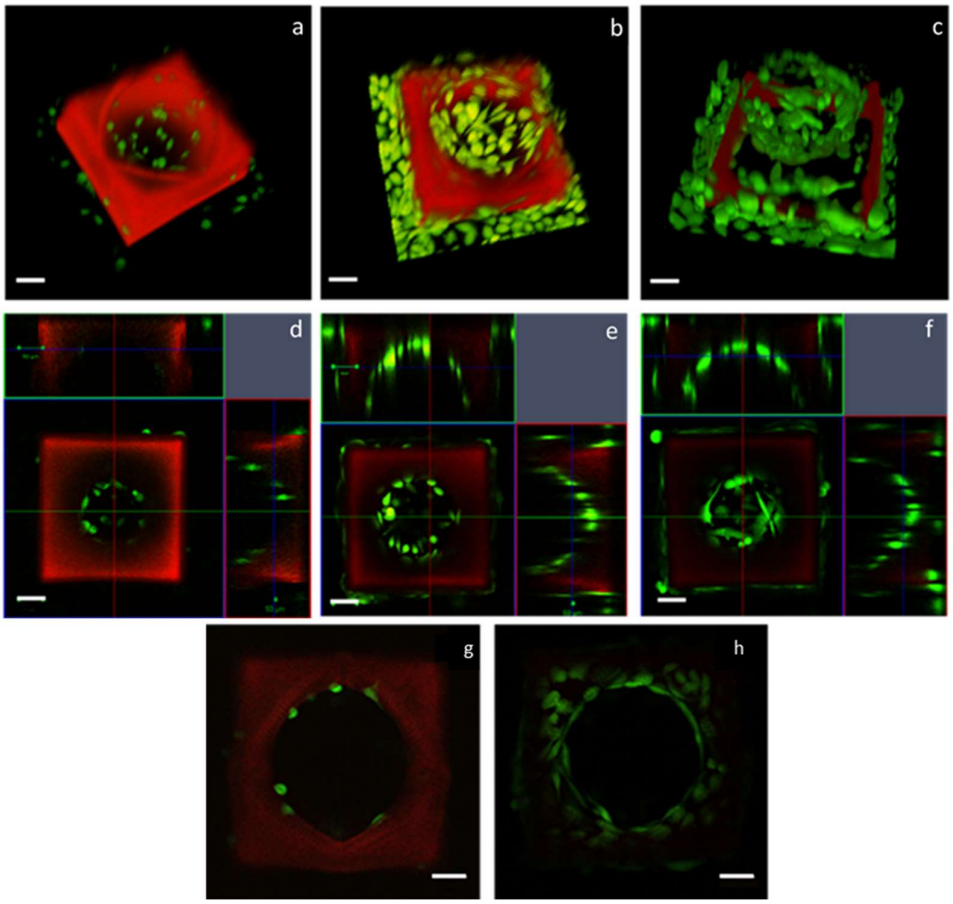


Figure 5.13: hCEC distribution along the printed niches. Confocal images of hCEC cells stained with Calcein AM live cell stain (green) after (a,d) 1 day, (b,e) 7 days, and (c,f) 14 days surrounded by the printed scaffold (red) in (a,b,c) 3D view and (d,e,f) orthogonal view. (g,h) Top z-stack of hCEC cells stained with live staining after (g) 1 day and (h) 14 day. After 14 days, the cells proliferated and migrated to the top of the scaffold. Scale bar 50 µm.

In figure 5.13g-h, the top z-stacks taken after 1 day and 14 days are shown to provide evidence that after seeding cells were not on top of the scaffold, but they had proliferated and migrated after 14 days.

A serial microscopic sectioning of the scaffold after seeding a high concentration of cells is shown in figure 5.14 (day 1) to highlight the variation in diameter of the architecture at different z-stack positions and therefore demonstrating the resolution of the 2PP technique.

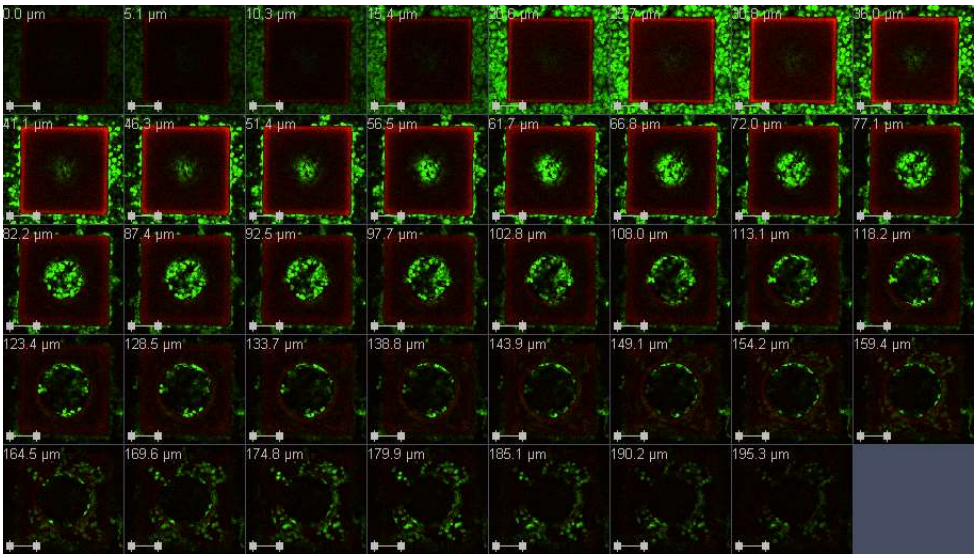


Figure 5.14: Representative confocal images in z-stack of hCEC cells stained with Calcein AM live cell stain after 1 day (seeded at high concentration). Each image represents a z-plane of the scaffold. From the distribution of the cells, it is possible to observe the scaffold diameter increasing from the bottom to the top, and that cells adhere to the walls of the scaffold throughout the interior of the structure. Scale bar 50 µm.

5.4 Discussion

As limbal epithelial stem cells migrate from the limbus area towards the centre of the cornea, they undergo differentiation and stratification and are eventually shed from the ocular surface. The mechanism underpinning this limbal

homeostatic process remains unclear, however, it was hypothesised here that the geometry and the stiffness of the crypt play a determinant role.

In the present chapter, the use of 2PP was investigated in order to produce structures mimicking the architecture of native limbal epithelial stem cell niches. 2PP has the highest lateral resolution among additive manufacturing techniques for printing soft materials, it rapidly turns CAD files into complex structures, and differently from the traditional manufacturing methods it does not require any moulds or masks (Truby and Lewis, 2016). Furthermore, due to the micro-dimensions of the niches, the main drawbacks of 2PP system, which is speed and reduced build volume, were not an issue. Different concentrations of GelMA and PI were explored initially by studying their printability, considered as the parameters able to develop a maintained structure. PEGDA 575 was then added to the selected material, and a stiffness gradient scaffold was printed. Subsequently, the susceptibility of the GelMA based scaffolds to enzymatic degradation and its swelling ability was performed. Finally, the proliferation of hCECs seeded on top of the material, and inside the niches was analysed.

Different concentrations of PI and GelMA were investigated based on 2PP printability to select appropriate printing parameters. It was not possible to obtain the polymerization of GelMA 10% (w/v) using this system. Nevertheless, increasing the percentage of GelMA (15% and 20%) and the PI, the probability that 2-photons, hitting the focal spot, and encountering the molecules to start the polymerization was higher. The gel formulation characterized by a

combination of lower percentages of P2CK and GelMA was selected, due to the fact that the reduced PI concentrations was less detrimental to cell viability. In addition, data from the previous chapter showed that a gel composition between 5% and 15% (w/v) GelMA could be used to produce a structure that presented a stiffness close to values determined for the human cornea.

Firstly, the influence of the printing parameters was evaluated by using 63x objective, demonstrating that the hatching distance and the geometry affected gel stability. Then, the scaffolds were printed according to the niche-structure developed by CAD as determined from measurements taken from histological sections of human tissue (Dua *et al.*, 2005). The results confirmed the suitability of the 2PP technique to develop stem cell niches, due to its high resolution. To develop a scaffold with tunable mechanical properties, two strategies were investigated. The influence of stiffness on cell differentiation is well accepted (Engler *et al.*, 2006; Discher *et al.*, 2005) and there is evidence of the presence of a stiffness gradient between the limbus and the cornea, which can drive the differentiation process by durotaxis (Foster *et al.*, 2014). The first strategy was achieved by increasing the hatching distance. Even if direct evidence of the correlation between hatching distance and elastic modulus was not demonstrated, it is likely that decreasing the hatching distance, the stiffness increased. This is supported by published literature which has confirmed that reducing the hatching distance (the distance between layers increases), the relative density increases (Louvis *et al.*, 2011). The technique developed in the second strategy involved the printing of two materials on top of each other, it

was possible to build a scaffold by using two different materials. It is the first time that this protocol has been performed using 2PP. Also in this strategy, the presence of the stiffness gradient was not proved on the printed scaffold. However, the macro-scaffold (8 mm flat scaffold) results indicated that the addition of PEGDA results in an increase of Young's modulus.

Regarding cell viability, hCECs were grown in media containing P2CK at different concentrations and compared to Irgacure since it is conventionally used for UV crosslinking and considered a biocompatible photoinitiator (Bryant *et al.*, 2000; Williams *et al.*, 2005; Fedorovich *et al.*, 2009). However, because of its molecular structure and spectral absorption characteristics, Irgacure is not suitable for 2PP at 780 nm (Ovsianikov et al., 2013). The result of the direct cytotoxicity test indicated that P2CK presents a time and concentration-dependent cytotoxicity. Literature suggests that the type of cells is a crucial parameter. For example, Ovsianikov et al. (2013) tested the cytotoxicity of P2CK at a concentration of 1.827 mM, using outgrowth endothelial cells (OEC) and osteosarcoma cell line (MG63), after 30 min of incubation. OECs showed statistically significantly lower viability compared to the control, while MG63s did not vary (Ovsianikov et al., 2013). In this thesis, the cells were seeded on top of the scaffold after the printing process. This allowed the gels to be washed extensively prior to cell culture, reducing the amount of unreacted PI present in the scaffolds. Although it was not possible to determine the amount of unreacted PI in the scaffolds (i.e. that the cells would have been exposed to) it is likely that the concentrations evaluated in the test were an overestimation of the actual amount in contact with the cells after the printing process.

GelMA is a well-known material used in a variety of applications, and is remarkably resistant to hydrolytic but not to enzymatic degradation (Coimbra et al., 2014; Kim et al., 2014). Degradation analysis is important due to the presence of Matrix metalloproteinases (MMPs), a group of proteolytic enzymes, that participate in the ECM remodelling during corneal wound healing (Ye et al., 2017; Couture et al., 2016). According to Ovsianikov et al. (2011), 100 CDU/mL of collagenase Type I led to a 2PP scaffold mass decrease of 80% after 5 h. This is a relatively short period of time compared to the degradation of the amniotic membrane scaffold. It has been observed that the degradation of AM occurs over a period of a few days to weeks. This has been reported *in vitro* by using collagenase solution and both in animal and in patients studies (Spoerl *et al.*, 2004; Ma *et al.*, 2010).

PEGDA 575 was therefore added to GelMA to decrease the high susceptibility of GelMA to enzymatic degradation. A combination of time-lapse and confocal microscopy was used to assess degradation, rather than gravimetric methods, because of the micrometric dimensions of the scaffolds. This method was previously used in the 2PP study reported by Käpylä and colleagues (Käpylä *et al.*, 2014). To widen the selection of synthetic biodegradable hydrogels applicable to the 2PP, they synthesized novel synthetic poly(α-amino acid) hydrogels (Poly(acrylic acid). They compared them to PEGDA in terms of polymerization and damage thresholds, voxel size, line width, post-polymerization swelling and deformation. They showed the suitability of these new hydrogels for 3D microfabrication.

It is worth noting however that microscopic methods of determining enzymatic degradation are less precise than gravimetric methods. For this reason, the results were confirmed by the analysis of the behaviour of the macro-scaffolds. The results showed that the addition of PEGDA drastically decreased the degradation rate. It is the first time that GelMA has been combined with PEGDA for 2PP applications. Ovsianikov investigated the use of GelMA with P2CK (Ovsianikov *et al.*, 2011), while Nguyen developed a 2PP scaffold made of PEGDA 302 and 742 with riboflavin as a photoinitiator. Wang et al. (2015) obtained a PEGDA-GelMA scaffold with infrared wavelengths using stereolithography and by using Eosin Y and triethanolamine as the photoinitiators. Other research has combined GelMA with PEG but using Irgacure as the photoinitiator and UV light as polymerization source (Bertassoni, Cecconi, *et al.*, 2014; Hutson *et al.*, 2011; Kim *et al.*, 2014). Although the method of polymerization presented in the previously cited papers is different from the one tested in this thesis, their results are in accordance with the data presented here, in that by adding PEGDA, the susceptibility of GelMA to enzymatic degradation decreases. The results showed that the addition of PEGDA to GelMA scaffold reduced the degradation rate, however the interaction mechanism between GelMA and PEGDA was not studied. Further work is needed to understand this interaction mechanism, and to establish the possible formation of GelMA-GelMA, PEGDA-PEGDA or GelMA-PEGDA chains. For example, a TNBS assay could be a suitable method to calculate the amount of GelMA (related to the lysin groups) before and after the collagenase treatment. In addition, the swelling ratio was investigated using the same technique, since it is an important factor for solute diffusion, cell growth,

and functionality. For 2P15 and 2P15-5, the swelling ratio was higher than 70% and close to that of the human cornea that are reported in a range between 82% and 86%, depending on the method used (Pircher *et al.*, 2003; Mikhailova *et al.*, 2016). The percentage water content is lower in 2P15-5 gel with respect to 2P15 after 24 h, possibly due to the addition of acrylic bonds in 2P15-5 that contributes to creating a hydrogel with a higher crosslinking density and a lower pore size. A possible drawback of the addition of PEGDA is the reduction of cell binding sequences necessary for directly binding cells, due to the fact that PEG is biologically inert (Zhang *et al.*, 2014). The results obtained when hCECs were seeded on 2PP flat scaffolds indicated that the addition of 5% v/v PEGDA to GelMA scaffolds did not affect cell adhesion and proliferation. However, increasing PEGDA to 20% v/v concentrations, the viability was reduced as demonstrated on macro-scaffolds.

To further investigate the behaviour of cells with respect to the architecture, hCECs were seeded onto scaffolds mimicking the stem cell niche geometry and cell proliferation and viability were monitored for 14 days. The results at 1, 7 and 14 days, indicated that cells proliferated inside the crypts. The cell seeding technique used in this study was not precise, causing the cells to be seeded both inside and outside of the niches. This posed challenges in accurately monitoring cell migration. The use of labelled cells, tracking software, optical tweezer lasers or microinjection techniques in combination with 2PP may overcome this limitation. Preliminary results showing the use of an optical tweezer for cell deposition within the crypts are presented in Appendix B.

In conclusion, the results presented in this chapter demonstrated that GelMA-PEGDA hydrogels can be developed in combination with 2PP techniques. The addition of PEGDA reduced the susceptibility of GelMA to enzymatic degradation without affecting cell adhesion and the water content (the latter of which was comparable to values published for the human cornea). Thanks to the high resolution of the 2PP system, it was possible to obtain a structure that mimics the native shape of LECs. The developed structures were biocompatible and allowed hCECs proliferation. However, the scaffolds produced with the inclusion of PEGDA were less stable than those printed only with GelMA. Therefore, to test the hypothesis that geometry has an impact on cell differentiation, the next chapter focused exclusively on GelMA scaffolds. Printed GelMA niches were seeded with primary limbal cells and differentiation was investigated according to the z-position.

6. Investigation of limbal stem cell differentiation in the 3D printed scaffold: assessing the influence of geometry and stiffness

6.1 Introduction

Scaffolds proposed for the treatment of corneal pathologies due to limbus damage should support a permanent source of epithelial progenitor cells to ensure the maintenance of corneal homeostasis. Such cells, if harvested from the human cornea, will ultimately change their phenotype and lose their stemness in prolonged 2D culture. For example, limbal epithelial cells outgrowing from an *ex vivo* explant on AM scaffolds progressively lose their stemness *in vitro*, as the distance from the explant increases (Kolli *et al.*, 2008). The overarching aim of this PhD was to recreate the key physical factors that can influence limbal cell differentiation to inform the design of scaffolds for cornea regeneration. The two main factors investigated were stiffness and geometry.

The separate effect of each component has already been investigated in a few research studies, but the results are still controversial and not fully clarified.

Recently, progress in the design of corneal scaffolds has been made by producing 3D spatially defined structures and geometries. Ortega and colleagues combined stereolithography with electrospinning to reproduce a micro-pocket ring (Ilida Ortega *et al.*, 2013; Ortega *et al.*, 2014). It is unclear whether these structures alone are able to recreate the limbal stem cell niche *in vitro,* and further investigations are required. Levis et al. developed a Real Architecture for 3D Tissue system, in which microscale grooves and ridges were reproduced on compressed collagen scaffolds to simulate the structure of limbal stem cell niches. Limbal stromal fibroblasts were embedded in the gel and human limbal epithelial cells were seeded on the surface. After 3 weeks of culture, the constructs formed numerous epithelial layers and maintained a mixed population of primitive and differentiated cells, with a high percentage of the cells lining the base of the crypts stained positive for the limbal stem cell marker p63α (Levis *et al.*, 2013). Their architecture well represented the interpalisadal grooves that stretch radially towards the cornea, termed limbal crypts (Shortt *et al.*, 2007), but was less representative of the enclosed structure described as epithelial limbal crypts by Dua and colleagues (Dua *et al.*, 2005).

The influence of stiffness on cell differentiation has been investigated by Foster et al. (2012) and Chen et al. (2014). They studied the behaviour of bovine corneal epithelial cells on flat scaffolds, but not human cells and not in combination with a 3D structure (Chen *et al.*, 2012; Foster *et al.*, 2014). Both studies concluded that the number of differentiated cells increased with increasing stiffness.

Since the pioneering work by Pellegrini et al. (1997), the method used in the treatment of LSCD pathology was based on the expansion of *ex-vivo* LESCs on inactivated 3T3 cells as a feeder layer. This protocol, known as cultured limbal epithelial transplantation (CLET) emulates the one adopted for the development of skin grafts (Rheinwald and Green, 1975). Recently, translational research aims to reduce the risk of xenotoxicity, and more effort has been made to develop animal-free culture systems. In this attempt, serum-free and feeder-layer-free protocol has been proposed for limbal stem cell expansion (Lekhanont *et al.*, 2009; Zakaria *et al.*, 2014).

6.1.1 Chapter objectives

In the previous chapters, macro-gels with an elastic modulus in the same order of magnitude of corneal tissue (chapter 3) and micro-scaffolds mimicking the geometry of the limbal crypts (chapter 5) were developed.

In this chapter, divided in two parts, the previous outcomes were used to investigate the key factors that play a role in controlling hLESCs differentiation. The aim of the first part was to study the effect of the increased stiffness of the macro-scaffolds, defined as flat scaffolds crosslinked by UV light, on hLESC differentiation:

- in normoxic (20% O_2) and hypoxic condition (5% O_2);
- with CnT-Prime (basal media) and CnT-PR-D media (differentiation media).

The aim of the second part was to study the impact of the geometry on LESCs differentiation and the objectives were:

- to study the distribution of the limbal stem cells seeded inside the micro-scaffolds in xeno-free conditions and to study their differentiation along the z-axis.
- To monitor the distribution of the limbal stem cells seeded inside the micro-scaffolds in the presence of a murine fibroblast feeder layer and serum-containing media and to study their differentiation along the z-axis.
- To study the ability of limbal epithelial cells, outgrowing from a biopsy, to colonize the printed scaffold, and their distribution along the z-axis.
- To study the synergic effect of hypoxia (20% O_2), stiffness and geometry on hLESCs differentiation.

6.2 Experimental design

For more detailed information regarding the commercial human Limbal Epithelial Stem Cells (c_LESCs), the extraction of tissue_derived human Limbal Epithelial Stem Cells (td_LESCs), the immunohistochemistry, qPCR and AFM methodologies, see Chapter 2: Materials and Methods. A table summarizing gel formulations and naming conventions can be found in appendix A.

PART ONE

6.2.1 Evaluation of the stiffness effect on limbal stem cell differentiation in normoxic and hypoxic conditions

To study the impact of gel stiffness on limbal stem cell differentiation, G5, G10, G15, G25 and G40 were prepared as explained in section 2.1.2. hLESCs were seeded onto the flat scaffolds (see protocol in section 2.3.3). The cells were cultured with basal (CnT-Prime) and differentiation media (CnT-PR-D), in normoxic (37^{o}C incubator at 20% O_2, 5% CO_2) and hypoxic (37^{o}C incubator at 5% O_2, 5% CO_2) conditions. After 10 days, when the cells covered the entire surface, two tests were performed:

(a) c_LESCs seeded on the gels were fixed for 10 min with PFA 4%, permeabilised, blocked to prevent non-specific binding and stained with anti-CK14 (limbal stem cell marker) and anti-CK3/12 (differentiation marker) antibody conjugated to Alexa Fluor 633 and Alexa Fluor 488, respectively. Samples were imaged by confocal microscopy. Three pictures for each condition were taken for two independent experiment (n = 2).

(b) qPCR was assessed to investigate the gene expression of corneal epithelial markers of c_LESCs seeded on gels at different stiffness (G10, G15, G25), in comparison to tissue culture plastic controls. Cells were cultured in normoxic and hypoxic conditions and with basal and differentiated media. KRT19 was used to quantify the epithelial progenitor gene and KRT3 for terminally differentiated epithelial gene (n=3).

PART TWO

6.2.2 Evaluation of scaffold geometry on limbal stem cell distribution and differentiation

6.2.2.1 Cell culture systems

To study the behaviour of limbal stem cells seeded on the 3D printed niches, two cell culture methods were used. In the first one, c_hLESCs were harvested and cultivated by using the basal media CnT-Prime, an animal-component-free culture medium developed for isolation and expansion of epithelial cells. In the second one, td_hLESCs were extracted from the limbus, and seeded on a feeder layer of irradiated 3T3 with a serum containing-media. For more detail about the cell culture conditions and the media formulation see section 2.3 (Cell culture). Unless otherwise stated, cells were cultured in 20% O_2, 5% CO_2 at 37°C.

6.2.2.2 Cell distribution and differentiation along the z-axis

To study the ability of the limbal cells to proliferate and differentiate inside the 3D printed structures, two strategies, summarized in figure 6.1, were performed:

1) c_hLESCs and td_LESCs suspensions (150,000 cells, in 50 µl) were seeded onto the micro-scaffolds. Later, the media was added to cover the entire surface of the scaffolds. For td_LESCs, a feeder layer of irradiated 3T3 cells were seeded onto the scaffold from 4h to 24h before adding the cornea epithelial cells. Cell morphology and cell growth were monitored daily using an inverted confocal microscope.

2) For the second strategy, to monitor the ability of cells to colonize the scaffold, a small cadaveric human limbal biopsy fragment was placed close to the scaffolds to allow its adhesion to the coverglass. Cell migration from the biopsy to the scaffold was monitored daily using an inverted confocal microscope.

After 10 days from cell seeding, when the cells fully covered the surface of the scaffolds, cells were fixed and immunohistochemistry was performed. The distribution of the cells along the z-axis was monitored by Hoechst staining. To study the differentiation process, c_hLESCs were stained with CK14 (limbal stem cell marker) and CK3/12 (corneal cell marker), while td_hLESCs were stained with p63 (limbal stem cell marker) and CK3/12 (corneal cell marker). The cell marker expression and distribution was assessed by confocal microscopy.

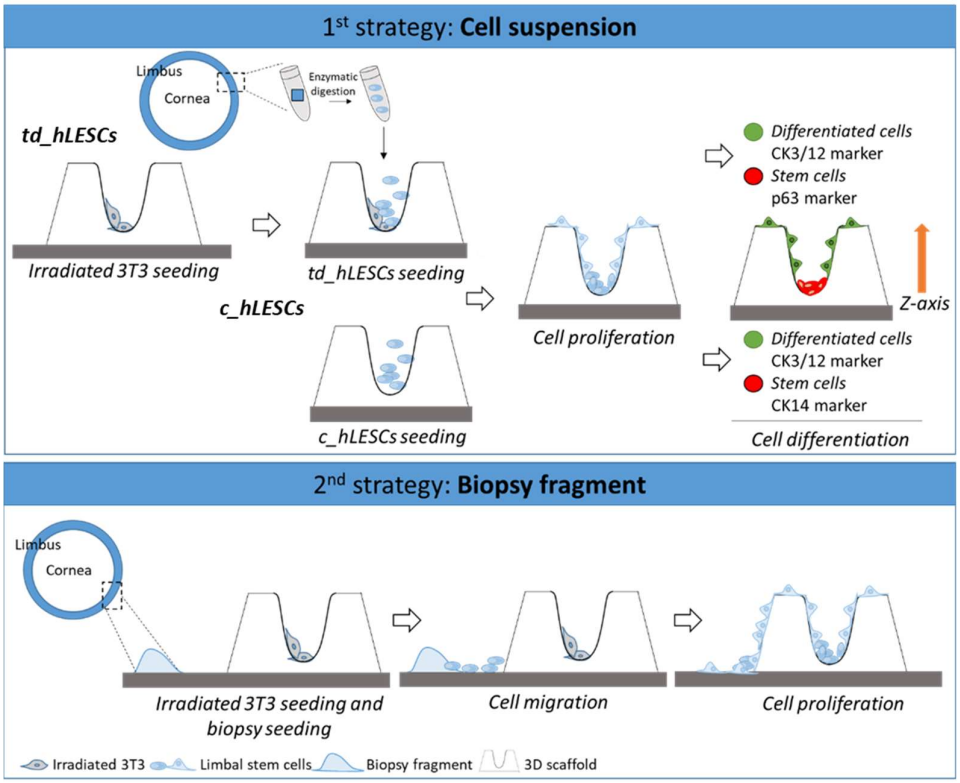


Figure 6.1: Representation of the two strategies adopted to study the cell distribution and differentiation along the z-axis of the 3D printed niches. In the first strategy, the cell suspension was seeded onto the scaffolds by using two cell culture conditions (xeno-free and with serum and with a feeder layer). The cell distribution was assessed by Hoechst, while cell differentiation was studied using CK14/p63 and CK3/12 as stem cells and corneal differentiation markers, respectively. In the second strategy, a biopsy fragment was obtained from human limbal tissue and placed close to the scaffolds. The ability of the cells to migrate and re-populate the niche was monitored by optical microscopy.

The experiments involving the use of c_hLESCs and td_LESCs were performed at the University of Nottingham and at the Veneto Eye bank (Mestre, Italy), respectively.

6.2.2.3 Evaluation of the effect of oxygen on limbal stem cell differentiation

To study the impact of oxygen levels on stem cell growth and differentiation, the scaffolds and cells were cultured in hypoxic conditions (multi-gas incubator at 5% O_2, 5% CO_2 at 37°C).

6.2.2.5 Evaluation of the stiffness of 3D printed structures

To study the stiffness of the printed niches, AFM was performed. The cantilever was positioned both on the area on top of the scaffold, and on a flat scaffold used to emulate the base of the scaffold, as represented in figure 6.2. For detailed information about AFM (Atomic force microscopy), see chapter 2, section 2.2.3.

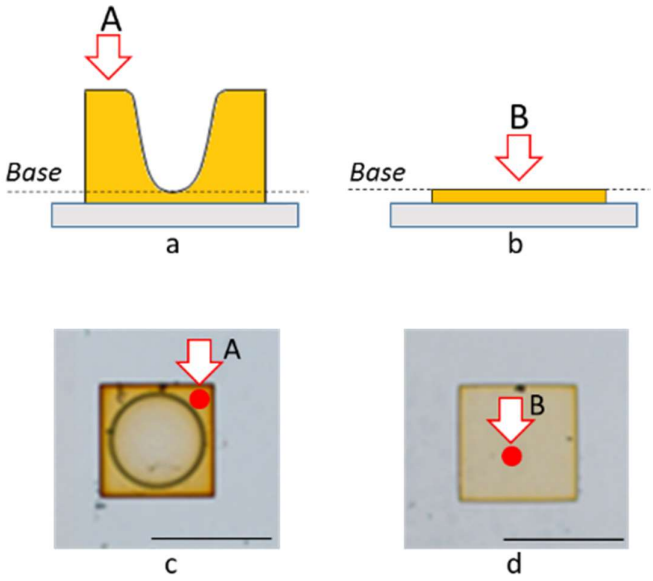


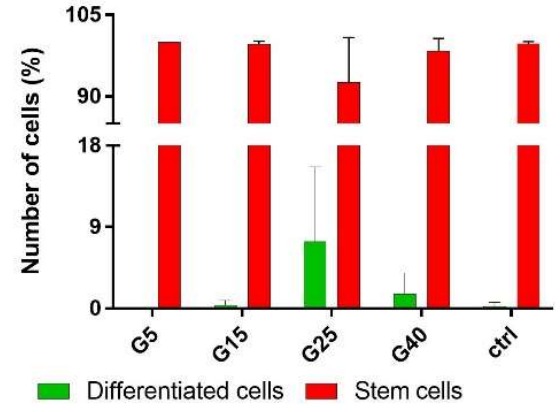
Figure 6.2: Representation of the areas on which the elastic modulus of the 2PP scaffold were mesaured by AFM. (a,b) Representation of the (a) niche-like and (b) flat printed scaffolds. (c,d) Optical microscopy images of the printed scaffolds. The red arrow indicates where measurements were taken. (a,c) The elastic modulus of the top of the scaffold was measured preforming the indentation on area A; (b,d) the elastic modulus of the bottom of the scaffold was measured on area B of a printed flat scaffold mimicking the base of the niche-like shape. Scale bar 300 µm.

6.3 Results

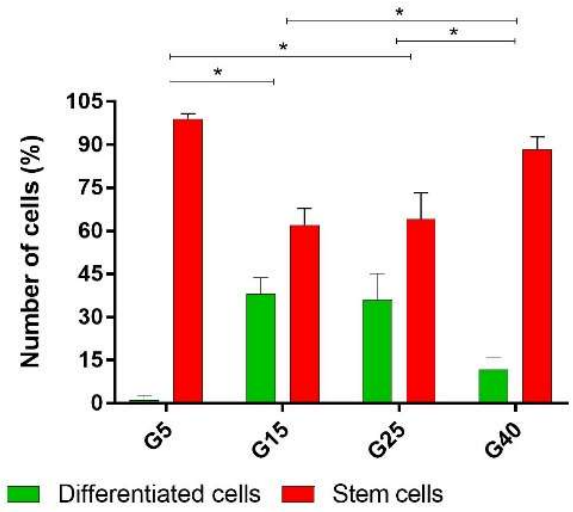
PART ONE

6.3.1 Stiffness had an impact on stem cell differentiation depending on the media composition

Cells were seeded on flat scaffolds and marker expression was evaluated with confocal microscopy. Confocal images in the normoxic culture conditions showed that the stiffness did not have a pronounced effect on stem cell differentiation. The number of stem cells on each gel was not statistically significantly different (figure 6.3a and 6.4). A limitation to take into consideration is that the G5 sample presented a lower number of cells in both tests, and it was difficult to handle it due to its softness. No images were taken in hypoxic conditions. To understand if the type of media could have an impact on the results in normoxia, a test was performed by using CnT-PR-D media, which is a fully defined, animal-component free medium designed by CELLnTEC for differentiation of epithelial cells. In this experiment, the number of differentiated cells increased significantly (G15, G25, and G40) on stiffer gels (figure 6.3b and 6.5). Due to the difficulties in handling G5, and due to the non-physiological elastic modulus of G40, the experiment was repeated using G10, G15 and G25, and images were taken by confocal microscope. The results confirmed that the number of differentiated cells did not increase significantly by increasing the stiffness in normoxic culture conditions.



a



b

Figure 6.3: Number of stem cells (c_hLESCs) and differentiated cells cultured on GelMA hydrogels (G5, G15, G25, and G40). The percentage was calculated as the ratio of red-labelled cells (stem cells) and green-labelled cells (differentiated cells) to the total number of cells on three areas of each sample (n=2) in (a) Cnt-Prime media and (b) CnT-PR-D differentiation media. Anova with Tukey's post hoc ($p \leq 0.05$).

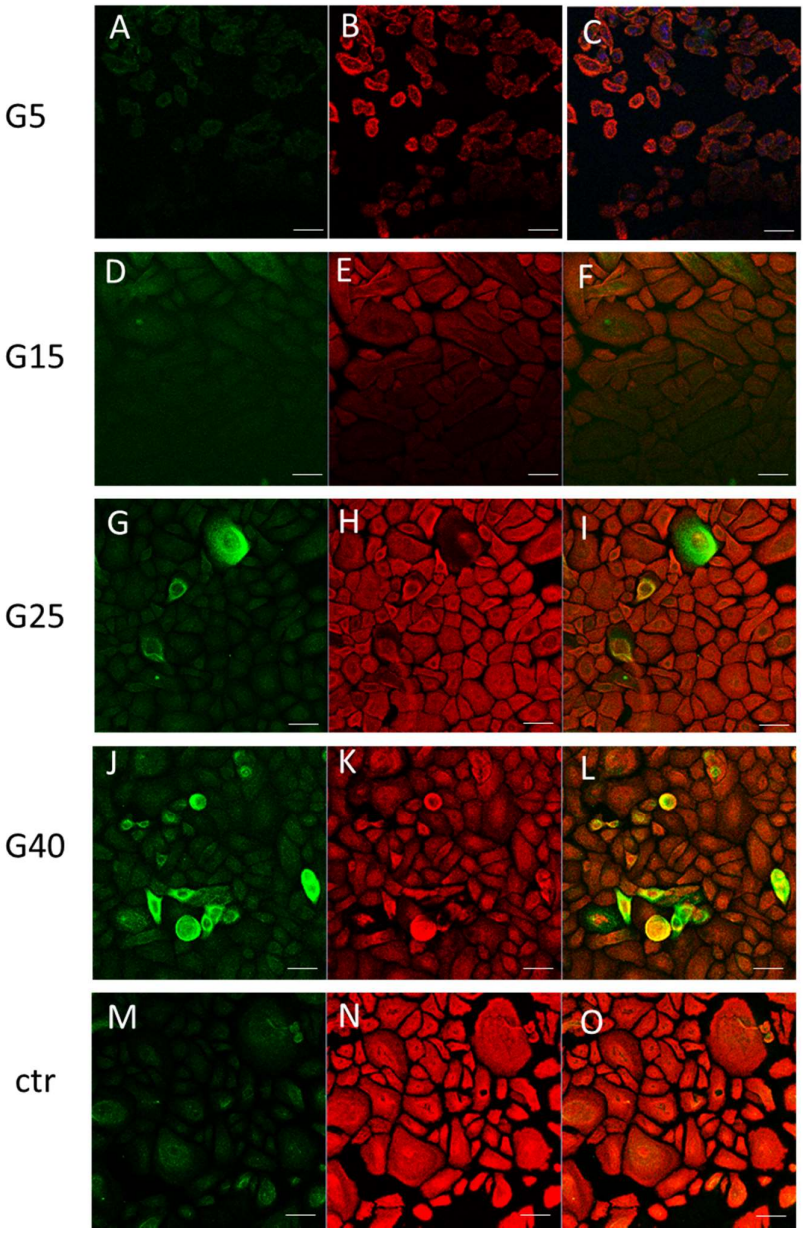


Figure 6.4: Confocal microscope images of limbal stem cells (c_hLESCs) grown on GelMA hydrogels (G5, G15, G25, and G40) and cultured in CnT-PR, the basal media. Green (differentiated cells), red (stem cells) and merged images are represented in (A,D,G,J,M), (B,E,H,K,N), and (C,F,I,L,O), respectively. Scale bar 50 µm.

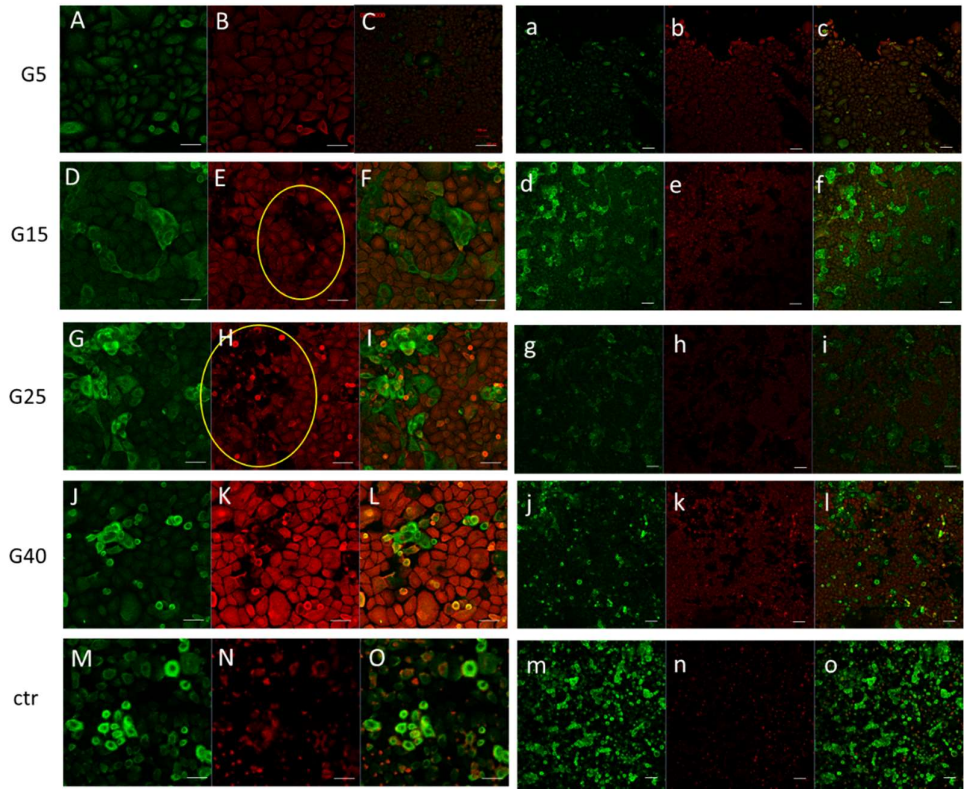


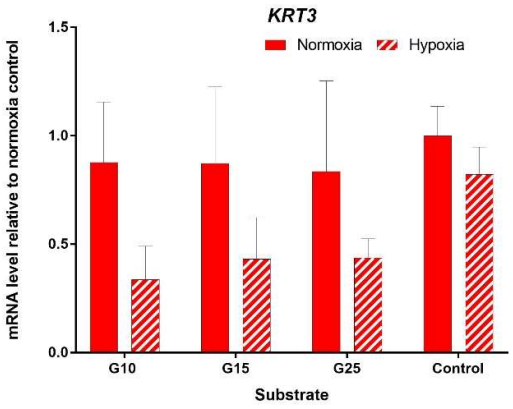
Figure 6.5: Confocal microscope images of limbal stem cells (c_hLESCs) grown on GelMA hydrogels (G5, G15, G25, and G40) and cultured in CnT-PR-D, the differentiation media. Green (differentiated cells), red (stem cells) and merged images are represented in (a,d,g,j,m, A,D,G,J,M), (b, e, h, k, n, B,E,H,K,N), and (c,f,i,l,o,C,F,I,L,O), respectively. (A-O) Scale bar 300 µm. (a-o) Scale bar 50 µm.

6.3.1.1 Phenotypic Gene Expression

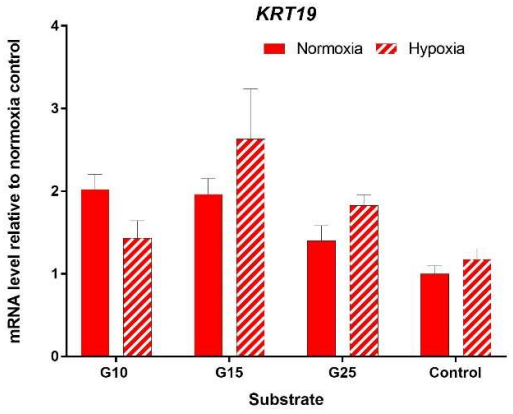
RT-qPCR analysis was carried out by Dr. Laura Sidney, at the School of Medicine department, at the University of Nottingham. Quantitative PCR (qPCR) was used to evaluate the changes in limbal epithelial phenotype in response to gel stiffness and oxygen concentration (Figure 6.6). Cells were cultured in basal and differentiation media. Two-way Anova was used to investigate the influence of stiffness and oxygen levels on cell differentiation. General trends observed in the expression of KRT3, a gene for corneal cells, indicated that stiffness had no

significant effect on cell differentiation, while a decrease in oxygen level reduced gene expression ($p \leq 0.05$, figure 6.6a). On the contrary, no significant effects of stiffness or oxygen concentration were observed in the expression of the gene KRT19 used as a marker of the stem cells phenotype (figure 6.6b).

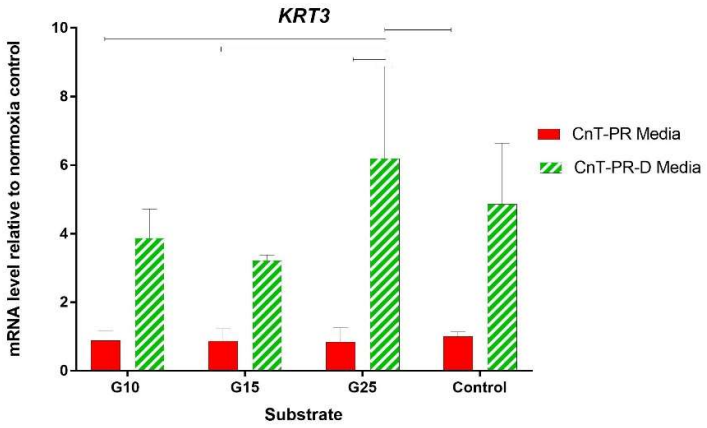
When hLESCs were cultured in differentiation media, the expression of KRT3 was significantly higher in all the gels compared to the basal media (figure 6.6c). For KRT19 gene expression, the only statistically significant differences were observed between the control and the tested materials (G10, G15 and G25, figure 6.6d).



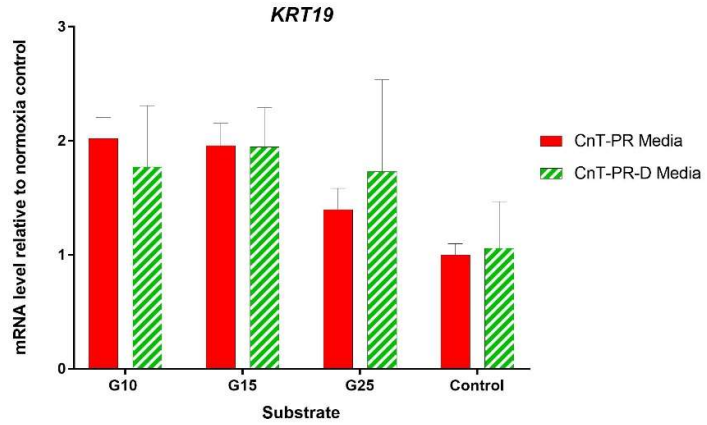
a



b



c



d

Figure 6.6: c_hLESCs gene expression in response to gel stiffness, media composition and oxygen concentration measured by qPCR. (a,b) Relative gene expression after 10 days culture in CNT-PR media, and (c,d) in CNT-PR-D media. (a,c) KRT3 expression and (b,d) KRT19 expression. Data represents mean relative quantitation ± SEM, (n=3). ANOVA with post-hoc Tukey's test ($p \leq 0.05$).

PART TWO

6.3.2 Cells assembled as homogenous monolayers in xeno-free culture conditions and formed colonies in the serum-media and feeder layer culture conditions

The suitability of the printed scaffold for limbal stem cell replacement was investigated with commercial limbal epithelial cells, and with primary limbal epithelial cells collected from a limbal biopsy. Both systems were able to support cell growth displaying typical polygonal epithelial morphology. However, in the xeno-free culture conditions the cells grew as homogenous monolayers of single-cells, whilst forming colonies in the serum-media and feeder layer condition. In figure 6.7, the cell morphologies in both conditions are shown.

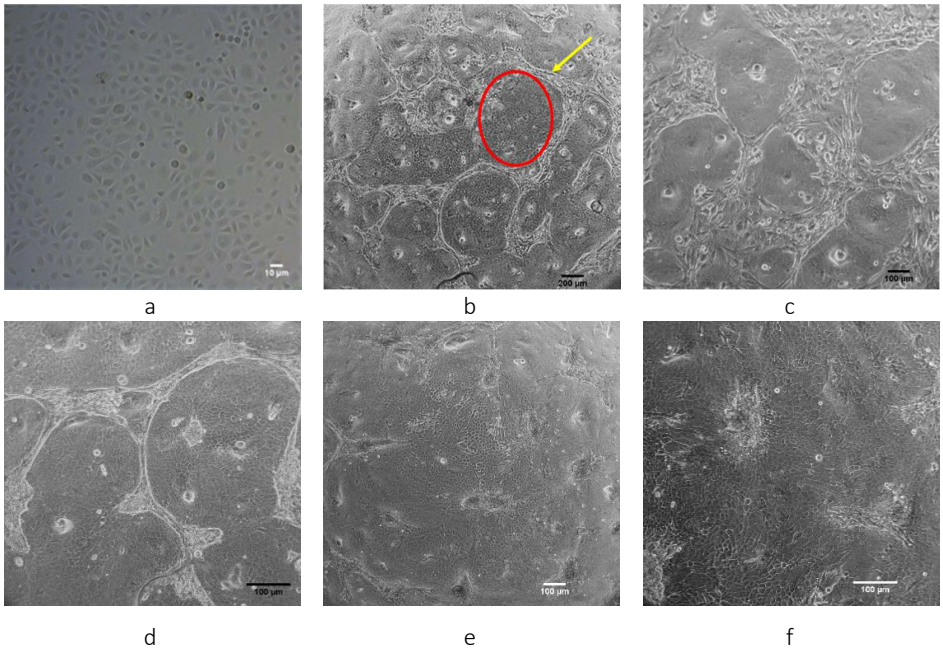
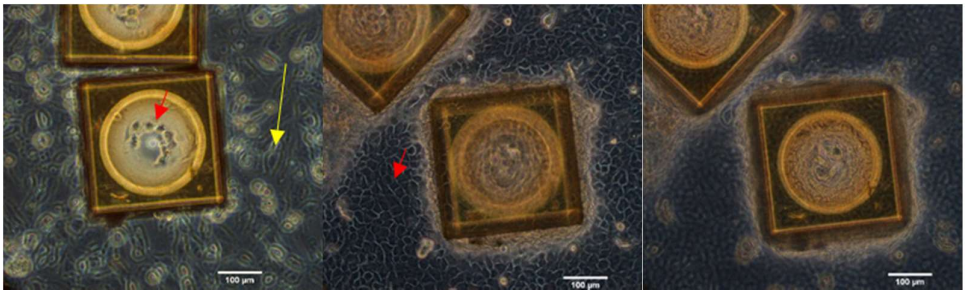


Figure 6.7: Cultivation of limbal epithelial cells. (a) c_hLESCs were cultured in a serum-free and feeder layer-free media. They did not present colony formation. (b-f) td_hLESCs extracted from a limbal biopsy were seeded on an irradiated 3T3 feeder layer. (b-d) The cornea epithelial cellsformed colonies (red circle), pushing away the fibroblasts (yellow arrow); (e-f) when the cells were confluent, the remaining feeder layer covered a small area, and were removed by changing the media.

6.3.3 Cells were distributed along the niche on the printed structures

6.3.3.1 First strategy: cell suspension seeded onto the scaffolds

A cell suspension was seeded onto the scaffold and the cell growth was monitored daily until the cells covered the scaffolds. For both cell types, cells proliferated and were distributed along the scaffold, from the base to the top (figure 6.8). The cell distribution was confirmed by Hoechst staining, represented in figure 6.9, for three z-positions: base, middle and top. However, no stratification was detected for both conditions in all the investigated scaffolds.



a *b* *c*

Figure 6.8: Proliferation of td_LESCs seeded on the 2PP scaffolds. (a) Cells immediately after seeding and (b,c) after 7 days. The focus is (b) on the top and (c) on the bottom of the scaffold. The yellow arrow indicates the feeder layer, while the red arrow indicates the cornea epithelial cells presenting a polygonal morphology.

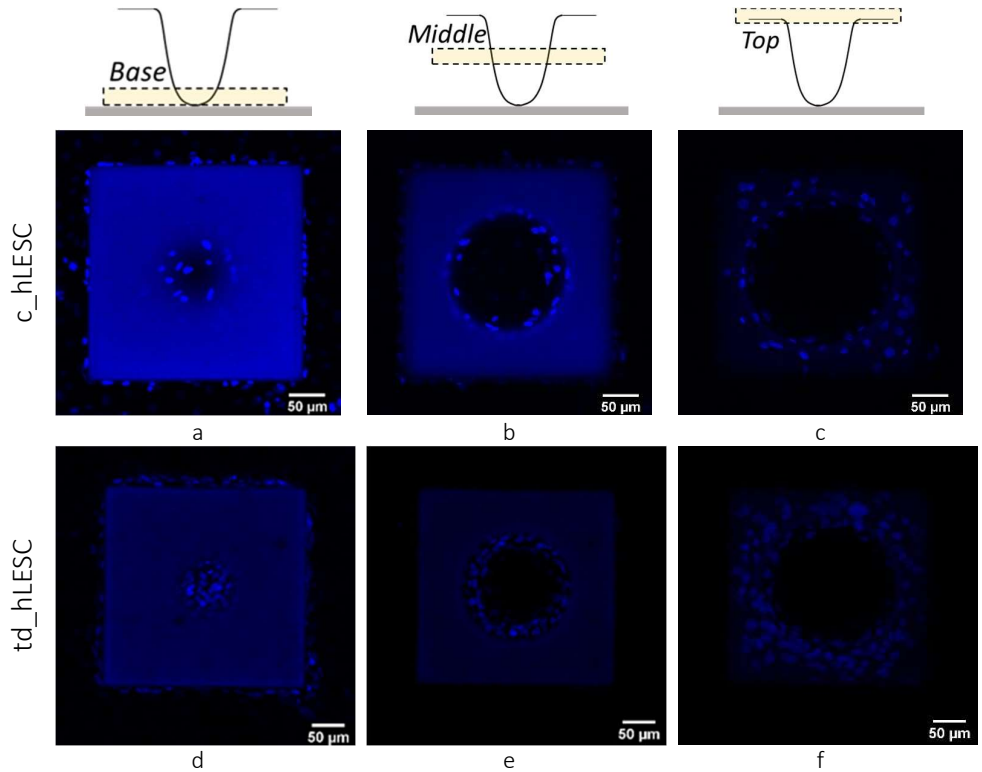


Figure 6.9: Z-stack confocal images of Hoechst-stained hLESCs. (a-c) c_hLESCs and (d-f) td_hLESCs at the bottom, middle, and top of the scaffolds. Cells are distributed along the scaffolds.

6.3.3.2 Second strategy: cells outgrown from the biopsy

The second strategy investigated the ability of cells outgrowing from the biopsy to colonise the scaffolds. The biopsy was placed close to the 3D-niche like structure. After a few days, depending on the dimensions of the biopsy, cells began migrating from the biopsy towards the scaffold (figure 6.10 a,b), and colonized the scaffold (figure 6.10 c-f). The Hoechst staining indicated that cells were distributed along the z-axis (figure 6.11). As for the first strategy, the cells did not stratify.

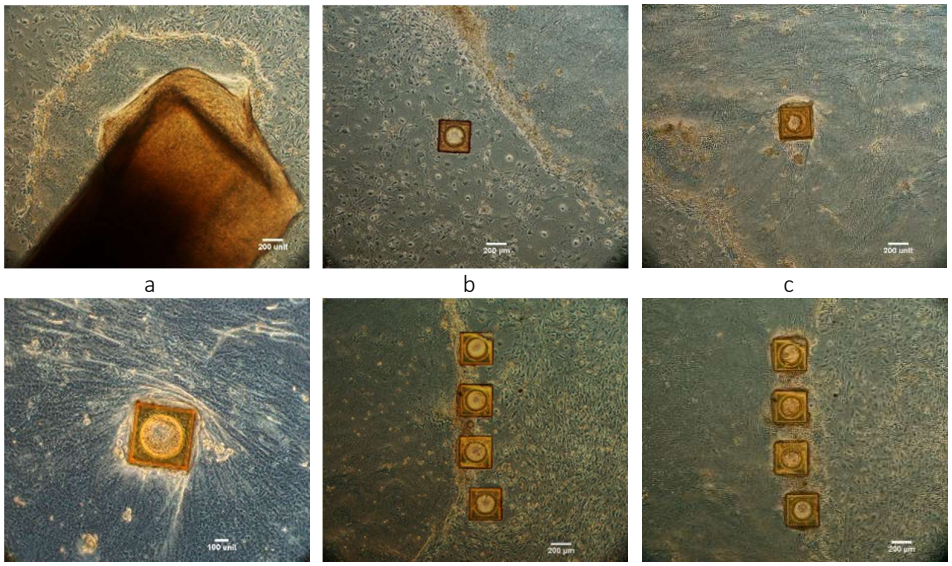
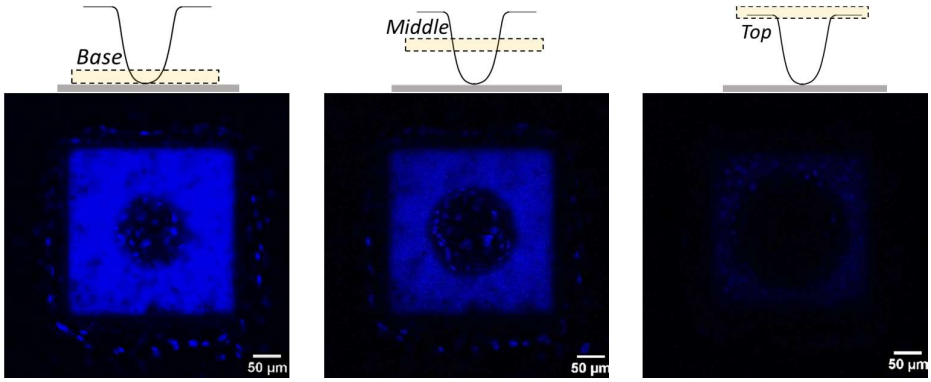


Figure 6.10: Cell migration from a limbus biopsy towards the scaffold. (a-d) first donor; (e,f) second donor. (a,b,e) Limbal cells started migrating towards the scaffolds; (c,d,f) after a few days, the cells approached the scaffolds, and covered their entire surface.



a b c

Figure 6.11: Z-stack confocal images of Hoechst-stained cells for the second strategy. Cells were distributed along the z-axis of the scaffolds.

6.3.4 Cells differentiated according to z-position

Cell differentiation was studied along the z-axis of the 2PP printed niche structure. The commercial cells showed a marker zonation (figure 6.12), presenting differentiated cells on the bottom (cytokeratin 3/12 marker, labelled in green), and stem cells on the top (cytokeratin 14 marker, labelled in red). The number of differentiated cells, and the z-point where the cells start expressing stem cell marker varied between samples.

A comparable result was obtained by using the primary cells extracted from the limbus and cultivated on a 3T3 feeder layer (figure 6.13). Differentiated cells were detected on the bottom (cytokeratin 3/12 marker, labelled in green), and stem cells on the top (p63 marker, labelled in red). However, in this condition, a mixed population was more highlighted, and the signal less clear. Only in one scaffold, it was possible to detect stem cells both on the bottom and on the top of the scaffold, stained after 4 days (Appendix C).

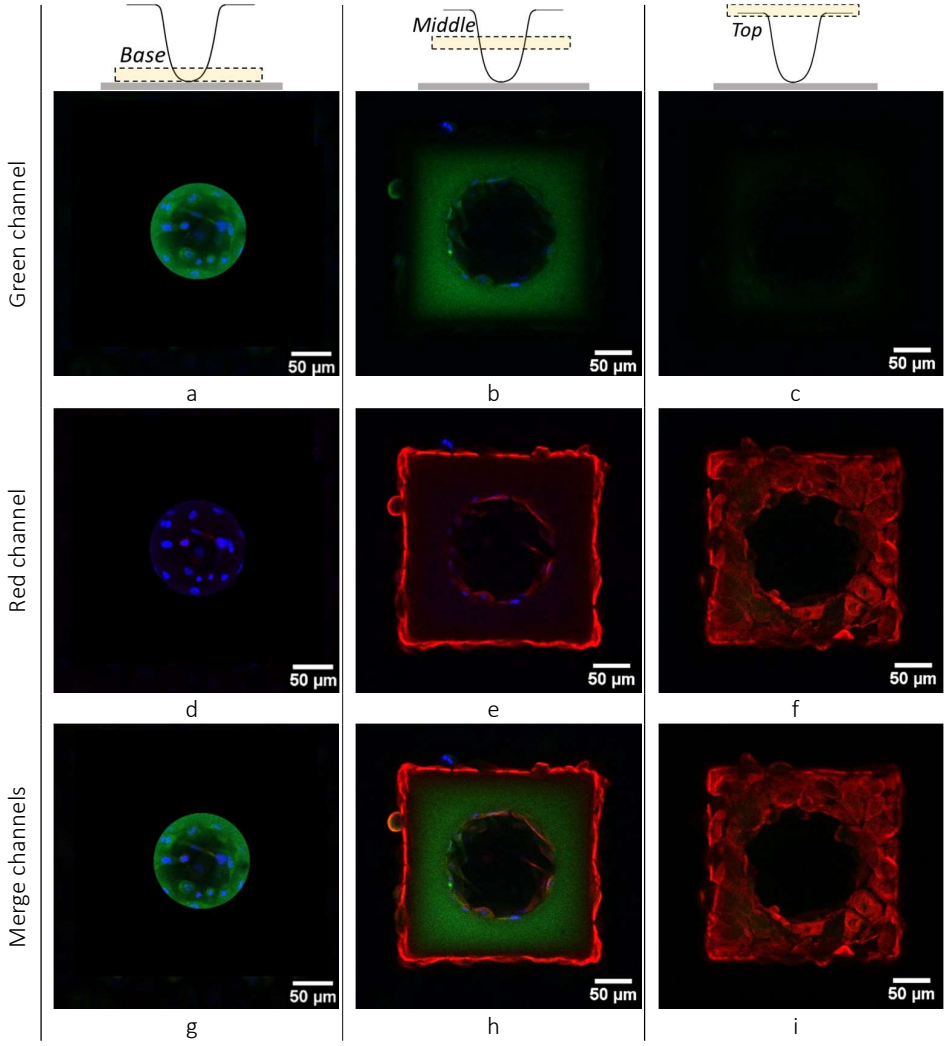


Figure 6.12: Series of confocal Z-stack images showing c_hLESCs seeded within the scaffolds, according to the first strategy (seeding cell suspension inside the niches). Three z-positions representing (a,d,g) the base, (b,e,h) the middle, and (c,f,i) the top of the scaffold are reported. Cells were stained with CK3/12 (green; differentiated cells), CK14 (red; stem cells) and Hoechst (blue; cell nuclei). (a-c) Green, (d-f) red and (g-i) merged channels are presented. The majority of the cells on the base expressed the differentiation marker, while at the top the majority expressed the stem cell marker. Images are representative of three independent experiments.

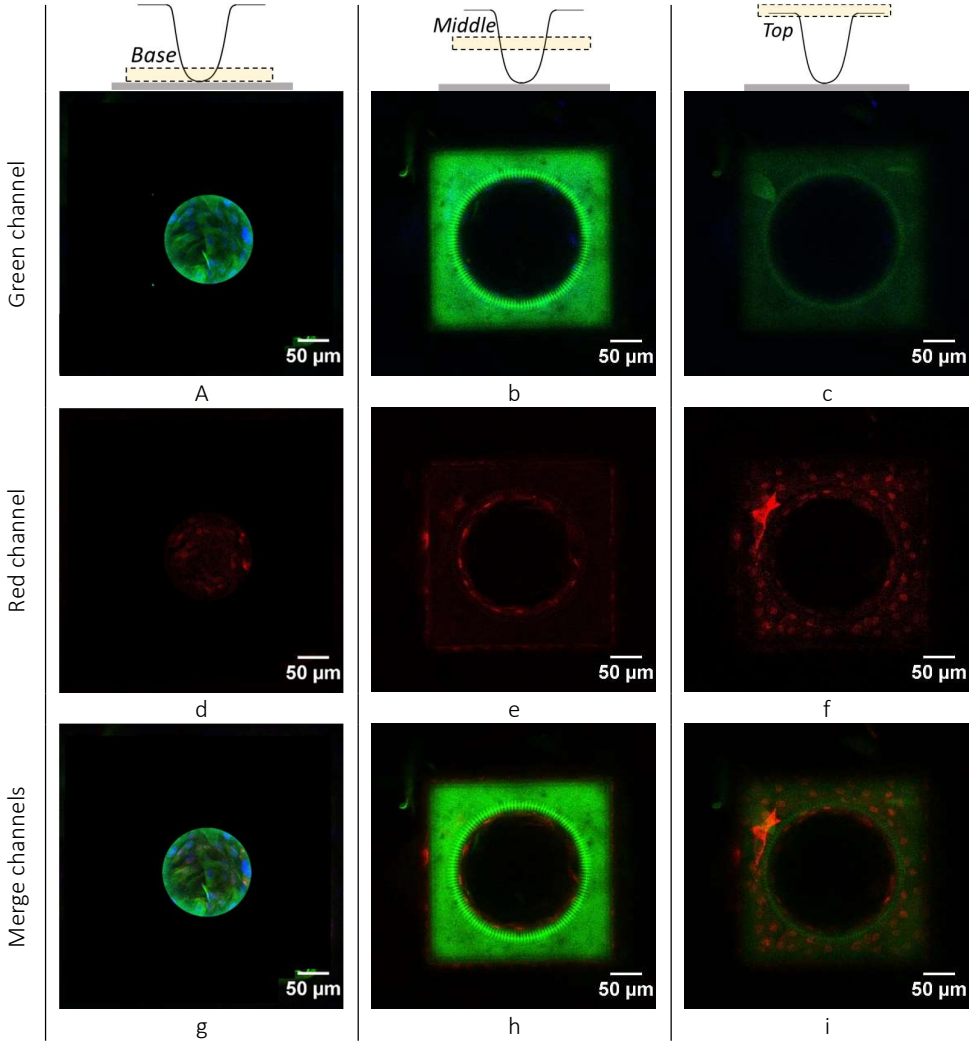


Figure 6.13: Series of confocal Z-stack images showing td_hLESCs seeded within the scaffolds, according to the first strategy (seeding cell suspension inside the niches). Three z-positions representing (a,d,g) the base, (b,e,h) the middle, and (c,f,i) the top of the scaffold are reported. Cells were stained with CK3/12 (green), p63 (red) and Hoechst (blue). (a-c) Green, (d-f) red and (g-i) merged channels are presented. The majority of the cells on the base expressed the differentiation marker, while on the top the majority expressed the stem cell marker. Images are representative of two independent experiments obtain by two biopsy.

6.3.5 Cells did not differentiate on micro-scaffolds with increased stiffness

To study the stiffness distribution along the z-axis, AFM analysis was conducted. Due to the limitation in the z-indentation of the tip, the base of the scaffold was not accessible and its properties could not be measured. For this reason, the properties of the base were measured on a flat scaffold, with the same printing parameters used for the base incorporated in the crypt scaffold. The results indicated that the top the scaffold was stiffer than the bottom, presenting an average of 64.3 kPa ± 34.7 and 15.5 kPa ± 9.5, respectively (figure 6.14).

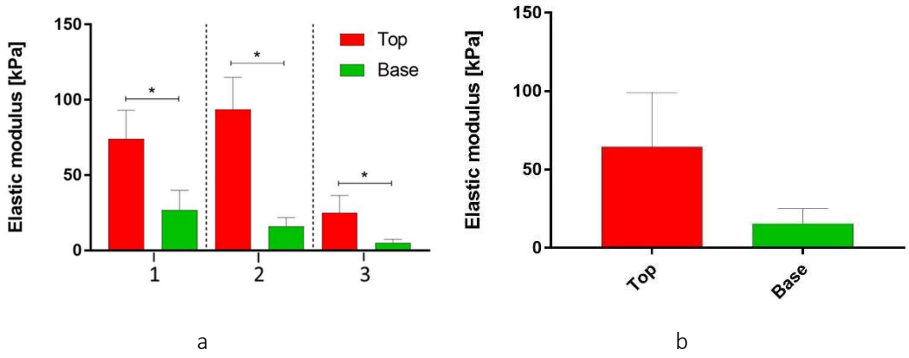


Figure 6.14: Surface elastic modulus of the scaffold according to the z-position. (a) Elastic modulus by AFM indicated that the stiffness at the top (red bar) was higher than the base (green bar) for all the experiments (experiment 1, 2, 3). (b) Average and standard deviation of the three experiments are presented (n=3). One-way ANOVA with post-hoc Tukey's test (*p≤0.05).

To understand if the z-position could affect the cell differentiation, two flat scaffolds with different heights, 20 (Elastic modulus = 4.9 kPa ± 2.5) and 200 µm (Elastic modulus = 28.7 kPa ± 7.2), were produced, and hLESCs were seeded onto them. Immunostaining and confocal images were performed as before. The results indicated that the cells expressed stem cell marker on both materials, independently of height and therefore the stiffness (figure 6.15).

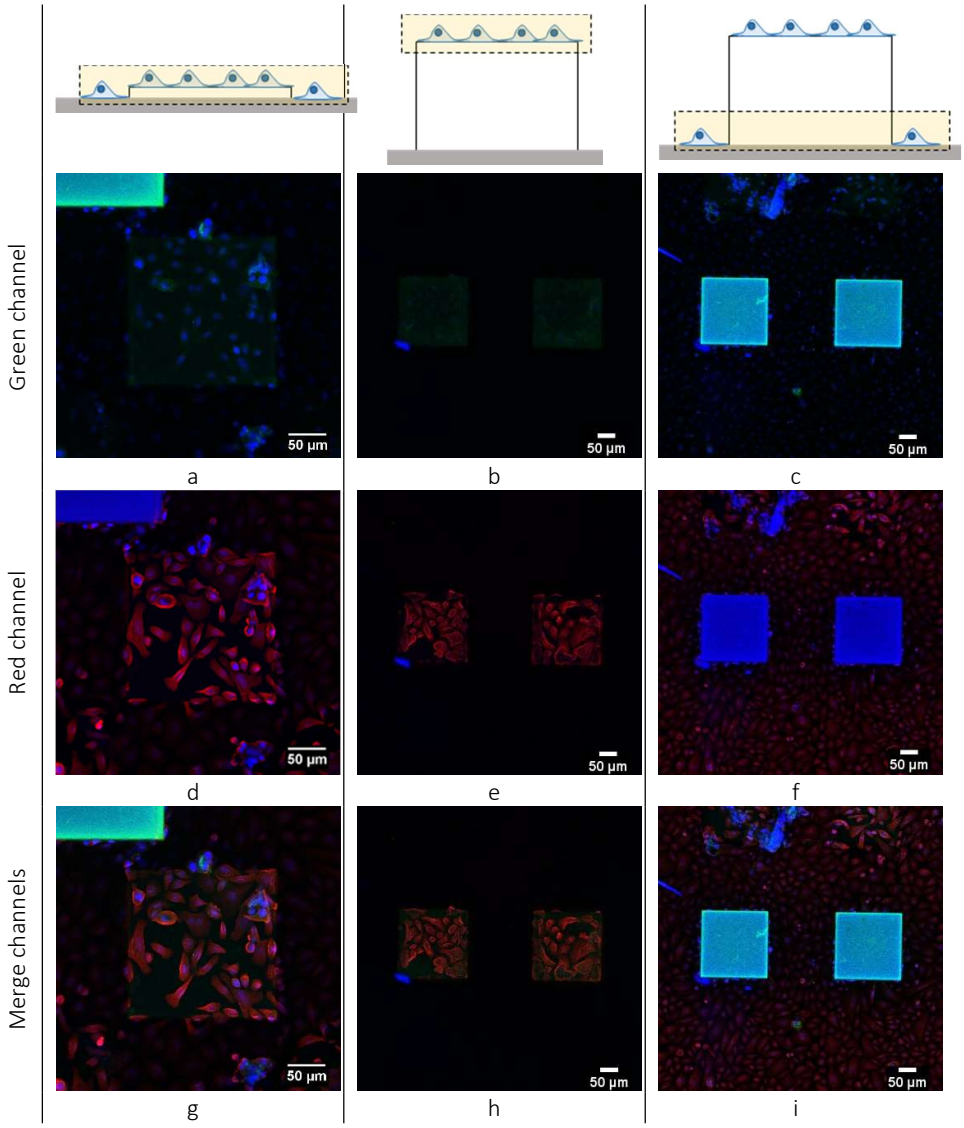


Figure 6.15: Confocal images of c_hLESCs on flat surfaces stained with CK3/12 (green; differentiated cells), CK14 (red; stem cells) and HOECHST (blue; cell nuclei). Cells were seeded on (a,d,g) flat scaffolds 20 µm in height and (b,e,h) 200 µm in height and (c,f,i). Green, red and merged channels are presented in the first (a-c), second (d-f) and third row (g-i), respectively. All the cells in these three conditions expressed the stem cell marker.

6.3.6 Effect of hypoxic environment on c_hLESC differentiation within the 2PP printed crypt shaped scaffolds

After cell seeding, the scaffolds were cultured in hypoxic conditions for 4 and 10 days. After fixing and staining the cells, the results indicated that the majority of

the cells on the base and on top of the scaffold expressed stem cell markers, independently from the z-position (figure 6.16). More experiment are needed to confirm these findings.

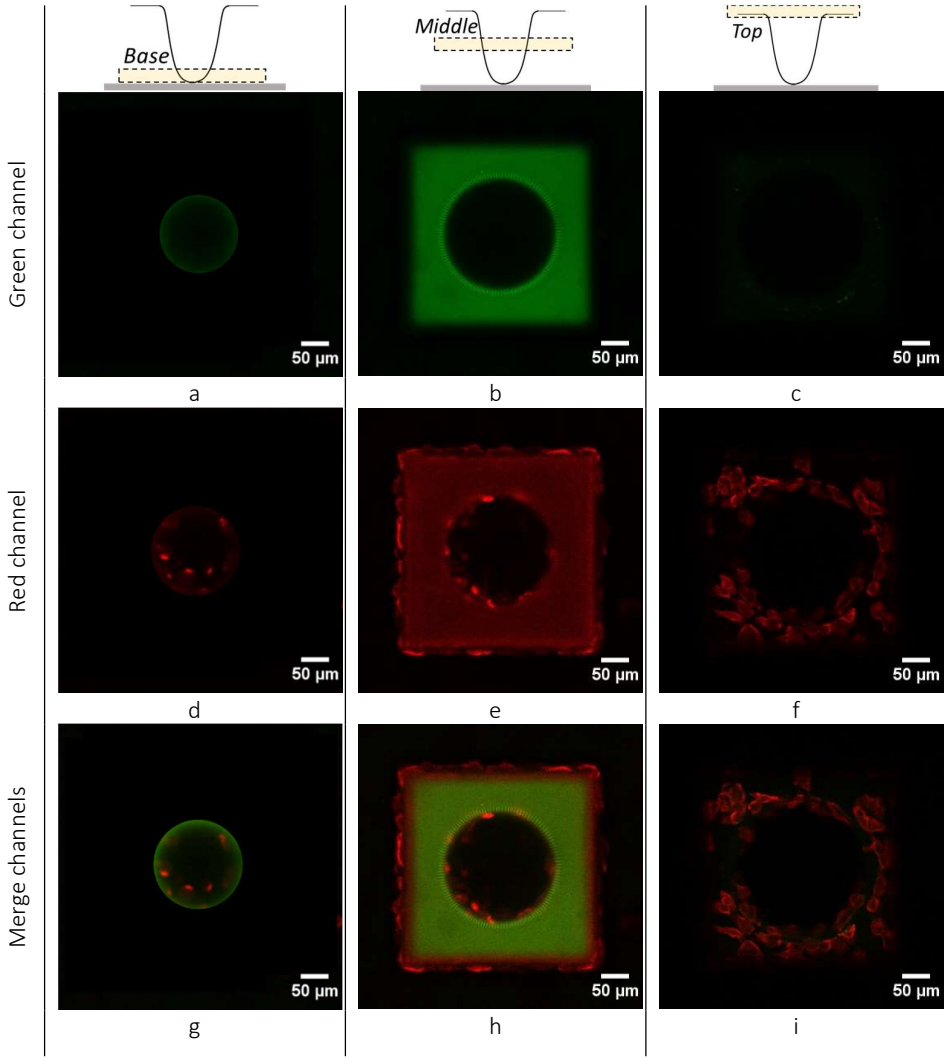


Figure 6.16: Series of confocal Z-stack images showing c_hLESCs seeded within the 2PP printed crypt shaped scaffolds, cultured in hypoxic condition and fixed after 10 days. Three z-positions representing the base (a,d,g), the middle (b,e,h) and the top (c,f,i) of the scaffold are reported. Cells are stained with CK3/12 (green), CK14 (red) and Hoechst (blue). Green, red and merged channels are presented in the first (a-c), second (d-f) and third row (g-i), respectively. The majority of the cells on the base and on the top of the scaffold expressed the stem cell marker. No cells expressing the differentiation marker CK3/12 were visualized.

6.4 Discussion and conclusion

In chapter 3, GelMA stiffness was investigated and compared to the stiffness of the human corneal tissue. In chapter 5, a biocompatible scaffold mimicking the precise structure of limbal epithelial stem cell niches was developed using a Two-Photon Polymerization system (2PP). The experimental work described in this chapter aimed at evaluating the influence of the GelMA stiffness and the precise geometry of the epithelial stem cell niche, without the use of signalling molecules, on stem cell differentiation in an *in vitro* system. The chapter was divided in two sections: in the first part, c_LESCs were seeded onto macro-scaffolds (flat gels crosslinked by UV-light), marker expression was monitored by confocal microscope and gene expression was evaluated by qPCR in normoxia, hypoxia and by using a differentiation media. In the second part, c_LESCs and td_LESCs were seeded inside the scaffolds mimicking the niches. Marker expression was monitored by confocal microscopy. Furthermore, to have a better understanding of the key factors that may have an impact on the differentiation process, cells were cultured in hypoxic conditions. Appendix D explores the use of nanosensors as an innovative technique to obtain a point-by-point characterization of the investigated scaffolds. As a proof of concept, pH-nanosensors were employed with the future aim to translate this technique to oxygen nanosensors.

Commercial cells were grown on a flat GelMA substrate produced at different stiffness values to understand if it was possible to control the cell differentiation process by changing this parameter. Overall, there was no clear trend due to the

variation of the stiffness. The analysis of the cells by confocal microscopy indicated that G25 was the material with the highest number of differentiated cells, but the increase was not significant. However, by using a differentiation media, this effect was enhanced, and the number of differentiated cells was significantly higher on G15 and G25 with respect to G5 and G40. These concentrations may represent the "sweet spots", and the elastic modulus obtained, between 80 - 260 kPa, may be a good range for further investigation. These results suggest that cells did not differentiate on soft materials, with stiffness values similar to those measured in the limbus, and on stiffer substrates, away from physiological values. Although it is known that the stiffness has an effect on cell differentiation, a well-defined range that gives an *in vitro* cell response, especially in the limbus area, has not been identified yet. Foster et al. (2014) found a difference in the localization of the Yes-associated protein (Yap), a transcriptional co-activator shown to mediate cellular response to mechanical stimuli, by using collagen scaffolds with a difference in stiffness between 65.3 and 15.3 kPa. However, a difference in the expression of cytokeratin 3 was also detected between 2900 Pa and 3 Pa collagen gels (Chen *et al.*, 2012). Moreover, it has been shown that changes in gene expression were only marginal between 40 kPa and 130 kPa, while significant modulations were seen on materials with non-physiological elasticity (1.74 MPa) (Moers *et al.*, 2013). It is important to note that cells from different species were used in these experiments. Additionally, media were prepared by following different protocols. The incorporation of growth factors is an essential aspect of the cell differentiation process (Sidney *et al.*, 2015). For example, some studies

incorporated insulin-like growth factor-I (IGF-I) that has been shown to induce the differentiation of LESCs into cells expressing the differentiated corneal cell marker, cytokeratin K12 (Trosan *et al.*, 2012).

Another aspect that is often underestimated or not fully explored is the role of oxygen tension on cell differentiation. Usually, cell lines and stem cells are cultured under ambient oxygen concentrations without paying attention to the metabolic milieu of the niche in which they grow *in vivo*. Many studies have focused on the identification of growth factors and signalling proteins (Scadden, 2006) rather than investigating hypoxic environments. Normoxia is usually defined by conventional standards of cell-culture practice, considering an oxygen tension of 20%. However, the level of oxygen may vary drastically depending on the tissue, and the correct identification of the actual oxygen concentration is not yet clarified, especially in the stem cell niche environment. For example, a study showed that Oct4 and Notch signalling, two important regulators of stemness, are activated by hypoxia (Simon and Keith, 2008), but there is no clear understanding of the impact of oxygen level variation on stem cell differentiation and proliferation (Wang *et al.*, 2016; Nakajima and Takeda, 2014).

In this chapter, normoxic and hypoxic conditions were defined as 20% O_2 and 5% O_2, respectively, and the effect of oxygen concentration on cell phenotype was studied when cells were cultured on substrates of different stiffness. At the gene level, qPCR confirmed the results obtained by confocal microscopy, highlighting that the use of differentiation media increased the expression of the

differentiated phenotype, compared to the use of basal media. The stiffness of the culture substrate did not have an impact. However, the cells cultured in hypoxia presented a lower level of KRT3 gene expression, compared to cells cultured on the corresponding gel in normoxia. Nevertheless more replicates are necessary, as the standard deviation was high and it affected the statistical significance. Overall, the results indicated that the soluble factors, provided by the media, and the oxygen tension of the culture environment were the main drivers of LESC differentiation, while stiffness played a secondary role. However, to confirm this finding, it will be necessary to expand the number of gene screened to a larger panel.

In the second part of the experimental work presented in this chapter, LESCs were cultured inside the niches in xeno-free conditions and in serum containing media on feeder layers. Since the pioneering work of Pellegrini et al. (1997), the most adopted technique to culture limbal stem cells is the use of a layer of mouse fibroblasts in combination with a serum containing-media for cell expansion. The most widely used culture media contains a number of ingredients derived from animal sources such as adenine, cholera toxin, hydrocortisone and triiodothyronine. However, to reduce the risk of disease transmission, tumorigenesis, and immunologic rejection, in the last few years new protocols have been explored. They involved the removal of the mouse feeder-layer, or the development of animal-free media (Lu *et al.*, 2012; Lekhanont *et al.*, 2009; Yu *et al.*, 2016). The use of xeno-free alternatives has a great advantage especially for clinical translation (Zakaria *et al.*, 2014).

In this chapter, both techniques were investigated. The CnT-Prime media was used for xeno-free culture. It has been used successfully with feeder layers (Meyer-Blazejewska *et al.*, 2010), and with isolated and frozen cells (Yamamoto *et al.*, 2010), demonstrating its ability to be used as a limbal stem cell media. However, there is not enough literature to have a clear understanding of its performance in comparison with other media (Zakaria *et al.*, 2010; González *et al.*, 2017). The major difference that was found in the present work, in accordance with the literature, is related to the formation of colonies. Following the protocol of Pellegrini et al., the cells extracted from the limbus were cultivated on a feeder layer of irradiated 3T3. This technique enhanced the growth of the keratinocytes in characteristic clonal types, including holo-, mero- and paraclones. In a cell population, the presence of holoclones, described as large round colonies with smooth and regular borders formed entirely by small cells with scarce cytoplasm, are an indication of limbal stem cells. LESCs isolated from the limbal crypts generated the highest proportion of holoclones demonstrating their stem cell-like characteristics (Dziasko *et al.*, 2014). Conversely, in the xeno-free system, the LESCs were maintained without the feeders, and they grew as homogeneous monolayers of single-cells, without the presence of colonies. For this reason, the number of limbal stem cells was quantified by immunohistochemistry. Even if the existence and proliferation of LESCs in the limbus is now accepted within the research and clinical communities, their precise distribution in this anatomically segregated region is still debated because of the lack of unequivocal markers expressed by LESCs. In this chapter, the stem cell markers CK14, p63 and late stage differentiation

marker CK3/12 were used, since they are commonly used for the identification of LESCs and corneal cells (Dua *et al.*, 2006).

The cell distribution according to the geometry was investigated in both cell culture models, xeno-free and with serum containing-media and using a feeder layer. Both techniques showed that the cells can adhere and proliferate along the niches, and no stratification was detected. The stratification may be obtained by increasing the duration of cell culture or by introducing an air-liquid interface. *In vitro* studies, aiming at reconstructing the corneal epithelium, have shown that culturing cells at the air-liquid interface (air-lifting) resulted in stratification and differentiation of corneal epithelial cells (Proulx *et al.*, 2010; Ang *et al.*, 2010). However, in the compressed collagen model Real Architecture for 3D Tissue (RAFT), the proliferation rate and the percentage of stem cells was reduced even if higher levels of stratification were seen (Massie *et al.*, 2014). For this reason, and to ensure that cells were not forced to differentiate independently of the substrate stiffness, limbal stem cells were not exposed to airlifting.

When cells were cultured on the 2PP crypt scaffold, according to the first strategy (cell suspension seeded onto the 2PP scaffolds), cells showed a marker-zonation. Cells on the bottom of the scaffold expressed differentiated markers, while cells on top expressed stem cell markers. It is interesting to note that the results were confirmed in both culture systems: xeno-free media and commercially available cells and with primary cells in serum containing media

and on a feeder layer. Two markers were used to identify limbal stem cells, nuclear expression of p63 and cytoplasmic expression of CK3/12. In only one case, immunohistochemistry indicated that the majority of the cells on the base expressed stem cell markers, but the experiment lasted 4 days instead of 10 days. This might indicate that cell differentiation occurred later than day 4. Few other studies have attempted to replicate the limbal niche and tried to control the differentiation process by tuning the geometry (Ilida Ortega *et al.*, 2013; Levis *et al.*, 2010) but none of them replicated the shape described by Dua et al. (2010). Furthermore, none of the studies used Two Photon Polymerization techniques to produce the scaffolds.

The second strategy (cells outgrown from the biopsy) showed that, placing the biopsy close to the niche, cells migrated and populated the scaffold. However, immunocytochemistry results were inconclusive and cell stratification was not observed. Nevertheless, this technique holds great potential for therapy, and has already been applied for the expansion of limbal stem cells and adapted in conjunction with electrospun-scaffolds (Ortega *et al.*, 2014).

Overall, the results of the culture of LESCs in niches that mimic the precise *in vivo* geometry presented in this chapter have indicated that the geometry has an impact on the differentiation process of LESCs. It is important to highlight that in the literature, the role of geometry has not been fully investigated either in the limbus or specifically in other epithelial stem cell niches (such as the gut).

To create a condition closer to the *in vivo* situation, and to understand if the oxygen concentration could have a more relevant impact on cell phenotype, cell-seeded scaffolds were cultured in hypoxia conditions (Mohyeldin *et al.*, 2010). The preliminary results indicated that the oxygen level had an effect on the cell marker expression, 'forcing' cells at the base to express stem cell marker. This finding would be the basis for future work investigating the possibility to obtain stem cells at the base, and differentiated cells at the top. An interesting work showed that through an oxygen-controlled method, it was possible to produce corneal epithelial sheets expressing cytokeratin 3 and p63 at the suprabasal and basal layers, respectively. The cells were cultured under hypoxia for 5 days, where they proliferated mantaining the expression of stem cell marker. Then, the re-oxygenation (20% O_2) promoted cell stratification and differentiation (Nakajima and Takeda, 2014). This oxygen-controlled method could be investigated with the use of a 2PP system to induce cells to stratify and differentiate on top of the scaffold (Nakajima and Takeda, 2014)

To have a confirmation that the geometry alone had an impact on the differentiation, the stiffness at the top and at the base of the 2PP scaffold was measured by AFM. The probe scans the sample surface and measures the atomic forces between the probe sample and the surfaces (Stylianou and Andreas, 2017). In this mode the AFM probe is used as an indenter, which applies vertical forces ranging from μN to tens of pN (Roa *et al.*, 2011). AFM was performed because it allowed the measurement of the elastic modulus at the same length scales at which cells interact (Selhuber-Unkel *et al.*, 2010). Indeed, it was

possible to test hydrogels in a hydrated state to mimic the cell culture conditions. It has also been shown to be an appropriate technique to measure soft materials (Doube *et al.*, 2010; Isaksson *et al.*, 2010) in the micro- and nano-scale (Li and Bhushan, 2002). A significant number of studies have been published on the measurement of the bulk stiffness of hydrogel materials (Anseth *et al.*, 1996; Lee *et al.*, 2009), but only limited research has reported the use of nanoindentation as a strategy to measure the nanomechanical properties of hydrogels (McConney *et al.*, 2010), and in liquid conditions (Zhu *et al.*, 2011).

The AFM results presented in this chapter are reported as averages of three experiments, and as single values. Variations in the test results arose due to the use of different cantilevers, water conditions, and the presence of a soft material with a high degree of adhesion to the surface. All of these parameters are extremely important during measurement and may contribute to the errors in recording nanomechanical measurements (Oyen, 2014; Drira and Yadavalli, 2013). However, there was a clear difference in stiffness between the base and the top of the scaffold for all the experiments performed. It is important to mention that the z-stiffness was not planned and might have been influenced by the printing process; there are no studies that have correlated the stiffness to the z-position of the scaffold. It is interesting to note that the elastic moduli obtained (E_{base}=15.5 kPa ± 9.5 and E_{top}=64.3 kPa ± 34.7) were in the same order of magnitude of the cornea (7.5-110 kPa, (Last *et al.*, 2012)).

Culturing cells on the flat 2PP scaffold of different heights and therefore different stiffness did not show a difference in the cell differentiation. Therefore, this result confirms the role of the geometry on the stem cell differentiation.

Figure 6.17 and 6.18 summarize the results that may explain why the geometry had an impact on the differentiation process. It is possible that the peculiar shape aided the creation of a microenvironment based on cellular secretions inside the niche that enhanced cell differentiation at the base, and not at the top. Another factor that could have had an influence in this process, and that requires further investigation, was the environment at the base of the scaffold. Few cells were present after seeding and the scaffold configuration could have created a "stressful" environment for the cells. In previous articles (Eberwein *et al.*, 2011; Moers *et al.*, 2013) it has been hypothesised that such an environment, for example cells adhering on pillars separated by large distances (micro-patterns of 11 µm rather than 5 µm) or seeded on a non-physiological stiff material, can enhance the expression of late corneal markers. This hypothesis could explain the inversion of the marker expression that has been found in the present model.

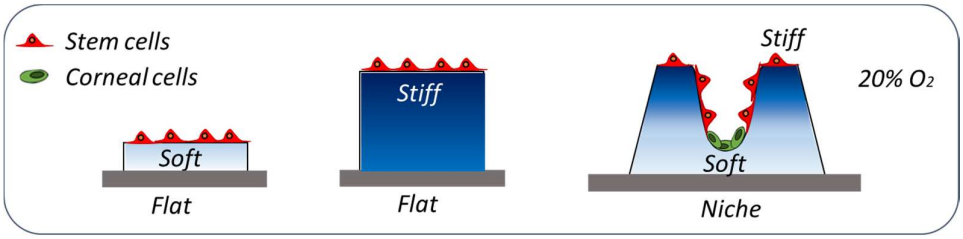


Figure 6.17: Representation of the results obtained by seeding LESCs inside the 2PP scaffold. Mechanisms involved in the limbal stem cell differentiation process. The geometry itself influences the cell differentiation process. The cells at the base of the scaffold express differentiation marker while cells on top express stem cell marker.

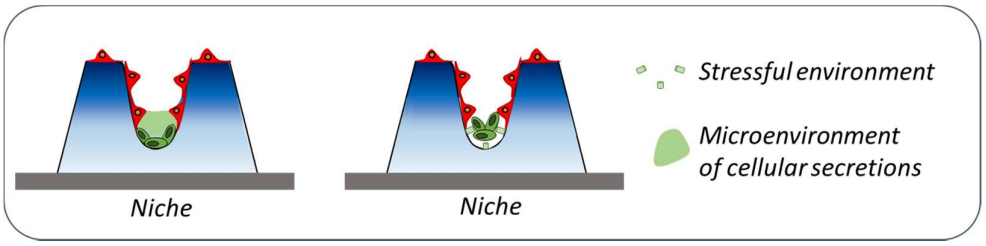


Figure 6.18: Representation of the mechanisms that could have been involved in the limbal stem cell differentiation process. The first hypothesis is that geometry is involved in the creation of a microenvironment of cellular secretion that is lost in flat scaffolds. The second hypothesis is that, differently from the top of the scaffold, the base presents a stressful environment. Both hypothesis, that need further investigation, could enhance the differentiation process at the base of the scaffold. Further investigation are required to understand the role of the oxygen concentration within the scaffold.

7. Summary, conclusion and future work

In the body, stem cells are located in unique microenvironments, called niches, where they can reside for an indefinite period of time and produce progeny cells whilst self-renewing (Ohlstein *et al.*, 2004). In the eye, niches are located within the limbus, an area between the cornea and the sclera, in anatomically defined structures called limbal stem cell crypts (LECs, Dua et al. 2005). After injury and during physiological turnover, limbal stem cells proliferate and differentiate into corneal epithelial cells while migrating to the centre of the cornea. The dimension of the LECs are approximately 200 µm where a cord of cells invaginates into the limbal stroma from the ridges located between the palisades of Vogt. The lack of this stem cell reservoir determines a pathology called limbal stem cell deficiency, that can be acquired or hereditary. According to data from the World Health Organization, the estimated number of people that suffer from corneal blindness is 4 million worldwide. However, only 100,000 corneal transplants are performed each year, primarily as a result of lack of access to suitable tissue (Whitcher *et al.*, 2001).

Scaffolds used for limbal stem cell expansion and transplantation currently used in clinics are generally taken from the amniotic membrane. Results obtained from randomized trials using this support are still controversial. The main

drawbacks are high inter and intra-biological variability and difficulty in the standardization of membrane preparation, thus making clinical output difficult to interpret (Rahman *et al.*, 2009).

To obtain a more reliable clinical outcome and to inform the design of novel scaffolds for cornea regeneration, understanding the mechanisms underpinning the differentiation process would represent a great advantage. Among the intrinsic and extrinsic factors that no doubt drive this process, the physical properties and the ECM architecture play an important role. Therefore, the overall hypotheses of this PhD was that the geometry and the stiffness of the LECs are key physical factors that influence stem cell phenotype and differentiation. The long-term vision of this thesis was the development of a new system for limbal stem cell transplantation with tunable mechanical properties and with a defined geometry mimicking the stem cell niche. Chapter 1 introduces the work by presenting the state of the art and the context of this thesis in three main aspects: (*i*) the limbus characteristics, (*ii*) the clinical context and the current solutions and (*iii*) the additive manufacturing techniques. In Chapter 2, the general materials and methods employed in this thesis are described. The results are presented starting from Chapter 3. In Chapter 3, the elastic modulus of scaffolds prepared by varying the percentage of GelMA was investigated. GelMa is obtained from gelatin, which is denatured collagen, it is the most abundant structural protein in the cornea, and is stable at 37°C upon UV and IR crosslinking. The results were compared to the bulk stiffness of the *ex-vivo* cornea obtained by rheological analysis and compression testing and to the surface stiffness from values obtained in the literature. Among the gels

investigated, those with a concentration between 5% and 15% (w/v) exhibited mechanical properties in the same order of magnitude of the cornea. The advantages of using hydrogels and in particular GelMA include the high water content comparable to soft tissues (Cushing and Anseth, 2007) and the presence of RGD-motifs that allow cells to adhere to the material directly without any surface functionalization. In addition, it was possible to modulate the stiffness by changing the GelMA concentration without altering the chemical factors (Nichol et al., 2010). The use of UV-light in the production of the macro-scaffolds (d = 8 mm and h = 1 mm) represented a fast system to develop solid-like gels. However, the geometry could not be controlled. Among additive manufacturing techniques, inkjet and 2PP systems were investigated with the aim of obtaining a precise geometry as observed and measured from histological sections. Inkjet printing is a quick, versatile, one-step technique, allowing great control over the deposition pattern (Gudapati *et al.*, 2016). Although with this technique it was possible to develop a 3D architecture with a stiffness gradient, its resolution was not sufficient to obtain a structure with dimensions comparable to the *in vivo* limbal stem cell niche. For this reason, the 2PP system was chosen as a more suitable printing technology. To use the 2PP system in combination with hydrogels, it is necessary to have a photoinitiator that can be activated by 2PP at a wavelength of 780 nm. In addition, it has to be water soluble and exhibit a high initiating efficiency to form radicals. However, the majority of current commercial photoinitiators do not present these characteristics (Schafer *et al.*, 2004). In the last few years, with the increased use of 2PP systems in biomedical applications, the number of research groups that have started to develop novel

photoinitiators (PI) appropriate for hydrogels has increased. However, at the moment, very few PI can be used for this application (Li *et al.*, 2013), and there is still a gap that needs to be filled.

The hypothesis investigated in Chapter 4 was that riboflavin is a suitable PI with excellent biocompatibility properties (Nguyen *et al.*, 2014). It has the advantage of being already used in ophthalmology to increase the strength of the cornea and the thickness of the collagen fibres, in conjunction with UV-A treatment (Labate *et al.*, 2015; Wollensak *et al.*, 2003; Raiskup and Spoerl, 2013). To test its properties as a PI, a flat, macro-scaffold was produced. Although some interesting results were obtained, the limitations, mainly due the amount of time required to crosslink GelMA and the weakness of the resultant gels compared to the standard PI (Irgacure), makes riboflavin unsuitable for use as a PI with UV light. In addition, riboflavin also proved to be inefficient at the 780 nm wavelength, which is used in the 2PP system. Therefore, it was not pursued and, as an alternative, P2CK was used for the remainder of the thesis. It is a novel PI first synthesised and reported by Vienna University of Technology (Li *et al.*, 2013).

In Chapter 5, the aim was the development of a 3D scaffold that mimicked the geometry of the native LEC as described by Dua et al. (2005). Primarily, the printability of PI and GelMA was tested by varying their concentrations. After this optimization step, a scaffold with a precise geometry was printed. Few studies that have tried to replicate the shape of the limbal niche (Ilida Ortega *et*

al., 2013; Levis *et al.*, 2013) but without the resolution and/or the enclosed structure produced in this thesis project. Moreover, the idea to produce this scaffold as a "plug" for cellular therapy and not as a complete scaffold to cover the cornea has not been explored yet. In addition to replicating the accurate geometry, two innovative strategies were investigated to obtain a scaffold with a variable stiffness, since there is evidence of the presence of a stiffness gradient between the limbus and the cornea, which can drive the differentiation process (Foster et al., 2014). The first strategy was achieved by increasing the hatching distance (distance between each layer during the 2PP printing process). The second strategy involved the use of two materials, GelMA and GelMA-PEGDA. The addition of PEGDA increased the elastic modulus of GelMA and reduced its susceptibility to enzymatic degradation, a physiological mechanism that occurs in the wound bed (Spoerl *et al.*, 2004; Ma *et al.*, 2010). Initially the cell response to the scaffold was tested with immortalized corneal epithelial cells, showing cell attachment and proliferation along the z-axis. Throughout the thesis, macro-scaffolds (d = 8 mm and h = 1 mm) were produced and tested to support the results obtained for the micro-scaffolds (d = 300 µm and h = 200 µm). In Chapter 6, the macro-scaffolds with a tunable stiffness and the micro-scaffolds with a precise geometry were tested with primary human limbal epithelial cells. The hypothesis was that the stiffness and the geometry would be able to maintain the stem cell phenotype and the differentiation process. In addition to these physical factors that have been extensively discussed in the previous chapters, the influence of oxygen tension and the use of chemical defined differentiation media was tested to understand the key points underpinning the differentiation

process. By increasing the stiffness, no clear trends were found in the results neither in the expression of cytokeratin (CK3/CK14, stem cell marker, and CK14, differentiation marker) nor in the gene expression (KRT3 and KRT19). However, the use of the defined media enhanced the differentiation process and increased expression of CK3/CK14 and gene KRT3 was observed. Although not significant, a difference in the gene expression KRT3 was found between normoxic and hypoxic conditions. Considering all the results, hypoxia seems to have a greater influence on stem cell differentiation than the substrate stiffness.

The results obtained by analysing the micro-scaffolds, produced by 2PP, indicated that the geometry itself plays a role in the differentiation process with differentiated cells identified at the base and cells on the top expressing stem cell markers. To better understand the factors that could have contributed to this outcome, the effects of stiffness and oxygen were investigated in combination. The stiffness calculated by AFM indicated that the base of the scaffold was softer (15.5 kPa ± 9.5) compared to the top (64.3 kPa ± 34.7). However, no difference was observed in the expression of the differentiation marker. In agreement with the results obtained for the macro-scaffolds, produced by UV-laser, it proved that the stiffness did not play a determinant role in this process. These results are in disagreement with recent literature (Foster *et al.*, 2014; Jones *et al.*, 2012), however, the difference between the stiffness values reported in these papers and in the present thesis could have influenced this outcome. Interestingly, the use of an atmosphere at 5% O_2 showed that the bottom of the scaffold presented an increased number of stem cells. These

results could represent the starting point for the investigation of oxygen-controlled methods inducing cells to stratify and differentiate on top of the scaffold.

- Specific conclusions about the work presented in ths thesis are the following: GelMA showed to be a good candidate as limbal epithelial carrier.
- Riboflavin did not allow GelMA to be crosslinked by IR.
- Geometry to mimic LECs can be developed by 2PP.
- 2PP structures can be printed with the combination of two materials in two consecutive steps
- No difference in the gene and marker expression was detected in the range of surface stiffness of 4.5-335.6 kPa.
- Gene (KRT3, cornea cells) expression was enhanced in normoxic condition (rather than hypoxia) and by the use of differentiation media.
- Limbal stem cells, cultured with and without a feeder layer, showed a marker-zonation depending on the geometry.

Overall, the hypotheses of this thesis were partially confirmed. It could not be proven that an increase in the gel stiffness would allow the control of LESC differentiation. However, the thesis results demonstrated the influence of the geometry on stem cell differentiation without the use of signaling molecules.

The 2PP approach is flexible and could be applied to the generation of stem cell niches of other tissues and as such, could represent a significant advance in regenerative medicine. For example, this technology would allow to print chemical gradients and to study their influence on LESC phenotype; an example

is the investigation of the influence of tenascin-C, since it has been reported that it is expressed in the limbus but not in the cornea (Yeung, 2008).

Future work

A key aspect of this research was the development of the micro-scaffold modelling the native shape and dimensions of the LEC. An obstacle that was encountered was related to the high autofluorescence of the scaffold, resulting from the presence of the P2CK PI. Overcoming this issue would allow obtaining less signal background during confocal imaging and more reliable results when used in combination with oxygen nanosensors. The autofluorescence was mainly due to the photoinitiator and not the GelMA. Therefore one possible solution could be to investigate the use of LAP photoinitiator (lithium phenyl-2,4,6-trimethylbenzoylphosphinate), which presents an absorbance peak that could be suitable for 2PP (365nm), biocompatible and water soluble. Cell seeding and analysis of the subsequent cell behaviour by techniques such as flow cytometry and qPCR was unsuitable due to the micrometric dimension of the scaffolds. In future investigations, the use of optical tweezers and cell tracking could be more better methods for precise cell seeding and monitoring of cell differentiation and migration within the niche. In addition, it would be interesting to print the scaffold on a support, such as a thin film, which would facilitate the execution of the tests and in a future perspective to aid the handling of the scaffold during surgery for clinical use. A technique could be the spincoating of a thin GelMA film on a coverglass before printing.

Regarding the macro-scaffolds and the stiffness impact on the cell differentiation, future work should focus on extending the study on a wider stiffness range. The qPCR analysis should include more replicates, and investigate the expression of more genes, such as KRT14, the gene encoding the CK14 cytokeratin that was detected by confocal microscopy. Moreover, it would be interesting to extend the investigation of the role of hypoxia associated with the presence of ECM. The use of the incubator at a definite 0_2 concentration is an easy and established method to control the environmental conditions. A precise tool to detect the effective oxygen concentration that could distinguish the oxygen lever point-by-point along the scaffold structure would be more appropriate, for example by using nano-oxygen probes or oxygen nanosensors.

References

Abahussin, M., Hayes, S., Knox Cartwright, N.E., Kamma-Lorger, C.S., Khan, Y., Marshall, J., Meek, K.M. (2009) 3D collagen orientation study of the human cornea using X-ray diffraction and femtosecond laser technology. *Investigative ophthalmology & visual science*. **50**(11), 5159–64.

Aghamohammadzadeh, H., Newton, R.H., Meek, K.M. (2004) X-Ray Scattering Used to Map the Preferred Collagen Orientation in the Human Cornea and Limbus. *Structure*. **12**(2), 249–256.

Ahearne, M., Yang, Y., Then, K.Y., Liu, K.K. (2006) Mechanical characterisation of UVA-riboflavin crosslinked collagen hydrogels. *European Cells and Materials*. **11**(SUPPL.2), 72.

Alekseeva, T., Hadjipanayi, E., Abou Neel, E.A., Brown, R.A. (2012) Engineering stable topography in dense bio-mimetic 3D collagen scaffolds. *European Cells and Materials*. **23**, 28–40.

Ali, M., Pages, E., Ducom, A., Fontaine, A., Guillemot, F. (2014) Controlling laser-induced jet formation for bioprinting mesenchymal stem cells with high viability and high resolution. *Biofabrication*. **6**(4), 45001.

Ang, L.P.K., Tanioka, H., Kawasaki, S., Ang, L.P.S., Yamasaki, K., Do, T.P., Thein, Z.M., Koizumi, N., Nakamura, T., Yokoi, N., Komuro, A., Inatomi, T., Nakatsukasa, M., Kinoshita, S. (2010) Cultivated human conjunctival epithelial transplantation for total limbal stem cell deficiency. *Investigative Ophthalmology and Visual Science*. **51**(2), 758–764.

Anseth, K.S., Bowman, C.N., Brannon-peppas, L. (1996) REVIEW Mechanical properties of hydrogels and their experimental determination. *Biomaterials*. **17**(17), 1647–1657.

Armstrong, J.P.K., Burke, M., Carter, B.M., Davis, S.A., Perriman, A.W. (2016) 3D Bioprinting Using a Templated Porous Bioink. *Advanced Healthcare Materials*. **5**(14), 1724–1730.

Barnes, Hutton, Walters (1989) *An Introduction to Rheology*.

Barron, J.A., Wu, P., Ladouceur, H.D., Ringeisen, B.R. (2004) Biological laser printing: A novel technique for creating heterogeneous 3-dimensional cell patterns. *Biomedical Microdevices*. **6**(2), 139–147.

Basu, S., Mohamed, A., Chaurasia, S., Sejpal, K., Vemuganti, G.K., Sangwan, V.S. (2011) Clinical outcomes of penetrating keratoplasty after autologous cultivated limbal epithelial transplantation for ocular surface burns. *American journal of ophthalmology*. **152**(6), 917–924.e1.

Bath, C., Yang, S., Muttuvelu, D., Fink, T., Emmersen, J., Vorum, H., Hjortdal, J., Zachar, V. (2013) Hypoxia is a key regulator of limbal epithelial stem cell growth and differentiation. *Stem Cell Research*. **10**(3), 349–360.

Bertassoni, L.E., Cardoso, J.C., Manoharan, V., Cristino, A.L., Bhise, N.S., Araujo, W. a, Zorlutuna, P., Vrana, N.E., Ghaemmaghami, A.M., Dokmeci, M.R., Khademhosseini, A. (2014) Direct-write bioprinting of cell-laden methacrylated gelatin hydrogels. *Biofabrication*. **6**(2), 24105.

Bertassoni, L.E., Cecconi, M., Manoharan, V., Nikkhah, M., Hjortnaes, J., Cristino, A.L., Barabaschi, G., Demarchi, D., Dokmeci, M.R., Yang, Y., Khademhosseini, A. (2014) Hydrogel bioprinted microchannel networks for vascularization of tissue engineering constructs. *Lab Chip*. **14**(13), 2202–2211.

Bertolotti, S.G., Previtali, C.M., Rufs, a. M., Encinas, M. V. (1999) Riboflavin/Triethanolamine as Photoinitiator System of Vinyl Polymerization. A Mechanistic Study by Laser Flash Photolysis. *Macromolecules*. **32**(9), 2920–2924.

Brahimi-Horn, M.C., Pouysségur, J. (2007) Oxygen, a source of life and stress. *FEBS Letters*. **581**(19), 3582–3591.

Bryant, S.J., Nuttelman, C.R., Anseth, K.S. (2000) Cytocompatibility of UV and visible light photoinitiating systems on cultured NIH/3T3 fibroblasts in vitro. *Journal of Biomaterials Science, Polymer Edition*. **11**(5), 439–457.

Van Den Bulcke, A.I., Bogdanov, B., De Rooze, N., Schacht, E.H., Cornelissen, M., Berghmans, H. (2000) Structural and Rheological Properties of Methacrylamide Modified Gelatin Hydrogels. *Biomacromolecules*. **1**(1), 31–38.

Burnham, N.A., Chen, X., Hodges, C.S., Matei, G.A., Thoreson, E.J., Roberts, C.J., Davies, M.C., Tendler, S.J.B. (2003) Comparison of calibration methods for atomic-force microscopy cantilevers. *Nanotechnology*. **14**(1), 1–6.

Buxboim, A., Ivanovska, I.L., Discher, D.E. (2010) Matrix elasticity, cytoskeletal forces and physics of the nucleus: how deeply do cells 'feel' outside and in? *Journal of Cell Science*. **123**(3), 297–308.

Capella, J.A., Kaufman, H.E. (1969) Human corneal endothelium. *Documenta Ophthalmologica*. **26**(1), 1–8.

Castro-Muñozledo, F., Gómez-Flores, E. (2011) Challenges to the study of asymmetric cell division in corneal and limbal epithelia. *Experimental Eye Research*. **92**(1), 4–9.

Catros, S., Fricain, J.-C., Guillotin, B., Pippenger, B., Bareille, R., Remy, M., Lebraud, E., Desbat, B., Amédée, J., Guillemot, F. (2011) Laser-assisted bioprinting for creating on-demand patterns of human osteoprogenitor cells and nano-hydroxyapatite. *Biofabrication*. **3**, 25001.

Chang, R., Nam, J., Sun, W. (2008) Effects of Dispensing Pressure and Nozzle Diameter on Cell Survival from Solid Freeform Fabrication–Based Direct Cell Writing. *Tissue Engineering Part A*. **14**(1), 41–48.

Chaudhuri, O., Gu, L., Klumpers, D., Darnell, M., Bencherif, S.A., Weaver, J.C., Huebsch, N., Lee, H.-P., Lippens, E., Duda, G.N., Mooney, D.J. (2015) Hydrogels with tunable stress relaxation regulate stem cell fate and activity. *Nature materials*. **15**(November), 326–333.

Chauhan, V.M., Giuntini, F., Aylott, J.W. (2016) Quadruple labelled dual oxygen and pH-sensitive ratiometric nanosensors. *Sensing and Bio-Sensing Research*. **8**, 36–42.

Chen, B., Jones, R.R., Mi, S., Foster, J., Alcock, S.G., Hamley, I.W., Connon, C.J. (2012) The mechanical properties of amniotic membrane influence its effect as a biomaterial for ocular surface repair. *Soft Matter*. **8**(32), 8379.

Chen, Z., de Paiva, C.S., Luo, L., Kretzer, F.L., Pflugfelder, S.C., Li, D.-Q. (2004) Characterization of Putative Stem Cell Phenotype in Human Limbal Epithelia. *Stem Cells*. **22**(3), 355–366.

Coimbra, P., Gil, M.H., Figueiredo, M. (2014) Tailoring the properties of gelatin films for drug delivery applications: influence of the chemical cross-linking method. *International journal of biological macromolecules*. **70**, 10–9.

Cotsarelis, G., Cheng, S.Z., Dong, G., Sun, T.T., Lavker, R.M. (1989) Existence of slow-cycling limbal epithelial basal cells that can be preferentially stimulated to proliferate: implications on epithelial stem cells. *Cell*. **57**(2), 201–9.

Couture, C., Zaniolo, K., Carrier, P., Lake, J., Patenaude, J., Germain, L., Guérin, S.L. (2016) The tissue-engineered human cornea as a model to study expression of matrix metalloproteinases during corneal wound healing. *Biomaterials*. **78**, 86–101.

Cushing, M., Anseth, K. (2007) Hydrogel cell cultures. *Science*. **316**, 1133–1134.

Dandona, R., Dandona, L. (2003) Corneal blindness in a southern Indian population: need for health promotion strategies. *The British journal of ophthalmology*. **87**(2), 133–41.

Davanger, M., Evensen, A. (1971) Role of the pericorneal papillary structure in renewal of corneal epithelium. *Nature*. **229**, 560–561.

Daya, S.M., Chan, C.C., Holland, E.J. (2011) Cornea Society Nomenclature for Ocular Surface Rehabilitative Procedures. *Cornea*. **30**(10), 1115–1119.

Desai, A.S., Chauhan, V.M., Johnston, A.P.R., Esler, T., Aylott, J.W. (2014) Fluorescent nanosensors for intracellular measurements: synthesis, characterization, calibration, and measurement. *Frontiers in Physiology*. **4**(January), 1–15.

Discher, D., Janmey, P., Wang, Y. (2005) Tissue cells feel and respond to the stiffness of their substrate. *Science*. **310**, 1139–1143.

Doube, M., Firth, E.C., Boyde, A., Bushby, A.J. (2010) Combined nanoindentation testing and scanning electron microscopy of bone and articular calcified cartilage in an equine fracture predilection site. *European Cells and Materials*. **19**, 242–251.

Drira, Z., Yadavalli, V.K. (2013) Nanomechanical measurements of polyethylene glycol hydrogels using atomic force microscopy. *Journal of the Mechanical Behavior of Biomedical Materials*. **18**(0), 20–28.

Dua, H.S., Azuara-Blanco, A. (2000) Limbal Stem Cells of the Corneal Epithelium. *Survey of Ophthalmology*. **44**(5), 415–425.

Dua, H.S., Faraj, L. a., Said, D.G., Gray, T., Lowe, J. (2013) Human corneal anatomy redefined: A novel pre-descemet's layer (Dua's Layer). *Ophthalmology*. **120**(9), 1778–1785.

Dua, H.S., Gomes, J.A., Singh, A. (1994) Corneal epithelial wound healing. *The British journal of ophthalmology*. **78**(5), 401–8.

Dua, H.S., Gomes, J.A.P., King, A.J., Maharajan, V.S. (2004) The amniotic membrane in ophthalmology. *Survey of Ophthalmology*. **49**(1), 51–77.

Dua, H.S., Kulkarni, B., Singh, R. (2006) Quest for limbal stem cells. *Clinical & experimental ophthalmology*. **34**(1), 1–2.

Dua, H.S., Miri, A., Said, D.G. (2010) Contemporary limbal stem cell transplantation - a review. *Clinical & experimental ophthalmology*. **38**(2), 104–17.

Dua, H.S., Saini, J.S., Azuara-Blanco, A., Gupta, P. (2000) Limbal stem cell deficiency: concept, aetiology, clinical presentation, diagnosis and management. *Indian journal of ophthalmology*. **48**(2), 83–92.

Dua, H.S., Shanmuganathan, V.A., Powell-Richards, A.O., Tighe, P.J., Joseph, A. (2005) Limbal epithelial crypts: a novel anatomical structure and a putative limbal stem cell niche. *The British journal of ophthalmology*. **89**(5), 529–32.

Dziasko, M.A., Armer, H.E., Levis, H.J., Shortt, A.J., Tuft, S., Daniels, J.T. (2014) Localisation of Epithelial Cells Capable of Holoclone Formation In Vitro and Direct Interaction with Stromal Cells in the Native Human Limbal Crypt. . **9**(4), 1–9.

Dziasko, M.A., Daniels, J.T. (2016) Anatomical Features and Cell-Cell Interactions in the Human Limbal Epithelial Stem Cell Niche. *The Ocular Surface*. **14**(3), 1–9.

Eberwein, P., Nohava, J., Schlunck, G., Swain, M. (2014) Nanoindentation Derived Mechanical Properties of the Corneoscleral Rim of the Human Eye. *Key Engineering Materials*. **606**, 117–120.

Eberwein, P., Steinberg, T., Schulz, S., Zimmermann, D., Accardi, R., Beck, D., Reinhard, T., Tomakidi, P. (2011) Expression of keratinocyte biomarkers is governed by environmental biomechanics. *European Journal of Cell Biology*. **90**(12), 1029–1040.

Encinas, M. V, Rufs, A.M., Bertolotti, S., Previtali, C.M. (2001) Free Radical Polymerization Photoinitiated by Riboflavin/Amines. Effect of the Amine Structure. *Macromolecules*. **34**(9), 2845–2847.

Engler, A.J., Griffin, M. a, Sen, S., Bönnemann, C.G., Sweeney, H.L., Discher, D.E. (2004) Myotubes differentiate optimally on substrates with tissue-like stiffness: pathological implications for soft or stiff microenvironments. *The Journal of cell biology*. **166**(6), 877–87.

Engler, A.J., Sen, S., Sweeney, H.L., Discher, D.E. (2006) Matrix Elasticity Directs Stem Cell Lineage Specification. *Cell*. **126**(4), 677–689.

Espana, E.M., Kawakita, T., Romano, A., Di Pascuale, M., Smiddy, R., Liu, C.Y., Tseng, S.C.G. (2003) Stromal Niche Controls the Plasticity of Limbal and Corneal Epithelial Differentiation in a Rabbit Model of Recombined Tissue. *Investigative Ophthalmology and Visual Science*. **44**(12), 5130–5135.

Fedorovich, N.E., Oudshoorn, M.H., van Geemen, D., Hennink, W.E., Alblas, J., Dhert, W.J. a (2009) The effect of photopolymerization on stem cells embedded in hydrogels. *Biomaterials*. **30**(3), 344–53.

Figueira, E.C., Di Girolamo, N., Coroneo, M.T., Wakefield, D. (2007) The phenotype of limbal epithelial stem cells. *Investigative Ophthalmology and Visual Science*. **48**(1), 144–156.

Foster, J.W., Jones, R.R., Bippes, C. a, Gouveia, R.M., Connon, C.J. (2014) Differential nuclear expression of Yap in basal epithelial cells across the cornea and substrates of differing stiffness. *Experimental eye research*. **127**, 37–41.

Funderburgh, J.L., Mann, M.M., Funderburgh, M.L. (2003) Keratocyte phenotype mediates proteoglycan structure: A role for fibroblasts in corneal fibrosis. *Journal of Biological Chemistry*. **278**(46), 45629–45637.

Gauvin, R., Chen, Y.-C., Lee, J.W., Soman, P., Zorlutuna, P., Nichol, J.W., Bae, H., Chen, S., Khademhosseini, A. (2012) Microfabrication of complex porous tissue engineering scaffolds using 3D projection stereolithography. *Biomaterials*. **33**(15), 3824–34.

Gibson, I., Rosen, D.W., Stucker, B. (2010) *Additive Manufacturing Technologies*. Boston, MA: Springer US.

Di Girolamo, N. (2015) Moving Epithelia: Tracking the Fate of Mammalian Limbal Epithelial Stem Cells. *Progress in Retinal and Eye Research*. **48**(April), 1–23.

González, S., Chen, L., Deng, S.X. (2017) Comparative Study of Xenobiotic-Free Media for the Cultivation of Human Limbal Epithelial Stem/Progenitor Cells. *Tissue engineering. Part C, Methods*. **23**(4), ten.tec.2016.0388.

Grieve, K., Ghoubay, D., Georgeon, C., Thouvenin, O., Bouheraoua, N. (2015) Three-dimensional structure of the mammalian limbal stem cell niche. *Experimental Eye Research*. **140**, 75–84.

Grobe, G.M., Reichl, S. (2011) Examining the Suitability of Riboflavin/UVA Treatment for Strengthening the Stromal Bioequivalent of a Human Cornea Construct. *Current Eye Research*. **36**(3), 217–231.

Gruene, M., Pflaum, M., Hess, C., Diamantouros, S., Schlie, S., Deiwick, A., Koch, L., Wilhelmi, M., Jockenhoevel, S., Haverich, A., Chichkov, B. (2011) Laser Printing of Three-Dimensional Multicellular Arrays for Studies of Cell–Cell and Cell–Environment Interactions. *Tissue Engineering Part C: Methods*. **17**(10), 973–982.

Gudapati, H., Dey, M., Ozbolat, I. (2016) A comprehensive review on droplet-based bioprinting: Past, present and future. *Biomaterials*. **102**, 20–42.

Gurkan, U.A., El Assal, R., Yildiz, S.E., Sung, Y., Trachtenberg, A.J., Kuo, W.P., Demirci, U. (2014) Engineering Anisotropic Biomimetic Fibrocartilage Microenvironment by Bioprinting Mesenchymal Stem Cells in Nanoliter Gel Droplets. *Molecular Pharmaceutics*. **11**(7), 2151–2159.

Haagdorens, M., Van Acker, S.I., Van Gerwen, V., Ní Dhubhghaill, S., Koppen, C., Tassignon, M.-J., Zakaria, N. (2016) Limbal Stem Cell Deficiency: Current Treatment Options and Emerging Therapies. *Stem Cells International*. **2016**, 1–22.

Hamrah, P., Sahin, A. (2013) Limbus and Corneal Epithelium. In *Ocular Surface Disease: Cornea, Conjunctiva and Tear Film*. pp. 29–33.

Hashmani, K., Branch, M.J., Sidney, L.E., Dhillon, P.S., Verma, M., McIntosh, O.D., Hopkinson, A., Dua, H.S. (2013) Characterization of corneal stromal stem cells with the potential for epithelial transdifferentiation. *Stem cell research & therapy*. **4**(3), 75.

Hatami-Marbini, H., Rahimi, A. (2015) Collagen cross-linking treatment effects on corneal dynamic biomechanical properties. *Experimental eye research*. **135**(April), 88–92.

Hjortdal, J.O., Kobayashi, A.S., Schlegel, W.A., Lawrence, C., Nave, C., Silver, F.H. (1996) Regional elastic performance of the human cornea. *Journal of biomechanics*. **29**(7), 931–42.

Hoch, E., Schuh, C., Hirth, T., Tovar, G.E.M., Borchers, K. (2012) Stiff gelatin hydrogels can be photo-chemically synthesized from low viscous gelatin solutions using molecularly functionalized gelatin with a high degree of methacrylation. *Journal of Materials Science: Materials in Medicine*. **23**(11), 2607–2617.

Hopkinson, A., McIntosh, R.S., Shanmuganathan, V., Tighe, P.J., Dua, H.S. (2006) Proteomic analysis of amniotic membrane prepared for human transplantation: Characterization of proteins and clinical implications. *Journal of Proteome Research*. **5**(9), 2226–2235.

Huang, M., Wang, B., Wan, P., Liang, X., Wang, X., Liu, Y., Zhou, Q., Wang, Z. (2015) Roles of limbal microvascular net and limbal stroma in regulating maintenance of limbal epithelial stem cells. *Cell and Tissue Research*. **359**(2), 547–563.

Hutson, C.B., Nichol, J.W., Aubin, H., Bae, H., Yamanlar, S., Al-Haque, S., Koshy, S.T., Khademhosseini, A. (2011) Synthesis and Characterization of Tunable Poly(Ethylene Glycol): Gelatin Methacrylate Composite Hydrogels. *Tissue Engineering Part A*. **17**(13–14), 1713–1723.

Ionescu, A.-M., Alaminos, M., Cardona, J.D.L.C., García-López Durán, J.D.D., González-Andrades, M., Ghinea, R., Campos, A., Hita, E., Pérez, M.D.M. (2011) Investigating a novel nanostructured fibrin–agarose biomaterial for human cornea tissue engineering: Rheological properties. *Journal of the Mechanical Behavior of Biomedical Materials*. **4**(8), 1963–1973.

Di Iorio, E., Barbaro, V., Ruzza, A., Ponzin, D., Pellegrini, G., De Luca, M. (2005) Isoforms of Np63 and the migration of ocular limbal cells in human corneal regeneration. *Proceedings of the National Academy of Sciences*. **102**(27), 9523–9528.

Isaksson, H., Nagao, S., Małkiewicz, M., Julkunen, P., Nowak, R., Jurvelin, J.S. (2010) Precision of nanoindentation protocols for measurement of viscoelasticity in cortical and trabecular bone. *Journal of Biomechanics*. **43**(12), 2410–2417.

Jayasuriya, A.C., Ghosh, S., Scheinbeim, J.I., Lubkin, V., Bennett, G., Kramer, P. (2003) A study of piezoelectric and mechanical anisotropies of the human cornea. . **18**, 381–387.

Jester, J. V, Petroll, W.M., Barry, P.A., Cavanagh, H.D. (1995) Expression of alpha-smooth muscle (alpha-SM) actin during corneal stromal wound healing. *Investigative ophthalmology & visual science*. **36**(5), 809–19.

Jones, R.R., Hamley, I.W., Connon, C.J. (2012) Ex vivo expansion of limbal stem cells is affected by substrate properties. *Stem Cell Research*. **8**(3), 403–409.

Käpylä, E., Sedlačík, T., Aydogan, D.B., Viitanen, J., Rypáček, F., Kellomäki, M. (2014) Direct laser writing of synthetic poly(amino acid) hydrogels and poly(ethylene glycol) diacrylates by two-photon polymerization. *Materials Science and Engineering: C*. **43**(OCTOBER), 280–289.

Keivyon, K.R., Tseng, S.C.G. (1989) Limbal Autograft Transplantation for Ocular Surface Disorders. *Ophthalmology*. **96**(5), 709–723.

Kim, J.D., Choi, J.S., Kim, B.S., Chan Choi, Y., Cho, Y.W. (2010) Piezoelectric inkjet printing of polymers: Stem cell patterning on polymer substrates. *Polymer*. **51**(10), 2147–2154.

Kim, P., Yuan, A., Nam, K.H., Jiao, A., Kim, D.H. (2014) Fabrication of poly(ethylene glycol): gelatin methacrylate composite nanostructures with tunable stiffness and degradation for vascular tissue engineering. *Biofabrication*. **6**(2), 1–12.

Kim, S.-H., Chu, C.-C. (2009) Fabrication of a biodegradable polysaccharide hydrogel with riboflavin, vitamin B2, as a photo-initiator and L-arginine as coinitiator upon UV irradiation. *Journal of biomedical materials research. Part B, Applied biomaterials*. **91**(1), 390–400.

Klebe, S., Coster, D.J., Williams, K.A. (2009) Rejection and acceptance of corneal allografts. *Current Opinion in Organ Transplantation*. **14**(1), 4–9.

Kolli, S., Lako, M., Figueiredo, F., Mudhar, H., Ahmad, S. (2008) Loss of corneal epithelial stem cell properties in outgrowths from human limbal explants cultured on intact amniotic membrane. *Regenerative medicine*. **3**(3), 329–42.

Kondrashina, A. V., Dmitriev, R.I., Borisov, S.M., Klimant, I., O'Brien, I., Nolan, Y.M., Zhdanov, A. V., Papkovsky, D.B. (2012) A phosphorescent nanoparticle-based probe for sensing and imaging of (intra)cellular oxygen in multiple detection modalities. *Advanced Functional Materials*. **22**(23), 4931–4939.

Koo Lee, Y.E., Ulbrich, E.E., Kim, G., Hah, H., Strollo, C., Fan, W., Gurjar, R., Koo, S., Kopelman, R. (2010) Near infrared luminescent oxygen nanosensors with nanoparticle matrix tailored sensitivity. *Analytical Chemistry*. **82**(20), 8446–8455.

Koroleva, A., Deiwick, A., Nguyen, A., Schlie-Wolter, S., Narayan, R., Timashev, P., Popov, V., Bagratashvili, V., Chichkov, B. (2015) Osteogenic differentiation of human mesenchymal stem cells in 3-D Zr-Si organic-inorganic scaffolds produced by two-photon polymerization technique. *PloS one*. **10**(2), 1–18.

Ksander, B.R., Kolovou, P.E., Wilson, B.J., Saab, K.R., Guo, Q., Ma, J., McGuire, S.P., Gregory, M.S., Vincent, W.J.B., Perez, V.L., Cruz-Guilloty, F., Kao, W.W.Y., Call, M.K., Tucker, B.A., Zhan, Q., Murphy, G.F., Lathrop, K.L., Alt, C., Mortensen, L.J., Lin, C.P., Zieske, J.D., Frank, M.H., Frank, N.Y. (2014) ABCB5 is a limbal stem cell gene required for corneal development and repair. *Nature*. **511**(7509), 353–357.

Labate, C., De Santo, M.P., Lombardo, G., Lombardo, M. (2015) Understanding of the Viscoelastic Response of the Human Corneal Stroma Induced by Riboflavin/UV-A Cross-Linking at the Nano Level. *PloS one*. **10**(4), e0122868.

Lai, J.Y., Lue, S.J., Cheng, H.Y., Ma, D.H.K. (2013) Effect of matrix nanostructure on the functionality of carbodiimide cross-linked amniotic membranes as limbal epithelial cell scaffolds. *Journal of Biomedical Nanotechnology*. **9**(12), 2048–2062.

Last, J. a, Thomasy, S.M., Croasdale, C.R., Russell, P., Murphy, C.J. (2012) Compliance profile of the human cornea as measured by atomic force microscopy. *Micron (Oxford, England : 1993)*. **43**(12), 1293–8.

Lee, S.-Y., Pereira, B.P., Yusof, N., Selvaratnam, L., Yu, Z., Abbas, A.A., Kamarul, T. (2009) Unconfined compression properties of a porous poly(vinyl alcohol)–chitosan-based hydrogel after hydration. *Acta Biomaterialia*. **5**(6), 1919–1925.

Lekhanont, K., Choubtum, L., Chuck, R.S., Sa-ngiampornpanit, T., Chuckpaiwong, V., Vongthongsri, A. (2009) A serum- and feeder-free technique of culturing human corneal epithelial stem cells on amniotic membrane. *Molecular vision*. **15**(June), 1294–302.

Levis, H.J., Brown, R.A., Daniels, J.T. (2010) Plastic compressed collagen as a biomimetic substrate for human limbal epithelial cell culture. *Biomaterials*. **31**(30), 7726–7737.

Levis, H.J., Massie, I., Dziasko, M. a, Kaasi, A., Daniels, J.T. (2013) Rapid tissue engineering of biomimetic human corneal limbal crypts with 3D niche architecture. *Biomaterials*. **34**(35), 8860–8.

Lewis, P.N., White, T.L., Young, R.D., Bell, J.S., Winlove, C.P., Meek, K.M. (2016) Three-dimensional arrangement of elastic fibers in the human corneal stroma. *Experimental Eye Research*. **146**, 43–53.

Li, X., Bhushan, B. (2002) A review of nanoindentation continuous stiffness measurement technique and its applications 10.1016/S1044-5803(02)00192-4 : Materials Characterization | ScienceDirect.com. . **48**, 11–36.

Li, Z., Torgersen, J., Ajami, A., Mühleder, S., Qin, X., Husinsky, W., Holnthoner, W., Ovsianikov, A., Stampfl, J., Liska, R. (2013) Initiation efficiency and cytotoxicity of novel water-soluble two-photon photoinitiators for direct 3D microfabrication of hydrogels. *RSC Advances*. **3**(36), 15939.

Ljubimov, a V, Burgeson, R.E., Butkowski, R.J., Michael, a F., Sun, T.T., Kenney, M.C. (1995) Human corneal basement membrane heterogeneity: topographical differences in the expression of type IV collagen and laminin isoforms. *Laboratory investigation; a journal of technical methods and pathology*. **72**(4), 461–73.

Lo, C.M., Wang, H.B., Dembo, M., Wang, Y.L. (2000) Cell movement is guided by the rigidity of the substrate. *Biophysical journal*. **79**(1), 144–152.

Lombardo, M., Lombardo, G., Carbone, G., Santo, M.P. De, Barberi, R., Serrao, S. (2017) Biomechanics of the Anterior Human Corneal Tissue Investigated with Atomic Force Microscopy. . **53**(2), 1050–1057.

Louvis, E., Fox, P., Sutcliffe, C.J. (2011) Selective laser melting of aluminium components. *Journal of Materials Processing Technology*. **211**(2), 275–284.

Lu, R., Bian, F., Lin, J., Su, Z., Qu, Y., Pflugfelder, S.C., Li, D.Q. (2012) Identification of human fibroblast cell lines as a feeder layer for human corneal epithelial regeneration. *PLoS ONE*. **7**(6), 1–6.

Ma, D.H.K., Lai, J.Y., Cheng, H.Y., Tsai, C.C., Yeh, L.K. (2010) Carbodiimide cross-linked amniotic membranes for cultivation of limbal epithelial cells. *Biomaterials*. **31**(25), 6647–6658.

Markovic, M., Van Hoorick, J., Hölzl, K., Tromayer, M., Gruber, P., Nürnberger, S., Dubruel, P., Van Vlierberghe, S., Liska, R., Ovsianikov, A. (2015) Hybrid Tissue Engineering Scaffolds by Combination of Three-Dimensional Printing and Cell Photoencapsulation. *Journal of nanotechnology in engineering and medicine*. **6**(2), 0210011–0210017.

Marshall, G.E., Konstas, A.G., Lee, W.R. (1991) Immunogold Fine-Structural Localization of Extracellular-Matrix Components in Aged Human Cornea .1. Types-I-Iv Collagen and Laminin. *Graefes Archive for Clinical and Experimental Ophthalmology*. **229**(2), 157–163.

Massie, I., Levis, H.J., Daniels, J.T. (2014) Response of human limbal epithelial cells to wounding on 3D RAFT tissue equivalents: Effect of airlifting and human limbal fibroblasts. *Experimental Eye Research*. **127**, 196–205.

McConney, M.E., Singamaneni, S., Tsukruk, V. V. (2010) Probing Soft Matter with the Atomic Force Microscopies: Imaging and Force Spectroscopy. *Polymer Reviews*. **50**(3), 235–286.

McKee, C.T., Last, J. a, Russell, P., Murphy, C.J. (2011) Indentation versus tensile measurements of Young's modulus for soft biological tissues. *Tissue engineering. Part B, Reviews*. **17**(3), 155–164.

Meek, K.M., Boote, C. (2004) The organization of collagen in the corneal stroma. *Experimental Eye Research*. **78**(3), 503–512.

Meller, D., Pires, R.T.F., Tseng, S.C.G. (2002) Ex vivo preservation and expansion of human limbal epithelial stem cells on amniotic membrane cultures. *The British journal of ophthalmology*. **86**(4), 463–71.

Meyer-Blazejewska, E.A., Kruse, F.E., Bitterer, K., Meyer, C., Hofmann-Rummelt, C., Wünsch, P.H., Schlötzer-Schrehardt, U. (2010) Preservation of the limbal stem cell phenotype by appropriate culture techniques. *Investigative ophthalmology & visual science*. **51**(2), 765–774.

Mi, S., Chen, B., Wright, B., Connon, C.J. (2010) Plastic compression of a collagen gel forms a much improved scaffold for ocular surface tissue engineering over conventional collagen gels. *Journal of Biomedical Materials Research - Part A*. **95 A**(2), 447–453.

Mikhailova, A., Ilmarinen, T., Ratnayake, A., Petrovski, G., Uusitalo, H., Skottman, H., Rafat, M. (2016) Human pluripotent stem cell-derived limbal epithelial stem cells on bioengineered matrices for corneal reconstruction. *Experimental Eye Research*. **146**, 26–34.

Miri, A., Al-Aqaba, M., Otri, A.M., Fares, U., Said, D.G., Faraj, L.A., Dua, H.S. (2012) In vivo confocal microscopic features of normal limbus. *The British journal of ophthalmology*. **96**(4), 530–6.

Miyashita, H., Higa, K., Kato, N., Kawakita, T., Yoshida, S., Tsubota, K., Shimmura, S. (2007) Hypoxia enhances the expansion of human limbal epithelial progenitor cells in vitro. *Investigative Ophthalmology and Visual Science*. **48**(8), 3586–3593.

Moers, K., Steinberg, T., Schlunck, G., Reinhard, T., Tomakidi, P., Eberwein, P. (2013) Substrate elasticity as biomechanical modulator of tissue homeostatic parameters in corneal keratinocytes. *Experimental Cell Research*. **319**(12), 1889–1901.

Mohyeldin, A., Garzón-Muvdi, T., Quiñones-Hinojosa, A. (2010) Oxygen in stem cell biology: A critical component of the stem cell niche. *Cell Stem Cell*. **7**(2), 150–161.

Molvaer, R.K., Andreasen, A., Heegaard, S., Thomsen, J.S., Hjortdal, J., Urbak, S.F., Nielsen, K. (2013) Interactive 3D computer model of the human corneolimbal region: crypts, projections and stem cells. *Acta ophthalmologica*. **91**(5), 457–62.

Murphy, J. (2013) More Details on Dua's Layer of the Cornea. [online]. Available from: http://www.reviewofoptometry.com/content/d/web_exclusives/c/41849/.

Nagasaki, T., Zhao, J. (2003) Centripetal movement of corneal epithelial cells in the normal adult mouse. *Investigative ophthalmology & visual science*. **44**(2), 558–566.

Nakajima, R., Takeda, S. (2014) Fabrication of corneal epithelial cell sheets maintaining colony-forming cells without feeder cells by oxygen-controlled method. *Experimental Eye Research*. **118**, 53–60.

Nakajima, R., Takeda, S. (2013) The efficient fabrication of corneal epithelial cell sheets by controlling oxygen concentration. *Experimental Eye Research*. **116**, 434–438.

Nanoscribe (2014) *Photonic Professional (GT) User Manual*. Eggenstein-Leopoldshafen, Germany: Nanoscribe GmbH.

Nelson, C.M., Jean, R.P., Tan, J.L., Liu, W.F., Sniadecki, N.J., Spector, A. a, Chen, C.S. (2005) Emergent patterns of growth controlled by multicellular form and mechanics. *Proceedings of the National Academy of Sciences of the United States of America*. **102**(33), 11594–11599.

Nguyen, A.H., McKinney, J., Miller, T., Bongiorno, T., McDevitt, T.C. (2014) Gelatin methacrylate microspheres for controlled growth factor release. *Acta biomaterialia*. **13**, 101–10.

Nguyen, A.K., Gittard, S.D., Koroleva, A., Schlie, S., Gaidukeviciute, A., Chichkov, B.N., Narayan, R.J. (2013) Two-photon polymerization of polyethylene glycol diacrylate scaffolds with riboflavin and triethanolamine used as a water-soluble photoinitiator. *Regenerative medicine*. **8**, 725–38.

Nichol, J.W., Koshy, S.T., Bae, H., Hwang, C.M., Yamanlar, S., Khademhosseini, A. (2010) Cell-laden microengineered gelatin methacrylate hydrogels. *Biomaterials*. **31**(21), 5536–5544.

O'Brart, D.P.S., Chan, E., Samaras, K., Patel, P., Shah, S.P. (2011) A randomised, prospective study to investigate the efficacy of riboflavin/ultraviolet A (370 nm) corneal collagen cross-linkage to halt the progression of keratoconus. *British Journal of Ophthalmology*. **95**(11), 1519–1524.

Odland, G.F. (1950) The morphology of the attachment between the dermis and the epidermis. *The Anatomical record*. **108**(3), 399–413.

Ohlstein, B., Kai, T., Decotto, E., Spradling, A. (2004) The stem cell niche: theme and variations. *Current Opinion in Cell Biology*. **16**(6), 693–699.

Ordonez, P., Chow, S., Wakefield, D., Di Girolamo, N. (2013) Human limbal epithelial progenitor cells express alphavbeta5-integrin and the interferon-inducible chemokine CXCL10/IP-10. *Stem Cell Research*. **11**(2), 888–901.

Orellana, B., Rufs, a. M., Encinas, M. V., Previtali, C.M., Bertolotti, S. (1999) The Photoinitiation Mechanism of Vinyl Polymerization by Riboflavin/Triethanolamine in Aqueous Medium. *Macromolecules*. **32**(20), 6570–6573.

Ortega, Í., Deshpande, P., Gill, A.A., MacNeil, S., Claeyssens, F. (2013) Development of a microfabricated artificial limbus with micropockets for cell delivery to the cornea. *Biofabrication*. **5**(2), 25008.

Ortega, I., McKean, R., Ryan, A.J., MacNeil, S., Claeyssens, F. (2014) Characterisation and evaluation of the impact of microfabricated pockets on the performance of limbal epithelial stem cells in biodegradable PLGA membranes for corneal regeneration. *Biomaterials Science*. **2**, 723.

Ortega, I., Ryan, A.J., Deshpande, P., MacNeil, S., Claeyssens, F. (2013) Combined microfabrication and electrospinning to produce 3-D architectures for corneal repair. *Acta biomaterialia*. **9**(3), 5511–20.

Ouyang, L., Yao, R., Mao, S., Chen, X., Na, J., Sun, W. (2015) Three-dimensional bioprinting of embryonic stem cells directs highly uniform embryoid body formation. *Biofabrication*. **7**(4), 44101.

Ovsianikov, A. (2009) *Investigation of Two-photon Polymerization Technique for Applications in Photonics and Biomedicine*. Cuvillier.

Ovsianikov, A., Deiwick, A., Van Vlierberghe, S., Dubruel, P., Möller, L., Dräger, G., Chichkov, B. (2011) Laser fabrication of three-dimensional CAD scaffolds from photosensitive gelatin for applications in tissue engineering. *Biomacromolecules*. **12**(4), 851–8.

Ovsianikov, A., Mühleder, S., Torgersen, J., Li, Z. (2013) Laser photofabrication of cell-containing hydrogel constructs. *Langmuir*. **30**, 3787–3794.

Oyen, M.L. (2014) Mechanical characterisation of hydrogel materials. *International Materials Reviews*. **59**(1), 44–59.

de Paiva, C.S., Chen, Z., Corrales, R.M., Pflugfelder, S.C., Li, D.-Q. (2005) ABCG2 Transporter Identifies a Population of Clonogenic Human Limbal Epithelial Cells. *Stem Cells*. **23**(1), 63–73.

Pati, F., Jang, J., Ha, D.-H., Won Kim, S., Rhie, J.-W., Shim, J.-H., Kim, D.-H., Cho, D.-W. (2014) Printing three-dimensional tissue analogues with decellularized extracellular matrix bioink. *Nature communications*. **5**, 3935.

Pellegrini, G., Dellambra, E., Golisano, O., Martinelli, E., Fantozzi, I., Bondanza, S., Ponzin, D., McKeon, F., De Luca, M. (2001) P63 Identifies Keratinocyte Stem Cells. *Proceedings of the National Academy of Sciences*. **98**(6), 3156–3161.

Pellegrini, G., Golisano, O., Paterna, P., Lambiase, a, Bonini, S., Rama, P., De Luca, M. (1999) Location and clonal analysis of stem cells and their differentiated progeny in the human ocular surface. *The Journal of cell biology*. **145**(4), 769–782.

Pellegrini, G., Rama, P., Di Rocco, A., Panaras, A., De Luca, M. (2014) Concise review: Hurdles in a successful example of limbal stem cell-based regenerative medicine. *Stem Cells*. **32**(1), 26–34.

Pellegrini, G., Traverso, C.E., Franzi, A.T., Zingirian, M., Cancedda, R., De Luca, M. (1997) Long-term restoration of damaged corneal surfaces with autologous cultivated corneal epithelium. *Lancet*. **349**(9057), 990–993.

Peppas, N.A., Hilt, J.Z., Khademhosseini, A., Langer, R. (2006) Hydrogels in biology and medicine: From molecular principles to bionanotechnology. *Advanced Materials*. **18**(11), 1345–1360.

Petsche, S.J., Chernyak, D., Martiz, J., Levenston, M.E., Pinsky, P.M. (2012) Depth-dependent transverse shear properties of the human corneal stroma. *Investigative Ophthalmology and Visual Science*. **53**(2), 873–880.

Pircher, M., Götzinger, E., Leitgeb, R., Fercher, A., Hitzenberger, C. (2003) Measurement and imaging of water concentration in human cornea with differential absorption optical coherence tomography. *Optics express*. **11**(18), 2190–2197.

Pitz, S., Moll, R. (2002) Intermediate-filament expression in ocular tissue. *Progress in Retinal and Eye Research*. **21**(2), 241–262.

Poole, C.A., Brookes, N.H., Clover, G.M. (1993) Keratocyte networks visualised in the living cornea using vital dyes. *Journal of cell science*. **106 (Pt 2**, 685–91.

Proulx, S., d'Arc Uwamaliya, J., Carrier, P., Deschambeault, A., Audet, C., Giasson, C.J., Guérin, S.L., Auger, F.A., Germain, L. (2010) Reconstruction of a human cornea by the self-assembly approach of tissue engineering using the three native cell types. *Molecular vision*. **16**, 2192–201.

Rahman, I., Said, D.., Maharajan, V.., Dua, H.. (2009) Amniotic membrane in ophthalmology: indications and limitations. *Eye*. **23**, 1954–61.

Raiskup, F., Spoerl, E. (2013) Corneal crosslinking with riboflavin and ultraviolet A. I. Principles. *The ocular surface*. **11**(2), 65–74.

Rama, P., Matuska, S., Paganoni, G., Spinelli, A., De Luca, M., Pellegrini, G. (2010) Limbal Stem-Cell Therapy and Long-Term Corneal Regeneration. *New England Journal of Medicine*. **363**(2), 147–155.

Rheinwald, J.G., Green, H. (1975) Formation of a keratinizing epithelium in culture by a cloned cell line derived from a teratoma. *Cell*. **6**(3).

Rizwan, M., Peh, G.S.L., Ang, H.P., Lwin, N.C., Adnan, K., Mehta, J.S., Tan, W.S., Yim, E.K.F. (2017) Sequentially-crosslinked bioactive hydrogels as nano-patterned substrates with customizable stiffness and degradation for corneal tissue engineering applications. *Biomaterials*. **120**, 139–154.

Roa, J.J., Oncins, G., Diaz, J., Sanz, F., Segarra, M. (2011) Calculation of Young's modulus value by means of AFM. *Recent patents on nanotechnology*. **5**(1), 27–36.

Romano, A.C., Espana, E.M., Yoo, S.H., Budak, M.T., Wolosin, J.M., Tseng, S.C.G. (2003) Different Cell Sizes in Human Limbal and Central Corneal Basal Epithelia Measured by Confocal Microscopy and Flow Cytometry. *Investigative Ophthalmology and Visual Science*. **44**(12), 5125–5129.

Rose, J., Pacelli, S., Haj, A., Dua, H., Hopkinson, A., White, L., Rose, F. (2014) Gelatin-Based Materials in Ocular Tissue Engineering. *Materials*. **7**(4), 3106–3135.

Ross, T.D., Coon, B.G., Yun, S., Baeyens, N., Tanaka, K., Ouyang, M., Schwartz, M. a. (2013) Integrins in mechanotransduction. *Current Opinion in Cell Biology*. **25**(5), 613–618.

Rwan, M., Niinikoski, J., HuntHirsch, T.K. (1972) In vivo measurements of oxygen tension in the cornea, aqueous humor, and anterior lens of the open eye. *Ophtahalmol*. **11**(2), 108–114.

Sangwan, V.S., Basu, S., MacNeil, S., Balasubramanian, D. (2012) Simple limbal epithelial transplantation (SLET): a novel surgical technique for the treatment of unilateral limbal stem cell deficiency. *British Journal of Ophthalmology*. **96**(7), 931–934.

Scadden, D.T. (2006) The stem-cell niche as an entity of action. *Nature*. **441**(7097), 1075–1079.

Schafer, K.J., Hales, J.M., Balu, M., Belfield, K.D., Van Stryland, E.W., Hagan, D.J. (2004) Two-photon absorption cross-sections of common photoinitiators. *Journal of Photochemistry and Photobiology A: Chemistry*. **162**(2–3), 497–502.

Schermer, A., Galvin, S., Sun, T.-T. (1986) Differentiation-related expression of a major 64K corneal keratin in vivo and in culture suggests limbal location of corneal epithelial stem cells. *Journal of Cell Biology*. **103**(1), 49–62.

Schlötzer-Schrehardt, U., Dietrich, T., Saito, K., Sorokin, L., Sasaki, T., Paulsson, M., Kruse, F.E. (2007) Characterization of extracellular matrix components in the limbal epithelial stem cell compartment. *Experimental Eye Research*. **85**(6), 845–860.

Schofield, R. (1983) The stem cell system. *Biomedicine & pharmacotherapy = Biomedecine & pharmacotherapie*. **37**(8), 375–80.

Schuurman, W., Levett, P. a, Pot, M.W., van Weeren, P.R., Dhert, W.J. a, Hutmacher, D.W., Melchels, F.P.W., Klein, T.J., Malda, J. (2013) Gelatin-methacrylamide hydrogels as potential biomaterials for fabrication of tissue-engineered cartilage constructs. *Macromolecular bioscience*. **13**(5), 551–61.

Secker, G.A., Daniels, J.T. (2009) Limbal epithelial stem cells of the cornea The Stem Cell Research Community, ed. *StemBook*, 1–18.

Selhuber-Unkel, C., Erdmann, T., López-García, M., Kessler, H., Schwarz, U.S., Spatz, J.P. (2010) Cell adhesion strength is controlled by intermolecular spacing of adhesion receptors. *Biophysical Journal*. **98**(4), 543–551.

Sengupta, C., Sarangi, M.K., Sau, A., Mandal, D., Basu, S. (2015) A case study of photo induced electron transfer between riboflavin and aliphatic amine: Deciphering different mechanisms of ET operating from femtosecond to microsecond time domain. *Journal of Photochemistry and Photobiology A: Chemistry*. **296**, 25–34.

Shanmuganathan, V. a, Foster, T., Kulkarni, B.B., Hopkinson, A., Gray, T., Powe, D.G., Lowe, J., Dua, H.S. (2007) Morphological characteristics of the limbal epithelial crypt. *The British journal of ophthalmology*. **91**(4), 514–519.

Shin, H., Olsen, B.D., Khademhosseini, A. (2012) The mechanical properties and cytotoxicity of cell-laden double-network hydrogels based on photocrosslinkable gelatin and gellan gum biomacromolecules. *Biomaterials*. **33**(11), 3143–3152.

Shirahama, H., Lee, B.H., Tan, L.P., Cho, N.-J. (2016) Precise Tuning of Facile One-Pot Gelatin Methacryloyl (GelMA) Synthesis. *Scientific reports*. **6**(August), 31036.

Shortt, A.J., Secker, G.A., Munro, P.M., Khaw, P.T., Tuft, S.J., Daniels, J.T. (2007) Characterization of the Limbal Epithelial Stem Cell Niche: Novel Imaging Techniques Permit In Vivo Observation and Targeted Biopsy of Limbal Epithelial Stem Cells. *Stem Cells*. **25**(6), 1402–1409.

Sidney, L.E., Branch, M.J., Dua, H.S., Hopkinson, A. (2015) Effect of culture medium on propagation and phenotype of corneal stroma–derived stem cells. *Cytotherapy*. **17**(12), 1706–1722.

Silva, K.R., Rezende, R.A., Pereira, F.D.A.S., Gruber, P., Stuart, M.P., Ovsianikov, A., Brakke, K., Kasyanov, V., Da Silva, J.V.L., Granjeiro, J.M., Baptista, L.S., Mironov, V. (2016) Delivery of human adipose stem cells spheroids into lockyballs. *PLoS ONE*. **11**(11), 1–14.

Simon, M.C., Keith, B. (2008) The role of oxygen availability in embryonic development and stem cell function. *Nature reviews. Molecular cell biology*. **9**(4), 285–96.

Spoerl, E., Wollensak, G., Reber, F., Pillunat, L. (2004) Cross-linking of human amniotic membrane by glutaraldehyde. *Ophthalmic Research*. **36**(2), 71–77.

Stylianou, A., Andreas (2017) Atomic Force Microscopy for Collagen-Based Nanobiomaterials. *Journal of Nanomaterials*. **2017**, 1–14.

Thoft, R.A., Friend, J. (1983) The X , Y , Z Hypothesis of Corneal Epithelial Maintenance. . **24**, 1442–1443.

Torgersen, J., Qin, X.H., Li, Z., Ovsianikov, A., Liska, R., Stampfl, J. (2013) Hydrogels for two-photon polymerization: A toolbox for mimicking the extracellular matrix. *Advanced Functional Materials*. **23**, 4542–4554.

Touhami, A., Grueterich, M., Tseng, S.C.G. (2002) The role of NGF signaling in human limbal epithelium expanded by amniotic membrane culture. *Investigative Ophthalmology and Visual Science*. **43**(4), 987–994.

Trosan, P., Svobodova, E., Chudickova, M., Krulova, M., Zajicova, A., Holan, V. (2012) The Key Role of Insulin-Like Growth Factor I in Limbal Stem Cell Differentiation and the Corneal Wound-Healing Process. *Stem Cells and Development*. **21**(18), 120911063620007.

Truby, R.L., Lewis, J.A. (2016) Printing soft matter in three dimensions. *Nature*. **540**(7633), 371–378.

Tsai, R.J.-F., Li, L.-M., Chen, J.-K. (2000) Reconstruction of Damaged Corneas by Transplantation of Autologous Limbal Epithelial Cells. *New England Journal of Medicine*. **343**(2), 86–93.

Tsai, R.J., Tseng, S.C. (1994) Human allograft limbal transplantation for corneal surface reconstruction. *Cornea*. **13**(5), 389–400.

Tseng, S.C.G. (1989) Concept and application of limbal stem cells. *Eye*. **3**(2), 141–157.

Tsubota, K., Toda, I., Saito, H., Shinozaki, N., Shimazaki, J. (1995) Reconstruction of the corneal epithelium by limbal allograft transplantation for severe ocular surface disorders. *Ophthalmology*. **102**(10), 1486–1496.

Waldock, A. (2000) Corneal transplantation: how successful are we? *British Journal of Ophthalmology*. **84**(8), 813–815.

Wang, L., González, S., Dai, W., Deng, S., Lu, L. (2016) Effect of hypoxia-regulated polo-like kinase 3 (Plk3) on human limbal stem cell differentiation. *Journal of Biological Chemistry*. **291**(32), 16519–16529.

Wang, Z., Abdulla, R., Parker, B., Samanipour, R. (2015) A simple and high-resolution stereolithography-based 3D bioprinting system using visible light crosslinkable bioinks. *Biofabrication*. **7**(4), 1–10.

Waring, G.O., Bourne, W.M., Edelhauser, H.F., Kenyon, K.R. (1982) The corneal endothelium. Normal and pathologic structure and function. *Ophthalmology*. **89**(6), 531–590.

Watt, F.M. (2000) Out of Eden: Stem Cells and Their Niches. *Science*. **287**(5457), 1427–1430.

West-Mays, J.A., Dwivedi, D.J. (2006) The keratocyte: Corneal stromal cell with variable repair phenotypes. *The International Journal of Biochemistry & Cell Biology*. **38**(10), 1625–1631.

Whitcher, J.P., Srinivasan, M., Upadhyay, M.P. (2001) Corneal blindness: A global perspective. *Bulletin of the World Health Organization*. **79**(3), 214–221.

Williams, C.G., Malik, A.N., Kim, T.K., Manson, P.N., Elisseeff, J.H. (2005) Variable cytocompatibility of six cell lines with photoinitiators used for polymerizing hydrogels and cell encapsulation. *Biomaterials*. **26**(11), 1211–8.

Wollensak, G., Spoerl, E., Seiler, T. (2003) Riboflavin/ultraviolet-A-induced collagen crosslinking for the treatment of keratoconus. *American Journal of Ophthalmology*. **135**(5), 620–627.

Wolosin, J.M., Budak, M.T., Akinci, M.A. (2004) Ocular surface epithelial and stem cell development. *Int J Dev Biol*. **48**(8–9), 981–991.

Worthington, K.S., Wiley, L.A., Bartlett, A.M., Stone, E.M., Mullins, R.F., Salem, A.K., Guymon, C.A., Tucker, B.A. (2014) Mechanical properties of murine and porcine ocular tissues in compression. *Experimental Eye Research*. **121**, 194–199.

Wu, Z., Su, X., Xu, Y., Kong, B., Sun, W., Mi, S. (2016) Bioprinting three-dimensional cell-laden tissue constructs with controllable degradation. *Scientific reports*. **6**, 24474.

Xiao, X., Pan, S., Liu, X., Zhu, X., Connon, C.J., Wu, J., Mi, S. (2014) In vivo study of the biocompatibility of a novel compressed collagen hydrogel scaffold for artificial corneas. *Journal of Biomedical Materials Research - Part A*. **102**(6), 1782–1787.

Xu, T., Jin, J., Gregory, C., Hickman, J.J., Boland, T. (2005) Inkjet printing of viable mammalian cells. *Biomaterials*. **26**(1), 93–99.

Xu, T., Zhao, W.X., Zhu, J.M., Albanna, M.Z., Yoo, J.J., Atala, A. (2013) Complex heterogeneous tissue constructs containing multiple cell types prepared by inkjet printing technology. *Biomaterials*. **34**(1), 130–139.

Yamamoto, N., Hirano, K., Kojima, H., Sumitomo, M., Yamashita, H., Ayaki, M., Taniguchi, K., Tanikawa, A., Horiguchi, M. (2010) Cultured human corneal epithelial stem/progenitor cells derived from the corneal limbus. *In Vitro Cellular and Developmental Biology - Animal*. **46**(9), 774–780.

Ye, H.Q., Maeda, M., Azar, D.T. (2017) Differential Expression of MT1-MMP (MMP-14) and Collagenase III (MMP-13) Genes in Normal and Wounded Rat Corneas. . **41**(10), 2894–2899.

Yeo, D.C., Wiraja, C., Mantalaris, A., Xu, C. (2014) Nanosensors for regenerative medicine. *Journal of Biomedical Nanotechnology*. **10**(10), 2722–2746.

Yeung, A.M. (2008) Limbal Epithelial Crypt. *Archives of Ophthalmology*. **126**(5), 665.

Yoshida, S., Shimmura, S., Kawakita, T., Miyashita, H., Den, S., Shimazaki, J., Tsubota, K. (2006) Cytokeratin 15 can be used to identify the limbal phenotype in normal and diseased ocular surfaces. *Investigative Ophthalmology and Visual Science*. **47**(11), 4780–4786.

Young, R.J., Chung, C.I. (1982) Introduction to Polymers. *Journal of Engineering Materials and Technology*. **104**(4), 297.

Yu, M., Bojic, S., Figueiredo, G.S., Rooney, P., de Havilland, J., Dickinson, A., Figueiredo, F.C., Lako, M. (2016) An important role for adenine, cholera toxin, hydrocortisone and triiodothyronine in the proliferation, self-renewal and differentiation of limbal stem cells in vitro. *Experimental Eye Research*. **152**, 113–122.

Yue, K., Trujillo-de Santiago, G., Alvarez, M.M., Tamayol, A., Annabi, N., Khademhosseini, A. (2015) Synthesis, properties, and biomedical applications of gelatin methacryloyl (GelMA) hydrogels. *Biomaterials*. **73**, 254–271.

Zakaria, N., Koppen, C., Van Tendeloo, V., Berneman, Z., Hopkinson, A., Tassignon, M.-J. (2010) Standardized limbal epithelial stem cell graft generation and transplantation. *Tissue engineering. Part C, Methods*. **16**(5), 921–7.

Zakaria, N., Possemiers, T., Dhubhghaill, S.N., Leysen, I., Rozema, J., Koppen, C., Timmermans, J.-P., Berneman, Z., Tassignon, M.-J. (2014) Results of a phase I/II clinical trial: standardized, non-xenogenic, cultivated limbal stem cell transplantation. *Journal of translational medicine*. **12**(1), 58.

Zeng, Y., Yang, J., Huang, K., Lee, Z., Lee, X. (2001) A comparison of biomechanical properties between human and porcine cornea. . **34**, 533–537.

Zhang, C., Hekmatfer, S., Karuri, N.W. (2014) A comparative study of polyethylene glycol hydrogels derivatized with the RGD peptide and the cell-binding domain of fibronectin. *Journal of Biomedical Materials Research - Part A*. **102**(1), 170–179.

Zhao, S., Fernald, R.D. (2005) Comprehensive Algorithm for Quantitative Real-Time Polymerase Chain Reaction. *Journal of Computational Biology*. **12**(8), 1047–1064.

Zhao, X., Song, W., Liu, S., Ren, L. (2016) Corneal regeneration by utilizing collagen based materials. *Science China Chemistry*. **59**(12), 1548–1553.

Zhu, J. (2010) Bioactive modification of poly(ethylene glycol) hydrogels for tissue engineering. *Biomaterials*. **31**(17), 4639–4656.

Zhu, Y., Dong, Z., Wejinya, U.C., Jin, S., Ye, K. (2011) Determination of mechanical properties of soft tissue scaffolds by atomic force microscopy nanoindentation. *Journal of Biomechanics*. **44**(13), 2356–2361.

Zorlutuna, P., Annabi, N., Camci-Unal, G., Nikkhah, M., Cha, J.M., Nichol, J.W., Manbachi, A., Bae, H., Chen, S., Khademhosseini, A. (2012) Microfabricated biomaterials for engineering 3D tissues. *Advanced Materials*. **24**(14), 1782–1804.

Appendix A

Table A.1: Nomenclature and formulation of **macro-scaffolds**. Hydrogels prepared by mixing GelMA and Irgacure (0.5% w/v) as photoinitiator (IR-gels), and crosslinked by UV-light (Chapter 3, 5 and 6).

Nomenclature	Macro-scaffolds (IR-gels)									
	G5	**G8**	**G10**	**G15**			**G20**	**G25**	**G30**	**G40**
				G15	**G15-5**	**G15-20**				
GelMA concentration (% w/v)	5	8	10	15	15	15	20	25	30	40
PEGDA concentration (% v/v)				0	5	20				
Light source	UV									

Table A.2: Nomenclature and formulation of hydrogels prepared by mixing GelMA and Riboflavin-TEOHA as photoinitiator (R-gels), and crosslinked by UV-light (Chapter 4).

Nomenclature		**R20 200-10**	**R20 400-10**	**R20 200-200**	**R25 200-200**	**R30 200-200**	**R40 200-200**	**R50 200-200**
GelMA concentration (% w/v)		20	20	20	25	30	40	50
Photo-initiator	Riboflavin (μm)	200	200	200				
	TEOHA (mM)	10	10	200				
Light source	UV, IR							

Table A.3: Nomenclature and formulation of **micro-scaffolds**. Hydrogels prepared by mixing GelMA and P2CK (0.3% w/v) as photoinitiator (2P-gels), and crosslinked by IR-light (Chapter 3, 5 and 6).

	Micro-scaffolds			
Nomenclature	**2P10**	**2P15**		**2P20**
		2P15	**2P15-5**	
GelMA concentration (% w/v)	10	15	15	20
PEGDA concentration (% v/v)	0	0	5	0

Appendix B

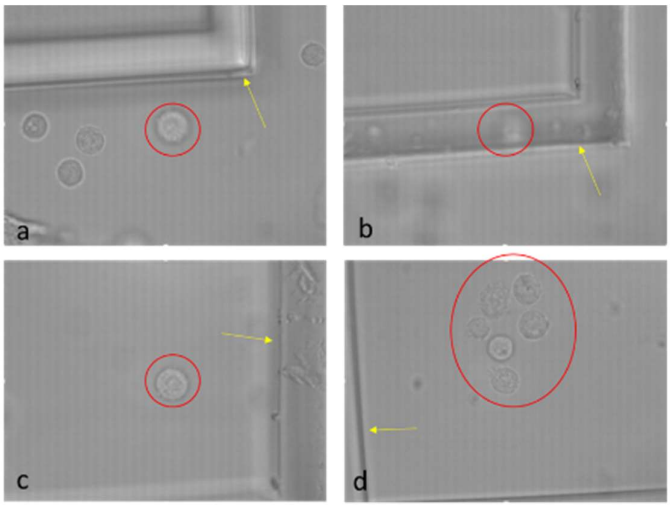


Figure B.1: Images of cells positioned inside the printed niches by optical tweezer. Red circles highlight the cells and the yellow arrows indicate the edges of the scaffold. (a-c) A cell is moved from outside to inside the 2PP scaffold. (d) A pool of cells were moved inside the niche. The experiment was performed by Dr. James Ware at the University of Nottingham.

Appendix C

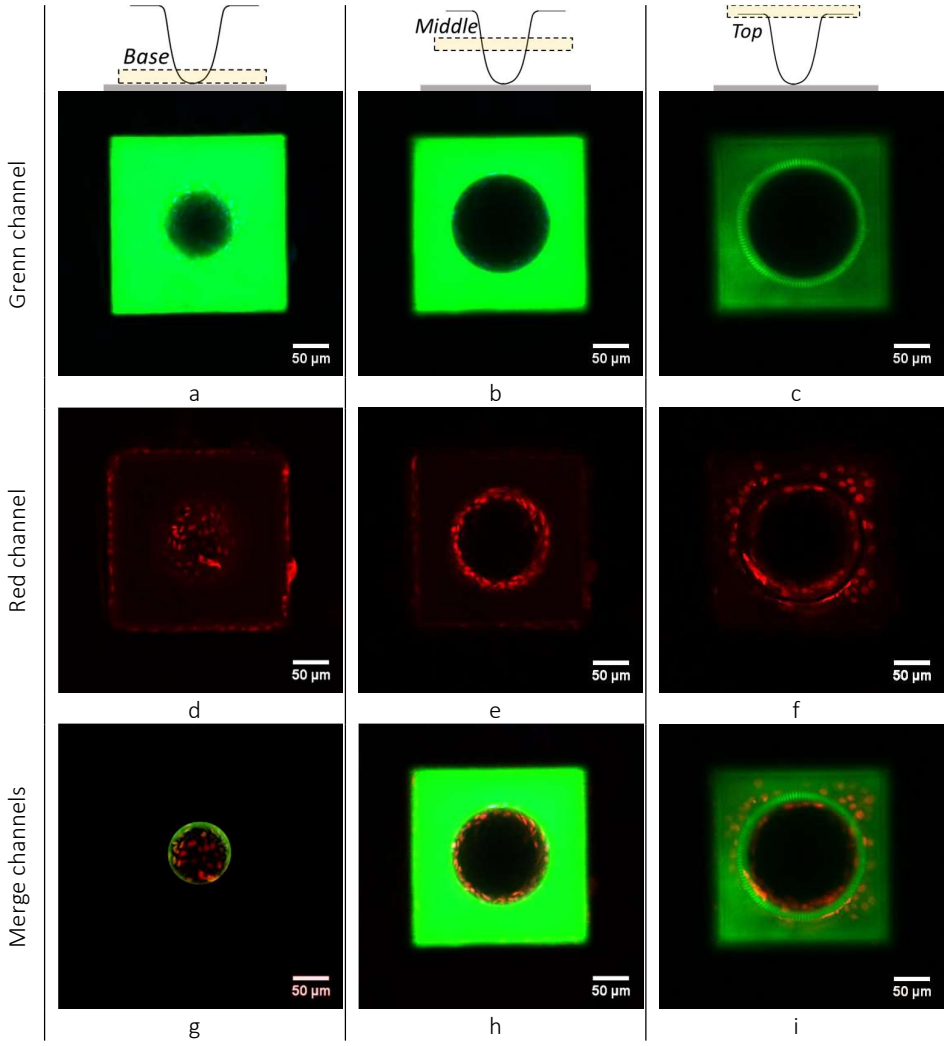


Figure C.1: Series of confocal Z-stack images showing td_hLESCs seeded within the scaffolds at day 4, according to the first strategy (seeding cell suspension inside the niches). Three z-positions representing (a,d,g) the base, (b,e,h) the middle, and (c,f,i) the top of the scaffold are shown. Cells were stained with CK3/12 (green), p63 (red) and HOECHST (blue). (a-c) Green, (d-f) red and (g-i) merged channels are presented. The majority of the cells on the base and on the top of the scaffold expressed the stem cell marker (p63). No cells expressing the differentiation marker were visualized.

Appendix D

Method: Investigation of the oxygen levels within the 2PP printed structures

Oxygen nanosensors represent an interesting and innovative system to investigate the distribution of oxygen levels in gels. As a preliminary proof of concept test, pH nanosensors were used to investigate the oxygen concentration within the 2PP printed structures (figure D.1). GelMa 15% (w/v) was mixed with deionised water, instead of PBS, in order to reduce the buffering capacity of the scaffold. Fluorescence pH nanosensors were mixed at different concentrations (30 mg/mL, 15 mg/mL, 8 mg/mL, and 3 mg/mL) with the gels before printing. The nanosensors were developed by Dr. Veeren Chauhan at the University of Nottingham (Desai *et al.*, 2014). Each nanosensor contains two types of fluorophore: an indicator and a reference. The indicator acts as a transducer, which produces a signal corresponding to the concentration of the analyte of interest. In contrast, the reference fluorophore, which acts as an internal control, produces a constant signal in the red channel and a variable signal in the green channel. The combination of indicator and reference fluorophores allows accurate measurements of changes in pH. The scaffolds were immersed in solutions at different pH (4, 7, and 10). The pH of the scaffold was quantified using confocal microscopy and calculating the ratio of the intensity emitted by the nanosensors in both the green and red channels.

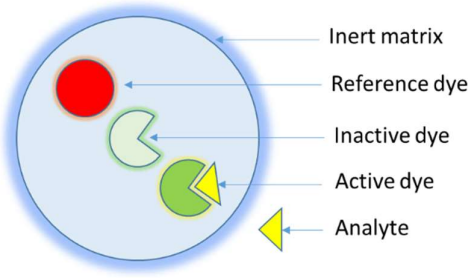
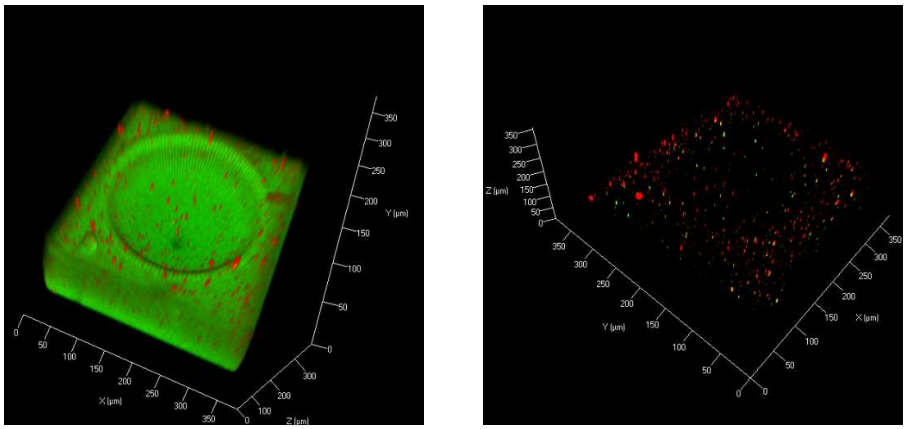


Figure D.1 : diagrammatic representation of a fluorescence pH nanoparticle (~ 50 nm). The pH can be quantified by measuring the ratio of the intensity emitted by the particles (green and red channels). Adapted from (Desai *et al.*, 2014).

Results: Nanosensors require further optimization to be able to detect point-by-point variations inside the micro-scaffolds

The concentration of nanosensors that could be printed with GelMA, without affecting the printing process, was 3 mg/mL. At this concentration, the nanosensors were successfully mixed and printed, as shown in figure D.2. If the concentration was increased above 3 mg/mL (8, 15, and 30 mg/mL), the scaffolds did not polymerise.

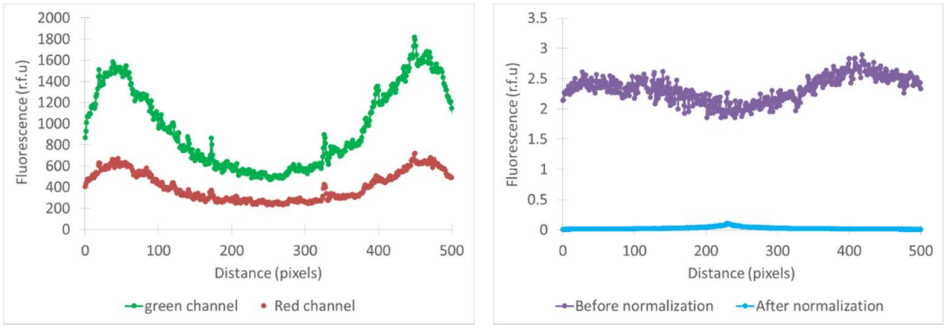


a b

Figure D.2: Confocal fluorescence microscopy images of 3D printed scaffolds prepared with nanosensors. (a) Scaffold before and (b) after auto fluorescence thresholding.

A point-by-point intensity analysis could not be obtained. Therefore, a line across the scaffold was drawn and the ratio between the red and the green

channel values was calculated (figure D.3). The change in intensity along the line was not linear, as it was affected by the auto-fluorescence intensity of the scaffold. The ratio, after height normalization, did not vary along the line.



a b

Figure D.3: Fluorescence intensity of a line across the 3D scaffold at pH 7. (a) Red and green channels and (b) fluorescence ratio before and after the height normalization.

To understand if the autofluorescence influenced the results, the scaffolds were placed in solutions at different pH and the intensity of the green and red channels was measured for all the scaffolds. The intensity of the control scaffold, without nanosensors, was subtracted to the intensity of the nano-scaffolds, and then the ratio between the green and red intensity values was calculated. The results (figure D.4) indicated that the red channel intensity did not change at different pH, as expected. Also the green channel intensity did not show any variations. The auto-fluorescence of the scaffold therefore masked the intensity signal of the nanosensors. No observable differences in fluorescence intensity between the different pH values were detected at pH 4 and 7 (figure D.4 b-d).

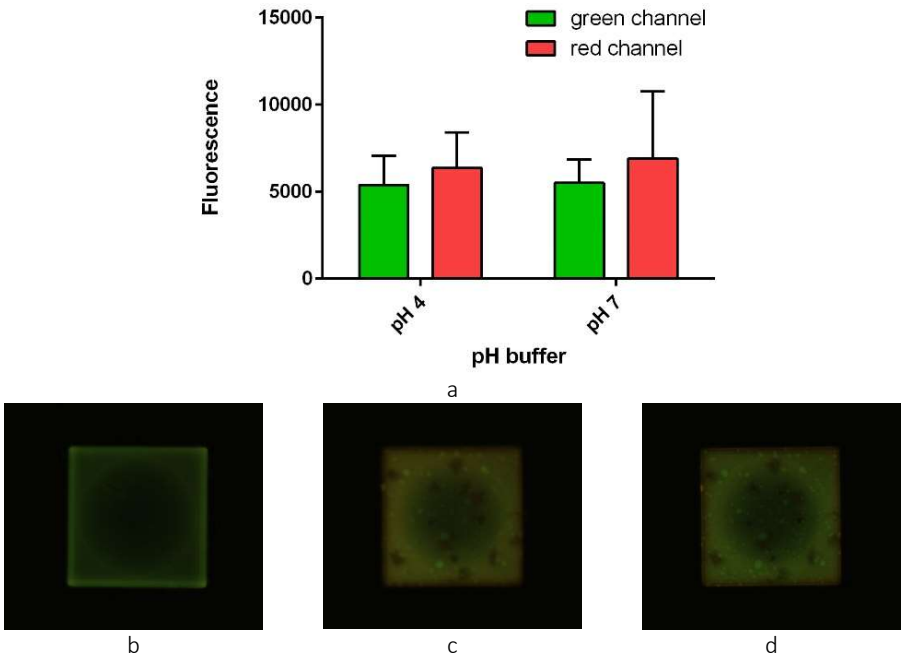


Figure D.4: Fluorescence intensity of the 3D nano-scaffold immersed in buffers at different pH. (a) Red and green channel intensity of the nano-scaffold at pH 7 and 4 (n=2). (b) Fluorescence images of the scaffold (b) without nanosensors, (c,d) with nanoparticles immersed in buffer at (c) pH 7 and (d) pH 4.

Discussion

The use of pH-nanosensors was investigated as a proof of concept for the oxygen-nanosensors. The use of oxygen nanosensors represents an interesting development to obtain a precise quantification of the oxygen spot-by-spot, especially in micro-scaffolds such as those obtained by 2PP technique. Previously, the use of oxygen-nanosensors gave interesting and consistent results (Chauhan *et al.*, 2016; Yeo *et al.*, 2014; Kondrashina *et al.*, 2012; Koo Lee *et al.*, 2010; Kondrashina *et al.*, 2012). However, this approach showed some limitations when applied to scaffolds obtained by 2PP system. To obtain reliable results, it would be necessary to optimize the printing parameters to increase

the number of particles embedded in the polymeric solution, and therefore reduce the background noise.